Forschungszentrum Karlsruhe
Technik und Umwelt

Wissenschaftliche Berichte
FZKA 6200
EUR 18621 EN

Nuclear Fusion Project Annual Report of the Association Forschungszentrum Karlsruhe/EURATOM

October 1997 – September 1998

Projekt Kernfusion

November 1998

Forschungszentrum Karlsruhe

Technik und Umwelt

Wissenschaftliche Berichte

FZKA 6200
EUR 18621 EN

Nuclear Fusion Project
Annual Report of the
Association Forschungszentrum Karlsruhe/
EURATOM
October 1997 - September 1998

Projekt Kernfusion

Forschungszentrum Karlsruhe GmbH, Karlsruhe
November 1998

Forschungszentrum Karlsruhe GmbH
Postfach 3640, 76021 Karlsruhe

ISSN 0947-8620

Forschungszentrum Karlsruhe

Technik und Umwelt

Wissenschaftliche Berichte

FZKA 6200
EUR 18621 EN

Nuclear Fusion Project
Annual Report of the
Association Forschungszentrum Karlsruhe/
EURATOM
October 1997 - September 1998

compiled by G. Kast
Projekt Kernfusion

Forschungszentrum Karlsruhe GmbH, Karlsruhe
1998

Contents

Page

Next Step Technology Programme 1

Plasma Facing Components

T 221 (G 17 TT 13) Plasma Facing Amour Materials (2) 2

T 226b, DV 7b Plasma Disruption Simulaton (1, 2) 4

T 227 (G 17 TT 25) Tritium Permeation and Inventory 7

DV 7a Tritium Permeability, Retention, Wall Conditioning and Clean-up (Dust Removal, Baking) 19

Vessel / in-Vessel

V 59 (T 362) Neutron Streaming Experiment for ITER 20

T 204/209/5 Plasma Arc Cutting of ITER Containment Vessel 22

T 216 (C 16 TT 76) Shield Blanket Fabrication and Testing (2) 24

V 60/1 Blanket Mock-up Fabrication and Testing (1) 25

Magnets

M 31 Development of 60 kA Current Leads Using High Temperature Superconductors 27

M 12 (N 11 TT 19) Preparation of the ITER TF Model Coil Test Facility
and
M 44 TFMC Installation and Test 30

M 45 ITER Coil Casing and Intercoil Structures 33

Remote Handling

D 327/2 (S74TD08) Interim Structural Design Criteria (ISDC) 37

Fuel Cycle

T 228 (G 18 TT 22) Cryopump Development 38

T 332b Plasma Exhaust Processing (2) 45

TEP 3 A Tritium Storage Getter Development (2) 48

TR 1 Tokamak Exhaust Processing 49

TR 2 Development of Tritium Instrumentation 50

TR 3 Extended Life Time Tests of Key Tritium Plant Components 52

TR 4 Tritium Recovery from Plasma Facing Components 53

TR 5 Tritium Recovery from Solid Wastes and Process Equipment Decontamination 54

Safety and Environment

SEA 3 (N 11 TD 72) Reference Accident Sequences – Magnet Systems (2) 55

SEP 2 Environmental Impact 56

Plasma Engineering

Gyrotron Development (includes ITER Tasks T 245/6, T 360 and ECH 3/1) 57

High Power ECH Windows (includes ITER Tasks T 245/6, T 360, ECH 2/1 and D 351) 60

T 246 Ceramics for ECR-Heating, Current Drive and Plasma Diagnostic 63

Studies for ITER / NET

ERB 5000 CT 950064	(NET/95-384)	ITER Magnets and TFMC Stress Analysis	65
ERB 5004 CT 970009	(NET/96-438)	High Voltage Components and Sensor Calibration for the ITER TFMC	67
ERB 5004 CT 970037	(NET/97-450)	ITER Tritium Plant Engineering Design	71
ERB 5004 CT 970082	(NET/97-458)	Acceptance Tests of Strands and Sub-Stage CICC's with Respect to Heat Treatment of TFMC Pancakes	72
ERB 5004 CT 970099	(NET/97-459)	Design and Related Analyses of the ITER Breeding Blanket	73
ERB 5004 CT 980021	(NET/98-433)	Definition of an ITER Primary Wall Module Medium Scale Mock-up Test Programme	75
ERB 5004 CT 980023	(NET/98-472)	ITER Reference Breeding Blanket Design (Stage 2); Materials Assessment, Pebble Bed and Tritium Analysis	76

Long-Term Technology Programme 79

Blanket Development Programme

HCPB Concept

WP B 1 DEMO Blanket Feasibility and Design

B 1.1.1	Segment Design Adaptation to New Specification	80

WP B 2 ITER Test Blanket Module Feasibility and Design

B 2.1.1	TBM Design, Analysis and Integration in ITER	82
B 2.2.1	TBM Ancillary, Equipment Design	85

WP B 3 ITER Blanket Module Fabrication

B 3.1.1	Development of Fabrication Methods and Manufacturing of Mock-ups	86
B 3.2.1	HEBLO Tests and Construction of Test Sections for HEBLO and HE-FUS3	88
B 3.3.4	Help in the Detail Design of an In-pile Test Module	92

WP B 4 Tritium Control and Requirement for Permeation Barriers

B 4.1.1	Tritium Permeation in the TBM and DEMO	93
B 4.2.1	Manufacturing of Test Section for Tritium Permeation Experiments	95

WP B 5 Tritium Extraction and Helium Purification

B 5.1.1	Design of Helium Purification and Tritium Extraction Systems	96

WP B 6 Demonstration of Blanket Safety

B 6.1.1	Safety Approach for the TBM and DEMO	99

WP B 7 Demonstration of Blanket Reliability

B 7.1.3	Contribution to Common Blanket System Data Base	102
B 7.2.2	TBM System Availability	102

WP B 8 Development of Ceramic Pebbles

B 8.1.1	Development of Li_4SiO_4 Pebbles	103
B 8.3.1	Contribution to the PIE of Li_4SiO_4 Pebbles Irradiated in the HFR Petten	106

WP B 9 Behaviour of Beryllium under Irradiation

B 9.1.1 Characterization and Optimization of Beryllium Pebbles 108

B 9.2.1 Behaviour of Beryllium Pebbles under Irradiation 111

WCLL Concept

WP A 2 ITER Test Blanket Module Feasibility & Design

A 2.1.3 MHD Evaluation and Diffusion Bonding Technique Application 114

WP A 3 ITER Test Module Fabrication

A 3.4.2 Adaptation of Diffusion Bonding to TBM Box Fabrication 116

WP A 4 Tritium Control and Permeation Barriers (PB)

A 4.1.2 Fabrication and Characterisation of Permeation Barriers made by Hot-Dipping 117

A 4.2.2 Permeation Reduction Factors (PRF) in Gas and Corrosion in Pb17Li 118

WP A 6 Safety related Activities for DEMO and ITER Test Module

A 6.2.3 Analysis of LOFA 119

WP A 7 Demonstration of Blanket Reliability

A 7.1.3 Contribution to Common Blanket System Data Base 120

A 7.2.3 TBM System Availability 120

WP A 10 MHD Effects

A 10.1.1 and A 10.2.1 Evaluation of Natural Convection and Turbulence, Natural Convection Experiments 121

Structural Materials

SM 1.2.1, SM 1.3.1 MANITU Irradiation Program 125

SM 1.4.1, SM 6.2.2 Effects of Radiation Hardening and He in LAM / Fatigue Properties under Irradiation 126

SM 2.1.4 Mechanical Properties and Microstructure of Reduced Activation Ferritic/ Martensitic Steels (RAF) 131

SM 2.2.1 Fatigue and Creep Properties of Base Material F82H mod. And OPTIFER IV 133

SM 3.8.1 Corrosion of RAF/M Steel in Liquid Pb-Li 136

SM 4.2.1 Weldability Tests (Diffusion Welding) 137

SM 5.1.1 Lifetime Prediction and Requirements for Material Data 138

SM 5.2.1 Fracture Mechanics Studies 139

SM 5.3.2 Procurement Specification for a RAF/M steel EUROFER 97 140

Materials for DEMO

Neutron Source

ERB 5004 CT 970072 (NET/97-453) Evaluation and Refinement of the Conceptual Design of the Experimenal Test Assembly of the D-Li Neutron Source 141

Nuclear Data Base

Nucelar Data Base 147

Activation Library 149

Safety and Environment

SEAFP 2 Long Term Safety Program 153

SEAL 1.3 Beryllium Behaviour under Irradiation 154

Socio-economic Research on Fusion (SERF)

Fusion as a Large Complex System 155

Appendix I Table of ITER / NET Contracts 156

Appendix II FZK Departments Contribution to the Fusion Project 157

Appendix III Fusion Project Management Staff 158

Next Step Technology Programme

The Association FZK-EURATOM contributes to various fields of the European Next Step Fusion Technology Programme. The work is strongly focused on the ITER Engineering Design Activity. Development of superconducting magnets and microwave heating systems are equally important for the stellarator project Wendelstein 7X.

FZK has upgraded the TOSKA magnet test facility to be able to test, successively, the prototype coil for W7X (from mid 1998 on) and the ITER toroidal field model coil (after 1999). Preparatory steps were qualification of the LCT background field coil for a field strength of 10 Tesla at superfluid helium temperatures, adaptation of the data acquisition system and operation of the cryogenic system including separate loops for 1.8 K and 4.5 K cooling circuits for the background field coil and the test coil, respectively. Conductor- and flat coil tests were performed for quality assurance of the W7X-conductor, paralleling the industrial fabrication of the prototype coil. The prototype coil for W7X was delivered to FZK, preparations for the test are ongoing at the time of this report.

Major modifications are being made to the power supplies and the fast switching system in view of high current (80 kA), fast discharge operation of the ITER model coil. The test programme for the ITER model coil was elaborated. A first test, beginning 1999, will be devoted to evaluating the performance of the coil in its self generated field. In a second test, the background field of the LCT-coil will be applied.

Forces on the coils (W7X and ITER) as expected in full machine operation shall be simulated in the TOSKA experiments. Finite element calculations are improved to describe stresses and displacements under load. Studies for ITER-EDA include magnet safety aspects and the mechanical behaviour of low temperature structural materials.

The extended engineering design activity for ITER leaves time for improvements on the microwave heating system. More power per generator unit, higher power efficiency and more flexibility in choosing the wavelength are development goals of the FZK gyrotron activity. Work splits into development of a coaxial gyrotron (1,5 to 2 MW power at 170 GHz) and of suitable high power windows. New materials as CVD diamond are qualified for use as water cooled disk windows that cope with up to 2 MW of transmitted power. Progress was made in increasing the output power of the test tubes to more than 1.7 MW.

In the field of Vacuum Technology and Fuel Cycle two important contributions are being made to the development and testing of prototypical components for the ITER machine. It has been demonstrated that cryopumping can cope with all requirements for the vacuum system of ITER including very short pumping/regeneration cycles to limit tritium accumulation on the panels. A half-scale prototypical cryopump is being manufactured under industrial contract and will be extensively tested at FZK.

Demonstration of a technical process for tritium recycling from the plasma exhaust with a decontamination factor in the 10^7 range is well underway in the Karlsruhe Tritium Laboratory (TLK). After the different conversion and separation steps have all shown excellent performance, a facility is being built the specifications of which have been adopted for the ITER Tritium Plant. Modelling has been continued on tritium behaviour in the environment.

A small number of individual activities, based on available expertise and testing facilities, has been ongoing for ITER contributing to the field of Plasma Facing Components. They cover three different aspects of First Wall behaviour under the impact of the plasma: tritium uptake, plasma erosion and cyclic heat load.

T 221 (G 17 TT 13)
Plasma Facing Armour Materials (2)

Within this task the tritium amount and thermal desorption behaviour of tokamak tiles, co-deposited layers and flakes is determined and tritium removal by burning shall be investigated.

In the previous Annual Report results on tritium amount and desorption behaviour of JET tiles have been discussed [1]. These tiles were employed during the first tritium campaigns in 1991 and were examined in detail - within a JET task - by full combustion thermogravimetry and thermal desorption [2].

In the reporting period JET carbon flakes received October 1997 were studied [3]. The flakes (~ 40 µ thick, up to 2 cm length) were collected from the bottom of the divertor after the campaigns (~ 2000 plasma pulses) from April to October 1996 (before the second tritium compaigns). The flakes were specified by JET to consist of carbon saturated with D and with a Be content of 0.5 wt% and a tritium activity of ~ 4 : 10^6 Bq/g [4].

The total carbon content of the flakes was determined by burning in oxygen and measuring the CO_2 concentration in the offgas by infrared spectroscopy and was found to be only 32.6 wt%. Optical microscopy and SEM analysis showed that the flakes are mostly pieces from flat layers (thickness ~ 100 µ), which consists of many sublayers (thickness several µ). In addition, metallic particles (consisting mainly of Fe, Ni and Cr, i.e. stainless steel components) were observed (fig. 1).

Fig. 1: JET flakes

In addition, element analyses were performed by wavelength dispersive X-ray microanalysis in the elemental range from beryllium to the actinides and by X-ray diffraction. Metallic and ceramic ingots up to 0.5 mm diameter were observed consisting of Al, Al_2O_3, Al-Mg, Mg_2Si, austenitic steel and nickel base alloys. The major phases are graphite with stratified layers of aluminium, austenitic steel and nickel base alloys up to 2 µm thickness on the surface and within the flakes. The graphite also contains about 3 % oxygen. The carbon fraction is higher than 80 % of the total material. This is in contradiction with the result of the burning test.

Tritium inventory and release kinetics has been studied by thermal desorption, purging with He + 0.1 % H_2 and heating continuously up to 1100 °C. The maximum release rate is observed at ~ 800 °C. The specific tritium inventory for different samples varied between $1.2 \cdot 10^7$ and $1.8 \cdot 10^7$ Bq/g. Huge weight losses of up to 40 % were observed after annealing.

In collaboration with the Fusion Centre, Moscow, the retention of deuterium in ion sputtered Be films and in co-deposited Be/D layers has been studied [5].

Deuterium retention in ion sputtered beryllium films and, as a reference, in beryllium plates irradiated with 400 eV D ions has been determined. The data on 400 eV D ion implanted beryllium are in a good agreement with the results for 0.5 - 10 keV ions published by other researchers. It has been found that the amount of deuterium retained at 300 and 600 K is about the same, suggesting a large role of radiation defects on deuterium retention even at 400 eV irradiation.

For 300 and 600 K irradiation the deuterium retention in thermally grown BeO film is of the same order as that in metallic beryllium. It is essential that the retained amount remains unchanged up to 900 K irradiation temperature which might be ascribed to the formation of additional deep traps for implanted deuterium.

Deuterium retention in ion sputtered beryllium oxide films appears to be smaller than that in thermally grown near-surface beryllium oxide films by about a factor three. This disparity might be due to differences in their microstructure and, in particular, different sizes of the crystallites.

It has been found that in the codeposition conditions used in present work, beryllium is deposited in the form of a polycrystalline beryllium oxide film. An important result is that deuterium concentration in the film increases with increase of substrate temperature. At 600 K the average deuterium concentration is calculated to be 0.032 D/BeO. The deuterium desorption flux from the film deposited at 300 K is less than that for 600 K deposition by a factor of ~ 5. Correspondingly the value of deuterium concentration in the film is calculated to be less than 0.005 D/BeO. Sticking coefficient of the ion sputtered beryllium atoms at the growing BeO film decreases with substrate temperature increase from 300 to 600 K by a factor of two.

In collaboration with TRINITI Troitsk, Russia, the production of redeposited graphite layers in disruption simulation experiments at the MK-200 UG pulsed plasma gun is investigated and the hydrogen uptake during plasma irradiation is determined.

Important results from the first series of tests (August to December 1997) were [6]:

- Redeposited graphite layer of about 1 µm thickness was produced at the graphite and tungsten collectors.
- Specific weight of redeposited graphite is ~1.2 g/cm^3.
- Retained deuterium is observed in the redeposited graphite layers produced in disruption simulation experiments.

- Deuterium atomic concentration was measured to be D/C = 2 - 30 % in the redeposited carbon layer.

- Deuterium concentration seems to depend on the collector temperature.

These studies have been continued in 1998.

Literature:

[1] R. Rolli, H. Werle, "Bestimmung der Tritiummenge in Graphit-Ziegeln von JET durch thermische Desorption", FZK Internal Report, PKF 098, September 1997.

[2] R.-D. Penzhorn et al., "Determination of tritium profiles in first wall fusion reactor tiles and development of a process for their detritiation", to be published in J. Nucl. Mater.

[3] R. Rolli et al., "Untersuchungen an Graphitflocken ("Flakes") vom JET-Divertor", FZK Internal Report, PKF 105, March 1998.

[4] A.T. Peacock, JET, private communication.

[5] A.P. Zakharov et al., "Investigation of Deuterium Retention in Ion Sputtered Beryllium Films and Composited Be/D Layers", Fusion Centre, Moscow, unpulished report, June 1998.

[6] N.I. Arkhipov et al., "First Investigation on Redeposited Graphite Layers", TRINITI Troitsk, unpublished report, December 1997.

Staff:

E. Damm
H.D. Gottschalg
E. Kaiser
H. Kleykamp
R. Pejsa
A.T. Peacock, JET
R.-D. Penzhorn
R. Rolli
V.M. Safronov, TRINITI Troitsk
F. Weiser
H. Werle
A.P. Zakharov, RAS Moscow
H. Ziegler

T 226b, DV 7b
Plasma Disruption Simulation (1, 2)

During the period to be reported here the main activities were on validation and application of the 2 dim radiation magnetohydrodynamic (R-MHD) code FOREV-2 for analysis of disruption erosion under realistic ITER conditions [1, 2]. One example of validation of FOREV-2 against results from disruption simulation experiments and results of a 2 dim analysis of MHD motion of plasma shields and of erosion by vaporization of the ITER slot divertor for power densities of the impacting hot plasma along the separatrix in the range of 3 to 100 MW/cm^2 are presented.

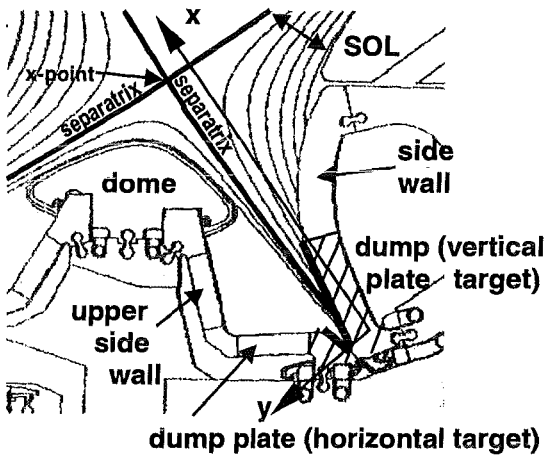

Fig. 1a: Poloidal cross section of the outboard wing of the ITER slot divertor and coordinate system for the 2 dim calculation.

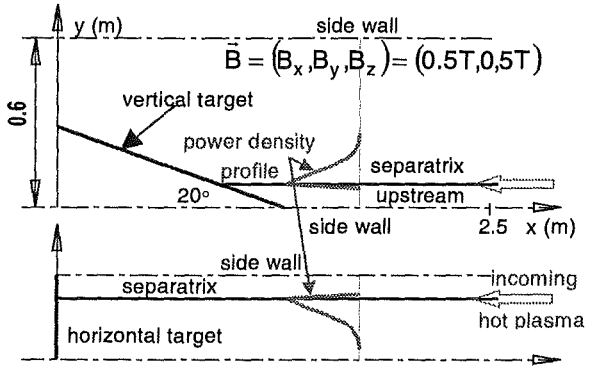

Fig. 1b: Simplified geometry for the 2 dim calculation for the slot divertor with vertical and horizontal target (dump plate) in poloidal plane. Incoming hot plasma along magnetic field lines .

The outboard wing of the slot divertor is shown schematically in Fig. 1a in the poloidal plane. The distance from the x point to the dump plate is about 2.0 m. The side wall distance is about 60 cm. The upper part of the side walls, the dump plate and most part of the dome are inclined (vertical target) with respect to the separatrix with downstream separatrix strike point (SSP). During disruptions and ELMs a shift of the separatrix can't be excluded [3]. Therefore the smaller dump plate and the tungsten dome could be hit during such an event too. In this case the following two different situations might arise: horizontal target and vertical target with separatrix upstream. This case is shown in Fig. 1b indicating the geometry as used in the 2 dim calculations with FOREV-2 and the asymmetrical (realistic) power density profile of the impacting hot plasma across the scrape off layer (SOL). In the case of separatrix downstream the power density profile is inverted in comparison with the case shown in Fig. 1b. For the vertical target the inclination angle is assumed to be 20°. In x direction the computational region extends up to 2.5 m. The unperturbed magnetic field lines B_0 have components in x- and z-direction according to $B_0 = (B_x, B_y, B_z) = (0.5\ T, 0, 5\ T)$. Thus the impact angle of the hot SOL plasma in toroidal direction is 5°.

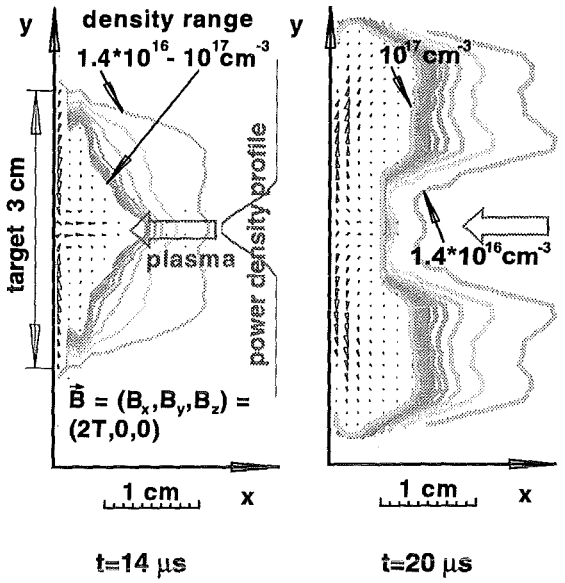

Fig. 2: Calculated contour plots of plasma density and plasma flow (Γ=nv, arrows) in a carbon plasma shield for a perpendicular graphite target, for the disruption simulation facility 2MK-200 CUSP. For further details see Fig. 3.

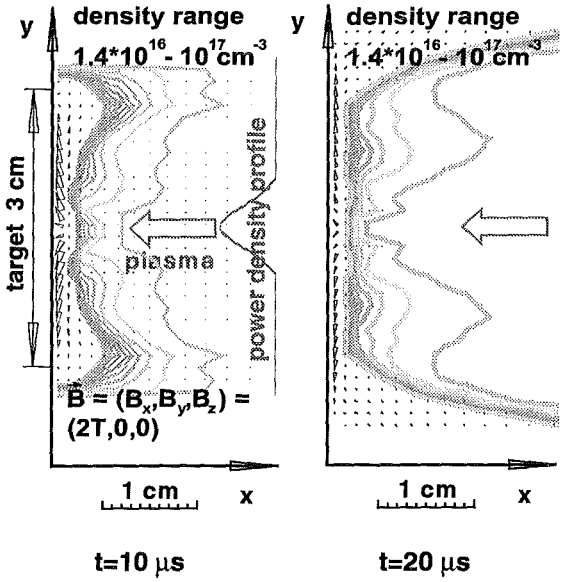

Fig. 3: Calculated contour plots of plasma density and plasma flow in a quartz plasma shield. Perpendicular quartz target, Gaussian power density profile of the hot plasma with peak value of 20 MW/cm^2. Guiding magnetic field is 2T.

Results of magnetized hot plasma target experiments performed at the plasma gun facilities 2MK-200 CUSP [4] and MK-200 CUSP [5] at TRINITI Troitsk with perpendicular and tilted targets were used for code validation. For perpendicular targets an erosion value of 0.2 μm was obtained for graphite and 0.75 μm for quartz under otherwise identical experimental conditions. The reason for the quite large difference in erosion was investigated with FOREV-2. The term quartz plasma is used below. The plasma actually consists of silizium and oxygen ions. Calculated 2 dim plasma density contours and the plasma flow $\Gamma = nv$ are shown in Figs. 2 and 3 for a carbon and a quartz plasma shield at two different times. At early times the carbon plasma close to the target flows across the magnetic field lines to the separatrix (inward flow) and then along the separatrix upstream. Later in time ($t \geq 20$ μs) the plasma flow close to the target changes its direction and flows outward as shown in Fig. 2 at $t = 20$ μs.

The target heat flux by electron heat conduction is shown in Fig. 4. During the period of plasma flow to the separatrix with high plasma density and low plasma temperature the target heat flux by electron heat conduction at the position of the SSP is small. After plasma flow reversal ($t > 20$ μs) the plasma density close to the target decreases but the plasma temperature increases and thus the electron heat conduction flux to the target increases again. The calculated erosion value is 0.25 μm in comparison with the measured value of 0.2 μm. It is fully determined by electron heat conduction.

Quartz has a smaller electric conductivity than graphite. The plasma shield is experiencing no lateral magnetic force and momentum transfer from the hot plasma ions is dominating the movement. The plasma close to the target all the time flows along the target in outward direction away from the separatrix as shown in Fig. 3. The outward flow just from the beginning results in a higher electron heat conduction flux to the target as shown in Fig. 4.

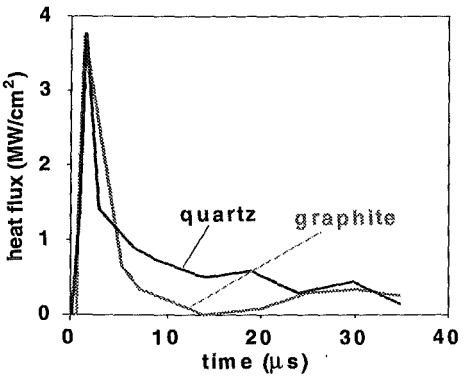

Fig. 4: Comparison of calculated electron heat conduction fluxes to the target at position of the separatrix strike point for a perpendicular graphite and quartz target.

Fig. 5 shows a comparison of measured and calculated time dependencies of erosion of quartz. The calculated erosion values are in good agreement with the measured ones. In the experiment the time dependent erosion left and right from the center differs because of the asymmetric power density profile of the magnetized plasma [6].

For ITER the disruptive hot SOL plasma of energy of 10 keV hits the target while flowing along the originally unperturbed inclined magnetic field lines B_0. The time evolution of calculated ITER target heat fluxes at the SSP is shown in Fig. 6 for the case separatrix upstream. Direct heating by the hot SOL plasma dominates the target heat load at 10 MW/cm² at least up to 1 ms. For 100 MW/cm² the radiative target heat load becomes about 0.15 MW/cm² and essentially remains constant up to 1 ms. At times later than 20 μs the radiative target heat load becomes the dominating heat load. Direct target heating by the hot SOL plasma after 100 μs becomes rather small indicating efficient target shielding by the plasma shield. Electron heat conduction fluxes are negligible. This is rather different to the situation at the disruption simulation experiments. Radiation fluxes to the upper side wall are shown in Fig. 7 at different times. Typical heat flux values are 0.15 MW/cm² as long as no side wall vaporization occurs. Afterwards the radiative heat load drops to about 90 kW/cm² and the deposition width increases up to 2 m. For horizontal targets the heat fluxes and the deposition widths are comparable.

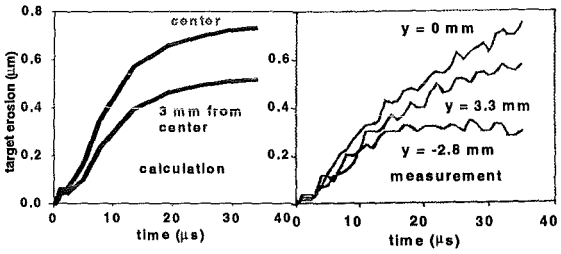

Fig. 5: Comparison of measured and calculated time dependent erosion of perpendicular quartz target at different positions.

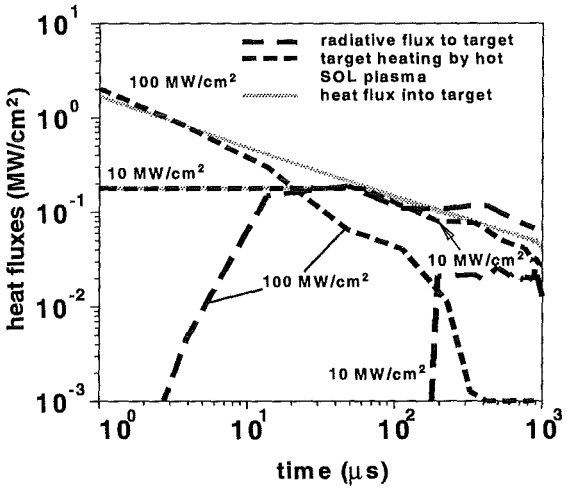

Fig. 6: ITER target heat fluxes at position of maximum erosion for vertical target and two different peak power densities.

The radiative heat load to the ITER slot divertor side wall scales linearly with the peak power density of the impacting hot plasma [6]. A first estimation on damage of side walls was performed for a vertical graphite target. For a peak power density of 10 MW/cm² and times up to 100 ms the surface temperature of tungsten side walls remains below 3000 K. At graphite side walls evaporation would start after 0.1 ms. Below 10 MW/cm² melting of tungsten side walls does not occur within 1 sec. For a peak power density of 100 MW/cm² melting and evaporation of tungsten and graphite side walls occur. After 1 ms tungsten side

walls start to melt over a length of about 1 m. Tungsten evaporation starts after about 5 ms. With graphite as side wall material evaporation of the upper side wall will start after 0.12 ms. After 1 ms peak erosion is 3 μm and the half width of the erosion profile is 1 m.

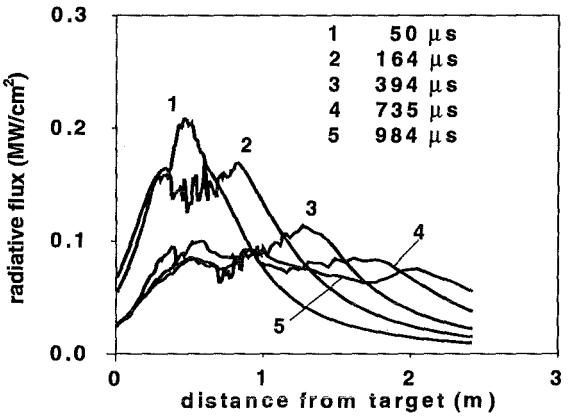

Fig. 7: Radiative fluxes from carbon plasma shield to upper side wall of the ITER slot divertor. Vertical target, realistic power density profile, peak power density 100 MW/cm^2 along magnetic field lines, side wall distance 60cm.

FOREV-2 allows a consistent 2 dim damage analysis of the rather complicated ITER slot divertor. The good agreement between numerical and experimental results from disruption simulation experiments at the CUSP facilities demonstrates the adequacy of the physical models used in FOREV-2. Information on the important question of long term stability and MHD movement of plasma shields will be gained from a numerical analysis of recently performed erosion experiments at the QSPA facility at Kharkov [7].

Literature:

[1] H. Würz, et al., "A first consistent analysis of erosion of the ITER vertical targets for disruptions and ELMs", 25th EPS Conf. on Controlled Fusion and Plasma Physics, Prag, June 29 - July 3, 1998.

[2] H. Würz et al., "A consistent 2D analysis of erosion of the ITER Slot divertor", 20th SOFT, Sept. 7 - 11, 1998, Marseille, France.

[3] J. Lingertat, et al., J. Nucl. Mater, 241 - 243, 1997, p. 402.

[4] N.I. Arkhipov, et al., Fusion Technology 1994, Vol. 1, p. 463, 1995.

[5] N.I. Arkhipov, et al., J. Nucl. Mater 233 - 237, 1996, p. 767.

[6] B. Bazylev, et al., FZKA-report to be published.

[7] V.V. Chebotarev et al., Fusion Technology 1996, Vol. 1, p. 351, 1997.

Staff:

B. Bazylev
F. Kappler
L. Landman
S. Pestchanyi
H. Würz

T 227 (G17 TT 25)
Tritium Permeation and Inventory

Subtasks: 16, 17

1. Introduction

Studies of processes in fusion power machines include the study of the interactions of the thermonuclear plasma with the materials of the first wall and the divertors. In today's fusion reactors these parts are mostly covered with graphite. The low atomic number and the high melting-point are advantageous for the use as plasma facing material. But the large adsorption and accumulation of hydrogen isotopes and the desorption due to heating, also the erosion of graphite by hydrogen are disadvantageous. Therefore the investigation of these processes is important for the qualitative and quantitative understanding of the hydrogen isotope balance as well as the trapping and release mechanisms of hydrogen isotopes in/from graphite.

In this report we describe an UHV setup, which was used for the "Temperature Programmed Desorption" (TPD) of hydrogen isotopes from graphite. It was developed and realized at the Otto-von-Guericke-Universität, Magdeburg, in cooperation with the Forschungszentrum für Technik und Umwelt, Karlsruhe, and the Max-Planck-Institut für Plasmaphysik, Garching. Furthermore, we describe the measurements of the released amounts of hydrogen isotopes from graphite and tungsten coated graphite samples and our results for the round robin experiment, which serves to investigate the comparability of the quantitative results of different analysis method.

2. Experimental setup

The investigations on the hydrogen isotope inventory in graphite samples required special experimental conditions is the setup: Owing to the loading of energy and the bombardment by hydrogen ions of the vacuum vessel walls in tokamaks the hydrogen ions are implanted or co-implanted with carbon into the graphite plates. The originated hydrogen-carbon bonds require high desorption energies and high temperature, respectively. Therefore, the vacuum system, the sample heating, the temperature measurement, and the measurement software were adapted to these requirements. For the measurements of the hydrogen inventory we used the "Temperature Programmed Desorption" (TPD).

2.1 Vacuum system

The UHV system used in our measurements (see Fig. 1 and Fig. 2) based on a combination of a turbo molecular pump (Balzers TPU 240) and a rotary vane pump (Balzers, DUO 016B). The chamber containing the sample holder is represented by a CF100-T-piece and evacuated by the turbo molecular pump. By the compact arrangement of the UHV system and the only use of copper gaskets a base pressure in the 10^{-10} mbar range can be reached in the vacuum chamber.

For the measurement of the total and the partial pressures a Bayard-Alpert ionization gauge (Leybold company, IE 414 +IM520) and a quadrupole mass spectrometer of the Transpector type (Leybold company) are used, respectively. Therefore, the quadrupole mass spectrometer and the ionization gauge are connected to the sample chamber via reducing coupling and elbows at equivalent positions with respect to the sample and with no direct line of sight between both.

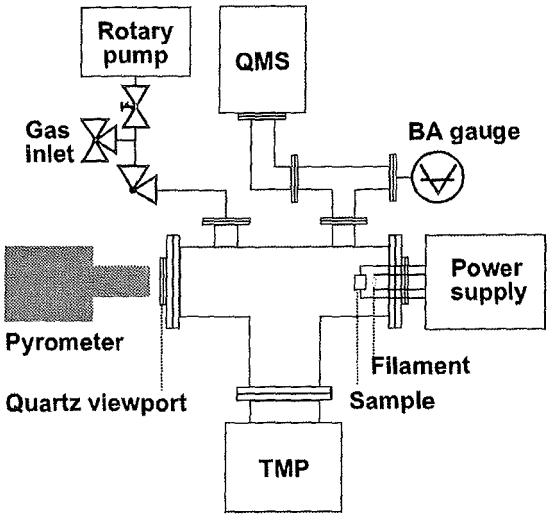

Fig. 1: Experimental setup
Bagauge - Bayard-Alpert gauge, QMS - Quadrupole mass spectrometer, TMP - turbo molecular pump [1].

For calibration of the two measuring systems a gas inlet system is connected with the vacuum vessel via an all metal leak valve. The gas inlet system can be differentially pumped by a rotary vane pump and the pressure can be determined by a Pirani gauge (Leybold company, TR305) [1].

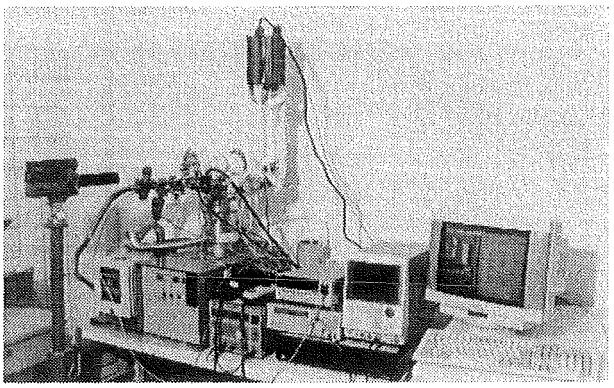

Fig. 2: Picture of the measurement arrangement.

2.2 Sample heating

In many preliminary investigations it was shown that a temperature up to 1900 K is needed for a complete outgassing of the samples. To ensure a low outgassing of the chamber walls it is necessary that the temperature of these walls is kept as low as possible. Other problems are the uniform heating of the samples, the adjustment of the sample holder to the sample shape and the measurement of the sample temperature. For all these reasons an electron bombardment heating from the rear side was chosen.

The advantages of this sample heating are the high reachable sample temperature (up to 2100 K), the good uniformity of heating and the use of a photo-electric pyrometer. The electron source, a hot tungsten filament cathode (with a temperature of about 2000 K), is fed by a laboratory transformer (NG 303, Ch. Beha GmbH) with a maximal power of 90 W. The hot filament cathode consists of a tungsten wire of 0.2 mm diameter, which is wound to a coil of 1 mm diameter and 14 turns. The acceleration energy is provided by a programmable high voltage transformer (PFG 10000 DC, Fa. Hüttinger, bias voltage from 10 to 1000 V).

A special sample holder was constructed for the above described sample heating. The first model of it is shown in Fig. 3. Due to the high temperature the holder consists of molybdenum wires with a thickness of 0.8 mm. The sample holder and the hot filament cathode are fixed to an electrical feed-through which is connected to the chamber wall too. The special shape of the sample holder is needed for the temperature measurement with a photo-electric pyrometer (SP-51, INFRA SENSOR GmbH, measuring range from 350 K to 2000 K) [1].

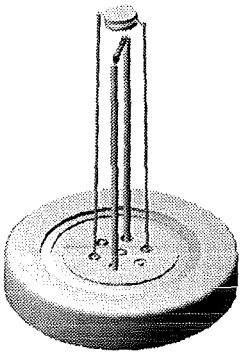

Fig. 3: First sample holder.

2.3 Measuring process

The measuring process is divided into partial processes: The preparation of the measurement includes the initialization of all gadgets and the recording of a residual gas spectrum using the secondary electron multiplier (SEM) of the quadrupole mass spectrometer (QMS). The gas spectrum is needed to determine the outgassing of chamber walls (after heating) and possible leaks in the vacuum apparatus.

For the measurement of the sample outgassing a time schedule is given. After the initialization of the quadrupole mass spectrometer and the residual gas analysis using the Faraday-cup of the QMS, the measurement starts with the increase of the heating current up to the maximum value. Then the accelerating voltage is linearly increased from 10 to 1000 V. It needs about 165 seconds. Then the maximum voltage is kept for 35 seconds. The measurement ends when the current is switched off. After one hour a second measurement wis started [1].

3. Determination of the released flux densities

3.1 Calibration of the quadrupole mass spectrometer

To analyze quantitatively the released gases during the measurement a calibration of the quadrupole mass spectrometer for the different occurring gases is required. Basically, a quadrupole mass spectrometer measures the currents caused by ions after ionization and partial cracking of original molecules. The partial pressure p_M can be given by equation (1)

$$p_M = \frac{I_M}{S_M}, \tag{1}$$

where I_M is the ion current and S_M is the calibrated sensitivity of the mass spectrometer at the mass M.

Due to the dependence of the mass spectrometer sensitivity on the properties of the vacuum system, the QMS was calibrated for the investigated gases in the used measuring system. Therefore, the Bayard-Alpert gauge was previously calibrated in the UHV-calibration system CS1001 (Leybold AG) by direct comparison with a reference gauge. Additionally, the Bayard-Alpert gauge was calibrated versus a Spinning Rotor gauge in the UHV system which is used for the TPD measurements. The resulting correction factor for the Bayard-Alpert gauge for a molecule mass M is given by

$$C_M^{BA} = \frac{P_M^{BA}}{p_M^{SRG}}, \tag{2}$$

where p_M^{BA} is the pressure measured by the Bayard-Alpert gauge and p_M^{SRG} corresponds to the Spinning Rotor gauge. The correction factors C_M^{BA} for all investigated gases can be seen in Table 1.

Table 1: Calibration factors for the investigated gases [1].

Gas	H_2	D_2	CH_4	CO	N_2	O_2	Ar	CO_2
Main Peak	2	4	16	28	28	32	40	44
C_M^{BA}	2.77	2.69	0.80	0.97	1.00	1.01	0.80	0.70
Used peak M	2	4	15	28	14	32	40	44
S_M	10.4	11.9	7.64	7.13	7.36	8.44	8.29	6.42

The correction factors and sensitivities of gases containing deuterium were not available for calibration measurements (HD, CD_4). They are calculated by averaging or the parameters were taken over from the equivalent gas.

In the second step the quadrupole mass spectrometer was calibrated against the Bayard-Alpert gauge. Therefore, the sensitivity of the quadrupole mass spectrometer for a selected gas is given by

$$S_M = \frac{I_M}{C_M^{BA} p_M^{BA}}. \tag{3}$$

p_M^{BA} is the total pressure of a gas with the main peak at mass number M measured by the Bayard-Alpert gauge during the calibration [1].

3.2 Calculation of the flux densities

The quantitative analysis of gas flow requires the determination of the flux densities $\Gamma_M(T)$ of atoms or molecules released from the sample at a certain temperature. A quadrupole mass spectrometer measures the ion currents of available gases, from which the partial pressures can be calculated. These pressures are the result of the superposition of gas flows from the sample (i.e. $\Gamma_M A$, when A is the area of the sample), from the chamber walls, and from the Bayard-Alpert gauge to the turbo molecular pump. In our case the pressure changes originating not from the sample can be neglected because of the low basic pressure in the chamber and the high release rates from the sample. Therefore, the total particle flux can be given by equation (4)

$$\frac{dN}{dt} = \Gamma_M A - \frac{dN_p}{dt}, \tag{4}$$

where N is the present particle number, N_p is the number of pumped particles, $\Gamma_M(T)$ is the flux density of the molecules released from the sample and dN_p/dt is the particle loss rate, which is given by

$$\frac{dN_p}{dt} = \frac{p_M S_{eff;M}}{kT_M}. \tag{5}$$

$S_{eff,M}$ is the effective pumping speed, p_M is the pressure in the chamber, T_M is the mean temperature in the chamber and k is the Boltzmann constant. The effective pumping speed $S_{eff,M}$ can be calculated with the nominal pumping speed S_N (160 l/s) and

the conductance C_M between pump and chamber related to the mass number M:

$$\frac{1}{S_{eff,M}} = \frac{1}{S_N} + \frac{1}{C_M}. \quad (6)$$

$$C_M = C_{Air}\sqrt{\frac{T_M}{T_{Air}}\frac{M_{Air}}{M}} \quad (7)$$

C_{Air} is the conductance of air, T_{Air} and T_M are the temperatures for air with the mass M_{Air} and for the gas with the mass M, respectively. The conductance for air was simulated with the help of the Monte-Carlo simulation program "Movak 3D" [2]. A value of 381.25 l/s was calculated for the used chamber geometry. Using the ideal gas law, equations (4)-(7) can be rewritten to

$$\Gamma_M = \frac{V}{kT_M A}\left(\frac{dp_M}{dt} + \frac{p_M S_{eff;M}}{V}\right). \quad (8)$$

The first term in equation (8) can be neglected for large pumping speeds like in our case. The flux density released from the sample is given then by

$$\Gamma_M = \frac{S_{eff,M}}{kT_M A}\frac{I_M}{S_M}. \quad (9)$$

The equation (9) is only valid, if the partial pressure in the ionization zone of the quadrupole mass spectrometer is the same as in the vacuum chamber and if the gas temperature in the ionization zone of the QMS is independent of the sample temperature [1].

Finally, the amount of hydrogen and deuterium Ψ_M released in the form of molecules with the mass M can be calculated from equation (9) by integrating the desorbed flux densities

$$\Psi_M = \frac{1}{\beta}\int_{T_0}^{T_E}\Gamma_M dT. \quad (10)$$

β is the heating ramp, T_0 and T_E are the starting and the end temperature of the TPD measurements. The total hydrogen and deuterium inventory, Q_H and Q_D, respectively, can be calculated from the amounts of all released hydrogen or deuterium containing molecules:

$$Q_{H,D} = \sum n_M^{H,D}\Psi_M. \quad (11)$$

$n_M^{H,D}$ is the number of hydrogen or deuterium atoms in a molecule with the mass number M [3].

4. Used samples

The samples for our measurements originate from the AxiSymmetric Divertor EXperiment ASDEX Upgrade. Fig. 4 shows a poloidal cut through one of the 16 identical sectors of the vacuum chamber of ASDEX Upgrade. For our investigations samples from the graphite covered lower inner and outer divertor are interesting. All used samples had a diameter of 10 or 12 mm and a thickness of 3 mm. The analyzed tiles consist of graphite type EK98 (1850 kg/m^3), an compressed and isotropic fine grain graphite with pores of about 1 µm. Some of the samples were coated with tungsten [3].

4.1 Graphite samples

The respective tiles were installed in March 1991 and removed after the experimental period from December 1994 to July 1995. Before the experiments were started the vacuum chamber with all inner wall components had been degassed for about five days at about 420 K. Previously, the graphite tiles were heated after the manufacturing and before installing at ASDEX Upgrade at 1800 to 2100 K for about two hours. In Fig. 5 the divertor tiles of sector 10 and the sample positions of this series are shown.

Samples from the B5 tile of the inner divertor and of the A2 tile of the outer divertor were not used. The lower part of the E tile is shadowed from the plasma by the upper part of the A tile. The samples of this part of the E tile were only reached by the background gas and/or neutral hydrogen atoms. Therefore, these samples can serve for the measurement of the background hydrogen and deuterium inventories [3].

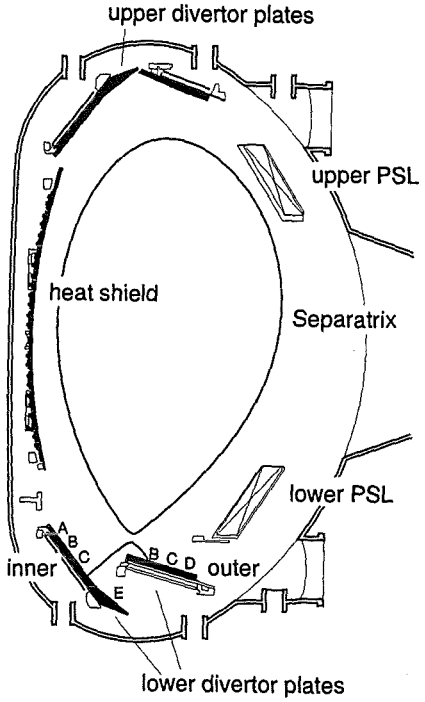

Fig. 4: Poloidal cut through the tokamak ASDEX Upgrade [3].

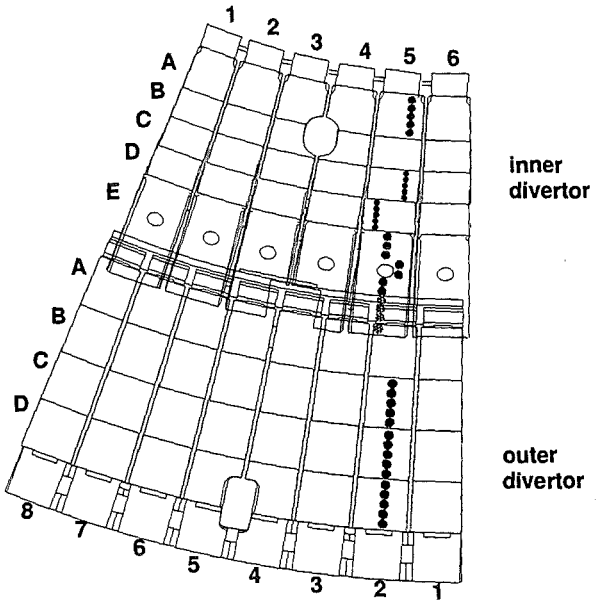

Fig. 5: Positions of the samples cutting from the sector 10 of the ASDEX Upgrade divertor plates (view from top) [3].

4.2 Tungsten coated samples

For the experimental period from December 1995 to July 1996 graphite divertor tiles with a 500 µm thick tungsten layer on the plasma exposed surface have been installed in the ASDEX Upgrade. As it can be seen in Fig. 6, the divertor tiles were located

In the CD region of the inner divertor and the BC region of the outer divertor. They were tilted in toroidal direction. Therefore, a part of each tungsten coated divertor tile is plasma shadowed by the adjacent tile. This area (shadow region) receives much less plasma flux than the non-shadowed part (plasma region) of the divertor tile.

In this experimental period about 700 discharges, 450 of it with additional heating by neutral injection, were performed. Mostly, deuterium was used as filling gas for the discharges, especially in the case of neutral injection. Nevertheless, an amount of hydrogen in the range of 10% to 20% was still present in the discharges, in the case of neutral injection with H^0 a value of 60% hydrogen (H) was found. Some discharges in the middle of the experimental period and the last 10 discharges were performed with hydrogen as filling gas. Finally, the mean H/D ratio in the plasma core can be estimated to about 0.5 [4].

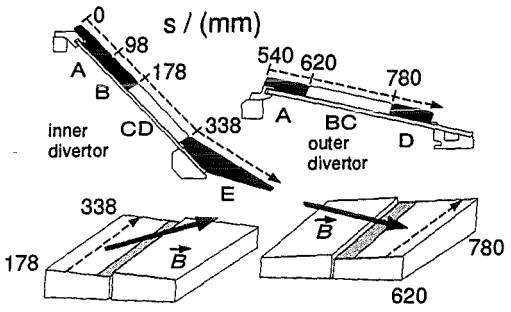

Fig. 6: Location of the tungsten coated divertor tiles of ASDEX Upgrade [4].

4.3 Round robin samples

The samples, with a size of 10x10x3 mm, were made from EK98 fine grain graphite. They were mechanically polished on one side. The samples were cleaned in an ultrasonic bath of isopropanole and degassed for 4 hours in a vacuum system at a temperature of 900°C and a pressure of $1 \cdot 10^{-5}$ mbar. Subsequently, the samples were cleaned in a hydrogen discharge at a pressure of $2 \cdot 10^{-2}$ mbar for the second time. After cleaning an amorphous, deuterated carbon film was deposited on the polished side. Therefore, the samples were fastened onto a stainless steel electrode in a 13.56 MHz radio-frequency plasma using CD_4 as precursor gas. Prior to the distribution to the different groups the round robin samples were analyzed with the $D(^3He,p)\alpha$ NRA at 790 keV [6].

5. Results

5.1 Graphite samples

5.1.1 Total inventories of analyzed gases

Fig. 7 shows the released amounts Ψ of H_2, D_2, HD, CH_4 and CD_4 as well as the total hydrogen and deuterium inventory (Q_H and Q_D, respectively) of samples from the inner and outer divertor of ASDEX Upgrade. The small contribution of higher hydrocarbons and mixed methane ($CH_xD_{y,x+y=4}$) can be neglected. The hydrogen molecules (H_2) have the main contribution for the amount of released hydrogen as well as HD for the amount of released deuterium. A part of HD (10-15% of all released D_2) originates, depending on the wall conditions of the vacuum vessel of the TPD setup, from the recombination of deuterium atoms with hydrogen atoms during the heating. Aside from H_2, D_2 and HD the hydrogen and deuterium atoms in compounds with carbon (CH_4, CD_4) contribute about 10% to 15% to the total released amount of hydrogen or deuterium.

The maximum of total inventory of hydrogen or deuterium calculated with the results of our measurements are of the order of $6 \cdot 10^{23}$ H/m^2 and $3 \cdot 10^{23}$ D/m^2 at the inner divertor tiles and nearly the half at the outer divertor. In comparison with the assumption of a saturated surface layer under the conditions of the ASDEX Upgrade divertor experiment (ion energies of about 100 eV) the inventories of hydrogen and deuterium are about three orders of magnitude larger. However the described inventories are two orders of magnitude lower than the total incoming hydrogen or deuterium fluence (F_{H+D}), resulting from the integration of the particle fluxes during the discharge experiments. The total numbers of hydrogen and deuterium atoms in the divertor tiles are about $3 \cdot 10^{24}$. These are two to three orders of magnitude higher than the stationary particle content in a typical ASDEX Upgrade discharge experiment (10^{21} to 10^{22}) [3].

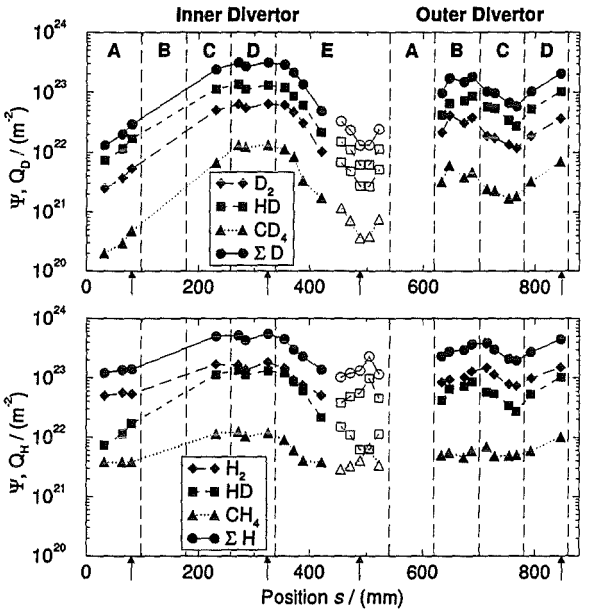

Fig. 7: Poloidal distribution of the released amounts of deuterium (top) and hydrogen (bottom) and their compounds and the hydrogen and deuterium total inventories in dependence of the sample position at the inner and outer divertor tiles of ASDEX Upgrade. [3].

5.1.2 Desorption spectra

Fig. 8 shows the desorption spectra of hydrogen isotope molecules (H_2, HD and D_2) of four samples from different positions of the divertor tiles. Due to the minor plasma contact the first two samples were cut out from the inner divertor tiles at sector A (s = 82 mm) and at the shadowed region of sector E (s = 488 mm). The second two samples were taken from the sector D of inner and outer divertor tiles (s = 324 mm and s = 846 mm), respectively, because the maximum inventories were measured here.

The spectra of all samples show a characteristic main peak at about 1150 K and further peaks or shoulders for hydrogen near a temperature of 600 K, 850 K and above 1300 K. It is supposed that the lower temperature peaks for hydrogen are probably caused by water in the near-surface region. It can be adsorbed during the storage of the samples at the air between the end of the ASDEX Upgrade experiments and the beginning of the TPD measurements. In contrary to the lower temperature peaks the high temperature shoulder can be originated by desorption of deep trapped hydrogen or hydrogen containing molecules from the chamber walls, the sample holder or other heated parts of the surrounding vacuum vessel. Above a temperature of 1600 K all hydrogen and deuterium were released from the sample.

In order to confirm the complete out-gassing of all analyzed gases during the TPD measurements, the samples were heated for few seconds about one hour after the first (main) measurement. Between the two measurements the samples remained in the vacuum system under vacuum conditions and at room temperature. These measurements show that all hydrogen and deuterium containing molecules were totally released during the main (first) measurement [3].

5.1.3 Depth distribution

In order to get information about the depth distribution of hydrogen and deuterium in the samples, a sample was cut into three pieces with a thickness of about 1 mm and the release of hydrogen and deuterium containing molecules from each piece was measured with TPD. Fig. 9 shows the obtained inventories of hydrogen and deuterium in comparison with those of a virgin sample.

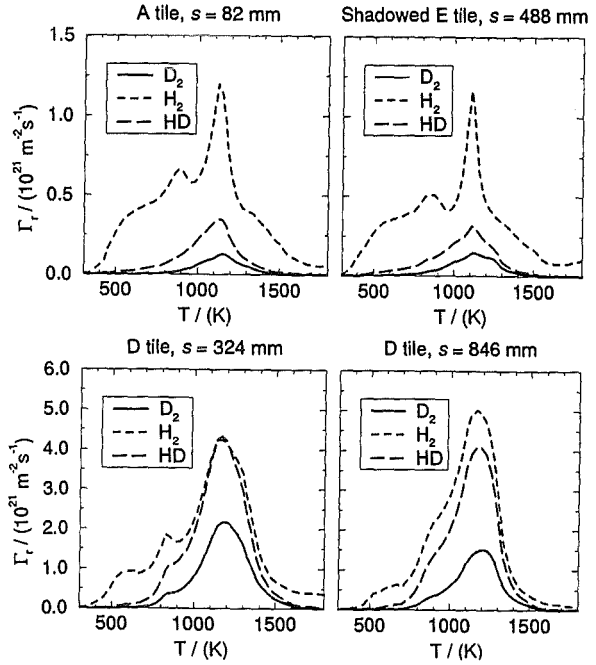

Fig. 8: Desorbed flux densities of H_2, HD and D_2 for chosen samples from region with minor plasma contact and from the separatrix region [3].

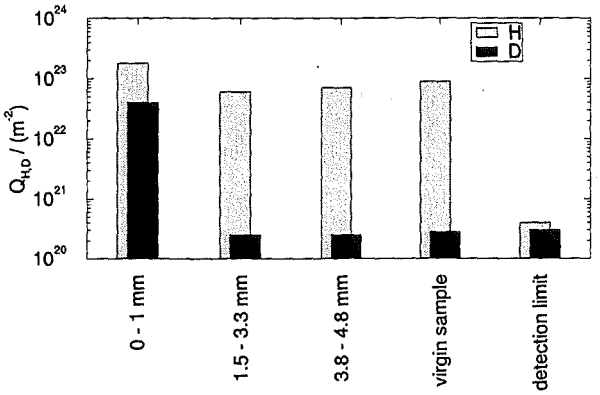

Fig. 9: Inventories of hydrogen and deuterium in pieces of a cut sample from the E tile (s = 421 mm) in comparison with a virgin sample [3].

A measurable deuterium inventory was only found in the first sample piece, situated nearest to the plasma exposed surface. This indicates that the maximum depth of deuterium in graphite is lower than 1.5 mm. In contrary to deuterium, the hydrogen inventory is only slightly reduced for the second and third sample piece. A difference of about $1.1 \cdot 10^{23}$ H/m^2 between the first piece and the other two sample pieces was found. This can be probably attributed to the hydrogen introduction by the plasma [3].

5.2 Tungsten coated graphite samples

As in the case of the graphite samples, the release of hydrogen isotopes from tungsten coated samples is dominated by H. The measured total hydrogen inventories are in the range of about $5 \cdot 10^{22}$ to $8 \cdot 10^{22}$ H/m^2 for all samples. While we assume that the largest part of the hydrogen amount is caused by near-surface water, taken up during the air exposure of the samples between the experiments at ASDEX Upgrade and the TPD measurements, the presented results and the discussion is restricted on deuterium [4].

5.2.1 Total deuterium inventories

Fig. 10 shows the total inventories of the tungsten coated samples, measured by TPD, in comparison with the results of the Nuclear Reaction Analysis (NRA) using the 790 keV ^{3}He(d,α)p reaction. Further shown are the distribution of the mean surface temperature during the discharges and the incoming fluence of deuterium. Due to the differences between the inventories of the shadow and the plasma region of the divertor tiles, the figure is divided into parts.

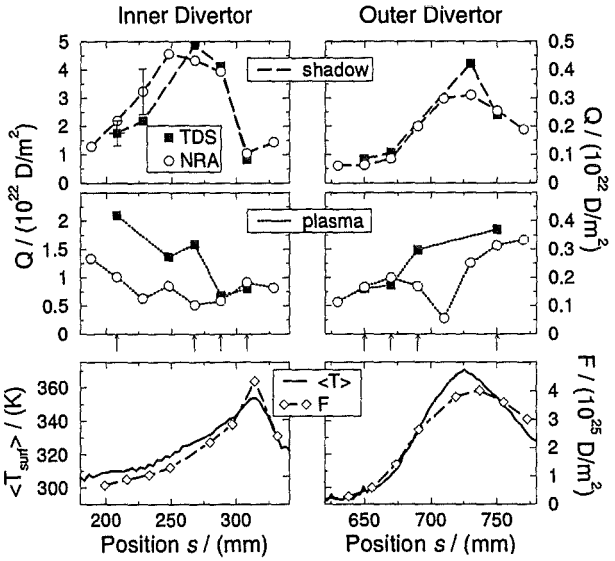

Fig. 10: Total inventories and near-surface inventories of deuterium, measured by TPD and NRA, of tungsten coated graphite samples of the inner and outer ASDEX Upgrade divertor in comparison with the mean surface temperature (T_{surf}) and the total incident deuterium fluence. The surface temperatures were measured by infrared thermography during neutral beam discharges. The fluence values were calculated by integration of the particle fluxes, obtained from the measurements with Langmuir probes [4].

The deuterium inventories of the inner and outer divertor and of the shadow and plasma region of a divertor tile differ considerably. The highest inventories of about $5 \cdot 10^{22}$ D/m^2 were found in the shadow region of the inner divertor tiles, outside of the separatrix region, where the inventory shows a minimum. The inventories of samples cut out from the outer divertor are generally smaller than the inventories of the inner divertor samples by an order of magnitude.

The inventories of the plasma region of the inner divertor decrease in direction to the separatrix and are smaller than the inventories of the corresponding shadow region. The smallest inventories were measured at the separatrix position of the inner divertor, as well as, for samples of the plasma region of the outer divertor by NRA, in opposition to the measurements by TPD, where the inventory reaches a maximum [4].

5.2.2 Desorption spectra of deuterium

Fig. 11 shows four TPD spectra for the shadow and plasma region of the inner and outer divertor tiles at the same time. For the different regions, where the samples were cut out, four different peaks can be distinguished. The first small peak or shoulder at about 600 K can only be seen at TPD spectra of outer divertor samples. Further typic peaks or shoulders are at about 900 K at spectra of samples from the shadowed region of the inner divertor. Furthermore all spectra show a large and broad peak in the range of 1000 K to 1200 K. For samples of the outer divertor tiles a different large peak is shown in the spectra [4].

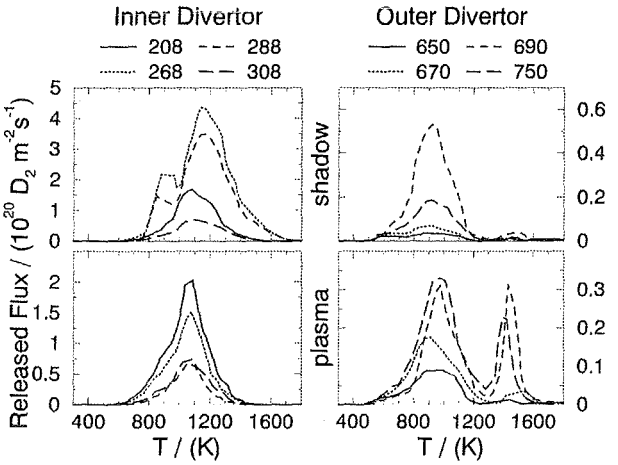

Fig. 11: Released fluxes of deuterium (D_2) of samples for the shadow and plasma region of the inner and outer divertor. The legend numbers are the sample position, as can be seen in Fig. 6 [4].

5.3 Round robin samples

Within the context of the round robin experiment two samples were analyzed in our laboratories. Therefore the hydrogen and deuterium inventories were measured with TPD. The obtained values of $1.32 \cdot 10^{18}$ and $1.19 \cdot 10^{18}$ D/cm^2 are in satisfactory agreement with the mean value of $1.57 \cdot 10^{18}$ D/cm^2 for the deuterium inventory, especially under consideration of the different analysis methods. Furthermore, the hydrogen inventory was determined with a value of $1.9 \cdot 10^{18}$ H/cm^2 for the first and $1.4 \cdot 10^{18}$ H/cm^2 for the second sample. Desorption peak temperatures at 1150 K for D_2, 900 K for CD_4, 830 K and 1150 K for HD were found. The results from the quantitative analysis are 53.8% as D_2, 38.5% as CD_4, 7.7% as HD for the first sample and 55.4% as D_2, 37.7% as CD_4, 6.8% as HD for the second round robin sample [6].

6. Discussion

6.1 Graphite samples

6.1.1 Comparison with other analysis methods

For a verification of the results of our TPD measurements some samples were investigated by three different ion beam analysis methods. The first method uses the measurement with a calibrated secondary ion mass spectrometer (SIMS) [5]. The samples were eroded by 5 keV Cs^+ ion beam. The emitted negative ions were analyzed and collected by a Faraday cup. Furthermore a deuterium depth profile from 10 µm down to 25 µm was determined by means of the results from the measurement of the incident Cs^+ ion fluence and the sputtered crater. In the second investigation the deuterium inventory up to the depth of 1µm was measured by a 790 keV ^{3}He(d,α)p nuclear reaction. Due to the surface roughness and the limited depth resolution depth profiles have not been calculated. As the third analysis method the elastic recoil detection analysis (ERDA) with a 2.6 MeV ^{4}He beam was used to measure the hydrogen amount in a surface layer of ≤ 1.8 µm. Fig. 12 shows the results of these ion beam analysis methods in comparison with the results of the TPD measurements.

The reason for the differences between the ion beam methods and the TPD measurements is the lower analyzing depth of the ion beam analysis methods. Whereas the total hydrogen and deuterium inventories can be determined by TPD, only a surface layer with a thickness of the order of few µm can be analyzed by the used ion beam analysis methods. For this reason it is assumed that a major part of the hydrogen isotopes is bound some hundreds of µm deep inside the graphite samples.

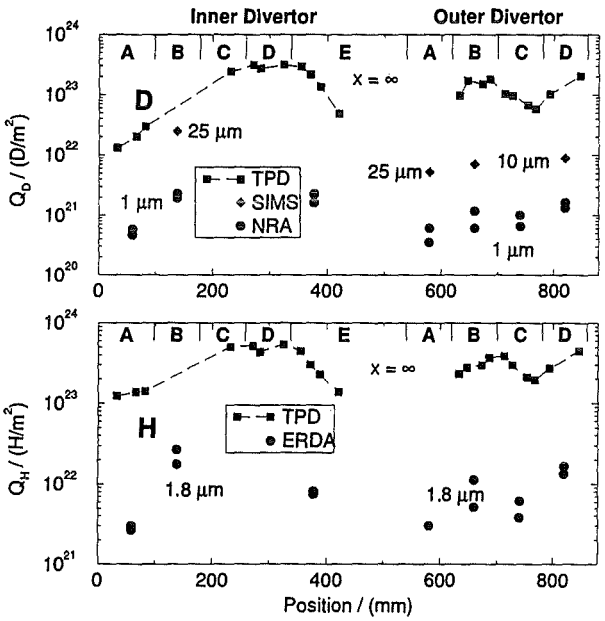

Fig. 12: Comparison of the hydrogen (Q_H) and deuterium inventories (Q_D) measured by TPD with the results of ion beam analysis methods [3].

Furthermore, the hydrogen and deuterium release measured from the ASDEX Upgrade divertor tiles by TPD and the maximum releases of the JET beryllium and carbon covered divertor plates found after the 4/94 to 3/95 experiments by NRA (down to 1 µm) are in the same order of magnitude. However for the similar measurements by ^{3}He(d,p)α nuclear reactions analysis the inventories of hydrogen and deuterium are one order of magnitude larger than these in ASDEX Upgrade divertor tiles [3].

6.1.2 Poloidal distribution of the hydrogen and deuterium inventories

Fig. 13 shows the determined hydrogen and deuterium inventories in comparison to the average target surface temperature and the fluence distribution along the divertor tiles. For the samples of the inner divertor these three distributions correlate with each other, except a small local minimum for the hydrogen and deuterium inventories at the separatrix position. Unlike the results for the inner divertor, the inventories of

samples of the outer divertor are generally lower by a factor of two and show a broad local minimum near the highest target surface temperature and the fluence maxima, indicating the separatrix position.

The differences between the total inventories of the inner and outer divertor plates and the minima of inventories at the separatrix position are probably caused by a higher surface temperature in the corresponding regions, leading to a depletion of the saturated surface/co-implantation zone. Furthermore, the desorption of hydrogen or deuterium from the graphite tiles into the plasma increases and the diffusive hydrogen flux into the graphite bulk is reduced, due to the smaller concentration of hydrogen at the higher surface temperatures. On the other hand the differences of the total inventories may be caused by the temperature differences between the single discharges, when the temperature of the divertor plates is high enough to desorb hydrogen.

Considering the relatively high deuterium inventory in the range of a few 10^{22} D/m^2 in areas with small plasma contact, i.e. in samples from the inner A tile and the shadowed region of the inner E tile, we assume, that the implantation of charge exchange neutrals has an essential importance for the total deuterium inventory. However, the fluxes of charge exchange neutrals are three orders of magnitude lower than the ion fluxes hitting the divertor plates, but particle energies of several keV are possible. That may compensate the low fluxes and could lead to this relatively high deuterium inventory.

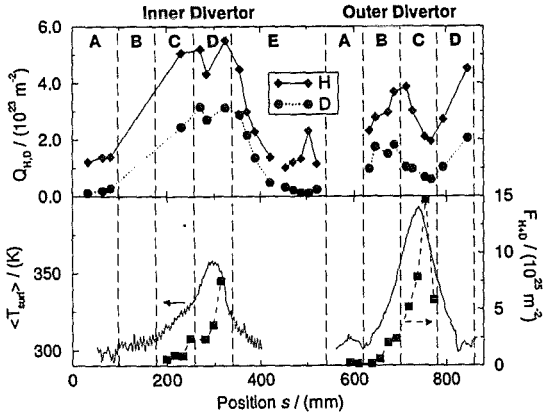

Fig. 13: Comparison of the distribution of the total hydrogen (Q_H) and deuterium inventories (Q_D) with those of the average target surface temperature (T_{surf}) and the total incident hydrogen and deuterium fluences (F_{H+D}) The total fluences were obtained by summarizing the single fluences per discharge for hydrogen and deuterium plasma, respectively [3].

The deuterium depth profile was measured by Sun et. al. [5] for samples, cut out from the B tiles of the inner divertor and tiles A, B and D of the outer divertor, by means of the SIMS method. In all samples, deuterium was found in a concentration of the order of several 10^{-4} D/C up to a depth of 10 till 25 µm, which is much larger than the implantation range. Comparing the depth profiles of the samples of outer and inner divertor tiles, the deuterium concentration in the range of the outer divertor decreases with increasing depth, whereas the deuterium concentration in the inner B tile shows a constant D/C ratio of 0.08 up to a depth of about 2 µm and only then it begins to decrease. The constant D/C ratio down to a depth of about 2 µm indicates a co-implanted layer with this thickness. However, the D/C ratio is reduced compared with the room temperature value of D/C=0.4. The most probable reason therefore is the higher temperature achieved during the discharges. For the amount of co-implanted deuterium, calculated from the above-mentioned values, a value of about $1.6 \cdot 10^{22}$ results, which is an order of magnitude lower than the value determined from the TPD measurements.

We can conclude from the above discussed results, that dominating processes for retention of hydrogen and deuterium are the diffusion and the subsequent trapping at inherent trapping sites at a depth of more than 25 µm. The hydrogen retention in the near surface layer is dominated by the co-desorption for the inner divertor outside of the separatrix region and by the formation of a several µm thick co-implanted layer and the build-up of a thin, several 10 nm thick saturated surface layer, respectively, for the separatrix region of the inner divertor and the outer divertor. In both cases, hydrogen and deuterium atoms are able to diffuse in considerable amounts into the graphite bulk. From the D/C concentration measured by Sun et al., the retention depth of hydrogen and deuterium in the divertor tiles can be estimated to be of the order of some hundred µm, consistent with the results of the TPD and of the ion beam analysis [3].

6.1.3 Hydrogen/Deuterium ratio

In Fig. 14 the poloidal distribution of the ratio of hydrogen to deuterium inventories, determined during the TPD measurements and during the surface analysis by means of the ion beam analysis methods NRA and ERDA, respectively, are represented. The shown ratios result from the fact, that the hydrogen release from the divertor tiles in our TPD measurements is larger by a factor of 2 to 4 than the amount of deuterium, in spite of a higher number of performed deuterium discharges. The expected ratio of the hydrogen and deuterium inventories from the numbers of discharges performed with hydrogen and deuterium, respectively, are in the range of about 0.2 to 0.4. The highest ratios of more than 10 H/D result for regions with small plasma contact as for the A tile and the shadowed region of the E tile of the inner divertor. Further, a higher ratio of the amounts of hydrogen to deuterium appears for the surface layer compared to deeper layer of the sample from the measurements by ion beam analysis methods. In contrary to this, constant values were found for the C and D tiles of the inner divertor as well as for tiles of the outer divertor. For the inner C and D divertor tiles ratios of the hydrogen and deuterium inventories of about 1.7 and for the outer divertor tiles of about 2.7, respectively, were calculated.

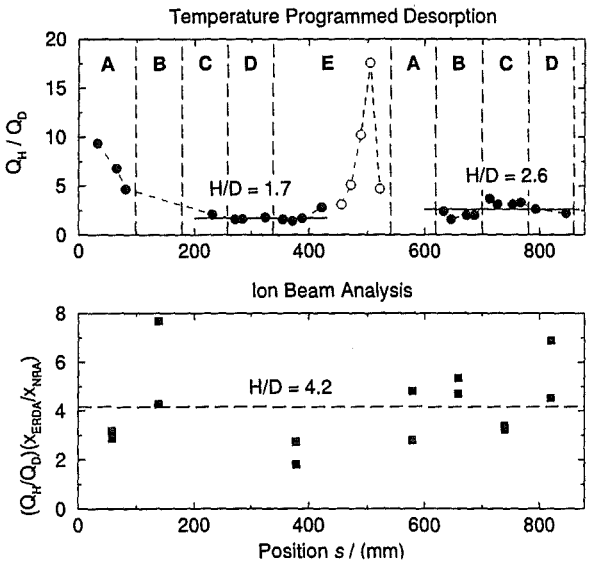

Fig. 14: Comparison of the poloidal distribution of the ratio of the hydrogen (Q_H) and deuterium inventories (Q_D) measured by (top) TPD with the results of the ion beam analysis methods NRA and ERDA. The open symbols in the upper part of the figure are the results from samples of the shadowed region of the inner E tile [3].

Possible processes for the high H/D ratio are a not complete out-gassing after the manufacturing process and an uptake of water due to the storage of the samples at the air. The dissociation of a small amount of the surface water and a subsequent diffusion of the resulting hydrogen atoms to inherent trapping sites as well as the diffusion of this water into the graphite along open pores and a later dissociation would be possible. Another possible process is the recycling of hydrogen atoms in the plasma caused also by the dissociation of surface water, but which has been taken up between the manufacturing and the installation of the tiles in the ASDEX Upgrade divertor. Furthermore, an increase of the hydrogen concentration in comparison to the concentration of deuterium would be possible by the isotope effects of the behavior of these gases in graphite, such as diffusion and recombination. Also a different history of the surface temperatures during the hydrogen or deuterium discharges can lead to a displacement of the corresponding ratio. However, the graphite tiles were degassed before installation at the ASDEX Upgrade divertor and the start of the discharge experiments. The highest hydrogen inventory is caused probably by the uptake of water between the end of the experiments and the beginning of the TPD measurements.

In order to examine the water uptake during the air exposure the amounts of hydrogen in two samples were measured after 90 days again. In Fig. 15 the resulted desorption spectra are represented. It can be seen, that the released hydrogen fluxes after 90 days of air exposure is larger than these in the first run, especially below the temperature of 600 K. However, the maxima of the desorbed fluxes in the second TPD measurement are lower by more than one order of magnitude as in the first investigation. Further, the uptake of water was confirmed by the fact, that a large release for mass 18 (H_2O) was detected at the lower temperature range, although the quadrupole mass spectrometer could not be calibrated for water. Comparing Fig. 15 with Fig. 8 , a similarity appears for the lower temperature range of the hydrogen spectra. The small shoulders in the spectra of H_2 and HD of the Fig. 8 could be a result of the release of near-surface water whereas the main peak of the desorption spectra has to be attributed to hydrogen which was trapped in C-H bonds at deeper regions in the samples. Furthermore, from the comparison of the spectra in Fig. 15 it results that hydrogen originates also from the dissociation of surface water which is not chemically bound to carbon atoms. However, it would be possible that water was absorbed in the samples. The hydrogen inventories released from these two samples are about $8 \bullet 10^{22}$ H/m^2, which is approximately identical with the values measured in deeper regions of a sample and in a virgin sample, which was not exposed to a plasma discharge.

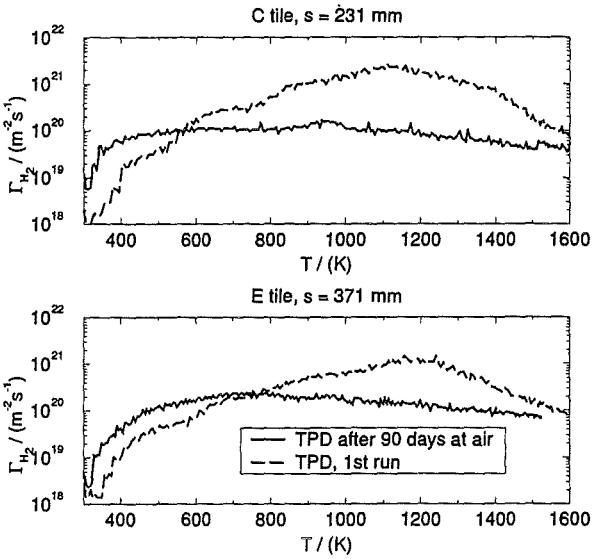

Fig. 15: Comparison of the desorbed hydrogen fluxes of the first and second measurement after 90 days air exposure of the two samples originated from the C and E tile of the inner divertor [3].

Furthermore, the water uptake due to air exposure can be also a reason for the dependence of the hydrogen deuterium ratio from the sample position and the poloidal distribution along the divertor plates. Consequently, a higher H/D ratio results in fields with small deuterium inventory, as the inner A tile and the shadowed region of the E tile or the outer divertor tiles. The similarity of the hydrogen and the deuterium distribution may not be explained by the effects resulting from the water uptake.

The total amount of hydrogen or deuterium atoms introduced in the divertor plates can be specified finally to about $2 \bullet 10^{24}$ atoms. This is corresponding to a mass of about 6 grams, $3 \bullet 10^{20}$ hydrogen or deuterium atoms per second and an average retained flux of nearly $5 \bullet 10^{19}$ m^{-2}s^{-1}. Comparing with a typical value of about 10^{20} to 10^{21} for a plasma discharge in ASDEX Upgrade the above-mentioned value is three orders of magnitude larger. A further comparison with the typical hydrogen puff rate of about 10^{20} to 10^{21} s^{-1} shows, that the major part of the hydrogen or deuterium inserted in the plasma chamber, is pumped by trapping in the divertor plates [3].

6.2 Tungsten coated graphite samples

The deuterium retention in tungsten coated divertor tiles differs from that in graphite tiles. The main process for tiles of the inner divertor is the co-deposition of deuterium with carbon ions from the plasma, such as for graphite tiles too, whereas the retention in outer divertor tiles is dominated by the implantation. Further the co-deposited layers in the plasma and separatrix region of the inner divertor is depleted, due to the increased temperature in these areas. Nevertheless, the deuterium inventories in these layers are of the same order of magnitude as those in graphite tiles, in spite of the fact, that only about 700 discharges were performed with a tungsten coated divertor compared to about 2000 discharges with a graphite divertor.

The total deuterium inventory in the tungsten coated samples is only by a factor of less than 2 larger as the near surface inventory, except for the separatrix region of the outer divertor, in contrast to graphite samples, where factors up to 100 were found. Therefore we assume, that the diffusion out of the co-deposited layer into the tungsten layer is limited by the tungsten/carbon interface. At the separatrix region of the outer divertor, the combination of high temperatures and fluxes leads to a depletion of the near surface layer and a larger diffusion

into the graphite bulk and the graphite substrate, resulting in a large deuterium inventory [4].

7. Summary

The desorption spectra of graphite and tungsten coated graphite samples cut out of the ASDEX Upgrade divertor tiles and of samples from the round robin experiment were measured by TPD. For this purpose an UHV setup with an electron-bombardment heater has been developed and realized, which allows a nearly uniform heating of the samples up to 2100 K with a heating ramp of about 10 K/s. The temperature of the sample surface can be measured in the range of 350 to 2000 K by means of a pyrometer. For the qualitative and quantitative analysis of the different released gases a calibrated quadrupole mass spectrometer is used [1].

The investigation of the graphite samples shows, that hydrogen and deuterium are released mainly in form of the molecules H_2, HD, D_2 and, with a contribution of about 10%, in form of the methane molecules CH_4 and CD_4. Therefore, the desorption of mixed methane and higher hydrocarbons can be neglected. The resulting desorption spectra show maxima of the hydrogen and deuterium release at about 1150 K, respectively. Further peaks and shoulders are caused by different processes of hydrogen and deuterium retention.

For graphite samples the co-implantation of hydrogen with carbon, the build-up of a saturated surface layer, the diffusion out of these layers into the graphite bulk and the subsequent bonding at inherent trapping play a great role. The inventories found in this diffusion zone, can be greater by a factor of up to 10 than the near-surface inventories in the separatrix region. Furthermore, we measured inventories for the outer divertor lower by a factor of about 2 compared with the equivalent position of the inner divertor, with respect to the separatrix. A possible reason for this fact is the higher surface temperature on the outer divertor tiles leading to a depletion of the co-implanted/saturated surface layer and a reduced diffusion into the sample. The maximum inventories at the inner divertor are of the order of $4 \cdot 10^{23}$ m^{-2} [3].

The hydrogen isotope inventory in tungsten coated samples taken from the inner divertor, is dominated by the build-up of a several µm thick co-deposited layer. They are of the same order of magnitude as the inventories measured in the graphite samples. Similar to graphite samples, the high surface temperatures in the separatrix region lead to a depletion of the co-deposited layer and to a deuterium inventory lower by a factor of about 5. Additionally, the diffusion of hydrogen out of the co-deposited layer into the tungsten layer is limited by the tungsten/carbon interface. For the outer divertor the measured inventories are also generally smaller than the inventories of the inner divertor by a factor of about 10. The hydrogen isotope retention in this region is dominated by the implantation and the diffusion out of the implantation layer into the underlying tungsten layer [4].

The origin of the measured inventories differs for hydrogen and deuterium. Whereas the deuterium inventories in the samples were determined by the deuterium fluxes from the plasma onto the divertor tiles during the discharges, the hydrogen inventories are caused by two different processes. At first, the hydrogen in the samples originates from the hydrogen flux from the plasma, equal to the introduced deuterium. This hydrogen is strongly bound by C--H bonds. Therefore, temperatures of more than 1500 K are necessary to desorb this kind of hydrogen. At second, the hydrogen inventory in the sample is partially caused by the uptake of water during the air exposure between the end of the ASDEX Upgrade experiments and the start of the TPD measurements. Temperatures only up to 800 K are needed for the desorption of this kind of hydrogen, because the hydrogen is weakly bound to the graphite lattice most probably in the form of H_2O [3].

Aside from the graphite and tungsten coated graphite samples two round robin samples were investigated. The deuterium inventories of these samples were determined and the results were compared with the results from other laboratories. The agreement is considerable in spite of the fact that the different analysis method imply different analysis depths [6].

Literature:

[1] D. Schleußner, D. Rössler, J. Becker, W. Knapp, Chr. Edelmann, C. Gracia-Rosales, P. Franzen, R. Behrisch, *Temperature Programmed Desorption from Graphite*, to be submitted to Journal of Vacuum Science and Technology.

[2] G. Class, K. Brockmüller and V. Hauer, *3D Monte Carlo Simulation of Molecular Movements and Photon Temperature load in Arbitrarlily Shaped Vacuum Vessels*, (Movak3D Manual, Karlsruhe, 1994)

[3] P. Franzen, R. Behrisch, C. Gracia-Rosales, D. Schleußner, D. Rössler, J. Becker, W. Knapp, Chr. Edelmann, *Hydrogen Isotope Inventory in the Graphite Divertor Tiles of ASDEX Upgrade as Measured by Thermal Desorption Spectroscopy*, (Nucl. Fusion, Vol 37, No 10, 1375--1393, 1997)

[4] P. Franzen, H. Maier, D. Schleußner, R. Behrisch, M. Balden, *Hydrogen Isotope Inventory in the ASDEX Upgrade Tungsten Coated Divertor Tiles*, (24th EPS Berchtesgaden, 1997)

[5] Sun, G., et al., J. Nucl. Mater., (in press)

[6] Behrisch et. al., *Qnantitative analysis of deuterium in amorphous a-c:D layers- a Round Robin Experiment*, to be published

Staff:

Chr. Edelmann
P. Franzen
V. Hauer
W. Knapp
M. Perl
D. Schleußner

Subtask 18, 19: Characteristic of co-deposited materials produced in plasma generator and via CD_4 chemical deposition.

Graphite and different CFC materials are favorite materials for future fusion reactors. On the other hand, it is well known that the erosion by chemical sputtering, its strong dependence on the plasma parameters and the permeation of tritium in carbon based materials may limit their application. Therefore a systematic study of the interaction between different carbon fiber composites (CFC) and a stationary hydrogen or deuterium plasma was started. The plasma generator PSI-1 proved to be well suited for investigating these plasma- surface interaction problems. The ion flux and the ion energy can be controlled independently in this device in the range of fluxes (10^{21} - 10^{23} D^+ m^{-2} s^{-1}) where no ion beam data are available.

In fusion experiments a close relation between erosion and codeposition is found. As endorsed in subtask 227 both processes will be studied in the plasma generator PSI-1. For the understanding of the codeposition mechanism target temperature measurements as well as ion flux dependent erosion yield data are required. With this aim in view, the chemical erosion, as a key element of the complex mechanism of carbon transport in a magnetized plasma, was studied for low ion energies and divertor like conditions. A strong decrease of the chemical erosion with increasing ion flux density was found when first measurements for flux densities up to 5* 10^{22} m^{-2} s^{-1} were carried out [1]. This result is in agreement with the theoretical predictions taking into account a formation of D2-molecules dependent on fluence density. These systematic measurements at high flux densities are a valuable extension of the ion beam experiments at lower flux densities and allow a rather safe extrapolation to ITER conditions. To complay with the request for ITER a comparison between different CFC-materials was carried out showing that the chemical erosion yield of the Si- doped graphite SEP NS 31 is significantly lower than that of the undoped CFC Concept II from Dunlop. For nearly identical discharge conditions there is no noticeable difference between deuterium and hydrogen plasmas; i.e. the isotope effects appear to be small.

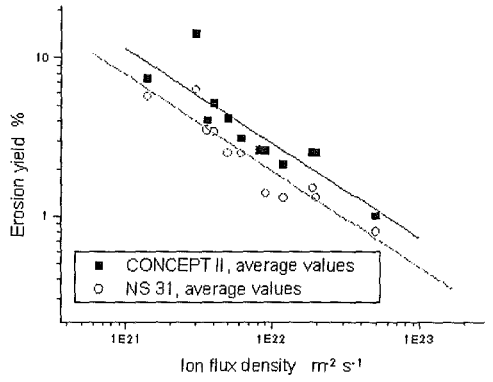

Fig. 1: Ion flux dependence of the chemical erosion yield in deuterium and hydrogen plasmas at a target temperature of 500°C

The generation of a-CD-coatings was established by physical sputtering of graphite and by injecting CD_4 into the plasma. We found that the formation of such coatings depends strongly on the plasma conditions and on the temperature of the collector material.

First tests revealed that such experiments lead inevitably to an overall coating of all in-vessel walls with undesired a-CD-layers, wich may strongly contribute to the carbon production rate. Especially the background signal for all erosion measurements will be influenced.

Furthermore, the collector temperature has an important influence on the growth rate of a-CD layers and temperature controlling is necessary. To this end, air cooled and water cooled target holders were tested under high heat flux conditions. By flow variation of the cooling medium stationary values of the target temperatures can now be realized between 100 and 700°C.

Experimental results achieved so far have been published at the PSI-conference in San Diego (1998)[1], at the EPS-conference in Prague (1998) [2] and at the 8th Carbon Workshop (Jülich, 1998) [3].

Literature:

[1] H. Grote, W. Bohmeyer, P. Kornejew, H.-D. Reiner, C.H. Wu, "Chemical sputtering yields of carbon based materials at high ion flux densities", 13th PSI-Conference, San Diego, May 18-22, 1998

[2] W. Bohmeyer, P. Kornejew, H.-D. Reiner, C.H. Wu, erosion of carbon fibre components (CFC)", 25th EPS Conference on Controlled Fusion and Plasma Physics, Prague, June 29-July 3,1998

[3] W. Bohmeyer, P. Kornejew, H.-D. Reiner, "Measurements of chemical erosion at PSI-1", 8th International Workshop on Carbon Materials, Jülich, September 3-4, 98

Staff:

W. Bohmeyer
H. Grote
G. Fußmann
P. Kornejew
H.-D. Reiner

Subtask 2: H/T Retention Studies in Neutron Irradiated Graphites, CFCs and Doped C Composites

Carbon-based materials and beryllium are candidates for protective layers on plasma-facing components of fusion reactors. In contact with the D-T-plasma these materials absorb tritium and it is anticipated that tritium retention increases with neutron damage due to neutron-induced traps, leading eventually to tritium inventories which represent a safety problem. Previous investigations indeed show that for carbon-based materials tritium retention increases with neutron damage in the range ≤ 0.1 dpa by two to three orders of magnitude [1, 2]. A similar effect, i.e. a 10 to 20 times larger tritium inventory in irradiated (~ 1.6 dpa) compared to unirradiated samples has been observed recently also for beryllium [3] and has been discussed in a previous Annual Report.

In the reporting period investigations of ITER representative CFC's (carbon fibre composites) have been completed [4].

Three types of CFC were studied: 2-d type CX2002 U (Japan), 3-d type N112 (SEP Bordeaux) and 2-d type A05 (Carbon Lorraine). The samples were irradiated in the tests CERAM and MACIF at temperatures between ~ 400 and 1000 °C to a fast neutron fluence corresponding to a damage between 0.4 and 1.8 dpa.

Tritium retention and its dependence on neutron damage is studied by loading unirradiated and irradiated samples at elevated temperatures in a H_2+5 ppm T_2 atmosphere (2 bar, 1000 °C, 6 h) and determining the tritium uptake by annealing (1100 °C, several h, purging with He+0.1 % H_2).

The main results of these studies with ITER representative CFC's are (fig. 1):

- For all three investigated CFC's (A05, N112 and CX2002U), tritium retention increases by about a factor seven with neutron damage in the range ≤ 0.3 dpa.
- For all dpa-values, tritium retention of N112 and CX2002U is comparable and about a factor three less than that of A05.
- For identical loading conditions, tritium retention values of this study for A05 and N112 are estimated to be within a factor two in agreement with previous data.
- It seems that at irradiation temperatures above 800 °C annealing of tritium traps take place. At 1300 °C about 70 % of the tritium traps are annealed within 2 h.

The dependence of tritium retention on neutron damage for beryllium and ITER representative CFC's is studied in an ongoing second series of tests using a loading gas with higher tritium activity (H_2 + 50 ppm T_2). The goal is to improve the accuracy of the experimental data.

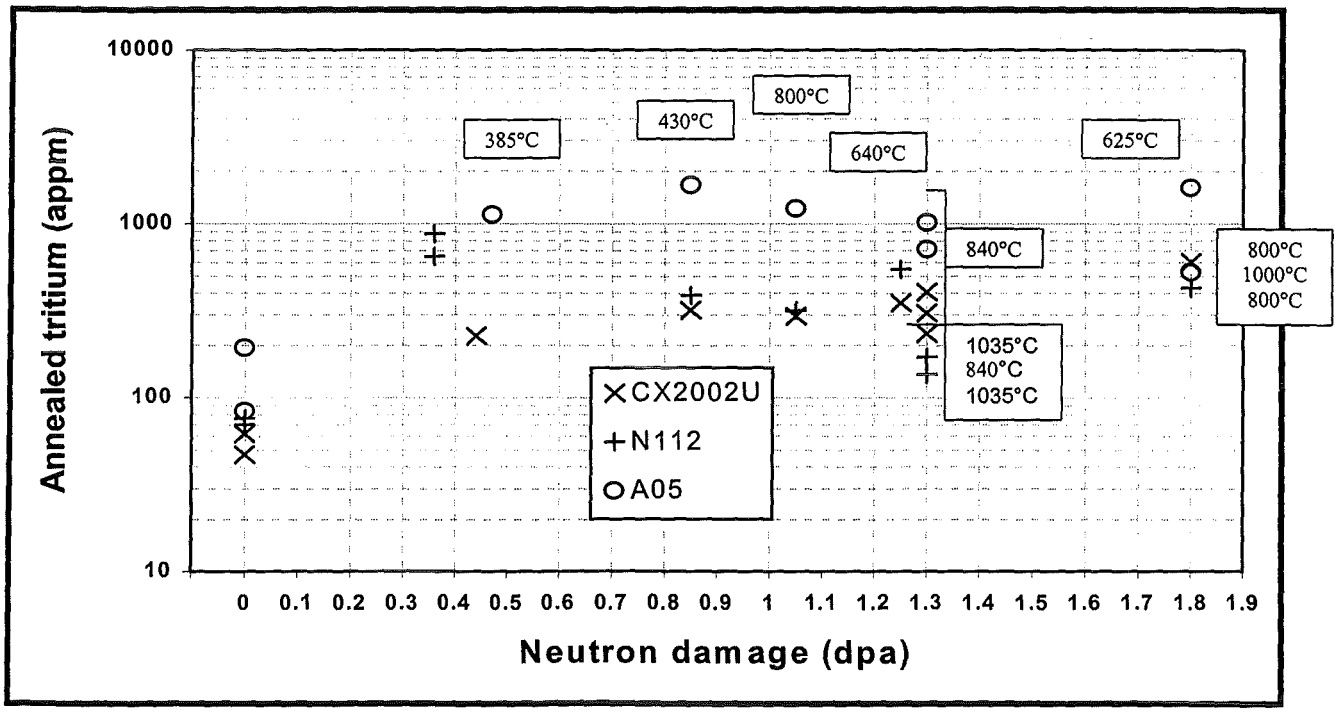

Fig. 1: Annealed tritium as function of neutron damage for ITER representative CFC's (parameter irradiation temperature).

Literature:

[1] H. Kwast, H. Werle, C.H. Wu, Physica Scripta T 64 (1996) 41.

[2] C.H. Wu et al., "EU Results of Neutron Effects of PFC Materials" ISFNT-4, Tokyo, April 6 - 11, 1997.

[3] R. Rolli, S. Rübel, H. Werle, C.H. Wu, "Influence of Neutron Irradiation on the Tritium Retention in Beryllium", Third IEA Int. Workshop on Beryllium Technology for Fusion, Mito City, Japan, Oct. 22 - 24, 1997.

[4] R. Rolli, H. Werle, C.H. Wu, "Influence of Neutron Damage on the Tritium Retention of ITER representative Carbon Fibre Composites (CFC's), "4th Int. Workshop on Tritium Effects in Plasma Facing Components, Santa Fee, May 14 - 15, 1998.

Staff:

E. Damm
R. Rolli
H. Werle
H. Ziegler

DV 7a
Tritium Permeability, Retention, Wall Conditioning and Clean-up (Dust Removal, Baking)

Within this task JET dust and flakes after D/T operation should be delivered on order of the NET/ITER team by JET to FZK for characterisation.

Sample preparation techniques and characterisation methods (optical microscopy, SEM, microprobe, total carbon content, burning + liquid scinitallation counting, thermal desorption) have been successfully tested with flakes recovered before the D/T operation (see T 221, this report) to determine:

- particle size distribution (optical microscopy)
- microstrucutre (optical microscopy, SEM)
- total carbon content (burning + CO_2 measurement)
- composition (SEM, microprobe)
- tritium content (burning + LSC, thermal desorption)
- tritium desorption behaviour (thermal desorption)

Until now no samples are available at FZK. Within a JET task, tiles recovered after D/T operation have been delivered to FZK. It will be tried to recover some dust from these tiles for characterisation.

Staff:

E. Damm
E. Kaiser
H. Kleykamp
R. Pejsa
R.-D. Penzhorn
R. Rolli
F. Weiser
H. Werle
H. Ziegler

V 59 (T 362)
Neutron Streaming Experiment for ITER

The neutronic performance of the ITER shielding system had been experimentally investigated by means of a compact mock-up assembly simulating first wall, shielding blanket, vacuum vessel and toroidal field coils [1]. As part of the ITER Task T218, neutron and photon flux spectra were measured and analysed for two positions inside the assembly [2,3].

In the ITER machine, however, the shielding efficiency will be significantly reduced by penetrations and channels in the blanket and in the vacuum vessel. One of the critical issues is a channel through first wall and blanket used for the mechanical attachment of the (shielding) blanket modules to the back-plate. The aim of ITER Task T362 is to provide experimental validation of the design parameters for such a streaming path with direct sight of the d-t plasma. Therefore, the mock-up used for task T218 was modified to include an open channel on the central axis (inner diameter: 2.8 cm), crossing the first wall and the shielding blanket, and a cavity positioned symmetrically at the end of the channel (inner dimensions: 14.8 cm x 4.8 cm x 5.2 cm, see Fig. 1).

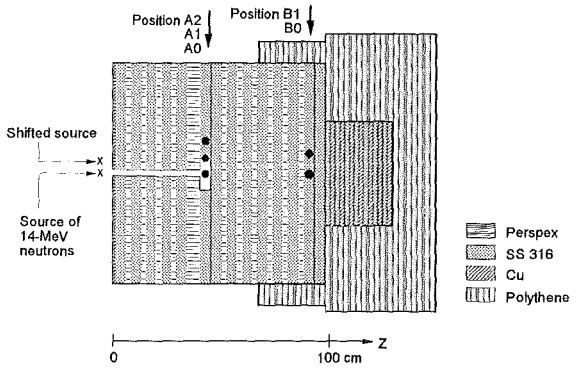

Fig. 1: Horizontal cut of the mock-up assembly with positions of the spectrum measurements

Neutron and photon flux spectra were measured at the same positions A (z = 41.4 cm) and B (z = 87.6 cm) as in the compact mock-up assembly. Now, the first one was located in the middle of the cavity. One series of measurements was carried out with the 14-MeV neutron source on the channel axis, and a second one with the source shifted off the axis (A0S, B0S; a lateral source shift of 5.3 cm was chosen resulting in an neutron incidence angle of 45° at the channel mouth). Additionally, the detectors were shifted. The detector positions A0 and B0 are located on the channel axis, whereas A1, A2 and B1 are shifted off the axis by 7.5 cm, 15.0 and 9.0 cm, respectively (Fig. 1).

A NE213 scintillation spectrometer was used for neutron spectra measurements in the energy range between about 1 MeV and 15 MeV and for flux spectra of γ-rays with energies E > 0.2 MeV. A set of gas-filled proportional counters was applied for the lower neutron energies, down to about E = 30 keV. The liquid scintillator NE213 had cylindrical shape with diameter and length of 3.8 cm. It's axis was perpendicular to the channel axis. All measured and calculated fluxes refer to this detection volume. The neutron fluxes measured with proportional counters were corrected for the different detector materials and shapes.

The results were analysed by means of three-dimensional Monte Carlo calculations with the MCNP-code, version 4A [4], using nuclear cross section data from the Fusion Evaluated Nuclear Data Library FENDL-1 [5]. In the MCNP calculations, the precise geometry of the mock-up, the neutron generator as well as the surroundings (building walls, assembly rack etc.) was taken into account; also the energy-angle distribution of the source neutrons was described in detail. Measured energy-integrated fluxes and ratios of calculated-to-experimental values (C/E) are presented in Tables 1 and 2 for neutrons and photons, respectively. More details are given in Refs. [7, 8].

At z = 41.4 cm, the open channel causes in the mock-up an increase by a factor of 9.7 of the neutron flux with E > 0.1 MeV, if the source is on the axis (A0), and by a factor of 1.2 with shifted source (A0S) compared to the compact assembly (A in Ref.[6]). For the neutrons with E > 10 MeV the enhancement amounts almost two orders of magnitude. This behaviour is reproduced by the calculations with small underestimations of about 10% for E > 0.1 MeV and of 20% for E > 10 MeV. The photon flux with E > 0.4 MeV is increased at z = 41.4 cm by a factor of 2.4 (A0/A) and 1.5 (A0S/A). This is also described by the MCNP calculations with a deviation of less than 20%.

At z = 87.6 cm, the neutron flux with E > 0.1 MeV is larger by a factor of 6.0 when comparing the open channel to the closed channel arrangement (B0/B of Ref. [6]) and by 1.1 only, if the source is shifted (B0S/B). For the photon flux the corresponding ratios are 5.8 (B0/B) and 1.6 (B0S/B). The underestimation by MCNP/FENDL-1 amounts to about 30% for the neutrons and 20% for the photons .

In conclusion, the comparison of measured flux spectra and MCNP/FENDL-1 calculations shows that the fast neutron and γ-ray radiation can be predicted within about 30% for the mock-up assembly with streaming channel. The same result had also been obtained in the case of the compact mock-up system. A general small underestimation of the radiation is observed with increasing penetration depth.

Literature:

[1] P. Batistoni et al., Neutronics shield experiment for ITER at the Frascati neutron generator FNG, Proc. of the 19th Symp. on Fusion Technology, Lisbon, Portugal, 1996, p. 233.

[2] Nuclear Fusion Project, Annual Report of the Association Forschungszentrum Karlsruhe/EURATOM, comp. G. Kast, FZKA 5858, EUR17512EN, page 44.

[3] Nuclear Fusion Project, Annual Report of the Association Forschungszentrum Karlsruhe/EURATOM, comp. G. Kast, FZKA 6050, EUR18156EN, page 23-25.

[4] J. F. Briesmeister (Ed.), "MCNP - A general Monte Carlo n-particle transport code, version 4A", Report LA-12625, Los Alamos, September 1993.

[5] S. Ganesan and P. K. McLaughlin, "FENDL/E – Evaluated nuclear data library, version 1.0", Report IAEA-NDS-128, International Atomic Energy Agency, Vienna, May 1994.

[6] H. Freiesleben et al., Measurement and Analysis of Spectral Neutron and Photon Fluxes in an ITER Shield Mock-Up, Proc. of the 19th. Symp. on Fusion Technology, Lisbon, Portugal, 1996, p. 1571-1574.

[7] H. Freiesleben et al., Measurement and Analysis of Neutron and Photon Flux Spectra in the Cavity, Report TUD-IKTP- 98/03, July 1998.

[8] S. Unholzer et al., Neutron and Photon Flux Spectra in an ITER Shield Mock-up with Open Channel, Proc. of the 20th Symp. on Fusion Technology, Marseille, France, 1998, Vol. 2, p. 1357-1360.

Staff:

U. Fischer
H. Freiesleben
W. Hansen
D. Richter
K. Seidel
S. Unholzer
Y. Wu

Table 1: Integrated neutron fluence per cm^2 and per source neutron for different neutron energy ranges and calculation / experiment ratio (C/E)

Position		Energy range / MeV			
		0.1 ... 1	1 ... 5	5 ... 10	> 10
A0 Source on axis	Experiment	(3.74±0.38)E-6	(3.64±0.20)E-6	(1.04±0.10)E-6	(3.98±0.10)E-5
	Calculation	(5.21±0.04)E-6	(4.82±0.07)E-6	(1.89±0.03)E-6	(3.11±0.04)E-5
	C/E	1.39±0.14	1.32±0.08	1.83±0.18	0.78±0.02
A0 Source shifted	Experiment	(2.25±0.23)E-6	(1.71±0.10)E-6	(0.42±0.04)E-6	(1.65±0.04)E-6
	Calculation	(2.54±0.03)E-6	(1.65±0.02)E-6	(0.46±0.01)E-6	(1.38±0.04)E-6
	C/E	1.13±0.11	0.96±0.06	1.08±0.11	0.84±0.03
A1 Source on axis	Experiment	----	(2.10±0.12)E-6	(4.79±0.46)E-7	(1.26±0.03)E-6
	Calculation		(1.79±0.01)E-6	(4.72±0.08)E-7	(1.11±0.02)E-6
	C/E		0.85±0.05	0.99±0.10	0.89±0.03
A2 Source on axis	Experiment	----	(1.25±0.07)E-6	(2.75±0.26)E-7	(5.97±0.16)E-7
	Calculation		(1.10±0.01)E-6	(2.66±0.07)E-7	(5.51±0.14)E-7
	C/E		0.88±0.05	0.97±0.09	0.92±0.03
B0 Source on axis	Experiment	(3.26±0.33)E-8	(1.45±0.08)E-8	(0.26±0.03)E-8	(2.19±0.06)E-8
	Calculation	(2.34±0.01)E-8	(1.18±0.01)E-8	(0.27±0.01)E-8	(1.35±0.04)E-8
	C/E	0.72±0.07	0.81±0.05	1.07±0.11	0.62±0.02
B0 Source shifted	Experiment	(8.32±0.84)E-9	(2.95±0.16)E-9	(0.49±0.05)E-9	(1.26±0.03)E-9
	Calculation	(6.10±0.04)E-9	(2.33±0.03)E-9	(0.44±0.01)E-9	(0.85±0.03)E-9
	C/E	0.73±0.07	0.79±0.05	0.90±0.09	0.67±0.03
B1 Source on axis	Experiment	----	(1.19±0.07)E-8	(1.84±0.18)E-9	(6.71±0.17)E-9
	Calculation		(0.76±0.01)E-8	(1.61±0.03)E-9	(4.09±0.01)E-9
	C/E		0.64±0.04	0.88±0.09	0.61±0.02

Table 2: Integrated gamma fluence per cm^2 and per source neutron for different gamma energy ranges and calculation / experiment ratio (C/E)

Position		Energy range / MeV	
		0.4 ... 1.0	> 1.0
A0 Source on axis	Experiment	(0.81±0.02)E-5	(1.43±0.04)E-5
	Calculation	(0.68±0.01)E-5	(1.13±0.02)E-5
	C/E	0.85±0.03	0.79±0.03
A0 Source shifted	Experiment	(4.27±0.12)E-6	(6.91±0.19)E-6
	Calculation	(4.21±0.06)E-6	(6.81±0.08)E-6
	C/E	0.99±0.03	0.99±0.03
A1 Source on axis	Experiment	(4.32±0.12)E-6	(7.16±0.20)E-6
	Calculation	(4.38±0.05)E-6	(7.31±0.08)E-6
	C/E	1.01±0.03	1.02±0.03
A2 Source on axis	Experiment	(3.13±0.09)E-6	(5.16±0.14)E-6
	Calculation	(3.11±0.06)E-6	(5.00±0.07)E-6
	C/E	1.00±0.03	0.97±0.03
B0 Source on axis	Experiment	(2.52±0.07)E-8	(3.65±0.10)E-8
	Calculation	(1.95±0.03)E-8	(2.91±0.05)E-8
	C/E	0.77±0.03	0.80±0.03
B0 Source shifted	Experiment	(0.68±0.02)E-8	(1.02±0.03)E-8
	Calculation	(0.58±0.01)E-8	(0.96±0.03)E-8
	C/E	0.85±0.03	0.93±0.04
B1 Source on axis	Experiment	(1.97±0.06)E-8	(2.91±0.08)E-8
	Calculation	(1.45±0.02)E-8	(2.19±0.03)E-8
	C/E	0.74±0.02	0.75±0.02

T 204/209/5
Plasma Arc Cutting of ITER Containment Vessel

Introduction

The objective of this technology programme is the development of cutting techniques for the field disassembly of segments of the ITER containment vessel, required for remote replacement in the event of failure of TF coils. The backplate consists of two stainless steel plates of 60 mm thickness with a gap of 40 mm, and the distance between the outer backplate wall and the vacuum vessel is not yet defined, but could be only 25 mm or even less. This represents a severe space limitation for the collection of dross and fumes required to avoid contamination of ITER and damage to adjacent surfaces.

During earlier work, the feasibility of plasma arc cutting of 100 mm stainless steel was successfully demonstrated under laboratory conditions. The current tasks were planned to optimise plasma arc cutting parameters of 60 mm stainless steel in different positions and to develop techniques for the confinement of blown dross in the narrow gap allowed between the segments.

Basic cutting experiments

An industrial 6-axis robot with horizontal torch cut vertical workpieces in both horizontal and vertical, down and up directions. The 7 bar plasma gas consisted of a mixture of argon (58 l/min) and hydrogen (30 l/min). The arc amperage of 600 A was the same as that used for the earlier 100 mm thick plate experiments. At the beginning and the end of the cut, the 480 mm/min cutting speed had to be reduced to ensure a complete cut, with a concomitant widening of the kerf.

A good quality cut with dross-free kerf was achieved; average peak-to-valley height of 0.06 mm, perpendicularity tolerance 2 mm, hollowness 0.55 mm, cut angle 2 degrees and maximum kerf width 10 mm (Fig. 1).

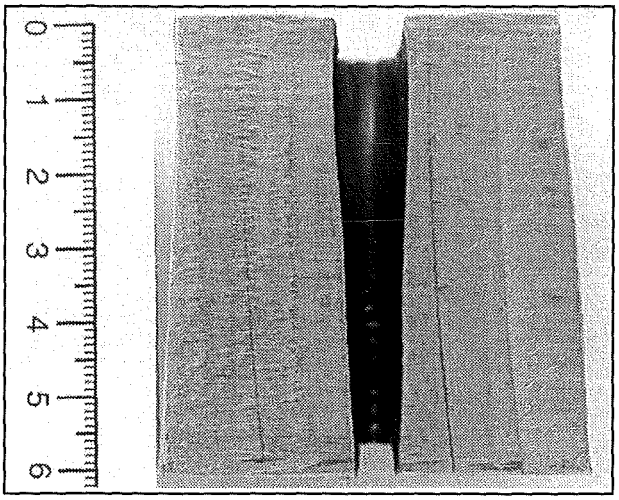

Fig. 1: Kerf profile of 60 mm reference cut

Backplate protection development

Experiments with a 3 mm water cooled copper plate fixed behind the 60 mm CrNi-steel plate were carried out. At 60 mm copper plate to workpiece spacing, the copper plate was only tarnished, while at a separation of 30 mm, the dross stuck to the copper plate and thermally damaged the plate at the cut start and finish.

A proprietary 7 mm ceramic weld backing of aluminum oxide was fixed on the 3 mm copper plate with the distance between the workpiece and protection at 23 mm. After the cuts the weld backing suffered considerable damage but the copper plate was untouched (Fig. 2).

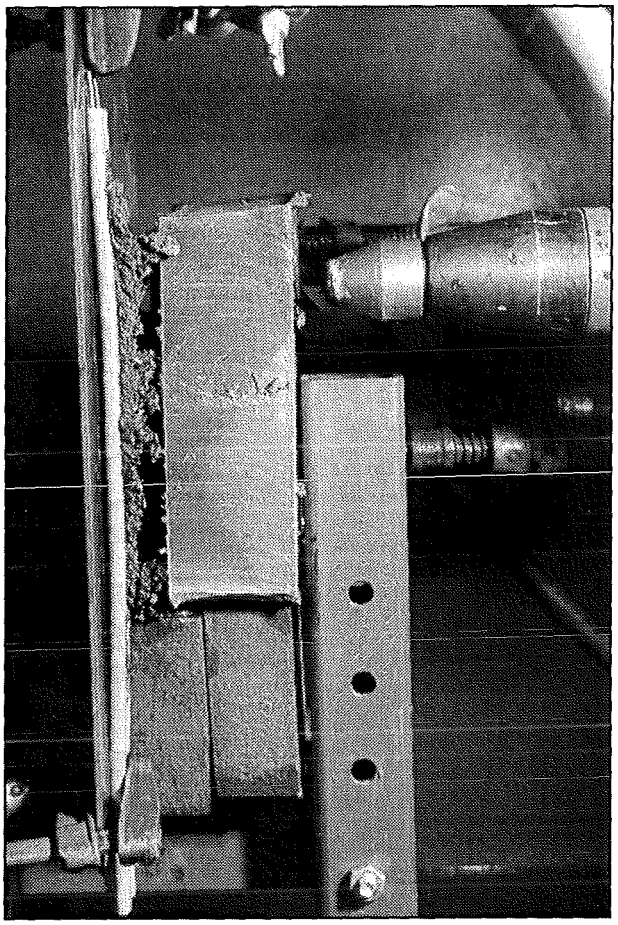

Fig. 2: Vertical cut with ceramic weld backing

The large flowrate of water (2 l/min) is not acceptable in ITER remote handling conditions so the water cooling was replaced by helium gas. The ceramic weld backing was replaced by silicon carbide plates (20 x 20 x 4 mm) attached on the 3 mm copper backing plate by a high temperature resistant adhesive. Silicon carbide has a melting point of 1,500 degree C, a better thermal shock resistance and thermal conductivity. The small gaps of about 0.5 mm between the plates allow a thermal expansion after heat input.

The volume of dross between the plate and backplate protection was such that it partially stuck the plate to the backside protection, so the plate was reciprocated normal to the cut direction by a pneumatic cylinder with an amplitude of 40 mm at a frequency of 1 Hz (Fig. 3). Cuts were successfully carried out with a distance of 15 mm between the workpiece and the backside protection. The total space required for backside protection was 22 mm (15 mm + 4 mm SiC plates + 3 mm copper plate).

In spite of the gas cooling and the small gap the copper plate remained undamaged. The silicon carbide plates were partially melted and there was only a small amount of dross sticking to the ceramic. Although, the thermal resistance of this backplate protection concept is sufficient, the backside plate has to be replaced after each cut.

The cut quality of the workpiece was good with a smooth surface and no dross at the lower side of the kerf.

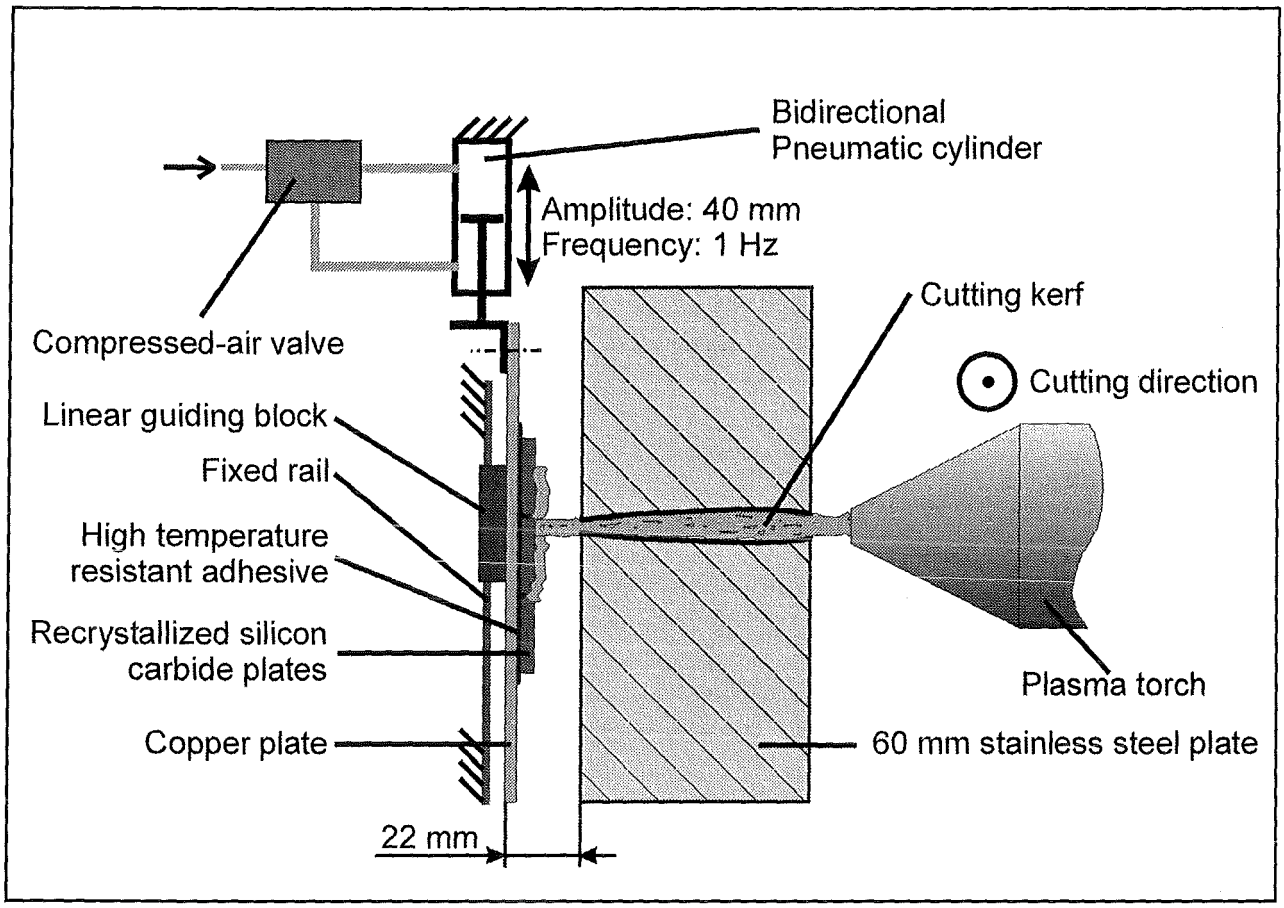

Fig. 3: Plan of backside protection scheme (top view)

Further proceeding

The target of a concept for a backside protection of plasma cuts through a 60 mm stainless steel plate with a 25 mm rear gap with no water cooling has therefore been achieved. Work is under way to extend these early results into a functional system. The scope of the current design and test programme includes the following points:

- Optimisation of edge start/stop parameters to allow for reweld in 60 mm plate
- Cutting tests in overhead position in 60 mm plate, including special torch protection devices
- Design, development and testing of prototype dross collection system with reciprocating backplate
- Tests of various high temperature resistant materials for melt flow absorption

Staff:

L. Wernwag
G. Schreck
H. Haferkamp
Unterwassertechnikum Hannover
des Instituts für Werkstoffkunde
Universität Hannover

T 216 (C16 TT 76)
Shield Blanket Fabrication and Testing (2)

As part of the ITER work package WP4.1 three small scale first wall mock-ups (MU) shown in Fig. 1 have been received in November 1997 for thermal fatigue testing in the FIWATKA facility. According to the first wall (FW) design at that time the MUs were manufactured by NNC and Framatome from DS- or PH-copper (Cu) and 316L stainless steel (SS) using the solid HIP joining technique. HIP joints are located

- between the SS shield blanket block and the Cu layer,
- between the two half shells of the Cu layer, and
- between the Cu layer and the embedded SS FW cooling tubes

The MUs did not have a Be protection layer.

In order to fatigue-test the HIP joints the MUs were designed such that under testing conditions and at the HIP joints they develop maximum stresses and stress ranges which are close to those in a real module [1].

Thermal fatigue testing of the three MUs in parallel was started in January 1998. Each testing cycle consisted of 200 seconds of thermal load (burn time) and of 100 seconds of no thermal load (dwell time). The heat flux to the MU surface was on the order of 78 W/cm². Temperatures in the MUs were measured in three positions (Fig. 1) and they compared well with the FEM calculated predictions.

After 13000 cycles without obvious defects [2], the MUs were sent to VTT for ultrasonic examination (NDE), which did not reveal any changes compared to the pre-test condition. Fatigue testing was continued, until 20000 cycles were reached in early August 1998. Again no obvious defect had developed. A final NDE will be performed after the final number of cycles, which is to be decided, will have been reached.

Literature:

[1] G. Hofmann, M. Kamlah; Selection of Test Conditions for Thermo-mechanical Tests of Small Scale ITER Primary Wall Mock-Ups; FZK Interner Bericht (December 1996)

[2] G. Hofmann, E.Eggert; ITER First Wall Small Scale Mock-Up Thermal Fatigue Testing in FIWATKA; FZK Interner Bericht (May 1998)

Staff:

E. Eggert
G. Hofmann

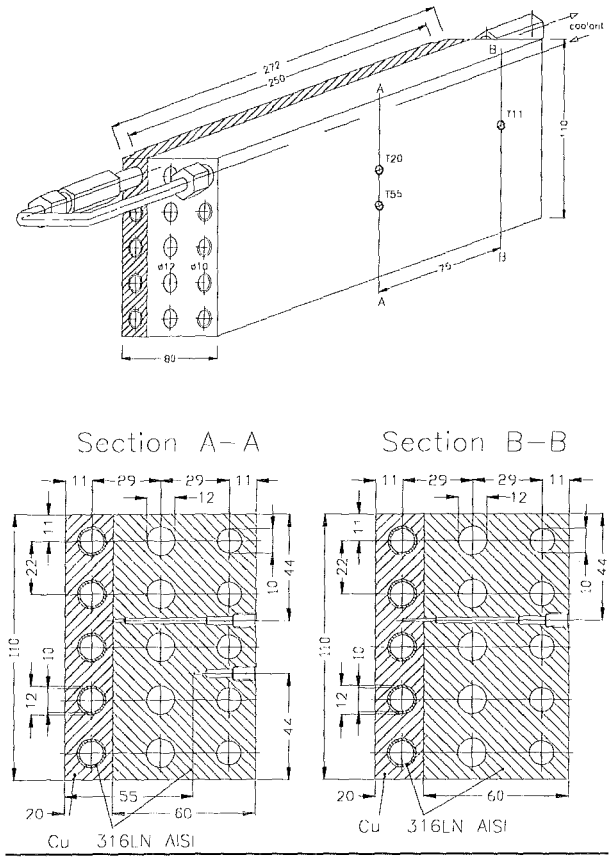

Fig. 1: ITER first wall small scale mock-up

Within the ITER project the EU has the lead in testing of first wall (FW) mock-ups. FW mock-ups are investigated under representative thermo-mechanical loading conditions at FZK and JRC. The mock-ups are manufactured from dissimilar materials (copper/steel and beryllium/copper/steel) with the proposed joining techniques, i.e. diffusion bonding, solid-HIP (hot isostatic pressing) and powder-HIP. Currently, medium sized FW specimen of SS316/copper with different copper alloys and different joining techniques, both, with or without beryllium layer, are under investigation against thermal fatigue under different thermal loading conditions at the respective laboratories.

Thus an activity in the frame of benchmark analyses has been initiated in order to make the experimental results from the different tests comparable. Elastic and plastic finite element calculations have been performed by four participating parties.

Currenty, the results of 3 participants are reported for the elastic analysis. FZK will summarize and compare the results of the complete benchmark. So far available, the results are in 'good agreement' due to the limits and criteria that have been formulated in advance.

Staff:

E. Diegele
G. Rizzi

V 60/1
Blanket Mock-up Fabrication and Testing (1)

Binary Be Pebble Bed Thermal, Mechanical and Pebble Filling Experiments

With reference to the binary pebble bed thermal-mechanical experiments in cylindrical geometry, a new experimental device named SUPER-PEHTRA has been built and tested. It operates with an heating power of 15 kW, in order to ensure an interference value comparable to that foreseen in the ITER breeding blanket also in presence of the volumetric swelling at the blanket-end-of-life.

As in PEHTRA [1], the pebble bed temperatures is measured by 32 thermocouples placed in one axial position in the central region of the test section. Besides this, at the same axial position, in SUPER-PEHTRA four pressure sensors measure the pressure exerted by the expanding pebble bed on the containing walls. The external tube is either water or air cooled. 80 thermocouples are used to measure the axial temperature distribution on the outer tube and on the heating rod.

Operational as well as calibration tests have been already performed. First experimental tests are in progress. The external tube is water cooled in order to achieve the desired maximum value of interference of about 0.3%. This value has required a maximum temperature in the beryllium bed of 350 °C coupled with a temperature of the outer tube of 60 °C and an average bed temperature of 160 °C.

The cooling of the outer tube with pressurized air allows to achieve an outer tube temperature of about 150-200 °C with an average bed temperature of 200-250 °C, comparable to that of the ITER breeding blanket for an interference value of about $\Delta\ell/\ell \approx$ 0.2-0.3%.

The pressure measurements performed so far have allowed to establish a relationship between the bed linear expansion $\Delta\ell/\ell$ and the pressure on the containment outer wall. For a bed linear expansion of $\Delta\ell/\ell \approx$ 0.3% a pressure of 0.7 MPa has been measured (see. Fig. 1)..

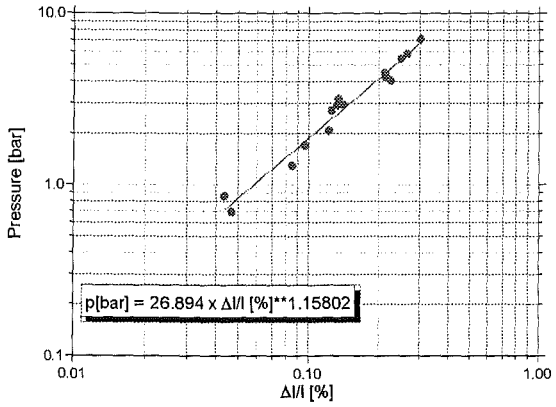

Fig. 1: Pressure on the containment outer wall as a function of $\Delta\ell/\ell$.

For the design of the ITER Breeding Blanket the interaction of the beryllium pebble beds with the structural material must be known. For this purpose a test facility for uniaxial compression tests has been built-up in a glove box. First tests with binary Be pebble beds (large pebble diameter ≈ 2 mm, small pebbles diameters between 0.1 and 0.2 mm) have been performed in a temperature range between ambient and 500 °C.

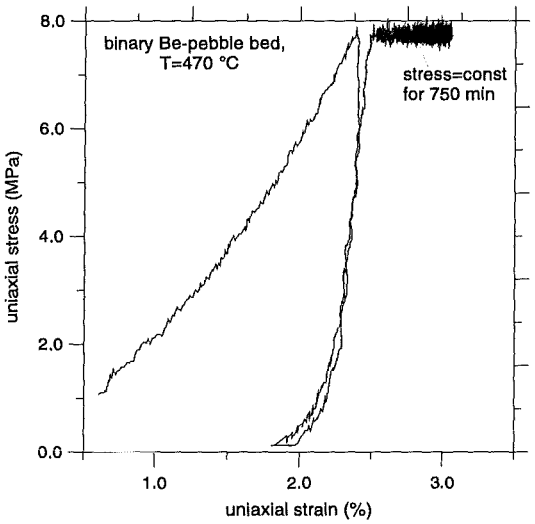

Fig. 2: Uniaxial compression test with binary beryllium pebble bed at 470°C. and 8 MPa

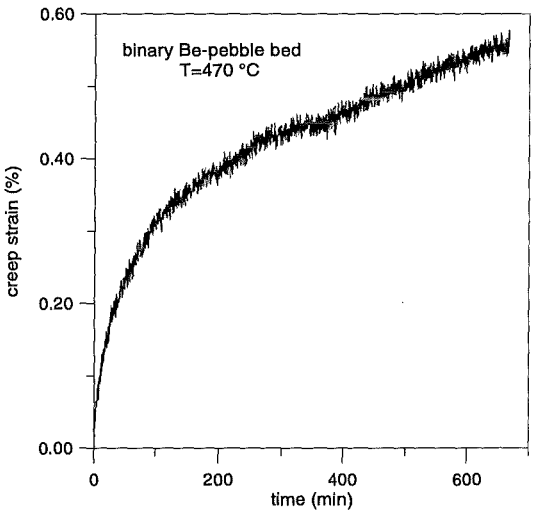

Fig. 3: Thermal creep of binary beryllium pebble bed at 470 °C and 8 MPa.

Figure 2 shows a first characteristic result: the first stress increase is characterised by pebble displacements and plastic deformations; the steep slopes of the first pressure increase and subsequent pressure increase indicate small elastic contributions to the strain. Keeping the stress constant at 8 MPa, the strain increases due to thermal creep as shown as a function of time in Fig. 3.

Further experiments will be performed in order to determine quantitatively the moduli of deformation and the creep behaviour.

Literature:

[1] M. Dalle Donne, et al., "Measurement of the Thermal Conductivity and Heat Transfer Coefficient of a Binary Bed of Beryllium Pebbles". Proceedings of the 3rd IEA International Workshop on Beryllium Technology for Fusion, Mito, October 22-24, 1997.

Staff:

E. Arbogast
M. Behnke
S. Müller
G. Piazza
J. Reimann
F. Scaffidi-Argentina
K. Thomauske

Mechanical behaviour of Binary Beryllium Pebble Beds

For the design of the ITER Breeding Blanket the interaction of the Beryllium pebble beds with the structural material must be known. For this purpose a test facility for uniaxial compression tests has been built-up in a glove box. First tests with binary Be pebble beds (large pebble diameter ≈ 2 mm, small pebbles diameters between 0.1 and 0.2 mm) have been performed in a temperature range between ambient and 500 °C.

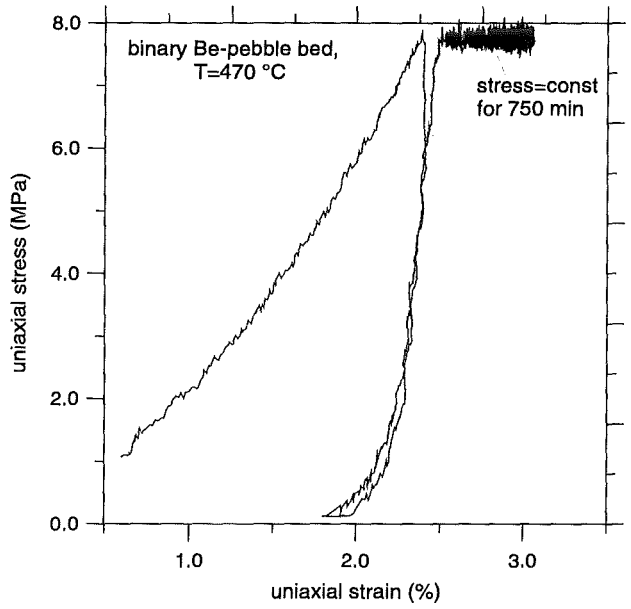

Fig. 4: Uniaxial compression test with binary Beryllium pebble bed at 470°C and 8 MPa

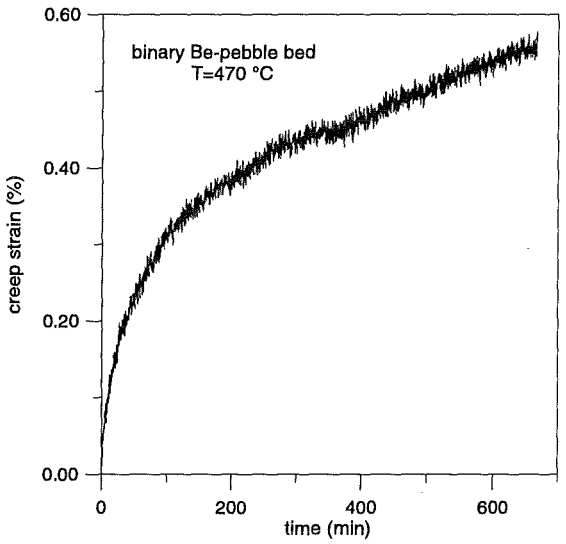

Fig. 5: Thermal creep of binary Beryllium pebble bed at 470 °C and 8 MPa

Figure 4 shows a first characteristic result: the first stress increase is characterised by pebble displacements and plastic deformations; the steep slopes of the first pressure increase and subsequent pressure increase indicate small elastic contributions to the strain. Keeping the stress constant at 8 MPa, the strain increases due to thermal creep as shown as a function of time in Fig. 5.

Further experiments will be performed in order to determine quantitatively the moduli of deformation and the creep behaviour.

Staff:

J. Reimann
E. Arbogast
M. Behnke
K. Thomauske

M 31
Development of 60 kA Current Leads Using High Temperature Superconductors

Introduction

The aim of the task is to develop a 60 kA current lead for the ITER Toroidal Field Coil system using high temperature superconductors (HTSc) in the temperature range between 4 K and 77 K to reduce the steady state heat load at the 4 K level. The task is being done in collaboration with the Fusion Technology Division of the Centre Recherches en Physique des Plasmas of the Ecole Polytechnique de Federale de Lausanne (CRPP-EPFL).

The development program is consists of three stages:

A-1 Test of different materials and concepts in 1 kA modules

A-2 Test of a 10 kA HTSc binary current lead using the material selected in stage A-1

B Design and test of a 20 kA HTSc binary current lead to prove modularity and scale-ability of the design

C After completion of stage B, a 60 kA current lead could be designed to replace an existing 80 kA current lead in the TOSKA facility. This stage is an option, the decision will be made after completion of stage B

Results of Stage A-1 (material selection)

1. Comparing the three configurations tested up to now, i.e., Bi-2212 tubes fabricated by Hoechst AG, Bi-2223 tapes manufactured by American Superconductor Corp. (ASC), and Bi-2223 tapes fabricated by FZK, there is no difference in the 60-K He mass flow rate which is adjusted thus to fix the temperature of the upper end of the HTSC module to 70 K.

2. Looking to the heat load at 4 K, the bulk material has a much lower value than the stabilized tapes, i.e., about a factor of 4. The contact resistances are however comparable.

3. Comparing the transient behaviour, there is a clear distinction between bulk and stabilized tape material. Important for the safety margin during quench is the time duration between 10 and 90 mV which is much larger for the tapes. The stabilized tapes are safer than the bulk material. The use of bulk material requires the design of an electrical bypass which has to be high resistive during normal operation and to have a low current response time in case of a quench.

4. The large degradation of the Bi-2223 tapes fabricated at FZK could be explained by the large stress sensitivity of the tapes even at room temperature. So, it was decided to develop mechanically reinforced tapes with an interior Ag8%Au matrix and an AgMg-alloy outer sheath.

As a consequence, it was decided to proceed with task stage A-2, i.e., the construction and test of a 10 kA HTSC binary current lead. As material, it was decided to use stabilized tapes because of their larger safety margin. The use of bulk material would need further research for optimization of electrical by-pass. In the mean time, also AgAu cladded Bi-2212 tubes have been developed by Hoechst. Because for the design of the 20 kA HTSC lead (stage B), two 10 kA modules are needed and due to the fact that at the time of decision the results of the 1 kA lead using reinforced tapes were not yet available, it was chosen to order one 10 kA module in industry and construct and built a second one at FZK.

Status of FZK 1-kA module

For the manufacturing of a second 1 kA module, 37 filamentary tapes were produced in an industrial technique of bundling AgAu sheathed monocores into an AgMg tube. The typical critical current densities achieved were 10 - 11.5 kA/cm^2 with best values of 15 kA/cm^2. The mechanical properties of the reinforced tapes were measured and compared to the numbers of the AgAu tapes used in the 1 kA module. At room temperature, the tolerable axial stress values for the pure AgAu sheathed tapes are about 20 MPa whereas for the reinforced AgAu/Ag-alloy tapes they are between 170 and 200 MPa depending on tape optimization.

The tapes were thermally cycled between 77 K and room temperature. Up to about 180 cycles, almost no dramatic degradation was observed. Even the use of a heater fan during warming up results in no dramatic current degradation. This also demonstrates the high mechanical stability of the tapes.

As a consequence, a second 1 kA module using reinforced Bi-2223 tapes was built and planned to be tested at CRPP. The results of these measurements are important for the design of a second 10 kA module.

Unfortunately, the manufacturing of the reinforced Bi-2223 tapes at FZK caused some problems concerning critical current and mechanical performance which have different reasons:

1. The optimization of the manufacturing process results in HTSC tapes being not reproducible considering critical current. This caused some delays in finishing the tape manufacturing.

2. A mechanical degradation resulting in a destructing of the tapes during warm up from 77 K to room temperature was observed recently which was probably caused by the soldering process during manufacturing of the HTSC module. It sems that the AgMg reinforcement sheath is much more sensitive during the soldering process than the pure AgAu tapes. Detailed investigations are under way.

As a consequence, the decision to built a second 10 kA HTSC module at FZK and to connect both 10 kA modules, i.e., the ASC and the FZK ones in parallel to form a 20 kA lead which is needed for stage B, had to be modified. A second ASC 10 kA module is foreseen to reduce delays. The development of the AgMg reinforced AgAu stabilized Bi-2223 tapes will continue because of their principally high performance. The construction of a FZK type 10 kA HTSC module will be started after completion and test of the 1 kA module.

Status of stage A-2 (construction and test of 10 kA lead)

The first 10 kA module was ordered from ASC. The design of the module is similar to those leads manufactured for the LHC project at CERN ,or for Fermilab, i.e., an appropriate number of Bi-2223 tapes sintered together, forming so-called stacks, and soldered on top of a sophisticated stainless steel support tube. At both ends, copper end caps are placed for current transfer to adapt the HTSC module into the apparatus of the customer. The support structure also serves as an additional heat sink in case of a quench. In our case, the safety requirement is such that the module has to withstand the full current of 10 kA for 10 s in case of loss of active cooling of the copper heat exchanger part of the lead without reaching room temperature. The number of tapes are such to get a critical current of at least 12 kA at 70 K. The total length of the lead is 600 mm. To have the possibility to measure current imbalances during transients, e.g., during

quench, four of the stacks are equipped with voltage taps. The voltages of both end caps are monitored too. In addition, four temperature sensors are positioned at 100%, 90%, 70%, and 50% of the HTSC length, measured from the cold end, to evaluate the temperature profile.

The 10 kA HTSC module was delivered in June 1998 but didn't fulfill the specifications regarding geometical tolerances, boundary conditions for operation in vacuum, and sensor equipment. The module was improved by ASC.

For reduction of the delay, as mentioned before, it was decided to order the incomplete HTSC module from ASC and one additional complete 10 kA module was delivered to have a back up solution for the construction of the 20 kA lead.

At the beginning of September 1998, both HTSC modules have been delivered from ASC. One of them is currently being installed in the test facility at CRPP and will be tested in October this year. Figure 1 shows a picture of one of the modules.

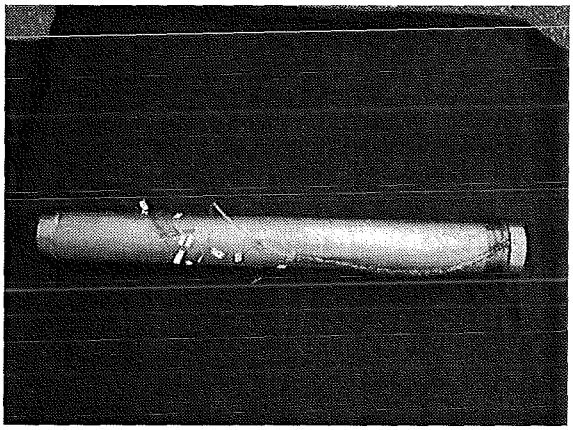

Fig. 1: Picture of the 10 kA HTSC module manufactured by ASC

A critical current measurement in a LN_2 bath was done at the manufacturer and the following results were obtained:

1. The critical current at 77 K and self field of the lead was about 9.5 kA. For 70 K, which is the maximum temperature in the experiment, this corresponds to a critical current of larger than 13 kA.. Figure 2 shows the critical current as a function of applied magnetic field perpendicular to the broad face of the tape as given by the manufacturer. In addition, the load line and the operation point of the lead are plotted. At 10 kA, the difference to the critical current would be about 40 %.

2. The U-I traces of four of the seven HTSC submodules show different shapes which is due to transverse resistances in the individual stacks caused by incomplete removement of tape coating before the sintering process of stack formation. Figure 3 shows the U-I traces. It should be mentioned that nevertheless all of the submodules fulfill the specifications with respect to critical current given by the conventional criterion of 1 μV/cm.

3. The contact resistances at the cold and warm ends were measured by using the voltage taps on top of one of the HTSC stacks and on top of the copper end pieces. The results are 3.1 and 16.7 nΩ, respectively, for both modules which is much lower than specified. Moreover, taking into account the fact that the contact resistance at 4 K is typically one order of magnitude smaller than at 77 K, the cold end resistance is expected to be very low.

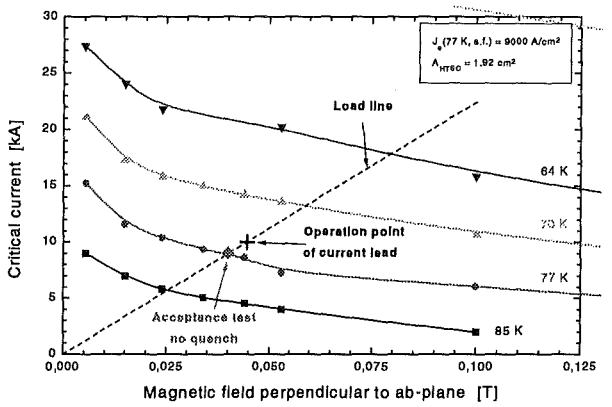

Fig. 2: Critical current vs magnetic field perpendicular to broad face of tapes for different temperatures and load line of the lead

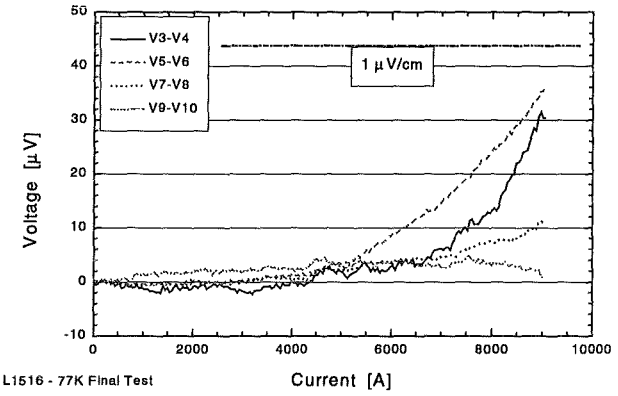

Fig. 3: Measured voltage as a function of transport current for the individual submodules of the 10 kA HTSC module.

The test at CRPP will cover both the steady state and transient behaviour of the current lead. The critical current of the HTSC module will be measured too. If I_c is larger than 12 kA and because the maximum current available in the test facility is limited to that value, the critical current would then have to be evaluated by increasing the upper temperure of the HTSC module. From the steady state tests, mainly the temperature profile along the whole lead, the thermal heat load at 4 K, and the 60 K He mass flow rate needed to fix the upper temperature of the HTSC module to roughly 70 K will be obtained. The transient test will be done to study the quench behaviour of the HTSC module and to compare the results to the expectations.

Outlook (Stage B - 20 kA HTSC current lead)

As for the 20 kA HTSC binary current lead, two 10 kA modules are needed, it was decided to use a modular concept even for this current range which allows an easy extension to higher currents, from an engineering point of view.

Due to the modular concept, the effect of current distribution as well as a detailed model of the contact region is being investigated.

In 1999, a 20 kA HTSC binary current lead will be constructed and tested in the STAR facility at FZK.

Literature:

R. Heller et al., "Status of the Development Program of a 60 kA Current Lead Using High Temperature Superconductors", *presented at 1998 Applied Superconductivity Conference,* Palm Desert, CA, 13.-18.Sept. 1998

Staff:

K. Bauer
G. Friesinger
R. Bußjäger (bis 31.7.98)
Dr. W. Goldacker
Dr. R. Heller
Dr. J. Krelaus (ab 1.7.98)
H. Orschulko
Dr. M. Quilitz (bis 30.6.98)
M. Tasca (ab 1.3.98)
S. Zimmer

M 12 (N 11 TT 19)
Preparation of the ITER TF model coil test facility

and

M 44
TFMC installation and test

The TOSKA facility at FZK Karlsruhe is being upgraded for testing the ITER TF model coil. The facility has been taken into operation in the following steps:

- Test of the LCT coil at 1.8 K (1996)
- Test of the stellarator prototype coil W-7X (1999)
- Start of the test of the TFMC (End 1999)

The first step qualified the LCT coil for the use as background coil for the TFMC test configuration. The basic facility with its electrical and cryogenic supply system as well as data acquisition and control was taken into operation. The specific facility configuration needed for the TFMC test is in progress. Specific components like a 80 kA dump circuit, two 80 kA current leads, a 20 kA power supply and supporting and handling tools are under construction.

The W-7X arrived on TOSKA site beginning July 1998. The installation work is running.

The fabrication of the TFMC in the European industry is in progress. Four of five pancakes were heat treated. The welding of the coil case is completed. The fabrication and the preparation of the test programme of the TFMC are accompanied by the special skills of the European superconducting laboratories. The areas of Euratom Association FZK are:

- Instrumentation (included in M44)
- Conductor measurements (NET Contract No.: NET/97-458)
- Mechanical material and component testing (EU Task No: M45)
- High voltage component delivery and testing (NET Contract No.:NET/96-438)
- Finite element analysis (NET Contract No.: NET/95-384)
- Electromagnetic and thermohydraulic analysis (included in M44)
- Transient voltage behaviour of the TFMC (included in M44)

The installation of the TFMC is scheduled for the second half 1999 and the test end 1999

1. TOSKA facility

The remaining components requiring development work are the 80 kA current lead and the 80 kA dump circuit. A 20 kA power supply, lifting beam and the supporting structure of the configuration (gravitational support) are under construction. Data acquisition and cryogenic supply system has to be configured for testing the TFMC.

The 80 kA current lead: Based on the experience gained with the 30 kA current lead the construction of 80 kA lead was started. The increased current by a factor 2.7 required some design changes for the cold and warm end of the current lead (Fig. 1). The number of superconducting Nb_3Sn inserts had to be increased from 2 to 3 [1-1]. These inserts are needed for adaptation of the length of the normal conducting part of the current lead in order to achieve an optimized operation at different current levels. A water cooled flexible busbar constructed from copper braids was successfully tested up to 80 kA in continuous operation. The copper current density was 45 A/mm^2. This development solved the space restrictions and alignment problems for joining the current leads with the Al busbars. The components for two current leads are being under construction.

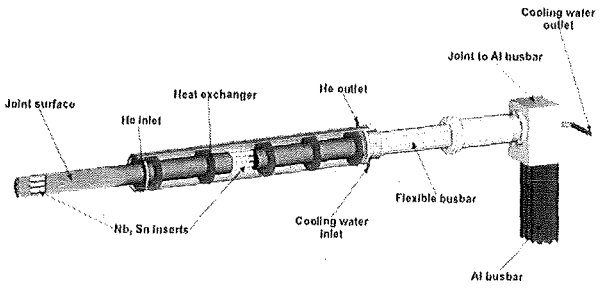

Fig. 1: A schematic view about the construction of the 80 kA current lead.

The 80 kA dump circuit: The circuit design is based on those used for the POLO and the LCT coil. The circuit was ordered at beginning of 1998 (Fig. 2). It will be designed and constructed by the Siemens AG, Erlangen. The commissioning will take place in April 1999.

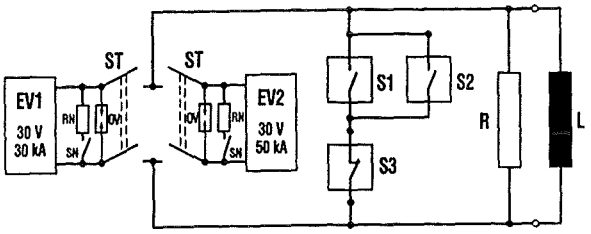

Fig. 2: The 80 kA dump circuit of the TFMC (EV: Power supply; ST: Separation switch; S1, S2, S3: Breakers, R: Dump resistor; L: TFMC; SN: Short circuit switch; RN: Current limiting resistor; OV: Overvoltage protection).

For investigating transient voltage behaviour of the TFMC winding type, conductors embedded in radial plates, discharges will be performed by the POLO dump circuit at 25 kA with a counteracting current switch.

The 20 kA power supply: The TFMC is supplied by a current of 80 kA by two existing power supplies (50kA and 30 kA) in parallel operation. Therefore a third power supply is needed for the operation of the LCT coil. The power supply was ordered January 1998. It now under construction in industry.

Tooling for assembling: A lifting beam for lifting the TFMC test configuration (about 120 t) in the TOSKA vacuum vessel was designed and ordered in industry. The support frame on which the TFMC, intercoil structure and the LCT coil rest has been constructed. The fabrication in the workshops is running. As consequence of a change in the test programme (Testing of the TFMC in the first run without LCT coil) the technical specification for an auxiliary structure replacing the LCT coil was elaborated together with the NET Team (see section 2).

The cryogenic supply and control system as well as the data acquisition: These systems are presently configured for the test of the W 7-X prototype coil and need adaptations for the TFMC test after completion of W 7-X prototype coil test programme.

2. Test programme of the TFMC [2-1]

In collaboration with the European superconducting laboratories a test programme for the TFMC was elaborated.

The goal of the test of the TFMC in the background field of the LCT coil is the verification of the overall engineering design of the TFMC for the electromagnetic, thermohydraulic, mechanical and electrical insulation properties.

The electromagnetic properties: They describe the relation between the magnetic field and current as well as the operation limits in the three dimensional superconducting space (I_c, B, T_{cs}). Typical properties of the superconductor like AC losses and critical currents are measured under operation conditions. Typical engineering design features like joints and instrumentation for protection can be tested under operation conditions.

The thermohydraulic properties: These are the basis for the operation of the sc magnet. Well defined operation parameters are needed for cooldown and warm up, the steady state operation and the mastering of fault conditions.

The mechanical properties: Large superconducting magnets need embedding of the sc cable in structural material. The force transmission to and the stresses in the structural material reflects the function of the engineering design. The measurement of the displacements between and from certain points has to be performed. The strain measurements on the surfaces of the structure in high loaded regions lead to the stress levels in the material.

The electrical insulation properties: The radial plates introduce a potential in the winding. Each radial plate potential has to be connected to its corresponding inner joint in order to give the radial plates a definite potential. Switching surges excite oscillations in the equivalent network which can lead to over voltages in the winding. The TFMC is the first coil in radial plate design. The TFMC shall be investigated considering these properties for the validation of network codes applied for the ITER full size coils later on.

Additionally, the radial plate winding type allows the investigation of the conductor insulation by partial discharge (PD) measurements. This method has the potential to observe conductor insulation over the life time of the magnet. This shall be also investigated for the TFMC.

Instrumentation: The TFMC is equipped with the common instrumentation of sc forced flow cooled magnets. The electromagnetic and thermohydraulic properties are measured by voltage taps, temperature sensors, pressure sensors and differential pressure sensors. The mechanical properties are investigated by displacement transducers and strain gauges. The electrical insulation properties investigations need a different patching of the radial plate voltage taps for operation and PD measurement.

The voltage tap location and the thermohydraulic instrumentation for the winding was fixed. The thermohydraulic and mechanical instrumentation of the TFMC case and intercoil structure (ICS) is in progress.

Test procedure: The test procedure of the TFMC can mainly be characterized by following sections: I) Cooldown; II) Testing of TFMC alone; III) Testing of TFMC in the background field of the LCT coil; IV): Cycling of the TFMC in the background field of the LCT coil; V) Warm up. Sections II to III contain each one check outs at low currents and ramping up the current in steps. At each step a slow ramp down, an inverter mode ramp down (inverter mode operation of the power supply means max. negative voltage) and a fast discharge (dump) will be performed.

The injection of heated supercritical helium slugs are integrated in these steps and the operation at higher temperatures (4 K to 9 K). In addition, pulse voltage tests and PD measurements will be performed.

2.1 Preparation of experiment evaluation

For prediction and an effective evaluation of the test results the preparation of the calculation tools and necessary input parameters gained from separate experiments are indispensable.

Electromagnetic properties: The scalability of the critical data in the superconducting space is indispensable necessity for assessing the TFMC design. The different operation conditions (higher current, lower field) need an experimental check of existing scaling laws. Validating Summer's rule for TFMC strands, I_c measurements were performed over the field and temperature range typical for the TFMC operation. Critical current measurements on reacted strands for controlling the heat treatment of the TFMC are performed under NET Contract No. NET/97-458.

The common homogeneous current distribution over the winding cross-section can no longer be applied for calculating the field of the TFMC [2-2]. The arrangement of discrete conductors leads to a strong field gradient over the conductor in the range of 1.6 T in the high field region. This has to be taken into account for assessing the operation limits of the TFMC. Field calculations were also performed in the joint region for assessing the operation of the joints considering their losses. An estimation of the ramp losses limits the ramp rate to about 700 A/s for being within the available cryogenic power of the TOSKA facility [2-3].

Thermohydraulic properties: The cable-in-conduit-conductor with a central cooling channel necessitates a new definition of the hydraulic parameters for the application of the codes SARUMAN and GANDALF which are used for the thermohydraulic analysis of the TFMC during quenching. Parameter studies were performed investigating the behaviour of normal regions with different boundary conditions [2-4],. Considering peak pressure (≈ 2 MPa) and peak temperature (≈ 120 K) both codes gave compatible results (operation condition: 80 kA, TFMC excited alone). Eddy current losses in the stainless steel structure were analyzed by the code CORFOU. The impact of heat diffusion from the radial plate to the conductor was investigated [2-5]. The increased mass flow induced by the heat flux to the conductor leads to a reduced length of the normal zone compared to quench without eddy current heating. A propagation of a normal zone at 4.5 K operation temperature in comparison with 9 K operation temperature was calculated. At 9 K the normal zone was about 10 times larger with a jump after 8 s caused by the eddy current heating (Fig. 3).

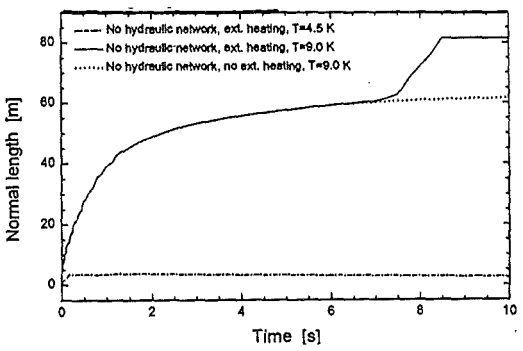

Fig. 3: Normal conducting length of the ITER TFMC as a function of time for a quench in the high field region with eddy current heating (external heating) of the radial plates and inlet temperatures of 4.5 K and 9 K. For comparison, the results of a calculation at 9 K without eddy current heating is plotted, too.

Mechanical properties: The mechanical analysis were performed in two steps, a finite element analysis of the conceptual design by FZK/IRS [2-5] and of the engineering design by the European industry consortium AGAN. The last one was the basis for an elaboration of the sensor location. The accompanying work is performed by FZK/IRS under NET Contract No. NET/95-384

Dielectric insulation properties: A network model with frequency dependent mutual inductance's for the TFMC is being prepared. The pulse deformation of PD pulses propagating through the TFMC winding and joint area was experimentally investigated by a model. The PD diagnostics should be applicable for this winding type according to results achieved (Fig. 4).

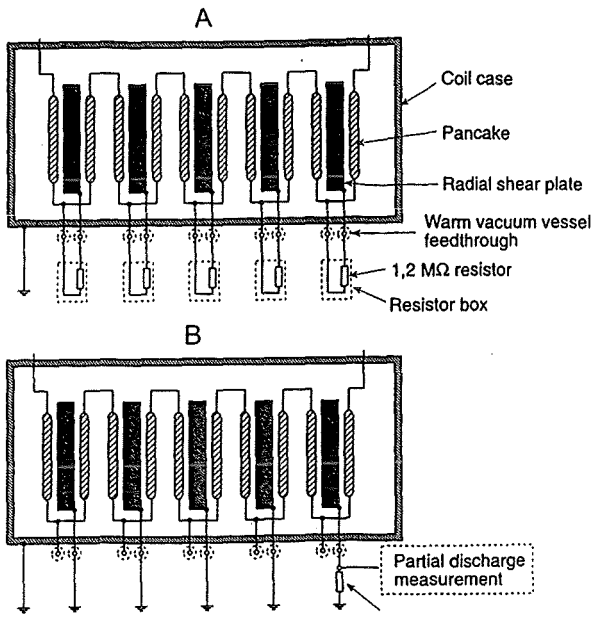

Fig. 4: Fixing the potential of the radial plates during operation with current (A)and during partial discharge measurements by AC voltage operation (B).

The electromagnetic, thermohydraulic and dielectric insulation analysis work is included in the TOSKA Task M44:

Literature:

[1-1] R. Heller, Th. Schneider, Optimization of the Niobium –Tin Inserts for the 80 kA Current Lead to be used in the TOSKA Facility for the ITER Toroidal Field Model Coil Test, Proc. ASC, Palm Springs,CA, USA, September 13-18, 1998

[2-1] A. Ulbricht, M. S. Darweschsad, J. L. Duchateau, H. Fillunger, S. Fink, G. Friesinger, R. Heller, P. Hertout, P. Libeyre, G. Nöther, S. Raff, F. Wüchner, G. Zahn, The Preparations for Testing the ITER Toroidal Field Model Coil (TFMC), Proc. 20th SOFT, Marseille, France, September 7-11, 1998, Paper #094

[2-2] R. Heller, Calculations for the magnetic field of the ITER Toroidal Field Model Coil, Interner Bericht F130.0016.012/M Forschungszentrum Karlsruhe, November 1997

[2-3] R. Heller, AC-loss calculations for the ITER Toroidal Field Model Coil, Interner Bericht F130.0016.012/L Forschungszentrum Karlsruhe, November 1997

[2-4] R. Heller, Intermediate Report, Thermohydraulic Properties of the ITER Toroidal Field Model Coil, Interner Bericht F130.0016.012/N Forschungszentrum Karlsruhe, Dezember 1997

[2-5] R. Heller, J. L. Duchateau, S. Nicollet, F. Prat, Numerical evaluation of the quench behaviour of the ITER toroidal field coil model coil, Proc. CEC Portland, OR, USA, July 28 – August 1, 1997

Staff:

A. Augenstein
H. Barthel
S. Darweschsad
G. Dittrich
P. Duelli
S. Fink
G. Friesinger
A. Götz
P.Gruber
A. Grünhagen
R. Heller
W. Herz
R. Kaufmann
A. Kienzler
L. Lang
O. Langhans
W. Lehmann
V. Marchese (since Sept. 1, 1998)
W. Maurer
I. Meyer
G. Nöther
U. Padligur
K. Rietzschel
P. Rohr
G. Schleinkofer
T. Schneider
K. Schwelkert
E. Specht
H.-J. Spiegel
M. Süßer
A. Ulbricht (for 2)
D. Weigert
F. Wüchner
G. Zahn (for 1)
H.P. Zinecker
V. Zwecker

M 45
ITER Coil Casing and Intercoil Structures

The aim of this technology task is the characterization of ITER coil casing structural materials during the manufacturing stage of Mock-ups. These investigations comprise base and weld metal qualification of industrial produced structural steel samples. In addition to that, several components were necessary to be investigated during the ongoing phase of the TFMC fabrication. Finally, for the candidate superconductor jacket materials 316LN and Incoloy 908 the fatigue crack growth rate has been characterized and the Final Report with respect to Contract NET/96-408, ITER Task Agreement N11TT15(p) was submitted to the NET team and accepted.

Base and Weld Metal Cryogenic Mechanical Characterization

Within this task a 90 mm thick plate of Type 316LN material provided by Alstom Company France was investigated. Besides, measurements were performed with provided ca. 50 mm thick GMAW (Gas Metal Arc Weld) weld samples. These tensile and fracture tests were carried out with specimens machined from the sample in transverse, longitudinal, and vertical orientations. In Figure 1 the provided plate metal sample and the position of the specimens are illustrated.

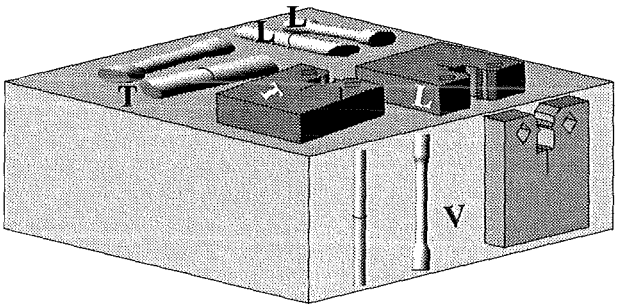

Fig. 1: 90 mm thick Type 316LN metal sample and the machined specimens from the plate

Table 1 gives the results with the carried out tensile tests at 7 K. The mechanical test results reveal the significant difference of obtained uniform elongation between vertical and long/transverse orientated specimens. Whereas the yield strength values can be assumed that they are within a natural scatter band. The ultimate tensile strength data seems to be inferior in case of vertical orientated base metal specimens compared to long/transverse machined specimens. The latter two tests with the base metal carried out up to ~4 % and ~9 % strain were performed for the reason of confirmation of obtained yield strength values and therefore they were not fractured ultimately.

Table 1 refers also to the measurements of the GMAW sample of the first trial welding procedure. Here also there is a significant difference between weld transverse and weld vertical orientation. This difference, however, results mainly from the performed weld process. The two ca. 50 mm thick Type 316LN plates were firmly hold during the welding process to avoid distortion. This resulted most probable high residual stresses during cool down of the final welded sample, thus giving less chance of elongation during tensile testing in weld transverse direction.

For the fracture toughness measurements of the 90 mm thick Type 316LN plate material two methods have been applied comprising two different kinds of specimens; Compact tension (CT) and JETT (EDM notched round bar). The plan of machining is illustrated in Fig. 1. According to this Figure a comparison of these two different type specimens can be done by considering the crack plane orientation. In addition, the CT specimens (63 x 60 x 14) were all side grooved having a 90° angle and a 0.5 mm depth. The width and thickness of these specimens were 50 mm and effective 14 mm respectively. The CT specimens were tested in LHe environment using the 200 kN tensile machine. The single specimen unloading compliance method according to ASTM E 813 was used for all these measurements.

Table 1: Tensile test results of Type 316LN 90 mm thick plate sample and the first trial GMAW weld sample at 7 K

Specimen orientation	Young's Modulus GPa	Yield Strength MPa	Tensile Strength MPa	Uniform Elongation %
Vertical	208	931	1522	31
Vertical	209	890	1512	31
Longitudinal	202	887	1635	49
Transverse	200	903	1608	47
Transverse	199	907	-	-
Longitudinal	200	900	-	-
Weld trans.	205	1091	1337	8
Weld trans.	203	1107	1278	8
Weld vert.	204	976	1533	30
Weld trans.	203	977	1165	10
Weld long.	195	1022	1508	49

In Table 2 all data obtained from the three orientations are collected together. The corresponding measured JETT (A novel J-integral test method using EDM notched round bars, previously described in [1]) results are related to the CT specimen findings considering the crack plane orientation. As obvious there is a large scatter between CT bound measurements in case of vertical machined specimens. The transverse machined CT specimen shows also significant high values compared to the JETT based vertical machined specimen. However, regarding the very high fracture toughness values this large scatter is reasonable.

Table 2: Fracture toughness properties tested with various type of specimens at 4.2 and at 7 K for base metal and weld metal

Specimen Type and orientation	Fracture Toughness, MPa √m LHe, CT	7K, JETT
CT- Vertical	280	-
CT-Vertical	310	-
CT-Longitudinal	356	-
CT-Transverse	270	-
JETT-Longitudinal	-	278 / 220
JETT-Transverse	-	355 / 314
JETT-Vertical		217 / 215
Weld CT-Transverse	172	-
Weld CT-Longitudinal	150	-
Weld JETT-Transverse	-	172 / 165
Weld JETT-Longitudinal	-	162 / 163

Filler Material Cryogenic Mechanical Investigations for Welding Qualification

This task was necessary to qualify the commercial filler materials which is foreseen for the welding procedure of ITER coil casing and intercoil structures. The company Belleli, Italy provided 8 samples of ca. 40 mm thickness. The samples were the result of a joining of 304 Type 40 mm thick plates. The used weld procedures were GTAW (Gas Tungston Argon ARC), SMAW (Shielded Manual Arc), and SAW (Submerged Arc). The goal was to test with the use of qualified weld filler wires the performance of high deposition rates allowing economical automatic welding. Tensile and JETT type fracture specimens were prepared from the mid weld position of the provided samples. Two tensile (4 mm diameter and ca. 20 mm reduced section) and two 6 mm diameter JETT fracture specimens were prepared from each sample. Additionally, the company provided from the same batches heat treated samples. The heat treatment of these samples were conducted at air at 800°C for 1 hour. Altogether 64 specimens were tested at 7 K using a newly designed multispecimen cryogenic test rig allowing to measure 4 specimens one after the other with the test facility. Table 3 below shows the chemical composition of the weld zone analyzed after the welding process.

As the chemistry of the weld zone shows high chromium and high manganese favors the solution of nitrogen a promoter for the austenitizer and responsible for the high strengths. Nickel on the other side suppresses the nitrogen solubility by meanwhile increasing the stability of the austenite. This balance of all this elements decides the strength and toughness level of the weldment. However, different other factors owing to the manufacturing variability (pores, inclusions, grain sizes, residual stress levels, and etc.) given by the filler material overall quality decides the general cryogenic behavior of the ready product. The tensile investigation results is given in Table 4 shows the significant lower Young's Modulus values compared to plate metal of similar Type 316LN stainless steels. The lower stiffness of the test specimens results in general from the weld microstructural quality. Especially, pores resulting from this high speed welding process reduce the Young's modulus considerable. The high yield strength of the weldments can be partly attributed to the existing residual stress components.

The one hour heat treatment at 800°C affects adversely the mechanical behavior with respect to uniform elongation, which is an indicator for material's toughness behavior. To check the effect of an hour heat treatment for this type of materials a standard plate material of Type 316LN were heat treated at 800°C and at 900°C for an hour. Two tensile and two JETT specimens were machined from these samples after the heat treatment process. Table 5 gives the results of these tensile measurements conducted with some of heat treated weld metal samples and the heat treated plate material.

The obtained low elongation values in case of plate material heat treated at 900 °C indicates that heat treatment above >800°C may affect the cryogenic mechanical values also in case of non welded structures.

The fracture toughness weld material qualification was performed with the 6 mm round bar specimens. The necessary severe EDM notch around the girth of the specimen was placed accurately inside the weld zone having a net diameter of 2 mm. Table 6 shows the obtained results with these measurements. Again the heat treated samples were inferior of those as welded samples. According to these findings the code 2684A were selected as one of most promising candidate filler wire.

Table 4: Tensile measurement results of deposited weld filler materials of as welded samples at 7 K

Code	Young's Modulus GPa	Yield Strength MPa	Tensile Strength MPa	Uniform Elongation %
2684A AW	190	1253	1550	17
2684B AW	186	1195	1565	17
2677A AW	180	1170	1513	33
2677B AW	167	1067	1447	31
2676B AW	136	1029	1155	6*
2676E AW	150	1083	1285	25
2676F AW	189	1058	1285	25
2675A AW	168	1127	1451	27

* Massive pores could be detected on the fracture surface

Table 5: Tensile measurement results of deposited weld filler materials of heat treated samples at 7 K

Code	Young's Modulus GPa	Yield Strength MPa	Tensile Strength MPa	Uniform Elongation %
2684A HT	193	893	1253	16
2677A HT	182	1162	1373	9
2677B HT	201	1117	1407	9
2675A HT	158	1064	1395	17
Plate 800°C	186	1070	1559	48
Plate 800°C	199	1069	1530	40
Plate 900°C	196	1030	1430	27
Plate 900°C	191	1042	1427	24

Table 3: Chemical composition of the investigated GMAW joined weld metals

Code	C	Si	Mn	P	S	Cr	Mo	Ni	Al	Cu	Nb	Ti	V	B	N
2684A AW	.02	.15	4.43	.013	.005	24.5	1.96	20.1	<.00	.07	<.01	.01	.06	.0014	.3263
2684B AW	.01	.38	7.43	.012	.005	20.0	3.23	15.5	<.00	.06	.02	<.01	.01	.0014	.2669
2677A AW	.04	.63	6.40	.020	.006	19.0	3.19	15.4	<.00	.11	.01	.03	.05	.0010	.2407
2677B AW	.04	.36	5.43	.012	.011	25.3	2.37	21.0	<.00	.01	.01	.03	.04	.0006	.2272
2676B AW	.02	.31	3.70	.016	.007	24.8	2.05	21.4	.04	.08	<.01	<.01	.05	.0007	.1963
2676E AW	.03	.64	6.31	.017	.005	19.1	3.22	15.4	.00	.11	.01	.01	.08	.0007	.2221
2676F AW	.03	.34	4.52	.016	.007	24.6	2.06	20.7	.01	.06	<.01	.06	.000	.0009	.1817
2675A AW	.02	.38	7.34	.013	.006	19.8	3.20	15.7	<.00	.06	.02	<.01	.10	.0016	.2389

Table 6: Fracture toughness measurement results of deposited weld filler materials of both samples as welded and heat treated ones at 7 K

Weld Process	Code	Fracture Toughness, MPa √m As welded	Heat treated
GTAW	2684A	174 / 166	142 / 195
GTAW	2684B	131 / 156	132 / 101
SMAW	2677A	173 / 154	87 / 83
SMAW	2677B	146	89 / 86
SAW	2676B	152 / 114	74 / 101
SAW	2676E	135	92 / 102
SAW	2676F	134 / 134	123
GTAW	2675A	148 / 171	99 / 120

Investigations on Mechanical Behavior of the Insulation of TFMC Jacket Structure at 4.2 K

To determine the sliding behavior of the TFMC jacket a component was manufactured by Ansaldo, Genoa. This component consisted of the original jacket covered partly with a Teflon tape prior the epoxy/GFRP/Kapton insulation. By a special clamping arrangement it was possible to pull out the jacket by tensile loading in the 4 K rig of the FZK's 200 kN cryogenic tensile test facility.

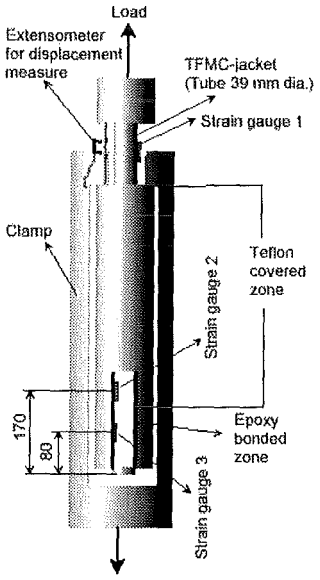

Fig. 2: Schematic illustration of the test sample.

Three strain gauges and one displacement transducer were placed in specific positions to obtain a maximum of information during the test. This test assembly was foreseen possible to simulate so far as the TFMC's jacket under operation.

The loading of the structure at LHe shows in an enlarged view (Figure 3) that the strain gauge No 3 has the similar unloading behavior after the debonding of the epoxy bonded zone. Strain gauge No 1 free of any secondary clamps shows from the initial loading stage a clear material behavior giving the stiffness of the tube. Strain gauge No 2 whereas shows also a similar unloading behavior as strain gauge No 1, however, the hysteresis gives the information about the friction of the tube inside the clamped region.

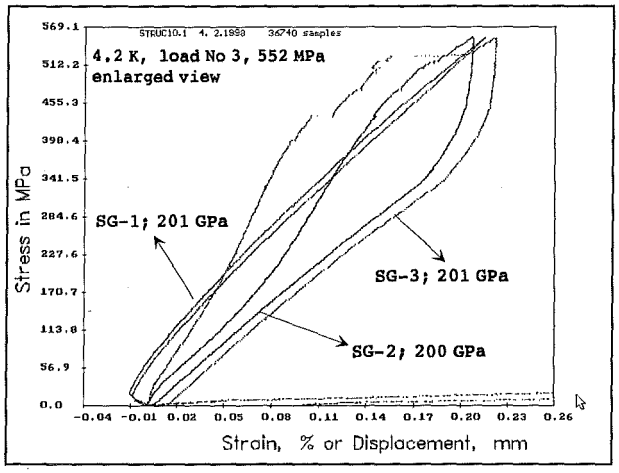

Fig. 3: The output signals of the transducers during the final loading at LHe.

Cryogenic Mechanical Loading of Mock-Up Structure for Outer Joint of ITER TFMC Task

Subject of this task was the testing of the provided mock-up structure produced by Alstom Company, France. The Load displacement behavior was one of the major interest from the viewpoint of structural mechanics. Figure 4 shows the built in structure inside the 4 K rig of the 200 kN tensile testing machine.

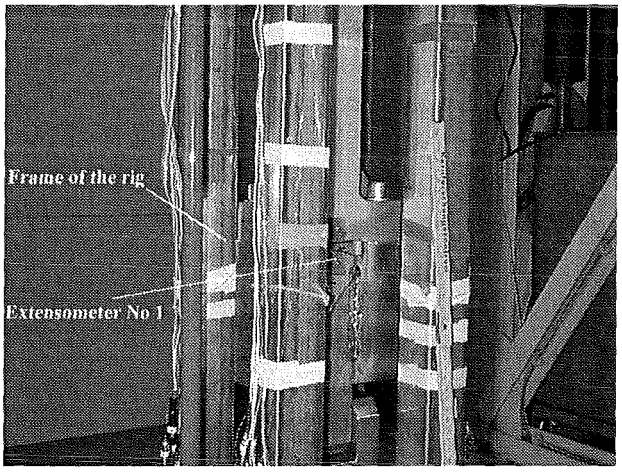

Fig. 4: Mock-up structure for the outer joint of ITER TFMC task prepared for the test at 4.2 K.

After cool down of the sample and observing via fiberscope the entire coverage of the sample by liquid helium, three load sequences were conducted. The cross head speed of the machine has been kept constant to 1 mm/min. The first load has been applied up to 81011 N. During this test no unusual events has been detected. The averaged extensometer output signals showed a slight plastic deformation of the sample. After unloading, the sample was loaded immediately again with the same cross head speed up to 184282 N. This time a significant plastic deformation occurred and a hysteresis of the load versus displacement curve could be observed in real time. After unloading, a last time loading were performed up to 147077 N observing a plastic deformation similar to the second load sequence but without any hysteresis. This can be attributed partly to strain hardening of the copper material and partly to the mechanical stiffening of the joint section.

Fatigue Crack Growth Rate of Jacket Materials

Subject of this task was the final cryogenic measurement results with respect to Fatigue Crack Growth Rates (FCGR) of Type 316LN and Incoloy 908 base metals used as jacket materials for ITER CS superconductors. Recently carried out FCGR measurements at load ratio R = 0.1 with aged jacket materials of Type 316LN (Valinox) and Incoloy 908 using small size ASTM standard CT specimens machined from an industrially manufactured jacket section bar resulted in preliminary data bases which were already reported [2]. The present tests are performed with same type of specimens but with an improved test technique using a newly developed software. These tests comprised beside the tests at two different load ratios, R=0.1 and R=0.4, also tests with unaged Type 316LN (Valinox) jacket materials to determine the eventual effects of aging on structural Type 316LN extruded materials. Figure 5 shows the FCGR properties of both aged alloys. An important result within this context is that between unaged and aged Type 316LN materials so far no significant differences could be detected with regard of these measurements. At higher ΔK regime (>30 MPa$\sqrt{m}$) the difference between Incoloy 908 and 316LN starts to be smaller compared to low ΔK regime.

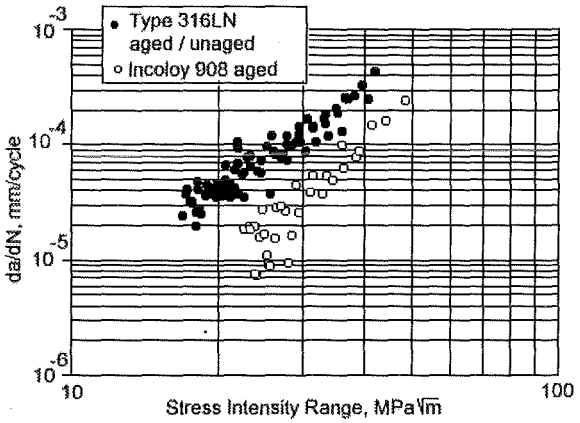

Fig. 5: Comparison of the investigated two type jacket materials at R=0.1 and at 7 K

Also increasing the load level from 0.1 to 0.4 resulted in a ca. 10 % increase of FCGR in case of Type 316LN, whilst for Incoloy 908 the found effect if any was insignificant.

Literature:

[1] Nyilas, B. Obst, and A. Nishimura, "Fracture Mechanical Investigations of Non Aged and Aged Structural Materials with EDM-Notched Round Bars at 7 K", Paper will be published in Advances of Cryo. Eng. ICMC, (1998)

[2] A. Nyilas, "Final Report on ,Characterization of Jacket Material,", Contract NET/96-408, May 1997

Staff:

A. Nyilas
H. Baumann

D 327/2 (S74TD08)
Interim Structural Design Criteria (ISDC)

Within the ITER activity to develop a specific design code for fusion devices ISDC (ITER STRUCTURAL DESIGN CODE) it was found that fracture mechanics consideration should be added as a design requirement. The appendix A16 of the french RCC code has been checked and is felt to be not appropriate in its current form.

New rules have been formulated on the basis of the british R6 fracture mechanics code. This approach is a two-criteria methods based on linear fracture mechanics and on limit analysis.

The advantage is, that if the method is verified for fusion application, in designing only linear calculations have to be performed by structural analysts.

These rules are currently tested with verification analyes for cracks of different size modelled at different locations of an ITER-like first wall geometry for various loading conditions.

Moreover, some simplified rules for FW geometries of rectangular shape are developed. This will reduce the work to be performed by analysing defect-free components.

Staff:

E. Diegele
G. Rizzi

T 228 (G 18 TT 22)
Cryopump Development

1. Introduction

Excellent progress has been made in the manufacturing of the various components of the TIMO (Test facility for ITER model pump and the model pump itself. However, some delay in schedule ocurred due to problems in the manufacturing process of the prototype main valve for closure between test vessel and pump. Nevertheless, the beginning of first operation of the TIMO facility is expected for November 1998.

In the component test facility TITAN the regeneration scheme for the ITER cryopumps was critically assessed within tests under ITER relevant conditions. Finally, a regeneration strategy was derived, which was chosen as point design described in the ITER Final Design Report.

A great deal of theoretical work focused on Monte Carlo simulation of pumping characteristics. The theoretical approach was cross-checked with experimental results from TITAN and finally transferred to the more complicated geometry of the TIMO facility. There, the simulation will be of great benefit to optimize the test programme so as to come out with the minimum number of experimental runs with the strongest evidence. It may also be used as a tool for interpretation of the measurement results.

The cryopump activities under ITER Task T228 (Green Book 6) will be continued as ITER-Task EU-VP1 (Green Book 8) and will predominantly be devoted to the parametric performance and endurance testing of the ITER model pump in TIMO and supporting tests of critical issues.

2. TIMO facility

TIMO is a facility especially developed for testing the 1:2 ITER model pump [1]. The facility is located in the experimental hall of FZK-ITP to benefit from the existing cryogenic infrastructure there. The model pump will be installed in a test vessel, according to UHV standards. The required high cryogenic coolant flows (supercritical helium (SCHe) at 5 K) will be provided by the 300 W LINDE facility via a novel 2600 l liquid helium (LHe) control cryostat. The coolant supply for the radiation shields and baffles with 80 K gaseous helium (GHe) is ensured by a separate 80 K helium cooling system. For controlling the various coolant flows, a cryogenic valve box is used.

At present, the construction of the facility has made good progress, based on a reduced scale 850 l LHe cryostat, which will be used for the acceptance tests, for putting the facility into operation and for the first stage of the test campaign. During the year, the test vessel, the 80 K system and the valve box (see Fig. 1) have been procured, set up and tested. In the following sections, the status of the individual units of TIMO are described in more detail.

2.1 The model pump

2.1.1 Manufacturing status

An order for fabricating the model pump was given in Nov. 96 to the industrial company Air Liquide (AL), Sassenage, France in form of a NET contract. This order covered the model pump with the pump housing, the main valve with actuator, the 80 K baffle, the 80 K shield system and the panels. The outline of the model pump is shown in Fig. 2. Included in the order was the cold valve box and the cryogenic transfer line from cold valve box to the model pump.

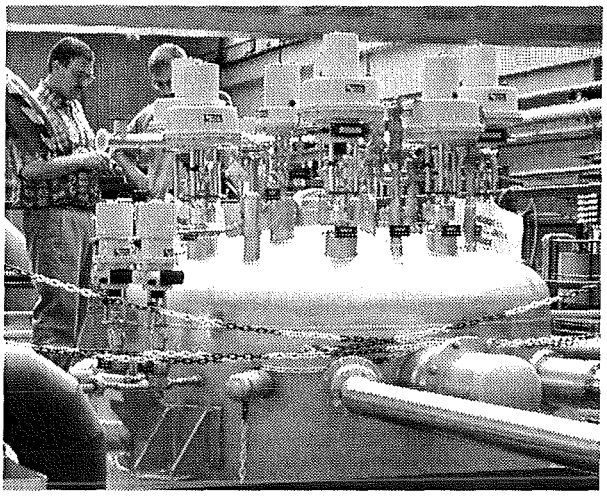

Fig. 1: View of the cryogenic valve box.

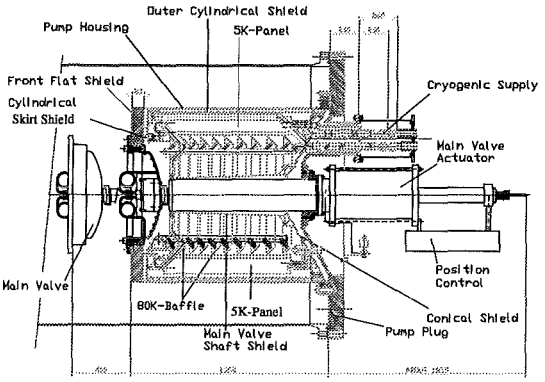

Fig. 2: Sketch of the ITER model cryopump.

The basic and detailed engineering was performed by the staff of AL. It included the state of requirements, definition of PID, lists and procedures, production of general arrangement and detailed drawings and the necessary design calculations. Most of the mechanical work was given by AL to subcontractors. The status of the manufacturing procedure was continuously monitored and discussed in regular progress meetings. The ongoing activities, problems and the project status were fixed in monthly reports.

The total time for manufacturing and delivery of the model pump to FZK was estimated to be 18 months at the beginning of the project, which would have resulted in July 98 as delivery date of the pump. Because of technical problems during the cryopump acceptance tests at AL premises, the delivery date is now expected for beginning of November 98. After delivery of the model pump to FZK two more weeks will be needed for the installation of the pump and the transferline to the cold valve box. Further two weeks are foreseen for the initial vacuum pump down of valve box and piping. Then, the on site acceptance tests will start.

2.1.2 Components

The coating of the cryopanels (860x160 mm^2, quilted design with three cooling channels) with activated charcoal was performed at FZK by an automatic procedure which had been developed within the activities for the component tests of the cryopump. The coating of each panel is performed side by side and in two steps, first the coating with a layer of an inorganic

bonding cement as adhesive, and then the spray coating of the activated charcoal particles onto the cement base layer. The arrangement of the 16 pumping panels inside the model pump is shown in Fig. 3.

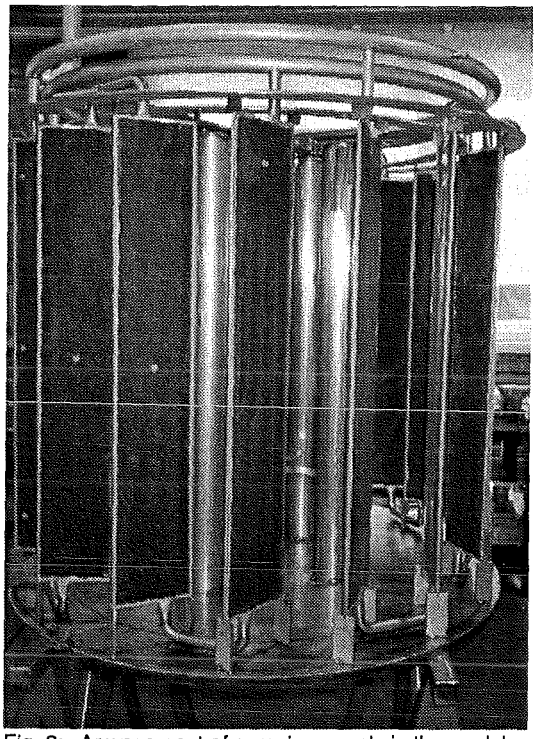

Fig. 3: Arrangement of pumping panels in the model pump.

Each coating step was documented and controlled by an additional sample reference plate (aluminium, 50x50 mm^2), which was placed aside the cryopanel during coating. Thus, a set of 64 reference sample panels (32 panel sides, two coating steps each) has been produced for quality assurance. Statistics has been made for the controlled drying process. An average sorbent coverage of about 400 g/m^2 after drying was determined.

To avoid thermal radiation to the panels driven at 5 K, the surfaces looking in this direction were blackened. After preparation by low pressure sanding, the surfaces were initially coated with a 50 - 100 µm thick nickel/chrome layer by plasma spraying. The finishing coating was made by a 100 - 150 µm thick layer of Al_2O_3/TiO_2. The aim was to get a surface with maximum absorption (more than 0.8) and low porosity to resist the operating conditions of the cryopump.

The pump plug delivered by FZK to AL was designed for a maximum allowable operation pressure of 10 bar abs. as a need resulting from the chosen safety concept based on oxygen-hydrogen explosion hazards (see section 2.5). Fig. 4 shows the plug, placed in front of the open test vessel.

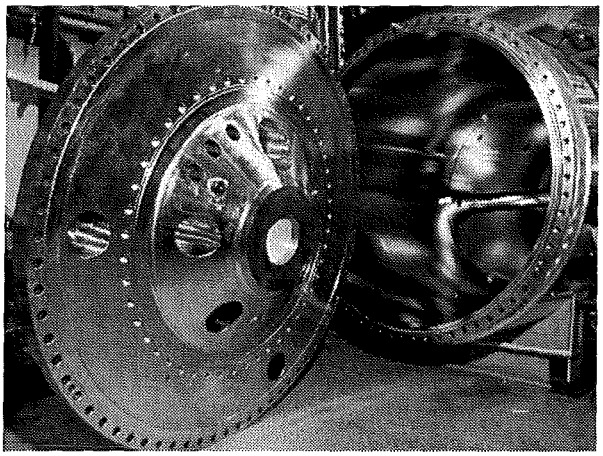

Fig. 4: View of the open test vessel and the pump plug.

2.1.3 Cryogenic requirements

The cryopump is operated intermittently. Starting from room temperature, the shields, baffle and sorption panels are cooled by 80 K GHe at 15 bar. After that, the sorption panels are cooled to 5 K by SCHe at a pressure of 4 bar while shields and baffle stay at 80 K. These are the conditions for the start of pumping. After loading of the panels according to the ITER relevant value, partial regeneration is started by feeding 80 K GHe into the cooling channels of the panels. According to recent results from component tests in TITAN (c.f. section 3) the required temperature for efficient release of the hydrogen isotopes from the charcoal sorbent is 85 K. Therefore, a short pulse of 300 K GHe can be used alternatively to achieve the 85 K level on the sorbent panel. After thermal release of the sorbed gas, the cryopump volume is pumped out and the panels are quickly recooled to 5 K.

To avoid poisoning of the charcoal sorbents, total regeneration of the panels is needed after a certain number of pumping cycles. That means, panels, baffle and shield will be heated up to around 300 K by GHe. Afterwards the standard cycling can start again. The different operation modes are summarized in Table 1.

Table 1: Operating modes of model cryopump.

Operating mode		Panel temperature [K]	Shields temperature [K]	Baffle temperature [K]
Stand by	A	5	80	80
Pumping	B	5	80	80
Partial Regeneration	C	5 ↔ 85 with 90 K GHe	80	80
Partial Regeneration	C'	5 ↔ 85 with 300 K GHe	80	80
Total Regeneration	D	5 ↔ 300	80 ↔ 300	80 ↔ 300
Quench (accidental air inbreak)	Q	5 ↔ 300	80 ↔ 300	80 ↔ 300

The need for cryogenic fluids is defined by the heat capacity of the shields, baffle and panels for the different temperature levels. During steady state pumping mode and regeneration mode the pump structures are heated by radiation, convection across the process gas inside the pump, heat load of the process gas itself and solid state conduction along the supply lines. Table 2 lists the calculated thermal heat capacities of the components and the heat loads for the different operating modes.

Table 2 Refrigeration parameters for model cryopump.

Component	Temp. level	Parameter	Value
Shields, Baffle, Piping	300/80 K	Thermal capacity from 300 K → 80 K	20.2 MJ
Shields, Baffle, Piping	80 K	Heat load during stand by mode ΔT=2 K for 200g/s GHe	2.0 KW
Shields, Baffle, Piping	80 K	Heat load during pumping mode ΔT=3 K for 200g/s GHe	2.8 KW
Shields, Baffle, Piping	80 K	Heat load during regeneration mode ΔT=20 K for 200g/s GHe	21.1 KW
Cryopanels, Piping	300/80 K	Thermal capacity from 300 K → 80 K	6.4 MJ
Cryopanels, Piping	80/5 K	Thermal capacity from 80 K → 5 K	1.43 MJ
Cryopanels, Piping	5 K	Heat load during stand by mode	0.04 KW
Cryopanels, Piping	5 K	Heat load during pumping mode ΔT=0.53 K across panel surface	0.15 KW

2.1.4 Pressure drop calculations

The cryopump has two main circuits which can be supplied by cryogenic fluids at different temperature levels, as shown in Table 1. The 80 K circuit includes the transfer line from the cold valve box to the cryopump, the various shields (see Fig. 2), the baffle and the return transfer line back to the cold valve box inclusive the valves in the lines. The 5 K circuit includes the transfer line from the cold valve box to the cryopump, inlet manifold to the pumping panels, 16 pumping panels grouped in four parallel sections, outlet mainfold, return transfer line to cold valve box and the valves in the lines.

The pressure drop calculations for both circuits were performed by AL using in house software. Results for the various operating modes and the quench case are given in Table 3. The quench corresponds to an accidental leakage of the pump housing which would allow a minimum air inlet of 3 kg/s with a maximum heat load of 600 kW onto the cryosorption panels.

For the theoretical calculations equivalent hydraulic diameters were used. These assumptions involve uncertainties for such complex channel geometries used within quilted design. To validate the results, tests were performed with the cylindrical shield, the conical shield and the baffle rings using gaseous nitrogen. For scaling reasons, same Reynolds numbers were used for the model gas N_2 as for the 80 K gaseous helium. It was found that the calculated pressure drops were too low. The correction factors for the cylindrical shield, conical shield and baffle are 1.07; 1.32 and 3.74 respectively (included in table 3).

2.1.5 Theoretical description of the pumping performance in the molecular flow regime by Monte Carlo analysis

The design of the model pump was developed in reference to the ITER primary vacuum pumping requirements which were included in the model pump specification as target values. The basic pumping performance of the model pump will be checked within the acceptance testing phase following the first beginning of operation. Therefore in parallel to the manufacturing, a theoretical study on the pumping efficiency was done to validate a sufficient pumping performance of the designed pump.

In order to determine the capture probabilities of the pump for different gases a series of Monte Carlo calculations was carried out for different openings of the pump main valve. The objective of these calculations was to check the assessments made by the manufacturer for the design study of the ITER candidate cryopump and of the model cryopump and to facilitate the transferring of the experimental results from TIMO test facility into the actual ITER operational conditions. The Monte Carlo analysis was performed with the MOVAK code using the pump geometry model developed on the basis of the final technical drawings for the model pump fabrication, see Figs. 5 and 2.

Table 3: Pressure drops in 80 K- and 5 K-circuits

	5 K-circuit					80 K-circuit		
	Stand-by Pumping Mode A&B	Partial Regeneration Mode C	Partial Regeneration Mode C'	Total Regeneration Mode D	Incidental Quench mode	Stand-by Pumping Mode A&B	Partial Regeneration Mode C+C'	Total Regeneration Mode D
Mass flow rate	250 g/s	40 g/s	55.3 g/s	52.5 g/s	3150 g/s	200 g/s	200 g/s	53 g/s
Pressure absolute	4 bar	15 bar	15 bar	15 bar	31 bar/ 20 bar	15 bar	15 bar	15 bar
Temperature	5 K	80 K/42.5 K	300K/100K	300K/100K	17 K	80 K	80 K/90 K	300 K
ΔP valve box IN	57 mbar	527 mbar	7.48 bar	7.64 bar	-	173 mbar	114 mbar	7.10 bar
ΔP transfer line IN	14 mbar	6 mbar	5.85 bar	5.2 bar	-	45 mbar	29 mbar	0.03 bar
ΔP cryopump	21 mbar	5 mbar	0.18 bar	0.13 bar	2.29 bar	718 mbar *	523 mbar *	0.43 bar
ΔP transfer line OUT	14 mbar	3 mbar	0.14 bar	0.10 bar	3.78 bar	46 mbar	33 mbar	0.03 bar
ΔP valve box OUT	36 mbar	270 mbar	0.31 bar	0.77 bar	4.81 bar	131 mbar	126 mbar	6.04 bar
Global calculated ΔP	141 mbar	812 mbar	13.96 bar	13.83 bar	10.88 bar	1113 mbar	826 mbar	13.64 bar

* with experimental correction factors

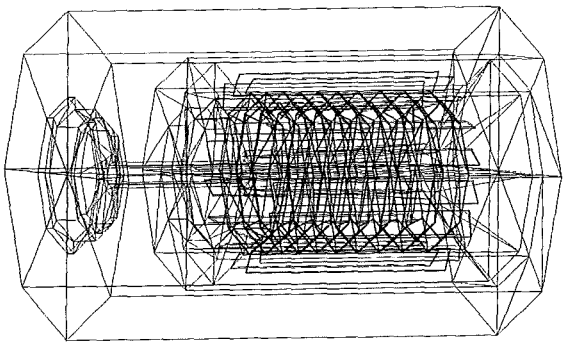

Fig. 5: Geometry representation of the TIMO pumping structure (model pump embedded in the test chamber) for the analysis with MOVAK

The created MOVAK model consists of six subassemblies: 5 K-panels, 80 K-baffle, complete 80 K-shield system, outer shell, vacuum test chamber and the inlet vacuum valve. The actual geometrical arrangement of pump components within the structure was fully taken into account.

To characterise the interactions between the gas molecules and the cryopanel surfaces the proper sticking coefficients for different gases were defined. The sticking coefficient of the charcoal surface for nitrogen was assumed to be equal to 1.0, for deuterium to 0.95 and for hydrogen to 0.90. The sticking coefficients for helium gas used in the calculations were derived from the recent experimental measurements at the TITAN facility. They are dependent on the temperature and coverage of the cryopanel and vary for the ITER relevant pressures, in the range from about 0.2 down to zero [2]. Further, it was assumed that helium is only pumped on the rear of the panels, which leads to worst case results.

The results of the simulations show that the model pump possesses the intrinsic capture probability of about 0.45 for all condensable gases (i.e. nearly half of the gas molecules which cross the pump orifice will be removed), whereas the capture probability for helium diminishes to 0.4. This illustrates the very weak dependence of the capture probability on the sticking probability due to the rather obstructive geometry of the baffles.

To determine the pumping speed of the whole TIMO pumping system by means of the MOVAK code, the reference plane for the calculations of the capture probability had to be placed in the vacuum vessel at the pressure measurement level. The estimated capture probability of the whole system was significantly decreased as compared to the corresponding value for the pump. The pumping speed of the whole system was attenuated as well, mainly due to the conductance of the chamber, the throttling effect of the valve on the molecular gas flow and finally, the relatively small ratio (0.15) between the model pump orifice cross-sectional area and the chamber cross-sectional area. However it must be emphasized, that the computed capture probabilities still lead to the higher specific pumping speeds as compared to the corresponding values assessed in the conceptual pump design phase, if related to the same reference plane.

Table 4: Capture probability and pumping speed of the ITER model pump for different ITER relevant gases.

Valve opening	Capture probability c [%]				Pumping speed at 273 K S [m^3/s]			
	$c(N_2)$	$c(D_2)$	$c(H_2)$	c(He)	$S(N_2)$	$S(D_2)$	$S(H_2)$	S(He)
100%	6.04	6.02	6.0	5.6	17.084	45.059	63.510	41.916
50%	4.5	4.5	4.44	4.1	12.729	33.682	46.997	30.688

2.2 80 K GHe system

The 80 K GHe system is reponsible for the cooling to the 80 K temperature stage. It is designed to circulate a mass flow of up to 200 g/s gaseous helium at a temperature of approx. 80 K and a pressure of 15 bar. The principle of the facility is heat exchanging between boiling nitrogen (LN_2) and circulated helium gas through a heat exchanger vessel. The supply and discharge streams and the operation of the cold blower are controlled automatically by a PLC. The system includes the following components:

- A heat exchanger designed as LN_2-bath and spiral tubes for the transfer of the gaseous helium,
- a cold blower (Barber Nichols Company),
- cryogenic lines for gaseous helium at 80 K and 15 bar operation pressure,
- cryogenic lines for LN_2 supply and the gaseous nitrogen exhaust and
- instrumentation of the facility including the measuring technique and a PLC (Siemens Siematic S7).

The facility was manufactured and delivered by the company Criotec Impianti from Turin (Italy) and has already been constructed at the TIMO site.

2.3 Status of the new cryostat

The orders for the manufacturing of a new 2600 l cryostat as well as for its interconnecting piping were given to industrial companies. Meanwhile, the detailed design studies and calculations for the cryostat have been finished and the drawings are ready.

The LHe bath of the cryostat will be used as a reservoir for the surplus of helium coming from the LINDE helium refrigerator during pumping and non pumping operation of the model pump. And it will be a thermostat for the SCHe cooling loop, especially for the peak loads during cooling down of the cryopanels of the model pump from 90 K to 5 K. An additional helium buffer inside the cryostat with a volume of 250 l at a max. operating pressure of 19 bar provides the SCHe cooling loop with more cold helium as the helium refrigerator is able to deliver during the fast cooling down of the cryopanels within 75 s.

In order to achieve the required temperature gradients (< 0.7 K) along the cryopanels during the pumping mode of the model pump, the new cryostat contains a cold blower for SCHe that allows a mass flow of 250 g/s at 4.5 K and 4 bar.

The different components like the cold blower, the cryogenic valves, the sensors for temperature, pressure, mass flow measurement and so on have already been ordered. The manufacturing of dewar, flanges, couplings and internal components has started.

2.4 Exhaust gas system

The TIMO facility has an exhaust gas and a blow off line, used for the discharge of waste gas, which is emitted over the roof to the atmosphere. The piping system is designed for an allowable operation pressure of 16 bar abs.

The exhaust gas system (diameter DN 50, length of 16 m) has primarily the function to discharge the exhaust gases during the regeneration of the ITER model pump. In addition all exhaust gases from different vacuum pump stations are also utilising this facility. The vacuum pump stations are needed for conditioning of the gas dosage system, the test vessel and the gas analysing system. The nitrogen gas used for the pneumatic actuator of the main vacuum valve of the model pump is also fed into the exhaust gas system, which has the advantage of flushing the line and prevents through this measure the enrichment of hydrogen in the pipes during the tests of the model pump. Additionally the exhaust gas pipes have also a security function. In the scenario where the overpressure in the model pump or the test vessel exceeds 0.1 bar, firstly a bursting disk will rupture and then a security valve will open and relieve the pressure.

If any accident condition occurs, like e.g. an unexpected pressure increase in the test vessel or a hydrogen explosion, the blow off line (diameter DN 150) has to discharge the explosion gases and to relieve the burst pressure to the atmosphere. Bursting disks for an overpressure of 0.2 bar have been installed between the test vessel, respectively the model pump and the blow off line.

The design and layout of the lines were carried out under close consideration of safety issues (see below), which resulted in the need to use components that withstand the maximum explosion pressure of about 10 bar. In the case of vacuum components, it has been necessary to spend time and money for additional special pressure tests supervised by the TÜV in order to verify that requirement. All the devices have now been purchased and the lines are currently being manufactured. The exhaust gas system will be ready on time, after having obtained final TÜV approval.

2.5 Safety report

A safety report concerning oxygen-hydrogen explosion hazards has been assessed and discussed with the approval authorities. Several scenarios were agreed upon and their potential worst case effects were estimated in detail and used as the basis for the development of a catalogue of safety measures for TIMO. The gas mixtures regularly foreseen for testing in TIMO are not explosive, i.e. their content of explosive gas species is much higher than the upper explosion limit. The usual pressure level during pump operation is by decades lower than the minimum ignition pressure.

The safety concept is based on the absolute limitation of the potential hydrogen inventory in the facility to the content of a 10 l high pressure bottle, which is about 74 mol. Related to that restriction, calculations were performed to derive the potential maximum explosion pressures. It was found that the most critical case is not the explosion of a stoichiometric hydrogen-air mixture, leading to underatmospheric start pressures, but the explosion of the mixture resulting from complete air rush into the system. In the latter case, maximum explosion pressures (i.e. without any relief device) of about 10 bar abs. for the model pump and 8 bar abs. for the test vessel were estimated. These values were chosen as design pressures for the components. On top of that, additional measures of primary, secondary and ternary explosion safety were included in the TIMO design, such as for example:

- Installation of a stationary gas warning device for hydrogen gas in air,
- use of explosion-proof electrical devices and installations,
- use of safety devices for fast pressure relief in the case of a detonation/deflagration.

3 Component tests

3.1 Cycling tests in temperature range between 5 K and 100 K

The cryopanels must be designed to withstand the temperature cycling within partial regeneration (5 K $\leftrightarrow$ 90 K) and total regeneration (5 K $\leftrightarrow$ 300 K). Therefore a cycling test campaign between 5 K and 100 K was performed in addition to the theoretical stress analysis [3] and the cycle tests between 80 K and 300 K already made [1].

For these long-term thermal cycling tests at FZK three cryopanels in quilted design (500x107 mm^2) were installed in the test cryostat of the HELITEX test facility [4]. As usual, the cycling test panels were coated by means of the technique developed at FZK-HIT. In order to avoid system-inherent fabrication defects during coating, the panels were not coated on the same day. Furthermore, components of different charges were applied for the preparation of the bonding material.

For the cycling tests, the test panels and the supply and return lines were installed in the piping system of the test cryostat. To ensure fully automatic operation during the long-term thermal cycling tests, the PLC system (Simatic S5-135U) and the process visualisation system (COROS-LSB, Siemens) were modified. During the cycling tests, all valve movements were to be carried out by means of the PLC. Before the start of the tests, the required process parameters as the temperature set points for the heating and cooling phases, the set points for the change from the open to the closed cooling circuit and the number of temperature cycles desired were chosen by the operator via an input mask of COROS. During the heating phases, 300 K helium gas was supplied from the compressor of the LINDE system and passed through the test panels at a mass flow of 25 g/s and a pressure of 15 bar. For cooling, SCHe with a temperature of 4.3 K was passed through the test section at a mass flow rate of 10 g/s and a pressure of 5 bar.

The long-term thermal cycling tests with a total of 7000 temperature cycles between 5 K and $\approx$ 100 K demonstrated that no degradation of the sorption layer occurs. At the end of the tests the total loss of activated charcoal amounted to 0.534 g. This corresponds to 0.23% of the sorption layer applied. Within the tests valuable experience was gained with the automatic controlling and monitoring architecture, which will also be used for the TIMO tests.

3.2 Desorption and poisoning tests

The experimental work in the component test facility TITAN was devoted to an extensive test campaign to develop the optimum cryopump regeneration schedule.

The operation of the cryopump is based on two different regeneration modes: The partial regeneration up to an intermediate temperature, foreseen as the standard step after each pump cycle, and the less frequent total regeneration up to ambient temperature. The limit temperature for partial regeneration has to be determined very carefully, as it has to reconcile the requirement for the almost complete release of the pumped gas load required to ensure high pumping speeds on the one hand with, on the other hand, the required effective reduction of cryo-

gen consumption during the subsequent re-cooling of the cryopanel.

Therefore, a study was performed in the TITAN facility at a parametric variation of the heating rate and initial gas load of an ITER cryopanel mock-up in order to investigate the dynamic desorption behaviour experimentally. The experimental strategy took pattern from thermal desorption spectroscopy. The loaded cryopanel was heated while the forepumps were active and the pressure evolution curves due to the gas release were measured. The narrow temperature range of thermal desorption is indicated by a corresponding pressure peak. In order to derive the quantitative information for the actual remaining gas load at a certain panel temperature, a numerical evaluation of the measured data sets was performed. A typical example of the experimental results is shown in Fig. 6 for deuterium. It shows a relatively weak influence of the gas load and heating rate on the peak temperature, which is between 70 and 80 K.

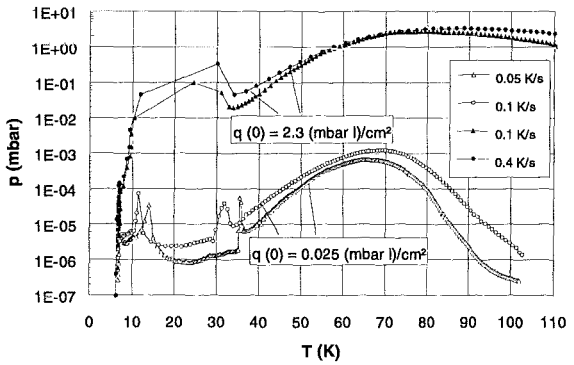

Fig. 6: Pressure evolution curves for thermal desorption of deuterium, at different heating rates and initial loadings q(0).

Analogous measurements were made for helium and protium as well as for the trace components (Ne, Ar, CO_2, CO, O_2, CH_4). The final desorption curves are given in Fig. 7.

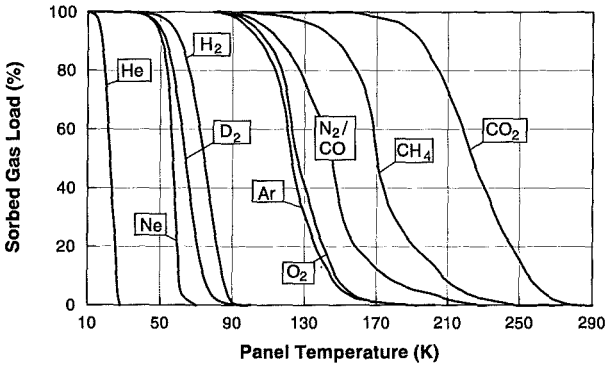

Fig. 7: Thermal desorption characteristics for the ITER cryopanel.

Judging from these test results, a minimum temperature of 85 K at the panel sorbent layer was considered to be necessary to achieve a quantitative gas release of helium and the hydrogens, which are more than 90 % of the exhaust gas mixture. This temperature is expected to be sufficient also for desorption of DT, which shows comparable thermodynamics; the radiochemical influence will be assessed in full detail in a parallel task at FZK-TLK.

To confirm the 85 K limit for partial regeneration, a further test campaign was launched to study the pumping performance over subsequent complete cycles with only partial regeneration in between. As discussed above, the impurities will completely accumulate at the chosen partial regeneration temperature. The objective of the multi-cycle test campaign was also to detect quantitatively any pump speed drifts caused by potential poisoning effects of the charcoal due to incomplete regeneration and accumulation. The gas composition during pumping and after partial regeneration was continuously monitored such that the corresponding mass balances could be set up for the individual gases. The composition of the gas released during regeneration is an important interface information for the detritiation facilities downstream of the fuel cycle. The tests covered a wide composition range of simulated ITER exhaust gases (the tritium fractions were replaced by D_2). They were made with two base mixtures (containing H_2 or D_2 as major component plus 3.8% of impurities), to which up to 10% inert gases (He, Ne, Ar, N_2) were added.

A typical result is shown in Fig. 8. It presents two sets of pumping speed curves, namely, the first 4 consecutive cycles and the curves for the 12th to the 16th cycle, plotted vs. the full ITER relevant cycle time of 900 s. The second set has been obtained at a panel which had been pre-loaded with a corresponding amount of impurities. The measured pumping speeds decrease with time and increasing cycle number. However, even after 16 cycles, the final pumping speed of about 1.5 l/(s·cm²) is still significantly better than the ITER-FDR requirement of 1 l/(s·cm²) after 10 cycles. In general, the average integral pumping speed loss per cycle is rather moderate. The results for other gas compositions are listed in Table 5. It is revealed that the combination of helium and protium is the most critical. However, for nearly all investigated mixtures it was found that the pumping speed stays higher than 1 l/(s·cm²)), even after 15 cycles of continuous operation.

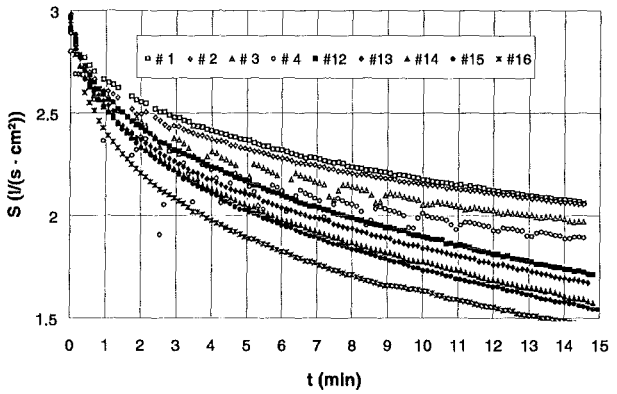

Fig. 8: Pumping speed changes during multi-cycle operation (cycles # 1-4 and 12-16) for a typical exhaust gas mixture (0.4 mol% O_2, 0.6% CO_2, 1% CH_4, 1.2% CO, 10% He, remainder D_2), caused by impurity accumulation.

Table 5: Investigated gas mixtures. Given is the measured pumping speed S at the end (900 s) of the 15th cycle.

System composition in %	S_{end} (#15) [l/(s·cm₂]
D_2-Base/He = 90/10	1.5
D_2-Base/Ar/He = 80/10/10	1.5
D_2-Base/N_2/He = 80/10/10	1.6
D_2-Base/Ne/He = 80/10/10	1.8
H_2-Base/He = 95/5	1.4
H_2-Base/He = 90/10	0.9
H_2-Base/Ne/He = 80/10/10	1.3

The total and individual mass balances always confirmed that the hydrogens and helium, but also neon, are completely released within rapid partial regeneration. By experimental varia-

tion of the impurity fractions it was shown that only the total amount of accumulated gas determines the poisoning, not the individual type of gas species. Helium is the gas most sensitive to poisoning effects and, thus, dominates the mixture behaviour. The measured overall deterioration of pumping speed is only due to the interaction between helium and the (partly blocked) charcoal pores, which is reflected by the helium enrichment process during pumping, which is becoming stronger over the cycles. That He enrichment is therefore a sensitive indicator of sorption performance. For the mixture from Fig. 8 with nominally 10 % He, a value of 47 mol% He at the end of the 16th cycle was measured to be compared with 37 % at the end of the first pumping cycle. This is due to the much smaller pumping speed of pure helium compared to the one for deuterium. For He-free mixtures, constant pumping speeds have been measured, i.e. the saturation capacity has never been reached.

The safety margin found as a result of the poisoning tests may theoretically allow for regeneration temperatures below 85 K and higher remaining gas loads. However, this is made impossible by the low crossover pressure between mechanical and cryogenic pumping, which would, in the case of higher gas loads, lead to a pressure induced desorption with unsatisfying time demands [5].

Therefore, the strategy outlined above is regarded as an optimum compromise between pumping efficiency and economic feasibility. The whole concept will be validated on the level of the prototype model pump in TIMO. In parallel, the total regeneration step, foreseen at 300 K, will also be subjected to critical assessment. With respect to the accumulation of high-boiling, water-like substances and to the limitation of potential tritium inventory in the cryopumping system, a three-step regeneration strategy has alternatively been developed [6].

Literature:

[1] Nuclear Fusion Project Annual Report of the Association Forschungszentrum Karlsruhe/EURATOM, October 1996-September 1997. Report FZKA 6050/EUR 18156 EN, FZK, pp. 26-32.

[2] Chr. Day and A. Schwenk-Ferrero, Sticking Coefficients for Helium and Helium Containing Mixtures at Activated Carbon under Liquid Helium Cooling Conditions. Presented at 14th International Vacuum Congress, Birmingham, UK, September 1998.

[3] A. Mack et al., Temperature Cycling Study, Final Report NET 96-421.

[4] H. Haas, Report on Long-term Temperature Cycling Test of Panels, Interner Bericht HIT 5/1998, FZK.

[5] Chr. Day, Report on Cryopump Component Tests Using the TITAN Facility, Interner Bericht HIT 6/1998, FZK.

[6] D.K. Murdoch et al., Tritium Inventory Issues for Future Reactors; Choices, Parameters, Limits. Presented at 20th SOFT, Marseille, France, September 1998.

Staff:

Chr. Day
A. Edinger
J. Grimm
H. Haas
T. Höhn
W. Höhn
M. Jäger
B. Kammerer
H. Knauß
J. Laier
A. Mack
S. Methe
H. Reinhard
K. Sachs
A. Schwenk-Ferrero
R. Simon
D. Stern
J. Weinhold
St. Zabeschek
D. Zimmerlin

T 332b
Plasma Exhaust Processing (2)

The Tritium Plant of fusion machines must rely on proven technology and on components thoroughly tested under relevant as possible conditions. For this purpose long-term tests are under way with the PETRA facility at the Tritium Laboratory Karlsruhe since about four years. The endurance experiments are carried out with concentrations of tritium and concentrations and type of impurities such as expected to take place in the plasma exhaust clean-up.

In the following some of the results obtained and experiences gained with several components are discussed.

1. Palladium/silver permeator

Palladium/silver permeators are considered essential components for the selective removal of hydrogen isotopes from a gas stream. In the plasma exhaust clean-up process they are used a) in the front-end zone to recover the unburned fuel from the exhaust gas and b) in the down-stream impurity processing loop to continuously remove hydrogen isotopes catalytically liberated from tritiated impurities.

To avoid phase changes of the palladium silver the permeator was kept, practically at all times, at a temperature of 350 °C or above. To prevent tritium permeation into the glove box the permeator is housed in a 50.8 l evacuated vessel. To maintain the vacuum in the vessel at low levels and allow continuous operation of the permeator over extended periods of time the tritium permeated through the permeator outer walls is constantly gettered with a ZrCo bed.

During routine processing of plasma exhaust gases two situations need to be contemplated: a) the long-term build-up of decay helium in the bulk of the palladium silver alloy when a steady state concentration of tritium establishes under constant upstream and downstream pressures and b) possible surface poisoning of the palladium silver by impurities in the process gas.

Helium, is known to be poorly soluble in palladium-silver. It will therefore tend to build bubbles in the alloy, which eventually may lead to material embrittlement. In practice loss of mechanical integrity could take place, which would become apparent by leak of impurities into the pure gas stream. For this purpose an infrared photometer (MEKOS) cell, capable of detecting carbon monoxide, was installed downstream of the pure gas exit of the permeator. The cell has a length of 500 mm and is designed to detect ppm concentrations of carbon monoxide in the permeated hydrogen gas stream. Within the duration of the tests now covering a period of more than four years of semi-continuous round the clock operation, no carbon monoxide was detected in the permeate, indicating that the mechanical integrity of the permeator has remained unchanged. This finding is substantiated by semi-empirical permeation curves that are being measured periodically with deuterium or deuterium tritide at constant pure gas pressures of 200, 300 and 400 mbar, which have given no indication of pinholes in the permeator palladium silver tubes.

Concerning the effect of impurities, it is necessary to take into account that deuterium tritide undergoes radiation-induced reactions with carbon monoxide. The principal reaction products are polytritiated hydrocarbons, tritiated water and carbon dioxide. A typical result for a mixture of DT (94 vol. %) and CO (3 vol. %) at a total pressure of approx. 1 bar is shown in Fig. 1. When the gas is also recirculated through the hot permeator a much more rapid rate of carbon monoxide consumption is observed, indicating that the permeator has a synergistic effect on the reaction rate.

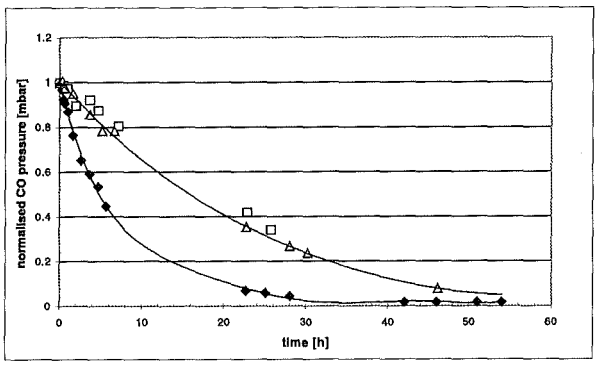

Fig. 1: Radiation-induced reaction of DT with CO: a) uncatalysed (white symbols, two runs) and b) catalysed by PdAg at 350 °C (black symbols).

The enhancement of the radiation-induced reaction rate by hot palladium silver was not, however, accompanied by a reduction in hydrogen permeation rate. Thus either only volatile products are produced when CO reacts with DT or possible deposits on the palladium silver surface are re-gassified by reaction with deuterium tritide present at large partial pressures.

When the permeator was exposed to 30 mbar partial pressure of polytritiated methanes in the presence of small partial pressures of hydrogen a progressive and fast permeator poisoning was detected that eventually stopped permeation completely. This poisoning was found to be fully reversible by two or three treatments with air at 350 °C.

The permeator of the PETRA facility, having a total permeation area 0.12 m^2, was routinely exposed to an equimolar mixture of deuterium and tritium (94 vol. %) containing helium, carbon oxides, polytritiated hydrocarbons and tritiated water (6 vol. %). After completion of a run the permeator was frequently subjected to a regeneration. Through all these exposures and treatments no noticeable degradation of the permeator has taken place.

In conclusion, the commercial, vacuum insulated permeator employed in this investigation was shown to operate reliably without any down-times, under conditions closely resembling those in the Tritium Plant, for a period of approximately four years.

2. ZrCo storage vessel

For tritium storage and handling a storage bed designed for the JET machine containing ZrCo instead of U was used. This bed, which is axially heated and cooled, served the following purposes:

- Delivery of DT to the primary system,
- Recovery of DT after completion of an experiment,
- Storage of DT, and
- Evacuation of the second containment of the permeator.

For DT delivery to the experiment the bed is heated up to 400 °C and the liberated gas is continuously pumped with a Normetex scroll pump in combination with a Metal Bellows pump. Under these conditions the disproportionation of ZrCo is avolded and isotope effects are minimised. In spite of numerous

loading/deloading cycles no detrimental effects neither with respect to hydrogen absorption kinetics nor storage capacity became apparent. A reduction in gettering rate was only noticed when hydrogen isotopes containing carbon oxides were passed through the bed. This poisoning could easily be reversed by heating the evacuated bed for several hours at 400 °C (diffusion of surface contaminants into the bulk). In general, only pure hydrogen permeated through the PdAg tubes was gettered with the ZrCo when an experiment was completed and the facility needed to be evacuated.

The accumulated experience has shown that ZrCo is an adequate getter for the storage and handling of tritium.

3. Magnetically suspended Edwards turbo molecular pump in combination with a Drystar forepump

The Edwards turbo molecular pump installed in the PETRA experiment is only operated sporadically each time the entire system needed to be evacuated or during grab sampling.

In general, upon completion of an experiment most of the hydrogen isotopes were first trapped in the ZrCo bed to avoid delivering an excessive amount of tritium to the Central Tritium Retention System of the TLK. Most of the remaining gas was then compressed into a 4 l stainless steel vessel and only after that was the remaining gas evacuated.

Even though the pumped gas was at times very aggressive, no pump failures were registered. The operation of the pump was at all times satisfactorily.

4. Infrared photometers

MEKOS and SPEKTRAN infrared photometers from Perkin-Elmer were used to investigate the kinetics of radiation-induced reactions. The long-term stability of these infrared photometers, achieved by an internal calibration with interference filters on a rotating disk, proofed to be highly valuable to follow these comparatively slow rate reactions.

The infrared photometers allow a quantitative determination of several gases in a mixture of approx. constant total pressure. Shortcommings of these photometers are the pressure dependence of the infrared absorption and the possible cross-contamination by other species, particularly reaction products.

Infrared photometers of the type employed in this work can be recommended for in-line continuous analysis of species in a strong tritium environment.

5. Siemens two stage doubled contained Metal Bellows pump

Two two stage double contained Metal Bellows pump from Siemens are installed in the PETRA facility. Their pumping efficiency is not dependent from the type of gas pumped. In combination with a NORMETEX scroll pump they constitute a pumping system capable of achieving vacua better than 1 mbar with all hydrogen isotopes. In this case the achievable vacuum does depend upon the type of hydrogen isotope or gas pumped.

6. NORMETEX scroll pump

This pump showed a very good and reliable operation without any downtimes. A significant dependency of pumping efficiency from the type of gas is attributed to back diffusion. The pumping efficiency increased markedly in the order protium, deuterium, tritium.

7. Small process ionisation chambers

The small process ionisation chambers developed at the TLK showed very good performance in a very aggressive gaseous medium over a period of several years. The ionisation chambers were regularly exposed to high concentrations of gaseous tritium, tritiated water, tritiated hydrocarbons, carbon oxides, etc. Because they can be heated up to 350 °C they are easy to decontaminate. Main drawback of these chambers (as well as of any chamber) is the necessity to apply a pressure correction when hydrogen or helium are used as "working" gas.

8. Gas Transfers

Waste gases from the PETRA facility were processed in the impurity processing loop of the CAPRICE facility. In the latter the tritiated impurities were treated catalytically to produce molecular tritiated hydrogen, which was send to the Tritium Transfer Station of the TLK. Gas transfer of the impurities were performed with a 4 l stainless steel vessel. Because these transfers were necessarily accompanied by contaminations, the two facilities have now been joined via a double walled tubing. This will permit in the future a direct transfer of gases from one facility to the other. Previous experience has shown that gas transfers are possible without measurable tritium losses.

9. Simatic AG95

For the safe control of the experiment PETRA during round the clock attended and unattended operation with up to 11 [bar x litre] of gaseous deuterium tritide a programmable logic controller (PLC) was used. The Simatic AG95 took over the following functions:

- Constitute the first safety level prior to the hard wired Safety Circuit,
- Control safety relevant absolute temperatures and pressures within pre-established upper and lower set points, and
- Control drifts between redundant and diverse safety related sensors to allow verification of sensor status.

The Simatic AG95 is considered a very reliable local control system during attended and unattended round the clock operation of a tritium facility.

Staff:

U. Berndt
R.-D. Penzhorn
E. Kirste

Subtask 2: Catalytic Cracking Process

The catalytic cracking process for the recovery of tritium from all torus exhaust gases was successfully demonstrated by operation of the technical facility CAPRICE (*Ca*talytic *Puri*fication *E*xperiment) at the Tritium Laboratory Karlsruhe (TLK) for more than three years with up to 7 g of tritium. Meanwhile the experiment has been substantially upgraded and is now part of the CAPER facility currently under commissioning.

The CAPRICE process employ heterogeneously catalyzed reactions such as water gas shift and hydrocarbon cracking combined with the Boudouard equilibrium. Depending upon the type of catalyst material and catalyst support such as aluminum oxide or kieselguhr, a specific amount of tritium is reversibly

locked up in the solid as a function of the actual operation temperature of the catalyst bed. The typical tritium inventory per mass unit of catalyst may also vary with the composition of the gas phase and particularly with the atomic fraction of tritium with respect to the total hydrogen isotope content. Hence catalyst beds can act as tritium sinks or tritium sources during transients in gas phase composition, but only slightly contribute to the total tritium inventory of a fusion reactor.

Two key methods are available for the experimental determination of the tritium inventory in solids:

Tritium containing samples can be burned in a moist, oxygen containing carrier gas stream. The off-gas is bubbled through water and the tritium content measured by liquid scintillation counting. This method is particularly appropriate at low tritium levels and of course measures the total tritium content, but requires representative grab sampling, which is nearly impossible for a large catalyst vessel, and destroys the sample material.

Another approach is known as isotopic dilution. In case of heterogeneous reactions, the method only account for the reversibly exchangeable tritium. The main advantage of this technique is that it can be applied in situ and leaves the solid unchanged.

The isotope dilution method is especially suitable to measure the reversibly bound tritium in technical catalyst beds and was employed to determine the characteristic source or sink capacities of the water gas shift reactor and of the methane cracking catalyst bed employed in the technical facility CAPRICE.

The tritium inventory of the two main catalyst beds was found to be strongly varying with the actual atomic fraction of T with respect to the total hydrogen isotope content Q = H + D + T. Hydrogen isotopes are immobilized in the catalyst pellets and cannot be removed by e.g. evacuation. However, at nominal operation temperatures of the beds an immediate isotope exchange with the gas phase was observed each time a tritium-containing catalyst bed was exposed to protium or deuterium, and vice versa protium or deuterium was liberated from the catalyst in case of tritium exposure. These exchange reactions were used to quantify the reversibly stored hydrogen isotope content of the two catalyst beds by gas chromatographic analysis of the gas phase and material balance under the assumption, that

1) all hydrogen isotopes are equally distributed between the solid phase and the gas phase as well as within the gas phase in species such as water or methane (no specific isotope effect),

2) the overall hydrogen inventory of the catalyst is constant and only varies with the temperature of the bed.

While the first postulate is anticipated to cause only minor errors the second postulate is more critical, but likely valid for gas mixtures containing hydrogen isotopes or hydrocarbons. Water present in the gas phase from e.g. methanation reactions, however, is well known to be sorbed by the ceramic catalyst support and therefore expected to alter the total hydrogen inventory of the catalyst bed. Hence carbon oxides or water were carefully excluded during the inventory measurements.

Online gas chromatography using specifically developed ionization chambers as detectors was applied as sensitive analytical tool to measure the isotopic abundance in gas batches processed subsequently over the catalyst beds. Only isotopic ratios rather than concentration ratios need to be measured for the isotope dilution method and hence the ion chamber signals are exclusively used to obtain the isotopic abundance of the equilibrated gas mixtures.

Significant differences were obtained for the hydrogen isotope inventories in the methane cracker catalyst (nickel on kieselguhr) or the water gas shift catalyst (zinc stabilized copper-chromite) of CAPRICE. For the methane cracker a total inventory of about 0.05 mole or 0.15 g tritium per kg of nickel on kieselguhr is obtained, when the gas phase contains 50 % of tritium in hydrogen. The water gas shift catalyst bed shows a total inventory of about 0.10 mole or about 1.2 g tritium per kg of zinc stabilized copper chromite, when the gas phase contains 50 % of tritium in hydrogen.

On account of the tritium levels found in catalyst beds their inventories need to be contemplated when a tritium accountancy of plasma exhaust facilities is performed.

Staff:

M. Glugla
K. Günther
R. Lässer
T.L. Le
R.-D. Penzhorn
K.H. Simon

TEP 3 A
Tritium Storage Getter Development (2)

Staff:

N. Bekris
R.-D. Penzhorn
M. Sirch

The intermetallic compound zirconium-cobalt has been selected by the ITER-Team as reference material for the storage of hydrogen isotopes in the Tritium Plant. This selection is founded on the very good gettering properties of zirconium-cobalt, which are only slightly less good than those of uranium. The single aspect of concern remaining with ZrCo is the tendency of this alloy to disproportionate at elevated temperatures in the presence of a high pressures of hydrogen.

To investigate the disproportionation of ZrCo an apparatus basically consisting of an UHV- tight ceramic vessel containing a platinum crucible, in which the getter material is placed, was used. To heat the powder a 5 kw high frequency power generator was used, the platinum crucible acting as the inductor. The ceramic vessel was joined to a 4 l gas volume via a manifold. Several sensors were used to measure pressures. With the equipment sorption/desorption experiments could be carried out within a broad temperature region under isochoric conditions. So far the experiments have covered a temperature range of 300 – 400 °C and up to 50 thermal cycles. As evidenced by a typical series of experiments performed at a temperature of 350 °C (see Fig. 1) it is possible to cycle thermally ZrCo at least 50 times without a measurable deterioration in its absorption properties.

The determination of isotherms for the ZrCo – H_2 system at low temperatures, i.e. 50 – 200 °C, is continuing. These measurements are being carried out in the ALTEX facility. The aim is to investigate the validity range of the van't Hoff equation.

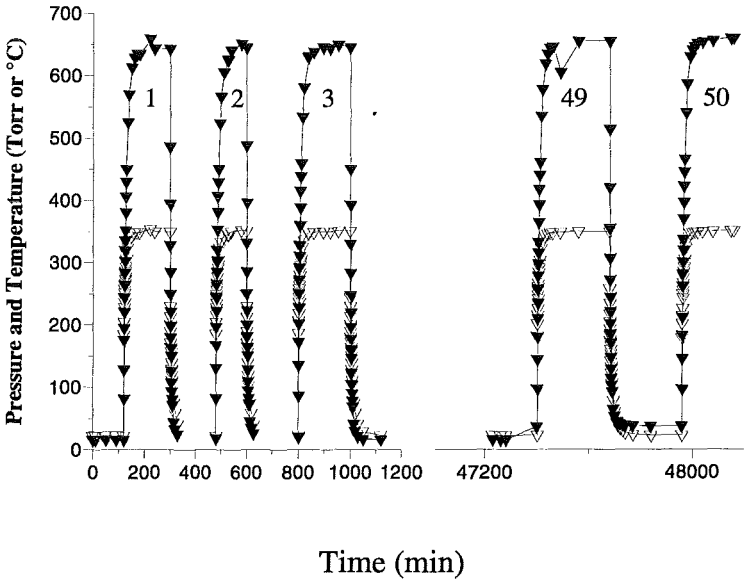

Fig. 1: Thermal cycling of ZrCo at 350 °C. The open symbols denote the temperature and the closed ones the pressure of hydrogen

TR 1
Tokamak Exhaust Processing

Demonstration of CAPER with Tritium

The technical facility CAPER, (*CA*PRICE/*PER*MCAT) which evolved from the CAPRICE (*Ca*talytic *Pur*ification *E*xperiment) experiment successfully operated with up to 7 g of tritium for more than three years at the Tritium Laboratory Karlsruhe (TLK) and from tritium experiments with a *perm*eator / *cat*alyst combination (PERMCAT unit) for counter current isotopic swamping, is currently being commissioned at the TLK.

While CAPRICE was used to simulate the front end permeator and the impurity processing system of the plasma exhaust processing of a tokamak, CAPER will include a technical PERMCAT as the final clean-up step.

A new inert gas glove box has been installed adjacent to the CAPRICE glove box. This new glove box houses the technical PERMCAT unit, which constitutes the main component of the final clean-up step to achieve overall decontamination factors of about 10^8, as currently required for tokamaks . In addition, an improved methane cracker combined with a water gas shift catalyst bed, an additional permeator and associated equipment such as vessels, sensors and pumps have been installed in this glove box. One of the pumps is a five stage positive displacement compressor with ceramic coated cylinders and pistons. This pump has been identified as particularly suitable to achieve high throughputs at low inlet pressures. Thirteen primary pipes, placed inside of an outer tube to provide a secondary containment that joins the "old" CAPRICE glove box with the "new" PERMCAT glove box, constitute the bridge between the three purification steps: front end permeator, impurity processing loop and counter current isotopic swamping. By these lines all three purification steps make common use of the HV pumping system and other services.

As scheduled within the task agreement of the European Technology Programme the installation of the facility is almost completed and first performance test will start at the beginning of 1999.

Staff:

M. Glugla
K. Günther
R. Lässer
T.L. Le
R.-D. Penzhorn
K.H. Simon

TR 2
Development of Tritium Instrumentation

Analysis of Tritiated Species by Laser Raman Spectroscopy

Spontaneous Raman spectroscopy using laser excitation is well suited to provide real-time quantitative analyses of chemical compositions in gas mixtures. Laser-Raman spectrometry is particularly advantageous for monitoring mixtures of hydrogen isotopomers containing tritium as well as deuterium, because of its excellent differentiation among the species.

The sensitivity of Laser-Raman spectrometry is usually only modest and is limited by the low Raman scattering cross-sections of most substances. Hence different techniques have been developed to enhance the sensitivity of Laser-Raman spectrometry. Angularly multiplexed multiple-pass laser excitation of the Raman volume has been applied for many years at the Tritium Laboratory Karlsruhe (TLK) and sensitivity enhancements of typically 15 were measured. However, Raman enhancement by angular multiplexing is achieved at the expense of a less compact optical system that is difficult to optimize and stabilize.

The sensitivity of Laser-Raman spectrometry can be dramatically improved through the use of an actively stabilized external resonator (ASER) to enhance Raman sensitivity relative to single-pass excitation. Therefore the applicability of Raman spectrometry to quantitative analyses of gas mixtures containing tritium has been consolidated for the first time by placing the entire optical system, including laser head, CCD Raman detector, and ASER, within the glove box necessary for secondary containment of tritium. This robust system can be accomplished due to the compact sizes and low thermal budgets of new lasers and spectrometers/CCD detectors now commercially available.

The Raman analysis system developed at the TLK, coined the LAser-RAman system (LARA), offers the unique advantages of unambiguous measurements of all molecular species within tritiated gas streams in a short measurement time (typically <1 minute) with highest possible Raman sensitivity and excellent mechanical stability, while simultaneously offering a reliable secondary containment for tritium.

The implementation of LARA into its own glove box facilitates its application for analyses in any of several major TLK subsystems, such as the Isotope Separation System (ISS) and the fuel-clean-up system CAPRICE/CAPER, as well as enabling self-contained experiments within LARA. Analyses can be conducted in LARA either by secondarily contained gas-line interconnections to the host subsystem or by an externally filled Raman cell introduced into the LARA glove box through its pass box. Anticipated applications of LARA to ISS include real-time analyses of hydrogen isotopomers exiting the separation columns to achieve control of destination uranium beds during separations, analyses of isotopomers and potential impurities (such as inleaking air) in the Feed-volume prior to injection into the separation columns (for planning and assessing control parameters during a separation campaign as well as for repeated tritium accountability checks), and the analyses of tritiated hydrogen isotopomer mixtures in the uranium beds subsequent to separations. Real-time molecular analyses, not only of process gases such as carbon oxides, but also of tritiated species such as tritiated methanes, could provide valuable information in fuel clean-up systems. Finally, once LARA has demonstrated its value in any of these potential applications, the design of LARA can provide a blueprint for the development of a dedicated Laser Raman system that can be incorporated directly within the glove box of that subsystem.

The laser for LARA produced nearly 7-W output power at 532 nm upon installation into the glove box. The actively stabilized external resonator was custom designed for LARA jointly by TLK scientists and industry, comprising a frequency modulator, a laser mode-matching lens of focal length 15 cm, an injection mirror with 98% reflection at 532 nm and curvature radius 5 cm, a nearly totally reflecting mirror mounted on a piezoelectric translator for active control of the external resonator length, two photodiodes to provide control and monitoring signals, and electronics based upon the Pound-Drever stabilization technique to achieve active stabilization of the external resonator length to lock onto the single frequency of the laser. For LARA, where the external resonator encloses a Raman cell filled with tritium gas, the active stabilization must be capable of maintaining its lock to the laser frequency even during the rapid evacuation of the Raman cell, which from atmospheric-pressure requires a calculated piezo-drive travel of 9.7 micrometers, for which the piezoelectric translator with 25 micrometer travel capacity is suitable.

The spectrometer/CCD for LARA, an ISA Triax-320 with 2000 x 800 pixel AR-coated back-illuminated CCD of 15 micrometer spacing, is the first compact high-resolution astigmatism-corrected spectrometer that is commercially available as an integrated package with a high-sensitivity scientific-grade CCD. The LARA spectrometer is equipped with a 2400 line/mm grating for the full range of important isotopomer Rotational Raman Spectrometry (RRS) and a 600 line/mm grating for Vibrational Raman Spectrometry (VRS). The gratings can be remotely selected via the Triax-320 serial connection to the CCD data acquisition computer.

The laser head, spectrometer/CCD, external resonator, and all additional optical components are firmly mounted upon a 0.9 x 0.75 m optical table system with vibration damping provided by actively controlled air legs. The LARA glove box encloses the optical table, control electronics for the CCD and the external resonator , a closed-cycle chiller for cooling the Peltier-effect cooling system for the CCD, and space for pumps and gas manifolds connected to the Raman cell.

The LARA Raman cell is custom-designed for the compact geometry needed for incorporation within the actively stabilized external resonator. Various options considered for construction of the LARA Raman cell led to the choice of a cubical cell of 35 mm sides with four diffusion-bonded windows sealed within CF16 flanges by UKAEA Special Techniques in England, as larger windows of similar construction had proven reliability in containing tritium gases in the TLK Raman setup with angular multiplexing. Due to the complexities of diffusion bonding fused silica windows, the clear aperture in these interferometrically flat windows is only 7 mm, so the Raman-collection windows are recessed inside the cell to enhance their acceptance angle, to reduce dead volume, and to make the gas-flow within the cell closer to one-dimensional, while the laser-transmitting windows are mounted as far from the cell center as possible to avoid laser-induced damage. Tests of these windows in the Verdi single-frequency laser beam show excellent interference fringes in reflection, confirming their interferometric quality.

The laser, turning mirrors, laser-focusing lens, Raman-collection lenses, and detector were initially assembled and aligned to achieve maximal Raman signals from nitrogen molecules in air of about 12000 cps. Insertion of the Raman cell was also shown to introduce no significant additional elastic scattering detected by the CCD at the spectral location of the hydrogen isotopomer RRS lines, which had been a potential concern in using such a compact Raman cell as in LARA. Then the phase modulator and external resonator mirrors were installed and aligned, while all connections for the actively stabilized external resonator were made. First tests carried out recently indicated enhancement factors of at least 10, and perhaps will be grater than 200 with

proper optimization and alignment. The full characterization of the LARA system may demonstrate detectabilities for tritiated molecules in the microbar range unprecedented by Raman spectroscopy.

Staff:

M. Glugla
D. Taylor (Guest Scientist)

TR 3
Extended Life Time Tests of Key Tritium Plant Components

Within the frame of a collaboration with JET a modification of the Active Gas Handling System of JET is in progress. In particular, it is intended to replace the formerly used getter beds by new components. Among them the incorporation of an improved PERMCAT unit has been planned.

To implement the modification a process flow sheet has been completed. The new PERMCAT version has been improved to achieve a much higher throughput. This will be accomplished by

- An increase of the number of permeation tubes from 6 to 21 and
- An increase in the length of the tubes from 530 to 900 mm.

While essentially linear scaling is achieved by increasing the tube number, the effect of length increase has exponential impact on throughput.

The PERMCAT component to be installed at JET is presently being manufactured at the workshop of FZK. Once completed it will first be tested without tritium at the TLK. Work on a further improvement of the PERMCAT catalyst is ongoing.

Staff:

M. Glugla
D. Niyongabo
R.-D. Penzhorn

TR 4
Tritium Recovery from Plasma Facing Components

Extensive tests with small graphite and CFC disks obtained from tiles previously exposed to the plasma of a fusion machine have been carried out to determine the total tritium content and to investigate the thermal release behaviour of co-deposited and implanted hydrogen isotopes. For the release runs the samples were mostly heated by high frequency heating. The experiments were performed maintaining the specimens under vacuum or under a moist sweep gas (air or noble gas).

Based on the results obtained a new facility carrying the acronym TIDE (Tritium Decontamination) is presently under construction. The facility is designed to perform detritiation tests with actual tiles of graphite or CFC with the aim of validating the small scale experiments. Tiles are rapidly heated up to temperatures above 1000 °C with a 330 kHz high frequency coil. Power is supplied by a 20 kW generator, which is now fully installed. A closed loop is under construction to process and collect the released tritiated gases. For safety reasons the experimental arrangement has been installed in a gas glove box having a nitrogen atmosphere.

The plasma-exposed graphite specimens were also characterised by Accelerator Mass Spectrometry at Rossendorf. For depth profiling a cesium sputter ion source is used. For the detection of tritium a test facility was installed at the 30 ° beam line of the 3 MV Tandetron. After acceleration the tritium ions are counted with a surface barrier detector. Deuterium, tritium, protium, carbon and beryllium profiles were determined before and after the thermal treatment (range 200 – 500 °C) with moist gases (air and noble gases) of plasma-exposed graphite disks drilled from TFTR and JET tiles. In addition, the tritium and deuterium concentration in the plasma-exposed layers were determined.

Staff:

N. Bekris
M. Friedrich (FZ Rossendorf)
W. Jung
R.-D. Penzhorn

TR 5
Tritium Recovery from Solid Wastes and Process Equipment Decontamination

The Tritium Laboratory Karlsruhe is equipped with numerous Tritium Retention Systems, installed locally next to every glove box, and a Central Tritium Retention System, which serves the whole laboratory. The local Tritium Retention Systems are designed to keep the activity levels in the glove boxes at very low values at all the times. They are also used to remove the tritium released into the glove boxes during normal operations or accidental situations. The Central Retention System removes the tritium from the ring-tubing, to which all glove boxes are connected. It therefore takes care of the tritium not removed by the local systems. Another function of the Central Retention System is to maintain at all times a pre-established under-pressure in all the glove boxes. In addition, in a section of the Central Retention System, the highly contaminated gaseous streams arising from the exhausts of the experimental and infra-structure primary systems are pre-processed. After a decontamination factor of typically more than 100 has been achieved the gases are released via the Central Retention System to stack.

All Tritium Retention Systems are maintained in round-the-clock operation in order to keep the activity levels in the glove boxes at levels barely above background. The Retention systems are based on the catalytic oxidation of released tritiated species into carbon dioxide and water followed by adsorption of the produced water on molecular sieve adsorber beds. Because of operational and redundancy purposes every Retention System has two molecular sieve beds.

The adsorber beds of the Central Tritium Retention System are routinely reactivated every 6-8 weeks, depending upon the tritium-related activities taking place in the laboratory. Those installed in the Local Tritium Retention Systems of glove boxes housing experiments and infrastructure systems are reactivated much less frequently because of the extremely low leak rates that these glove boxes normally have, i.e.: < 0.1 %/h.

In total 160 beds containing 2.4 tons of molecular sieve adsorber have been regenerated employing the facility AMOR. In this facility the beds are processed sequentially in closed loop operation. Nitrogen is used as carrier gas. The beds are heated progressively up to a final temperature of 300 °C. The liberated tritiated water is removed from the carrier gas initially with a condenser and towards the end with another molecular sieve bed. The latter is itself regenerated after several consecutive molecular sieve bed regenerations. Under the above described conditions the water content of a bed can be reduced from initially about 10 to less than 0.5 % by weight, respectively. The performed regenerations have been accomplished without contamination of personnel or the environment. The recovered tritiated water (in total approx. 240 l) has been disposed-off by the Central Decontamination Department of FZK.

Staff:

H.-D. Adami
U. Besserer
R.-D. Penzhorn

SEA 3 (N 11 TD 72)
Reference Accident Sequences – Magnet Systems (2)

Subtask 2: Magnet System Safety

Within the subtask SEA 3.2 FZK investigates the thermal behavior of magnet systems during accidents.

In the period reported here code application and validation of MAGS have been major parts of the work.

The MAGS module CRYOSTAT has been improved such that we can now handle mixtures of N_2, Helium and H_2O. In this context also a two phase capability was incorporated. However, this is only possible for module CRYOSTAT, module GANDALF, by its solution method cannot operate in the two phase regime. Another model that was worked on is the arc model. While the module SHORTARC simply uses an experiment based formula for arc voltage as a function of arc current, the new model, developed at University of St. Petersburg, considers energy and mass balance for the arc cavity and an energy balance for the plasma. Included are models for electrical conductivity of the ionized plasma and the ablation of the material on the cavity surface. The model is a stand alone code and will be included to MAGS as a new module.

The accident that has been investigated for ITER is the 'unmitigated quench in a coil of the TF system'. In such an accident theoretically the complete stored energy of the TF system may be dumped into the coil with the initiating quench. While the quench is initiated locally the total mass of the coil is necessary to absorb this energy at acceptable temperatures. Therefore the spread velocity of quench within a TF coil is very important. For a complete thermal modeling of a TF coil the coil structure is too complicated. The frequent change of thermally good and bad conductors, i.e. copper and insulation require a huge mesh and tremendous computing times. To overcome this situation a characteristic number can be determined e.g. a 'jump time' being the time necessary for quench to 'infect' a neighboring turn. Three different situations can be distinguished: jump to the next radial turn, jump to the next axial turn in the same radial plate and jump to the next axial turn in the next radial plate. The jump times found range between 20 s and 38 s. Compared to the time needed for a quenched piece of conductor to be heated up to steel melting temperatures (30 s to 40 s) it is clear that local melting of the coil cannot be prevented. Additionally such high temperatures impair also the insulation quality of the insulator. I.e. the current path, which under regular conditions is through each turn of the coil may alter such that after insulation failure the current flows only through a fraction of the turns. In this case the shorted turns are excluded as a mass for heat storage, however, the total mass of the coil is required as mentioned above. The investigation shows that it is likely that during this accident not all energy can be absorbed in the TF system and the accident may impair also on other systems within the cryostat.

Other accidents considered are leak accidents for the cryostat. The air or N_2 leaks, analyzed with the updated code did not show new results. A Helium leak has been analyzed for the first time. It was assumed the Helium of the coil cooling system can be simulated by a single volume of initially 0.6 MPa and an initial temperature of 5 K. The analysis shows, that at the beginning of the transient a Helium puddle is formed at the bottom of the cryostat, being dried out after about 20 s. At about this time the pressure has reached already its final value of 0.02MPa. The surface temperatures of the cryostat and the vacuum vessel reduce from their initial value of 300 K and 400 K to values between 180 K and 220 K. The heat of the walls is used to rise the temperature in the volumes.

The Q3D experiment, investigating the quench behavior along the conductor as well as between adjacent conductor turns in a coil, have been finished and is documented in a report [1]. Recalculation of the experiments was started and significant differences between analysis and experiment are found. This and the results of recalculation of the QUELL experiments [2] with a conductors having a central channel indicate strongly the need on an update of the heat transfer relations in the GANDALF code.

To support the TFMC experiments performed at FZK-ITP an input deck for MAGS has been set up [3]. Recalculation of this experiment will be done to get experience in use of eddy current analysis in the radial plates and the coil case.

Literature:

[1] W.Kuhn: Experimentelle Untersuchung der dreidimensionalen Quenchausbreitung in zwangsgekühlten supraleitenden Spulen. FZK 6086 (1998)

[2] M.Biemüller: Sensitivitaetsanalysen und Rechnungen zu QUELL mit dem Programmsystem MAGS. FZK Interner Bericht

[3] M.Biemüller: Rechnungen zur ITER Toroidalfeld Modellspule mit dem Programmsystem MAGS. FZK Interner Bericht

Staff:

M. Biemüller
G. Bönisch
W. Kuhn
R. Meyder

SEP 2
Environmental Impact

Probabilistic dose assessments for accidental atmospheric releases of various source terms (based on a draft working document of NSSR-2) which contain either tritium and/or activation products were performed for Greifswald, Germany, and Cadarache, France, which were considered to be potential sites for ITER at the beginning of the investigations /1, 2/. Mainly potential individual doses and areas affected by protective measures were evaluated for three types of accidents, all of them placed in the event sequence categories IV ('extremely unlikely events') and V ('hypothetical sequences'). The results were also compared to site independent dose limits defined in the frame of ITER. In addition, routine releases into the atmosphere and the hydrosphere have been considered.

Annual doses from routine releases (CAT-I) are below 0.1 mSv/a for the aquatic scenarios and are close to 1 mSv/a for the atmospheric source terms. In none of the release scenarios of category CAT-IV the ITER limits were exceeded. In addition, relevant characteristic quantities (e.g. 95% fractiles) of the early dose distributions from the hypothetical scenarios of type CAT-V are below 50 mSv or 100 mSv, values which are commonly used as lower reference values for evacuation in many potential home countries of ITER. These site specific assessments, together with those performed in 1997, confirmed that the proposed release limits and thus the derived dose limits for a generic ITER side are unlikely to exceed the national criteria for evacuation. Other protective actions such as sheltering, relocation and food banning were investigated and only banning of agricultural products was found to be important.

The further development of the computer code 'Plant-OBT' for describing the OBT formation and translocation in wheat plants was terminated by mid 1998 /3/. Comparative calculations performed with experimental data from 1995 and 1996 showed, however, that our present understanding of the processes seems not to be deep enough to describe the OBT formation in the seedlings of winter wheat by using only a limited number of environmental parameters. In particular, the dynamics of the OBT formation could not be reproduced in detail. The final OBT content at the time of harvest, however, could be predicted within a bandwidth of a factor of two. Nevertheless, the results allowed to modify the present OBT model in UFOTRI, the accident consequence assessment code for tritium releases /4/. These changes result in a lower OBT formation rate and thus a lower dose from the ingestion pathways. However, this version will not be released before the confirmation of the model changes by further experimental data.

Within the BIOMASS (BIOspheric Modelling and ASSessment) project testing of tritium models for routine releases into the atmosphere and hydrosphere has started. Up to now three different scenarios have been set up covering both fixed environmental conditions to test individual model features and using on measured data from a site in Canada to test the overall performance of existing assessment codes for routine releases. NORMTRI /5/ together with a computer code describing the water movement in the upper soil are participating in the comparative calculation study. The first results will be evaluated by the end of 1998.

Literature:

[1] W. Raskob, I. Hasemann, Dose Assessment for Greifswald and Cadarache with updated source terms from ITER NSSR-2. Report FZKA-6101, Forschungszentrum Karlsruhe, 1998

[2] W. Raskob, Dose Assessments for Potential European Sites with Updated Source Terms from ITER, Poster at the 20th SOFT conference, Marseilles, October 5 - 9, 1998

[3] S. Strack, S. Diabaté and W. Raskob Modellrechnungen zur Biokinetik von Tritium in Pflanzen, Radioaktivität in Mensch und Umwelt, 30. FS-Jahrestagung, 28.9. - 2.10.98, Lindau (in German)

[4] W. Raskob, Description of the New Version 4.0 of the Tritium Model UFOTRI Including User Guide, Report KfK-5194, Kernforschungszentrum Karlsruhe (1993)

[5] W. Raskob, Description of the Tritium Model NORMTRI for Releases under Normal Operation Conditions. Report KfK-5364, Kernforschungszentrum Karlsruhe, 1994

Staff:

J. Ehrhardt
I. Hasemann
W. Raskob

Gyrotron Development (includes ITER Tasks T 245/6, T 360 and ECH 3/1)

1. Introduction

Electron cyclotron resonant heating (ECRH) is one of the major candidates for additional heating and current drive (170 GHz, 50 MW) and for start-up (90-140 GHz, 3 MW) on the ITER tokamak and will be the main start-up and heating scheme on the stellarator W7-X (140 GHz, 10 MW) at IPP Greifswald, Germany.

The main physics advantage of ECRH is the possiblity of well-localized power absorption, where the deposition region is defined by the crossing of the ECR layer with the rf-beam. The technology advantages of ECRH are as follows. Antennas can be located far from the plasma, thus avoiding impurity release and providing decoupling of heating from particle refuelling. Compact optical antennas allow very high injected power densities (in excess of 100 MW m^{-2}), implying the use of fewer ports. Millimeter-wave vacuum windows provide a tritium barrier in the waveguide separating the vessel from the source so that the sources can be placed in a "hands-on" location distant from the plasma.

Gyrotrons operating in the frequency range between 110 and 170 GHz with an output power ≥ 1 MW are under development at FZK Karlsruhe. In particular, extensive development work has been done on a 1 MW, $TE_{22,6}$ gyrotron at a frequency of 140 GHz having a conventional hollow waveguide cavity [1], [2] and on 1.5 MW coaxial cavity gyrotrons designed for operation in the $TE_{28,16}$ and $TE_{31,17}$ mode at frequencies of 140 and 165 GHz, respectively [3]. The limiting factors of conventional cavities can be considerably reduced with the use of coaxial cavities, which offer the possiblity of operation in high order volume modes with reduced mode competition problems. Furthermore, the presence of the inner conductor practically eliminates the restrictions of voltage depression and limiting current. Therefore gyrotrons with coaxial cavities have the potential to generate, in CW operation, rf-output powers in excess of 1 MW at frequencies above 140 GHz.

Important development goals of a 1 MW, 140 GHz cylindrical cavity gyrotron operated in CW, as required for W7-X, such as the depressed collector technology, the advanced built-in quasi-optical (q.o.) mode converter, the window concept and the investigation of the influence of reflected power on the efficiency are also prerequisites for the coaxial cavity gyrotron development and therefore in these areas the development of cylindrical cavity 1 MW gyrotron will provide an important input for the development of a coaxial 2 MW gyrotron for ITER.

2. Conventional Cylindrical Cavity Gyrotron

Fig. 1 shows the schematic layout of the 1 MW gyrotron with conventional cylindrical cavity and Brewster angle window. The gyrotron is designed for operation in the $TE_{22,6}$ mode which is converted into a linearly polarized free space field distribution by a quasi-optical mode converter using a short dimpled-wall launcher. The total efficiency is increased by energy recovery with a single-stage depressed collector (SDC).

Even small reflections of output power can have a large influence on the power generated inside the cavity. The $TE_{22,6}$ mode, 1 MW, 140 GHz gyrotron has been used to investigate the behaviour of the oscillations under the influence of external reflections. The gyrotron was equipped with a single disk window of Si_3N_4. The angle of the disk was chosen to be 70.36° which corresponds to the Brewster angle for this material. For this angle the reflections vanish independent of frequency. This

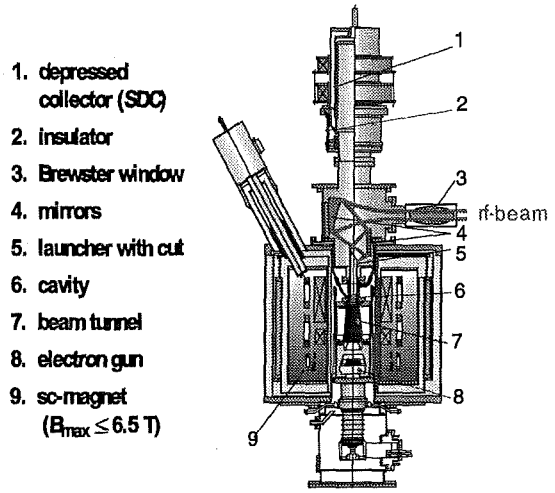

Fig. 1: Schematic layout of advanced 1MW gyrotron

allows to produce and to change the reflections outside the gyrotron under well controlled conditions. The measurements showed a strong influence of reflections on the output power [5]. For power reflections less than 5 % a reduction of the generated power of more than a factor of 3 has been found. By tilting the calorimetric load required for the power measurement by about 2°, an increase in output power of 20 % could be found, resulting in an output power of 1.6 MW (U_c = 88 kV, I_b = 50.1 A) at 140 GHz and an efficiency of 36 % (60 % with SDC). At the design beam current of 40 A the output power increased to 1.4 MW with 56 % efficiency (SDC). In Fig. 2 the rf-output power as function of the beam current is given. A maximum output power of 2.1 MW (U_c=90 kV, I_b = 70A) has been measured at 140 GHz with an efficiency of 34 % (50.5 % with SDC)[4],[5].

The possibility of slow broadband frequency step tuning (1 min) by variation of the magnetic field level in the cavity has been demonstrated [2,4,6]. Successful experiments with broadband fused quartz and silicon nitride Brewster angle windows gave up to 1.5 MW at 45-50 % efficiency (SDC) for all operating mode series in the frequency range from 114 to 166 GHz (frequency tuning in 3.7 GHz steps).

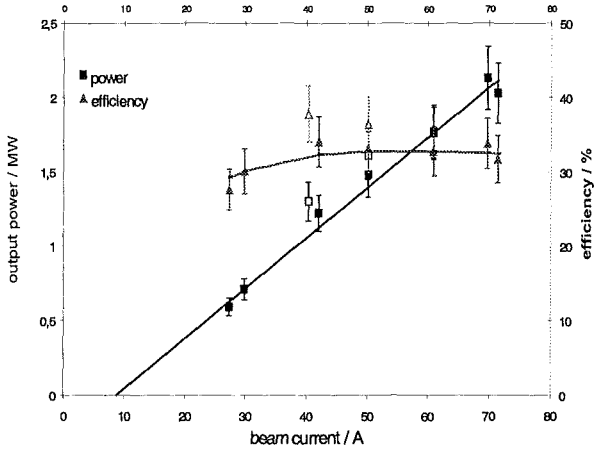

Fig. 2: Output power and efficiency as function of beam current.

3. Advanced Coaxial Cavity Gyrotrons

Coaxial cavity gyrotrons operated at 140 GHz in the $TE_{28,16}$ mode and at 165 GHz in the $TE_{31,17}$ mode with an rf output power of 1.5 MW are under development at FZK. In order to investigate the basic operating problems in a first step experiments with a gyrotron equipped with an axial waveguide output have been performed. The achieved results of 1.2 MW output power at 27 % efficiency were in good agreement with numerical calculations [7]. In a second step, the 140 GHz, $TE_{28,16}$ gyrotron has been operated with a dual rf-beam output. For the first time the possibility of internal splitting of the generated rf-power has been demonstrated successfully (2 x 0.5 MW, 7 ms, 29 % with SDC) [8]. The development of rf-windows is progressing very fast. CVD-diamond windows with a transmission capability even above 2 MW at the frequencies considered seem to be close to realization. Therefore, in the recent experiment the 165 GHz, $TE_{31,17}$ gyrotron has been equipped with a quasi-optical (q.o.) system [9] for transmission of the rf-power through a single window.
The measurements have been performed in pulsed operation with up to 15 ms pulse duration. The rf-output power has been

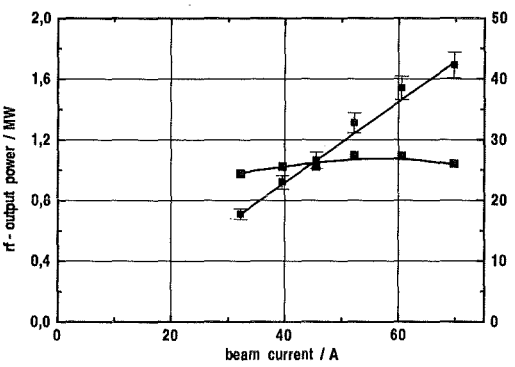

Fig. 3: Output power and efficiency as function of beam current

measured calorimetrically. The microwave diagnostic system allows to measure the frequency and to observe whether there is single or multimode oscillation during a pulse. A concentricity of the electron beam relative to the coaxial insert and to the outer cavity wall within ≤ 0.2 mm has been achieved by adjusting both the superconducting-magnet and the coaxial insert.

The $TE_{31,17}$ mode has been found to oscillate with a frequency of 164.98 GHz, in very good agreement with the design. A large single-mode operating range has been observed. A maximum power of 1.7 MW was measured at a cathode voltage of 93.2 kV and a beam current of 70 A. With a retarding collector voltage of 24.2 kV this gives an efficiency of 35.2 %. The maximum efficiency of 27.3 % without SDC was measured at 1.2 MW near the design values: cathode voltage 92 kV, beam current 52 A.
With a retarding collector voltage of 33.2 kV this corresponds to 40 % efficiency (with SDC). Fig. 3 shows the output power and efficiency as function of beam current. Fig. 4 gives the output power and efficiency as function of the collector depression voltage for 1.2 MW and constant magnetic field.

In order to demonstrate the feasibility of the technical realisation of a coaxial cavity gyrotron a new electron gun has been designed and is under fabrication [10]. The features of the gun (cooling of the inner rod, possibilities of alignment, cathode technology) are as needed for a long pulse (up to CW) gyrotron. Experiments with this new gun are under preparation.

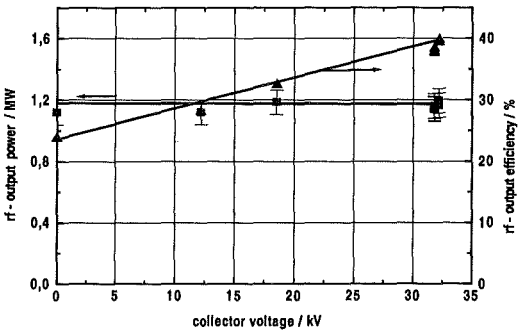

Fig. 4: Output power as function of collector depression voltage

Literature:

[1] Dammertz, G., Braz, O., Kuntze, M., Piosczyk, B., Thumm, M., Conf. Digest 22nd Int. Conf. Infrared and Millimeter Waves, 1997, Wintergreen, Virginia, USA, 150-151.

[2] Braz, O., Dammertz, G., Kuntze, M., Thumm, M., Int. J. of Infrared and Millimeter Waves, **18**, 1465-1477 (1997).

[3] Piosczyk, B., Braz, O., Dammertz, G., Iatrou, C.T., Kuntze, M., Michel, G., Möbius, A., Thumm, M.: Conf. Digest. 23rd Int. Conf. Infrared and Millimeter Waves, 1998, Colchester, U.K., Invited paper, pp. 168-169.

[4] Dammertz, G., Kuntze, M., Braz, O., Koppenburg, K., Piosczyk, B., Thumm, M., Conf. Digest. 23rd Int. Conf. Infrared and Millimeter Waves, 1998, Colchester, U.K., pp. 276-277.

[5] Kuntze, M., Borie, E., Braz, O., Dammertz, G., Illy, S., Michel, G., Möbius, A., Piosczyk, B., Thumm, M.: Proc. 20th Int. Symp. on Fusion Technology (SOFT), 1998, Marseille, France, Vol. 1, pp. 489-492.

[6] Dammertz, G., Braz, O., Kuntze, M., Piosczyk, B., Thumm, M., Proc. 10th Joint Workshop on ECE and ECRH, 1997, Ameland, NL, 483-488.

[7] Piosczyk, B., Braz, O., Dammertz, G., Iatrou, C.T., Kern, S., Kuntze, M., Möbius, A., Thumm, M., Flyagin, V.A., Khishniyak, V.I., Malygin, V.L., Pavelyev, A.B., Zapevalov, V.E., IEEE Trans. on Plasma Science 25(3), 460-469 (1997).

[8] Piosczyk, B., Braz, O., Dammertz, G., Iatrou, C.T., Illy, S., Kuntze, M., Michel, G., Möbius, A., Thumm, M., IEEE Trans. on Plasma Science 26(3) (1998).

[9] Michel, G., Thumm, M., Wagner, D., Conf. Digest 22nd Int. Conf. Infrared and Millimeter Waves, 1997, Wintergreen, Virginia, USA, 25-26.

[10] Piosczyk, B.: Conf. Digest. 23rd Int. Conf. Infrared and Millimeter Waves, 1998, Colchester, U.K, pp. 394-395

Staff:

J. Anderer (Uni Karlsruhe)
A. Arnold (from 1.1.98, Uni Karlsruhe)
H. Baumgärtner
E. Borie
O. Braz (Uni Karlsruhe)
H. Budig
G. Dammertz
P. Grundel
S. Illy
K. Koppenburg
H. Kunkel
M. Kuntze
W. Leonhardt
G. Michel (to 31.3.98, Uni Karlsruhe)
B. Piosczyk
J. Szczesny
M. Thumm
R. Vincon

High Power ECH Windows (includes ITER Tasks T 245/6, T 360, ECH 2/1 and D 351)

1. Introduction

High unit power, in excess of 1 MW, and high-efficiency gyrotrons significantly lower the cost of Electron Cyclotron Wave (ECW) systems by reducing the size of the auxiliary support equipment (power supplies, cooling system, number of SC-magnets, ...). Continuous wave (CW) operation is required for some of the anticipated ITER applications: 3 s for start-up, 100 s for heating to ignition and 100-1000 s for current drive. In order for the ECW systems to perform these functions a window has to be developed to serve as both the tritium containment barrier on the torus and as the output window on the tube. The former application is technically more demanding as the torus window must also serve as a high pressure barrier during off-normal events (0.5 MPa overpressure capability), should not use FC-cooling liquid, must not degrade unacceptably under modest neutron and γ (including x-rays) irradiation, and, in the case of cryo-cooling, must be prevented by a cold trap from cryo-pumping.

A very promising material is Chemical Vapor Deposition (CVD)-diamond which nowadays can be manufactured in window disks of up to 120 mm diameter and 2.5 mm thickness [1]. A water-cooled diamond window would provide two very important advantages, namely employing a cheap and simple as well as effective coolant.

2. CVD-Diamond Window

Metallization/bonding techniques for CVD-diamond disks have been developed in collaboration with DeBeers. The disadvantage of the first method which uses Al-based braze (GB6-EU-T245/6) is the relatively low allowed bakeout temperature of the window unit of 450°C (guaranteed by DeBeers). Further tests have been performed on metallized disks which have been bonded with Au-based brazing on both sides to Inconel 600 cylinders to form part of a full window assembly (outer disk diameter = 50 mm, disk thickness 1.8 mm, window aperture = 40 mm). The Inconel cylinders are strengthened by Molybdenum rings in order to reduce thermal expansion during bakeout. These sub-assemblies have been subjected to the bakeout cycle of a gyrotron up to 550°C with the result that the bonding at both sides started to leak. This shows that the Au-based braze is not as elastic as the former Al-based braze that is only bakeable up to 450°C. The next bonding/ brazing tests will be performed either with Molybdenum (small thermal expansion) or with Copper (elastic) waveguide sleeves.

The design of a 118 GHz, 0.5 MW, 210 s CVD-diamond window was finished and the window has been manufactured at TTE.

The universal design (Fig. 1) allows tests in an evacuated HE_{11}-transmission line at CEA Cadarache and also direct mounting to a 118 GHz TTE-gyrotron. The window has an aperture of 80 mm (100 mm outer disk diameter), a thickness of 1.6 mm, a loss tangent of only $6 \cdot 10^{-6}$ (world record!), a thermal conductivity of 2050 W/mK (at room temperature) and has also been bonded using the Al-braze technique. The window will be tested in December 1998 at CEA Cadarache when the long-pulse 118 GHz gyrotron will be available.

In collaboration with the JA Home Team high-power tests on a 170 GHz gyrotron equipped with a CVD-diamond window were performed [2]. The window aperture is 83 mm. The poly-crystalline diamond disk has a diameter of 96 mm, a thickness of 2.23 mm, a loss tangent of $1.3 \cdot 10^{-4}$, a thermal conductivity of 1800 W/mK (at room temperature) and was bonded with the Al-braze technique. The tests were very successful (450 kW, 8 s: 3.6 MJ). The maximum window center and edge temperatures were measured to be 150°C and 13°C, respectively, with a saturation time of approximately 5 s.

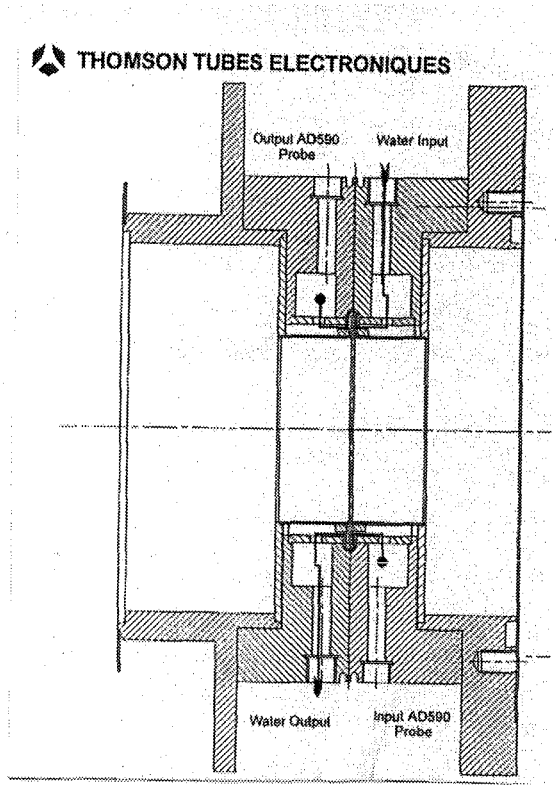

Fig. 1: Layout of the 118 GHz, 0.5 MW, 210 s diamond window

Three CVD-diamond disks with 100 mm outer diameter and 1.8 mm thickness have been ordered at DeBeers for the development of a 140 GHz, 1 MW, CW prototype gyrotron for W7-X (with single-stage depressed collector efficiency > 45 %).

Following previous ITER work on ECW gyrotron window development (see GB6-EU-T245/6), which demonstrated the availability and the up-scaling potential of CVD-diamond grades with low dielectric losses, neutron irradiation tests were extended to fluences of 10^{21} n/m^2 (E > 0.1MeV). Even at this damage level (10^{-4} dpa) which corresponds to the recommended upper fluence level for cryogenically-cooled Sapphire windows, no critical radiation enhanced losses were observed at 90 GHz and 145 GHz (see also GB7–EU–T246). No in-beam effects at 800 Gy/s (electrons) and 0.75 Gy/s (X-rays) were observed (see GB7-EU-T246). Therefore the preparation for forthcoming irradiation tests of actual window component material was set to this fluence level. The unsettled issue of degradation of thermal conductivity at 10^{-5} dpa damage level was the reason for a pending special neutron irradiation at 10^{-4} dpa of specimens for thermal conductivity measurements.

In the material characterisation for actual CVD-diamond window materials, several disks of white grade material with diameters of 100 – 119 mm and thickness between 1.6 mm and 2.3 mm were investigated which were produced at DeBeers. In the latest disks, internally named "SUPER-FZK" (100 mm dia. x 1.60 mm) and "Star of FZK" (119 mm x 2.25 mm), the center showed low losses which were constant between 70 K and 370 K (Fig. 2) just like the permittivity of 5.67 [3,4].

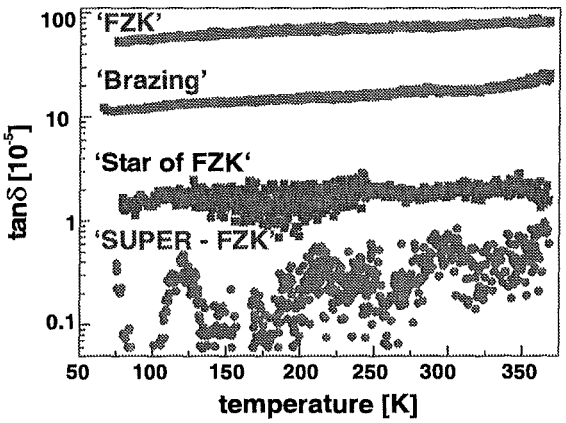

Fig. 2: Temperature dependence of tanδ at 145 GHz

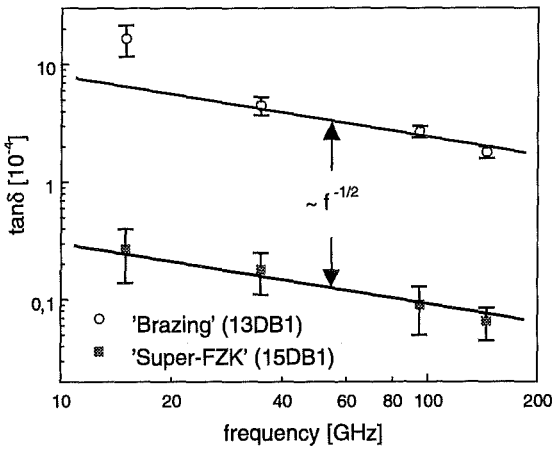

Fig. 3: Frequency dependence of the locally inhomogeneous "Brazing" - window (13DB1) and the homogeneous "Super-FZK" - window (15DB1).

Inhomogeneities in mm-wave properties which were important in earlier disks were checked in terms of variations in the surface contributions from the nucleation and the growth face as well as in terms of distribution of losses across the area of the disks. The recent large disks which had the starting layer removed from the nucleation side did not show any significant differences in the losses between the nucleation and the growth side. Over a mapped inner area of 70 mm diameter losses were found at 145 GHz not exceeding $1 \cdot 10^{-5}$ for the "SUPER-FZK" disk and not exceeding $2 \cdot 10^{-5}$ for the "Star of FZK" disk. The window material development was supported by dielectric property measurements of grades from potential alternative European and American sources. A first set of 12 mm diameter disks for mechanical strength tests were received from corresponding white grade material. The typical values for the 0.26 mm thick disks of 700 MPa for the growth side under tension fit well into a relationship established for strength data observed from another source studied in the framework of a separate CVD-diamond development task [5]. The apparent correlation of ultimate bending strength with diamond grain size implies strength data as high as 2000 MPa to be expected for the nucleation side under tension. Compared to standard technical ceramics (such as alumina), CVD-diamond of a given quality has a remarkably high Weibull modulus (m > 20), i.e. very small distribution of the strength values.

3. Design and Optimization of ITER Window Unit

The proposed ITER ECH window unit employs a single, edge-cooled (water, e.g. 20°C) CVD-diamond disk in a corrugated HE_{11} waveguide with 52 mm inner diameter, with an outer disk diameter of 77 mm and a thickness of 1.482 mm (4 λ/2). Thermal computations show that for larger outer disk diameters the peak temperature is unaffected. Thus due to the high thermal conductivity of the diamond, the exposed window edge area does not have to be large to obtain significant heat transfer. This implies that the window diameter can be minimized, which has the added benefit of reducing the cost. For a power of 1 MW at 170 GHz, a loss tangent of $1 \cdot 10^{-5}$, a thermal conductivity of 1800 W/mK (at room temperature) and a heat transfer coefficient of 12 kW/m²K (water flow: 13.5 l/min, water velocity: 2 m/s) to the cooling the central window temperature will not be higher than approx. 40°C and the edge temperature is about 25 °C. Simulations also show that steady state conditions are generally achieved in under 3 s and that a 2 MW window should be feasible [6]. Owing to the temperature independence of the CVD-diamond loss tangent, also the approximately 100°C hot torus cooling water could be used to cool the window. Simulations of an "encased" window, a window in which the edge of the disk has been covered with a 0.4 mm thick layer of electrodeposited copper (tritium barrier in case of broken window disk), show that this is feasible without a significant decrease in heat transfer rate.

Finite element stress calculations including brazing/bonding stress show that the maximum principal stress is located in the window brazing (205 MPa) and is always present. During a 0.5 MPa static overpressure event the stress increases to 290 MPa and the transmission of 1 MW microwave power finally increases the stress to 300 MPa. All these stress values are upper limits since a rigid connection between brazing collar and window disk was assumed. Because the ultimate bending strength of white CVD diamond is approximately 600 MPa all stresses are well below the admissible limits.

A complete design of the window unit has been performed with the aim to get a compact device. The drawings are available. Considerations on water flow, pressure drop and heat exchange coefficient are included. Modelling experiments using a copper disk equipped with an electrical heater have been performed (Fig. 4).

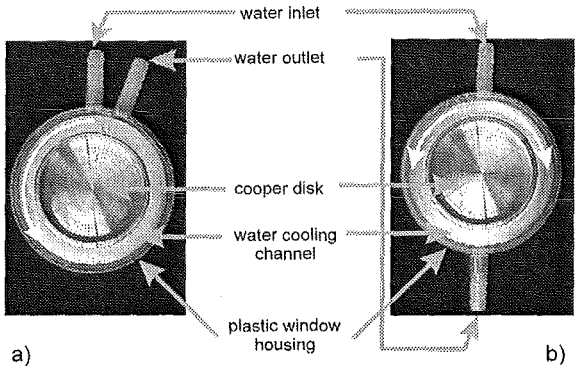

Fig. 4: Photograph of the two types of dummy windows
a) Enforced water flow circular around disk
b) Parallel water flow around window.

Through the optional use of a double window, window failures could be easily detected (as on the JET LH and ICRH systems). A very high vacuum (≈ 10^{-9} Torr) can be achieved within the interspace between the two window disks. Since the total volume is small, vacuum pumping can be done with only one VAC-Ion pump. Any failure of either window is detectable as a pressure rise on the ion pump even in the case in which a lower grade vacuum (≈ 10^{-5} Torr) is present on the opposing surface. Bandwidth calculation show, that the disk distance should be e.g. 52.9 mm = 30 λ.

Investigations of windows for step tunable gyrotrons were also undertaken. For this application, a Brewster angle window is used. Prototype quartz and silicon nitride Brewster windows were installed on a gyrotron and used to demonstrate "fine" step tuning (Δf ~ 3.7 GHz) in a band from 114 to 166 GHz. High output power around 1.5 MW has been obtained at all frequencies. It was also demonstrated that the power absorbed by a Brewster window is generally lower than that by a conventional window.

Literature:

[1] Thumm, M, Int. J. of Infrared and Millimeter Waves, 19, 3-14, (1998).

[2] Kasugai, A., D.C. Ballington, A. Beale, J.R. Brandon, O. Braz, T. Kariya, K. Sakamoto, R.S. Sussmann, K. Takahashi, M. Tsuneoka, T. Imai, M. Thumm, Review of Scientific Instruments, **69**, pp. 2160-2165 (1998).

[3] Spörl, R., R. Schwab, R. Heidinger, V.V. Parshin, Proc. of ITG Conf. on Displays and Vacuum Electronics, Garmisch-Partenkirchen, 1998, ITG-Report 150, 369-374.

[4] Heidinger, R., R. Spörl, M. Thumm, J.R. Brandon, R.S. Sussmann, C.N. Dodge, 1998, DVD diamond windows for high power gyrotrons, Conf. Digest 23rd Int. Conf. IR & MM Waves, Colchester (UK), 1998, Invited paper, pp. 223-225.

[5] Spörl, R., R. Heidinger, G. Kennedy, C. Brierly, Mechanical properties of free-standing CVD wafer, Proc. 9th CIMTEC, Florence, 1998, in press

[6] Singh, V.V.P., E. Borie, A. Arnold, O. Braz, M. Thumm, Int. J. of Infrared and Millimeter Waves 19, 1998, in press.

Staff:

A. Arnold (from 1.1.98, Uni Karlsruhe)
E. Borie
O. Braz (Uni Karlsruhe)
R. Heidinger
P. Severloh
R. Schwab
V.V.P. Singh (guest scientist for 4 months)
R. Spörl
M. Thumm

T 246
Ceramics for ECR-Heating, Current Drive and Plasma Diagnostic

With the completion of the cryogenic irradiation work on sapphire and quartz [1], the mm-wave studies were especially directed towards the characterization and post-irradiation studies of rapidly progressing advanced window materials, in particular CVD diamond. The development opens the way for continuous wave operation of Megawatt gyrotrons which is the key problem for electron cyclotron (EC) heating systems. In addition to this work which was mainly performed at 145 GHz, dielectric property measurements were extended to neighbouring frequency ranges (such as 90 – 100 GHz [2]) to widen the data base for broadband transmission, which is also required in EC diagnostic systems. Results in the present fields did not show any particularly new features in permittivity. There the discussion is limited to the observed mm-wave loss parametrized by the dielectric loss tangent (tan δ).

Inhomogeneities in the mm-wave losses of large CVD diamond discs which were important in the earliest discs studied were particularly investigated in terms of variations in the surface contributions from the nucleation and the growth face as well as in terms of distribution of losses across the area of the discs [3]. For this purpose, the experimental facilities were further refined to provide a dense loss mapping [4]. Among the several discs of white grade material grown by DeBeers, two discs were of special concern as they were to serve later in actual high power window tests initiated by the FZK gyrotron group. The two discs were internally named "SUPER-FZK" (100 mm dia x 1.60 mm) and "Star of FZK" (119 mm dia x 2.25 mm). In these discs, inhomogeneties were not observed along the growth axis – probably due to effective removal of lossy surface layers by polishing – and within an inner area of at least 70 mm in diameter. While loss in the SUPER-FZK disc did not exceed the tan δ level of $1 \cdot 10^{-5}$, the larger disc showed significant increases towards the edges, but did not exceed $2 \cdot 10^{-5}$ in the inner area (cf. Fig. 1) [5].

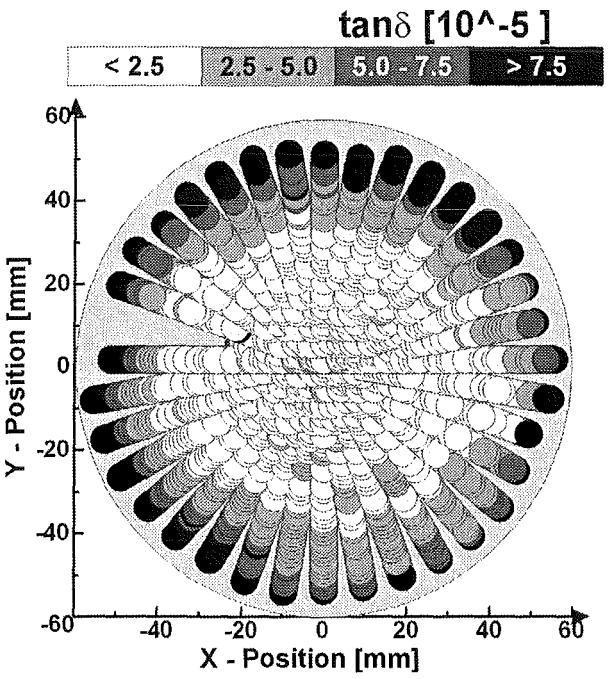

Fig. 1: Mapping of the dielectric loss tangent in "Star of FZK" CVD diamond window taken at 145 GHz

The neutron irradiation testing of the advanced window materials, CVD diamond and high resistivity (H.R.) silicon, was extended to fluences of 10^{21} n/m^2 (E > 0.1 MeV). This damage level (10^{-4} dpa) corresponds to the recommended upper fluence level for cryogenically-cooled Sapphire windows. The loss levels for undoped H.R. silicon even came down to the ultralow loss levels of Au-doped H.R. silicon, apparently because of effective trapping of free charge carriers at the structural defects. The loss observed at ambient temperature for two test discs of CVD diamond ("up-scale grade", "window grade") is given in Table 1. Clearly no major influence of radiation damage is observed neither at 90 – 100 GHz nor at 145 GHz [6].

Table 1: Pre- and post irradiation studies on specially developed CVD diamond grades for high power EC windows

a) Frequency: 145 GHz

Internal specimen code	Pre-irradiation studies dielectric loss tanδ [10^{-4}]	Post-irradiation studies at ≈10^{-5} dpa tanδ [10^{-4}]	Post-irradiation studies at ≈10^{-4} dpa tanδ [10^{-4}]
DB 6 (scale-up grade)	0.2 (± 0.1)	0.20 (± 0.05)	0.30 (± 0.05)
DB 7 (window grade)	0.10 (± 0.05)	-	0.20 (± 0.10)

b) Frequency: 90 GHz

Internal specimen code	Pre-irradiation studies dielectric loss tanδ [10^{-4}]	Post-irradiation studies at ≈10^{-5} dpa tanδ [10^{-4}]	Post-irradiation studies at ≈10^{-4} dpa tanδ [10^{-4}]
DB 6 (scale-up grade)	-	0.35 (± 0.10)	0.30 (± 0.05)
DB 7 (window grade)	0.10 (± 0.05	-	0.20 (± 0.05)

A first set of 12 mm diameter discs for mechanical strength tests were received from white grade CVD diamond material. The typical values for the 0.26 mm thick discs of 700 MPa for the growth side under tension fit well into a relationship established for strength data observed from another source studied in the framework of a separate CVD-diamond development task [7]. The apparent correlation of ultimate bending strength with diamond grain size implies strength data as high as 2000 MPa to be expected for the nucleation side under tension. Compared to standard technical ceramics (such as alumina), CVD-diamond of a given quality has a remarkably high Weibull modulus (m > 20), i.e. very small distribution of the strength values.

Literature:

[1] R. Heidinger, A. Ibarra, J. Molla, Pre- and post-irradiation studies on mm-wave losses in reference window materials for electron wave systems, J. Nucl. Mater., in press

[2] R. Heidinger, R. Schwab, F. Königer, A fast sweepable broadband system for dielectric measurements, Proc. 23rd Int. Conf. on Infrared and MM-Waves, Colchester (UK), 7.-11.9.98

[3] R. Spörl, R. Schwab, R. Heidinger, V.V. Parshin, CVD diamond for high power gyrotrons: Characterization of dielectric properties, Proc. Int. Conf. on Display and Vacuum Electronics, Garmisch-Partenkirchen, 29.-30.4.98

[4] R. Schwab, R. Heidinger, R. Spörl, Open resonator set-up for spatially resolved and temperature dependent mm-wave property measurements, Proc. 23rd Int. Conf. on Infrared and MM-Waves, Colchester (UK), 7.-11.9.98

[5] R. Heidinger, R. Spörl, M. Thumm, J.R. Brandon, R.S. Sussmann, C.N. Dodge, CVD diamond windows for high power gyrotrons, Proc. 23rd Int. Conf. on Infrared and MM-Waves, Colchester (UK), 7.-11.9.98

[6] M. Thumm, O. Braz, R. Heidinger, R. Spörl, A. Arnold, P. Severloh, ITER ECRF Coaxial Gyrotron and Window Development, ID-No. GB7-EU-T360, Final Report (1998)

[7] R. Spörl, R. Heidinger, G.R. Kennedy, C.J. Brierley, Mechanical properties of free-standing CVD diamond wafer, Proc. 9th Conf. Modern Material + Technology, Florence, 14.-19.6.98

Staff:

R. Heidinger
P. Severloh
R. Spörl

ERB 5000 CT 950064 (NET/95-384)
ITER Magnets and TFMC Stress Analysis

Under this contract finite element analyses for two subtasks have been performed:

a) Stress analysis for the ITER Toroidal Field Model Coil (TFMC), the Intercoil Structure (ICS) and the LCT coil to test the TFMC in the background field of the LCT coil in the TOSKA cryostat in cooperation with the EU Home Team,

b) stress analysis for the ITER coils in co-operation with the ITER Joint Central Team.

This work, from which previous activities are reported in [1], has been continued.

TFMC analysis

During the Engineering Design (ED) phase our task was to take part in the control and assessment of the Finite Element Analysis which was done by the industrial consortium AGAN.

Concerning the intercoil structure (ICS) a major task of the ED was to reduce the weight by about 25 % without reducing its stiffness intolerably. It turned out that the ED design run into the same problems as the conceptual design (CD): high joint deformation and rather high stress concentrations at the highly loaded side wedge. Due to lack of space not all design improvements resulting from our study [2] could be realized. To reduce the peak loadings meantime the TFMC current is reduced from 80 kA to 70 kA. Some details of the final ED are given in [3].

Concerning the testing preparations of the TFMC [4] we took part in the determination of the mechanical instrumentation of the ICS. It aims at the control of a) the global ICS frame deformation, b) the load transfer between TFMC and ICS and between the ICS and the LCT coil as well where some friction behaviour has to be observed and c) highly loaded side wedges.

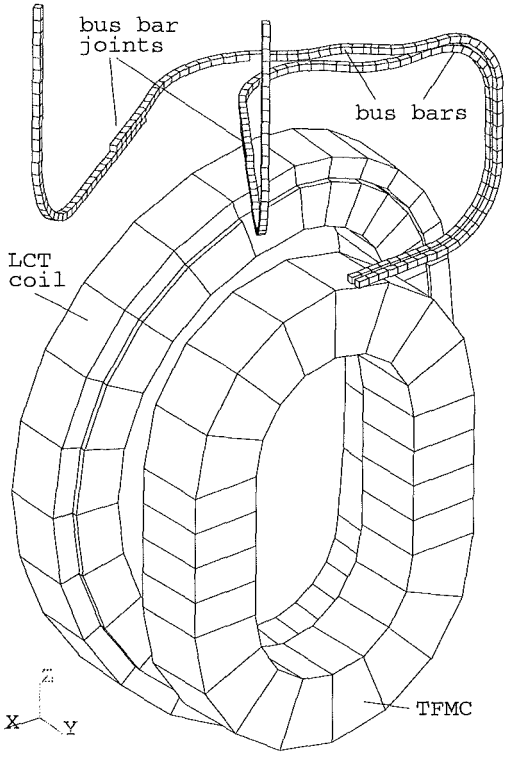

Fig. 1: Electro-magnetic model to determine the bus bar Lorentz force loading

A recently starting task was to perform finite element analysis required for the design of the bus bar supporting. Fig. 1 shows the electro-magnetic model to calculate the Lorentz force loading of the bus bars in the magnetic field of the TFMC and LCT coils. The optimum supporting design was determined in a following step by mechanical analyses of the bus bars under the calculated force loading (Fig. 2). It allows for some movement of the coils due to both the cool down and the Lorentz force loading but results in small bus bar displacement and stresses.

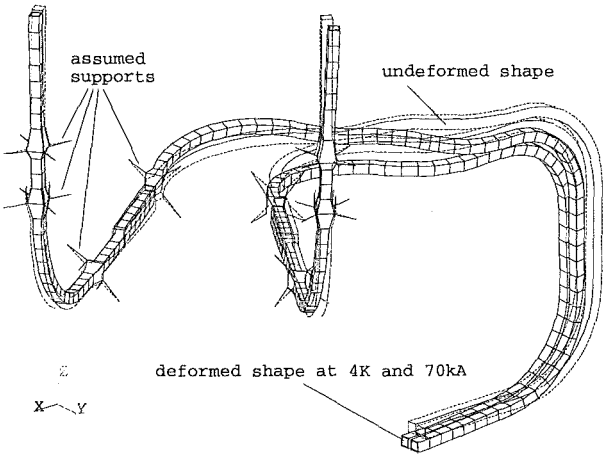

Fig. 2: Mechanical model of bus bars

In a further detail analysis the impact of bending moments on the contact behaviour in the joint box (Fig. 3) was determined. It turned out that sufficient contact pressure is maintained along the whole contact area under the bending moments of the displaced bus bars.

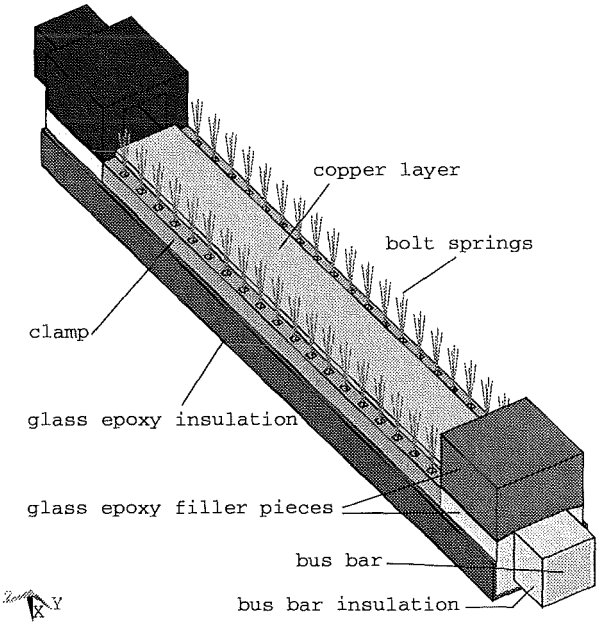

Fig. 3: Local model of bus bar joints (lower half)

ITER stress analysis

The local analysis of plate-cover welding seams of the TF winding pack has been finished [5]. In this study the sub-modelling method of the ANSYS Finite Element code has been used to do the local analysis of the stresses by using the results of the global ITER TF coil model [6]. The position of the local model has been varied around the perimeter of the coil and the radial and toroidal direction of the TF coil. The depth of the welding

seams has been varied from 1 mm to 10 mm. The analyses have shown that in highly loaded regions the originally designed stitch welds produce intolerable stress concentrations near the plate-to-plate insulation for all welding depths. Therefore, at the inner leg and the inner curved regions of the TF coil continuous welds are necessary. By this measure the maximum Tresca stress in the welding seams of the investigated regions remain within the allowable limits for a 5 mm deep weld. However, this is only valid, if the impregnation process can guarantee a sufficient filling of the assembly gaps below the welding seams. The report now is part of the final design report (FDR, Appendix B).

The new global model for the BDPA-97 (final design) was delivered by the JCT. To allow for extended parameter studies and optimisation of the design we linearized this model replacing all non-linear contact elements by linear springs and adequate coupling of nodal degrees of freedom. In a first parameter fitting process the out-of-plane deformation was chosen to be the objective function to approximate the non-linear solution. Future optimisation studies may need a special objective function.

A further study concerns the detailed behaviour of the rounded inner legs of the TF coils pressed on the scallop shaped grooves of the outer cylinder (OC) under Lorentz force loading. Between the OC and the casing of the TF coil leg is an assembly gap which closes at TF coil magnetisation. The question arises whether the grooves together with the rounded inner legs are able to rule out some assembly imperfections by sliding under load into the perfect position. Furthermore, whether the non-symmetric contact due to imperfections leads to unacceptable local peak stresses, e.g. in the winding pack insulation.

Fig. 4 shows a 36° equatorial slice of the inner part of the toroidal assembly containing the central solenoid between inner and outer cylinder and the inner legs of the TF coils with winding pack, insulation and casing. Due to the '3D extension' of the cross section the orthotropic 3D material properties allow for correct stresses, e.g. in the insulation. The assembly imperfection is introduced by a tangential shift of the middle coil leg by some millimeters. First results concerning the sliding behaviour are under discussion.

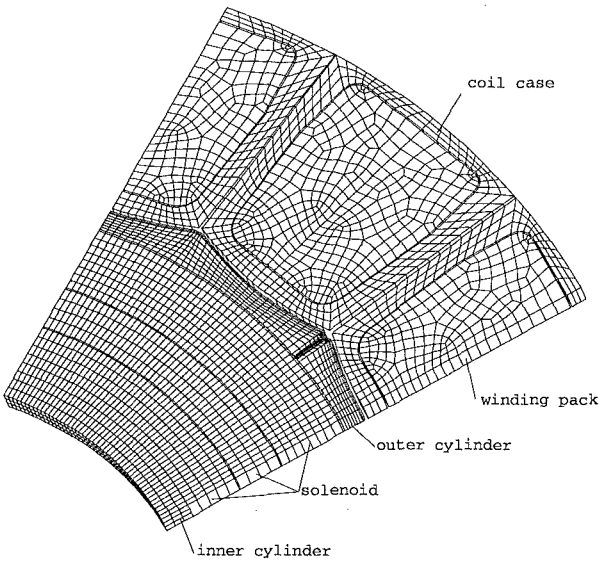

Fig. 4: Cross section model to study the coil / outer cylinder contact behaviour under assembly imperfections

Another study concerned the possibility for a TF coil single test. The determination of the operation limits and a suitable method for acceptance testing of series coils are mandatory for large and expensive magnet systems before assembling them in the toroidal configuration. But D shaped toroidal field magnets are assigned to the operation in a toroidal configuration. Single coil operation may lead to unacceptable bending moments with overloading of the mechanical structure.

Such tests only can be performed with a suitable reinforcement structure. This has been demonstrated with the EURATOM LCT coil at FZK/ITP. In collaboration with the ITP a conceptual check whether this can also be applied to the ITER TF coils was performed. By FEM analysis an optimum support structure for the ITER coils was determined allowing tests with some over-current (80 kA) without over-stress of the coil and conductor [7].

In the ITER EU Domestic Assessment [8] of the final design report FDR our contributions concerned the mechanical behaviour of the central solenoid, the crown/TF coil case interface and the TF coil outer leg based on our experience gained with the ITER global model.

Literature:

[1] 'Nuclear Fusion Annual Report of the Association Forschungszentrum Karlsruhe/EUTRATOM',
Oct. 1994 – Sept. 1995, FZKA 5688, EUR16749EN
Oct. 1995 – Sept. 1996, FZKA 5858, EUR17512EN
Oct. 1996 – Sept. 1997, FZKA 6050, EUR18156EN

[2] P. Decool, P. Libeyre, B. Dolensky, R. Meyer, S. Raff: 'ITER TF Model Coil – Finite element analysis of modifying the intercoil structure – side wedge extension – pads and horizontal plates reinforcement', EU Home Team Report, June 1997

[3] P. Libeyre, B. Crepel, P. Decool, H. Fillunger, B. Glassl, U. Hoeck, R. Kreutz, R. Maix, R. Meyer, R. Penco, S. Raff, E. Theisen, N. Valle: 'From Conceptual to Engineering Design of the ITER TFMC', Proc. 20th SOFT, Sept. 7-11, 1998, Marseille, France

[4] A. Ulbricht, M. Darweschsad, J.-L. Duchateau, H. Fillunger, S. Fink, G. Friesinger, R. Heller, P. Hertout, P. Libeyre, G. Nöther, S. Raff, F. Wüchner, G. Zahn: 'The Preparations for Testing the ITER Toroidal Field Model Coil (TFMC)', Proc. 20th SOFT, Sept. 7-11, 1998, Marseille, France

[5] R. Meyer: 'Structural Analysis of ITER Coils – Local Analysis of Plate Cover Welding Seams of the Winding Pack', EU Home Team Report, March 1998

[6] C.T.J. Jong: Analysis of the mechanical behaviour of the ITER magnet system', ECN-C-96-011, March 1996

[7] M. Darweschsad, G. Friesinger, A. Grünhagen, R. Heller, W. Herz, B. Kneifel, P. Komarek, W. Maurer, R. Meyer, G. Nöther, S. Raff, M. Süsser, A. Ulbricht, F. Wüchner, G. Zahn: 'The Test of the EURATOM LCT Coil at the Outermost Limits at 1.8 K as Example of Single Coil Testing of D Shaped Toroidal Field Coils', Fifteenth International Conference on Magnet Technology, Beijing, 1997

[8] A. Pizzuto et al.: 'Overall Mechanical Structure (including Vessel, Back Plate, Support Structure and Cryostat)', ITER Final Design Report, Technical Assessment, April 1998

Staff:

R. Krieg
R. Meyer
S. Raff

ERB 5004 CT 970009 (NET/96-438) High voltage components and sensor calibration for the ITER TFMC

Background

The nominal operation voltage of the ITER toroidal field (TF) coils is 10 kV across the winding. The ITER TF model coil has been designed and is being constructed by the ITER Home Team of the European Union therefore for 10 kV, too. In the frame of the POLO Project the technology of superconducting poloidal field coils for tokamaks were developed in the frame of a task of the European Fusion Technology Programme end of the eighties. Typical high voltage components needed for such coil were developed. The experience gained shall be applied by the ITER TF model coil. Therefore the FZK / ITP took over the obligation to organize the fabrication and the pre-testing of these components in the frame of a NET-Contract. The following components shall be delivered to the industry consortium AGAN to be installed on the ITER TF model coil:
30 axial insulation breaks
3 radial insulation breaks
3 instrumentation wire feedthroughs
11 high voltage instrumentation cables with joint technique.
Based on the existing calibration facilities for temperature sensors (80) and Hall plates (2) the calibration of these sensors for the TFMC will be performed within this task ,too.

1. Axial and radial insulation breaks

The axial insulation break is needed to insulate all cryogenic supply lines which are on ground potential from the high voltage potential of the winding (Fig. 1). Since the pancakes or layers are cooled in parallel for reducing the pressure drop a larger number of them is needed for every forced flow cooled coil.

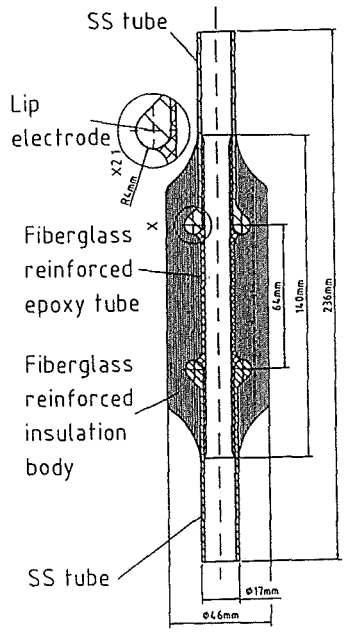

Fig. 1: Cross-section of the axial insulation break.

The radial insulation break is needed for insulating and supporting the conductor end of the winding in the terminal against ground (Fig. 2).

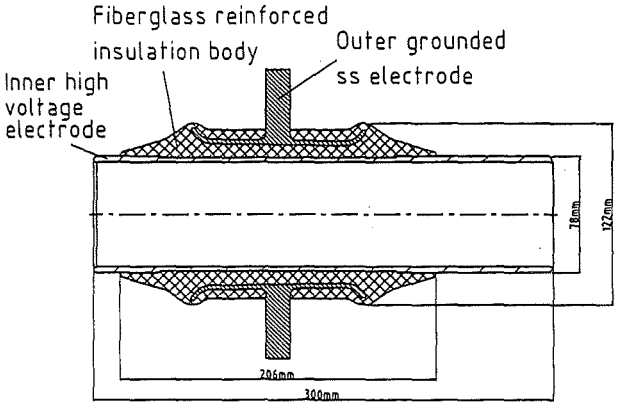

Fig. 2: Cross-section of the radial insulation break.

Both insulation breaks have to withstand the hydraulic pressure and the high voltage during all operation modes. They have to remain leak tight against vacuum over the life time of the coil.

The tube ends of the helium supply on grounded and high voltage side have to be surrounded by the insulating material. The tube ends have to be shaped according to compatible electric field strength in the material and on the boundary surfaces for avoiding slide discharges.

The electrode material is stainless steel. The insulation material is fiberglass reinforced epoxy resin fabricated by filament winding technique. The matching of the different thermal contraction coefficients is achieved by a defined glass content.

2. Instrumentation wire feedthrough

The instrumentation wire feedthroughs are needed for bringing out the co-wound quench detection wires in the central channel of the bus bars in the bus bar terminal.

The feedthrough is designed for 20 instrumentation wires and has to be leak tight for a pressure of 30 bar (Fig. 3).

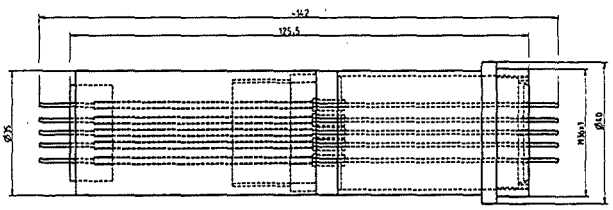

Fig. 3: Cross-section of the instrumentation wire feedthrough.

3. High voltage instrumentation cable with terminals

Instrumentation at high potential is needed for the operation of the coil like voltage taps for quench detection and temperature sensors. The voltage taps or the wires of the temperature sensors leave the winding at the conductor joints or conductor terminals. Therefore they have the high voltage potential of this location while the potential difference between the wires is usually about(<100 V). This fact leads to a cable design with twisted wire pairs surrounded by a high voltage screen, the high voltage insulation, a grounded screen and a protective low voltage insulation This construction was used for the POLO coil with PTFE (Teflon) as insulation material. A polyimid insulation

(Kapton) shall be used for the TFMC to offer the possibility to integrate the high voltage instrumentation cables in the fiberglass reinforced epoxy insulation system of the TFMC

Together with the low temperature high voltage cable also a suitable joining technique at the ends of the cable is required. One end has to be connected to the feedthrough at the cold coil and the other end at the warm vacuum vessel feedthrough. The same type of high voltage vacuum feedthrough connector will be applied as developed for the POLO coil. On the cold end side a suitable potential guiding and integration in the fiberglass reinforced epoxy insulation has to be performed. A Kapton cable test sample was proposed for testing the bonding between Kapton and epoxy resin (Fig. 4). A specification for a Kapton cable was elaborated.

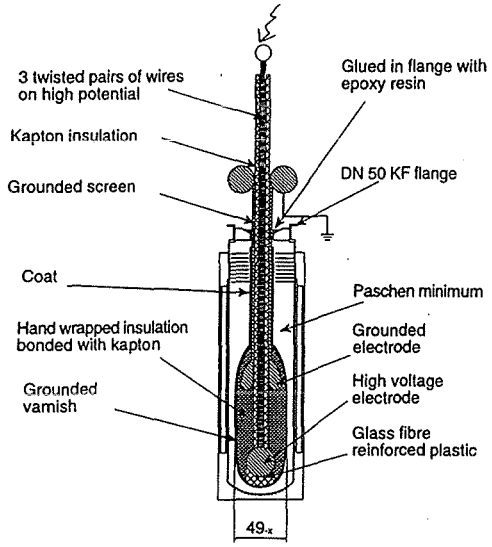

Fig. 4: Schematic view of a test sample for testing the resin bonding with Kapton in Helium at the Paschen minimum.

4. Testing of axial and radial insulation breaks and instrumentation wire feedthroughs

These components are needed in a larger quantity. Therefore well designed and prepared testing methods are indispensable. The most important aim of the testing is the confirmation of the mechanical integrity of the component under operation conditions. If the mechanical integrity is confirmed the electrical integrity is very likely according to experience gained. Therefore the high voltage tests are performed for simplification at 293 K (room temperature) in air. The test voltage applied is twice the nominal voltage accompanied by a partial discharge (PD) measurement.

Table 1: Testing of basic components, prototype and series testing

Test	Thermal cycles		Pressure cycles up to proof pressure			Leak tests at proof pressure			High voltage DC, AC (PD)		
Temperature	77 K	4 K	293 K	4 K	293 K	293 K	4 K	293 K	293 K	4 K	293 K
Component	Prototype	Series testing									
Axial break	2x	1x	5x	5x	5x	Yes	Yes	Yes	Yes	No	Yes
Radial break	2x	2x	5x	5x	5x	Yes	Yes	Yes	Yes	Yes	Yes
Feedthrough	2x	1x	5x	5x	5x	Yes	Yes	Yes	n.a.	n.a.	n.a.

The test facility for the axial insulation breaks and feedthroughs respectively, is designed for testing of eight insulation breaks or feedthroughs in one thermal cycle down to 4 K. Each specimen has its own hydraulical circuit for leak testing and pressure cycles completely separated from the other ones (Fig. 5). One test cycle with eight test objects needs about 2 weeks and 500 l liquid helium. No high voltage test can be performed in this facility.

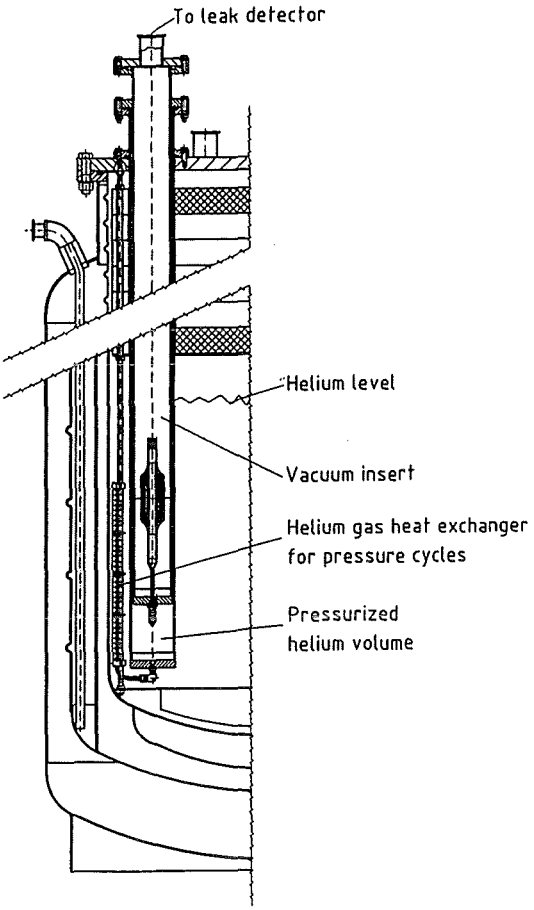

Fig. 5: The test facility for the axial insulation breaks or feedthroughs. Eight specimens can be tested in one thermal cycle. Each specimen has its own hydraulic circuit independent from the other ones.

The radial insulation breaks are tested in an other facility (Fig.6). Only one object can be tested in one thermal cycle. The facility is suitable for thermohydraulic and electrical tests at 4 K but not in one thermal cycle. Only the relatively small volume is filled with liquid helium in order to test the pressure loading in the correct pressure direction. The measurement of specified leak rate of 10^{-8} mbar•l/s cannot be achieved caused by He diffusity of the O-ring seals at the cryostat lid which lead to a background in 10^{-4} - 10^{-6} mbar•l/s range. Therefore a guard vacuum cap has to be welded over the outer part for leak testing. The radial insulation break welded in the test flange is shown in Fig. 7.

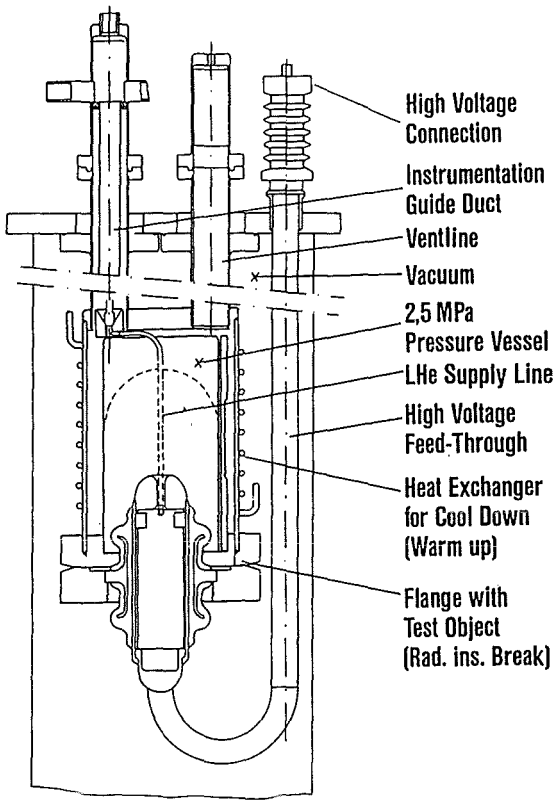

Fig. 6: The test facility for the radial insulation break for leak testing and high voltage tests.

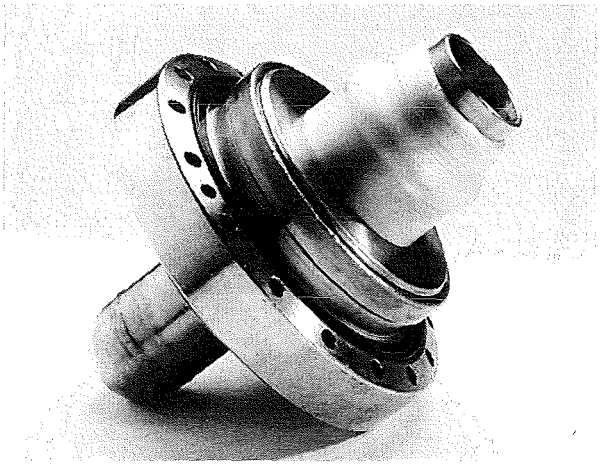

Fig. 7: Radial insulation break welded in the test flange.

The radial insulation breaks were electron beam welded in an eccentric flange after the testing (Fig. 8). In order to assure the tightness of the weld seam, the insulation breaks were exposed again a thermal cycle down to liquid nitrogen temperature and then leak tested atmospheric pressure against vacuum.

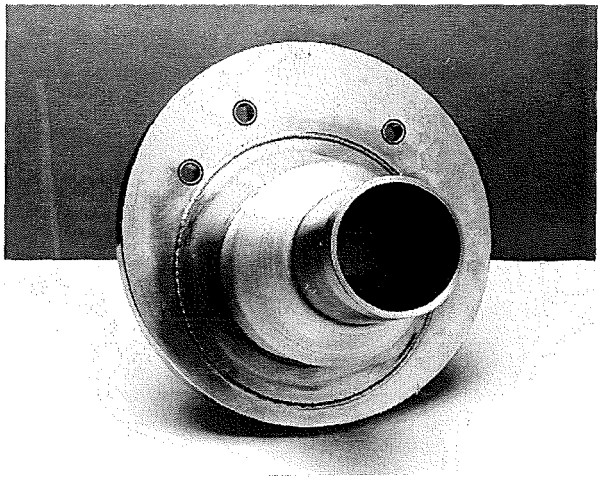

Fig. 8: Radial insulation break welded by electron beam welding in the eccentric flange.

21 axial insulation and breaks 3 radial were tested and delivered up to now to AGAN (Alstom).

5. Testing of a Kapton cable sample

A test arrangement was proposed (Fig. 4) to examine the bond between the present available Kapton dummy cable and the epoxy resin insulation used by AGAN. Alstom delivered a similar test sample (without grounded electrodes). The Kapton cable is glued in a flange that is mounted on a cryostat. So at the room temperature side it is possible to connect the copper wires of the dummy cable with high voltage. At the cold side the cable ends at a high voltage electrode which was surrounded by the epoxy resign insulation. The insulation of the cable and the epoxy resin part is covered by a screen or a conductive paint connected with ground potential. After a high voltage test at room temperature the sample was cooled down. Several high voltage tests were performed varying the pressure of the helium gas in the cryostat between $2.2 \cdot 10^{-2}$ mbar and 1000 mbar abs. The temperature was between 93 K and 154 K depending on the pressure. The test showed that the sample withstood 10 kV_{rms} and that the bond (Kapton - fiberglass reinforced epoxy resin) remained stable. The unusual high partial discharge was explained by a relatively large void inside the hand wrapped fiberglass reinforced epoxy resin. This led to a breakthrough channel in the epoxy hand wrap from the terminal electrode to the conductive coating at ground potential on the outside.

6. Summary

- The present state of high voltage component fabrication looks like follows:

Compo-nent	To-tal	In fabri-cation	On stock	In test	Tested	Deliv-ered	Note
Axial break	30	finished	9	-	-	21	2 spare parts
Radial break	3	finished	-	-	-	3	1 spare part
Feed-throughs	3	finished	1	-	2	-	-
Instrumen-tation cable	11 X 10 m						Specification ready, cable ordered
Connectors	11						Not yet started

The fabrication and delivery of insulation breaks and feed-throughs is compatible with the TFMC fabrication progress. For the instrumentation cable the alternate design has to be elaborated to start with the fabrication of parts.

- 80 TVO temperature sensors were delivered by AGAN (Noell) for calibration July 16, 1998 and given back calibrated at September 17, 1998. Hall plates for calibration were not delivered up to now by AGAN.

Literature:

[1] K. Bauer, S. Fink, A. Völker, A. Ulbricht, F. Wüchner, V. Zwecker, High voltage component delivery and sensor calibration for the ITER TF model coil, Contract ERB 5004 CT 97 0009 (NET/96-438), Intermediate report July 30, 1998, Interner Bericht F130.0026.012/B, Forschungszentrum Karlsruhe, July 1998

[2] K. Bauer, S. Fink, G. Friesinger, A. Ulbricht, F. Wüchner, The lelectrical insulation system of a forced flow cooled superconducting magnet, accepted for publication in Cryogenics, September 1998

Staff:

K. Bauer
S. Fink
M. Süßer
H.-J. Spiegel
A. Ulbricht
A. Völker
F. Wüchner
V. Zwecker

ERB 5004 CT 970037 (NET/97-450)
ITER Tritium Plant Engineering Design

Within the frame of the Engineering Design Activity Phase of ITER a concept for an Automated Control System (ACS) for the Tritium Plant has been defined. This design has been fully adopted by ITER and incorporated into the Design Description Document (DDD).

A detailed cost estimation has also been carried out and submitted to ITER. The cost estimation was based on the DDD's of seven tritium processing systems. Basic relevant data were also obtained from the TLK facilities

- CAPRICE for plasma exhaust clean-up
- Tritium Storage for fuel storage and handling and
- Central Process Control System.

More recently, proposals concerning the sequence and co-ordination of future activities during the construction phase of ITER have been made. Fundamental aspects that need to be met during plant design and construction as well as during the definition of specifications have been addressed. Attention was drawn to the problems that may arise at the interface process ACS and solutions are proposed [1].

[1] Process Control System Concept for the ITER Tritium Plant, T. Vollmer, K. Borcherding, R. - D. Penzhorn, G. Kopp, D. Murdoch, J. Koonce, Proc. 20th SOFT, Marseille, France 7-11 Sept. (1998).

Staff:

K. Borcherding
G. Kopp, Siemens
R.-D. Penzhorn
T. Vollmer

ERB 5004 CT 970082 (NET/97-458) Acceptance Tests of Strands and Sub-Stage CICC's with Respect to Heat Treatment of TFMC Pancakes

The reaction heat treatments (HT) of the pancakes of the TFMC have to be controlled by measurements on short samples co-reacted with the pancakes. At each HT two pancakes are heat treated simultaneously, that means 5 HT (DP1 to DP5) for the TFMC are necessary. A sample holder containing 10 strand samples was thermally bonded to the pancake surface of each HT. Additionally, 6 sub-stage 316L jacketed CICC's (3 x 3 x 4 strand cable) were co-reacted with the DP2 heat treatment, of what 3 CICC's have to be prepared with additional steel (added steel) after the HT representing the influence of the radial plates within the TFMC.

Furthermore, 10 strand samples and 6 sub-stage Incoloy 908 jacketed CICC's (again 3 with added steel) are foreseen for co-reaction with the Incoloy dummy pancake.

So far, the strand samples of both heat treatments DP1 and DP2 were investigated in our high field test facility (FBI). The 316L jacketed sub-stage CICC's are in preparation for testing.

At 4.2 K the critical current (I_c) versus magnetic field (B) and axial strain (ε) at B = 13 T has been measured. An I_c-criterion of 1 μV/cm was used at all tests. The I_c vs B data of 3 strand samples each from DP1 and DP2 are plotted in Table 1.

Table 1: Critical current data between 10 and 13.5 T at 4.2 K

	Critical Current (A)				
Sample	10 T	11 T	12 T	13 T	13.5 T
DP1A3a	211.9	179.5	149.8	123.0	108.1
DP1A5b	222.1	189.1	160.1	131.5	115.8
DP1A6a	215.2	179.3	149.0	123.3	108.9
DP2C3a	215.4	182.1	152.1	124.5	110.6
DP2C4a	213.6	183.6	154.2	126.0	111.7
DP2C5a	217.2	182.9	153.7	125.1	110.6
Aver.DP	215.9	182.3	153.2	125.6	111.0
Aver.M27	224.5	186.7	156.6	126.9	110.3

The average I_c values (Aver. DP) of these measurements are compared with those data obtained from the former ITER Task No. NIITT45, GB5-M27 (Aver. M27), shown in Table 1 and Fig. 1 respectively.

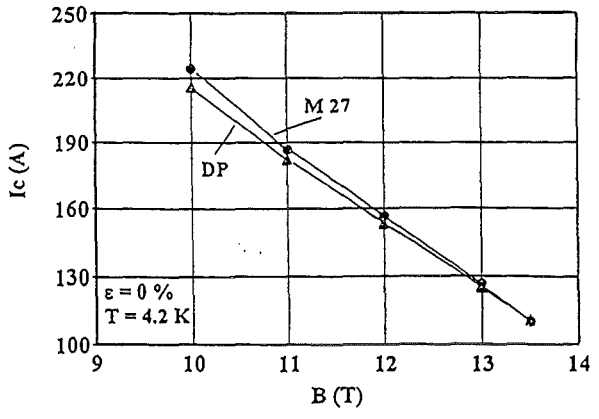

Fig. 1: Comparison of average I_c vs B data between these (DP) and former tests (M 27).

The Nb_3Sn strands (LMI) tested and the nominal heat treatment time and temperature are comparable of both tasks, but the heat treatments are carried out at different ovens. While the high field values are the same of both curves, the low field ones are considerably lower for the DP curve (Fig. 1).This may be an indication of a higher reaction temperature of the DP samples (due to temperature inhomogenities within this oven) with respect to the M27 ones.

The typical strain dependance of the critical current measured at 13 T and 4.2 K is presented in Fig. 2. After loading to ε = 0.55 % (run 19) and the following unloading to the plastic strain of ε = 0.32 % (run 20) I_c behaves reversible.

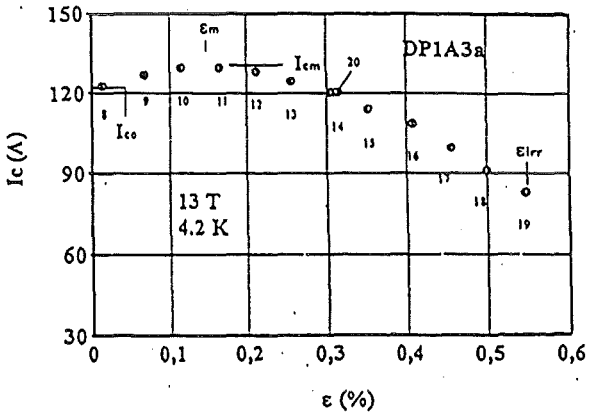

Fig. 2: Strain dependance of critical current of sample DP1A3a reacted with DP1.

The characreristc data of the I_c vs ε curves are (Fig. 2) :

- Critical current at ε = 0 %, I_{co}
- Max. crit. current at $\varepsilon = \varepsilon_m$, I_{cm}
- Strain at I_{cm}, ε_m
- Irreversible strain, ε_{irr}

These data of all samples measured are summarized in Table 2, including the average data of these tests (Aver. DP) and those of the former investigations (Aver. M 27).

Table 2: Characteristic crit. current and strain data of I_c vs ε measurements at 13 T and 4.2 K.

Sample	I_{co}(A)	I_{cm}(A)	ε_m(%)	ε_{irr}(%)
DP1A3a	122.0	130.0	0.15	≥ 0.55
DP1A5b	130.8	135.0	0.12	≥ 0.50
DP1A6a	122.3	130.0	0.16	≥ 0.62
DP2C3a	124.0	130.0	0.15	≥ 0.46
DP2C4a	125.0	132.0	0.16	≥ 0.55
DP2C5a	124.0	135.0	0.17	≥ 0.54
Aver.DP	124.7	132.0	0.15	≥ 0.54
Aver.M27	127.8	135.9	0.14	≥ 0.52

The I_c vs ε results of these tests are the same as the former ones. Furthermore, a comparison of both data of the I_c vs B and I_c vs ε tests between the DP1 and DP2 samples show no significant scattering. That means the failure of the oven during the reaction of DP2 at reaction temperature seems not to have a negative effect on these data.

Staff:

H.Kiesel
W.Specking

ERB 5004 CT 970099 (NET/97-459) Design and Related Analyses of the ITER Breeding Blanket

In the frame of the Reference ITER Breeding Blanket Design, a series of activities have been performed at the FZK with the scope of enlarge and assess the data base for the beryllium pebble beds.

The heat transfer parameters (i.e. thermal conductivity and heat transfer coefficient) of the binary beryllium pebble bed have been obtained and correlated as a function of temperature and of the interference between bed and constraining walls, due to the differential thermal expansion [1]. The correlations allow an easy application for the calculations in the blanket.

The equation correlating the experimental results for the thermal conductivity and suggested for ITER design purposes is:

$$k[W/mK] = (7.3145 + 1.00652 \cdot 10^{-4} \cdot T_m) \cdot \left(1 + 7.259 \cdot \frac{\Delta\ell}{\ell}[\%]\right)$$

The equation correlating the experimental results for the heat transfer coefficient and suggested for ITER design purposes is:

$$\alpha[W/cm^2K] = 6.138 \cdot 10^{-2} \cdot f \cdot \exp(0.0035332 \cdot T_w)$$

with:

$$f = 4.023 + 54.63 \cdot \frac{\Delta\ell}{\ell}[\%] \qquad for \quad \frac{\Delta\ell}{\ell} \geq 0.015$$

and

$$f = 1 \qquad for \quad \frac{\Delta\ell}{\ell}[\%] < 0.015\%$$

In case of $\Delta\ell/\ell = 0$ the experimental results for the temperature dependence of k and α are valid for T_m and T_w in the temperature range 130°C-600 °C. The values for the case of $\Delta\ell/\ell > 0$ are measured in the temperature range between 10° C and 160° C and are valid for $\Delta\ell/\ell$ [%] in the range 0-0.1 %.

To confirm assumptions about the electrical resistivity of the beryllium pebble bed in the course of the electromagnetic analyses for the Reference ITER Breeding Blanket, this property has been also investigated [2].

The measurements so far performed at room temperature show that in case of the single size 2 mm pebble bed, the resistivity of the bed decreases drastically to about 10^{-4} Ωm by applying an external pressure. After this first drop, the resistivity shows an almost linear decrease with the applied pressure. The same trend appears for the single size 0.1-0.2 mm pebble bed, but the resistivity values are about one order of magnitude higher than in the case of 2 mm pebbles. At room temperature, the lowest resistivity values were found for the case of a binary pebble bed (pebble diameter Φ= 0.1-0.2 mm and Φ= 2 mm) as shown in Fig. 1.

Tritium and helium gas-release behavior is a complex function of both temperature and time at temperature. Helium release data are available for fully dense Be samples irradiated in the EBR-II to a fast neutron fluence ($E_n > 0.1$ MeV) of about $6x10^{22}$ cm^{-2} and than annealed at temperatures from 450 °C to 1200 °C [3,4]. In general, no measurable tritium and helium release is observed from the specimens annealed to temperatures of 600 °C and lower. Although tritium is released from the specimen at 700 °C, no helium release is observed, probably because of insufficient detection sensitivity in the QMS analysis setup. A direct comparison of the tritium and helium gas release behavior is shown in Fig. 2, for specimens annealed up to 1200 °C. A sharp gas-burst release peak is observed in the case of samples heated on a segmented ramp to an anneal temperature of 1200 °C. Hence the quality of the QMS data are not as good as the tritium data, however the results are unambiguous that both tritium and ^{4}He are released concurrently from the heated specimens during the burst-release phenomenon. One infers from this result that the tritium and helium reside in common bubbles in the irradiated material.

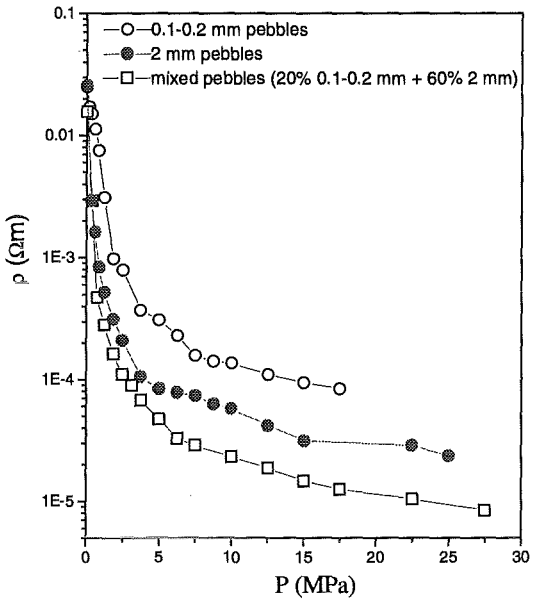

Fig. 1: Electrical resistivity as a function of pressure at room temperature [2].

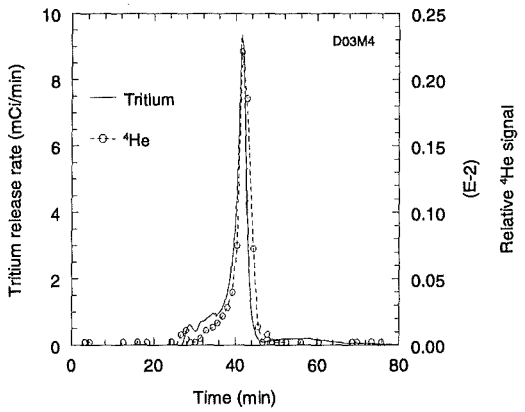

Fig. 2: Comparison of tritium release rates measured with the in-line ion chamber with ^{4}He release rates measured with the quadrupole mass spectrometer (QMS) for Be specimen annealed to 1200 °C [3,4].

In Figure 3 low temperature swelling data are plotted as a function of He content and compared with both Billone's correlation [5] and ANFIBE predictions [6,7].

At irradiation temperature lower than 100 °C Billone's correlation and ANFIBE predictions are in very good agreement, and both match very well the experimental results. At T=350 °C the Billone's correlation tends to underpredict some experimental data, thus the use of ANFIBE predictions is an upper bound to Billone correlation. The validity of the comparison depends essentially on the relevance of the He measurements in the samples after post-irradiation examinations to the He contained in the specimens during irradiation.

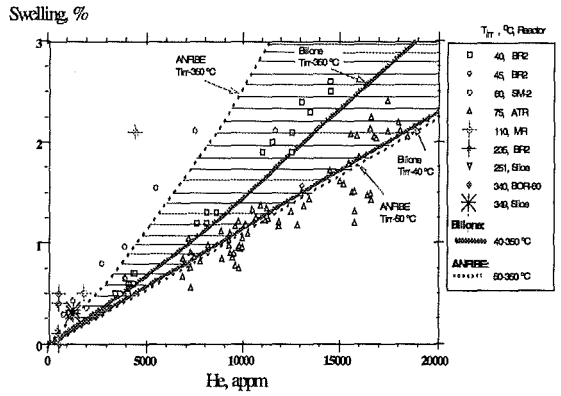

Fig. 3: Low temperature Be swelling as a function of He content.

Clearly, what is needed for validation of correlations/code predictions for ITER application is a set of data for Be irradiated at temperatures from 400-600 °C with well characterized He content in the range 3000-9000 appm.

However, very accurate post irradiation examinations (PIE) of well characterized beryllium pebbles irradiated in the EBR II fast reactor at neutron fluences of 2700-3700 appm helium and at 390°C have been recently performed [8]. Density measurements on 3-mm FRP pebbles irradiated at 390 °C under a fast neutron fluences of about 1.6×10^{22} cm^2 ($E_n > 1$ MeV) and with a helium content of 3595 appm [8] following irradiation gives $\rho = 1.795 \pm 0.011$ g/cm^3 and prior to irradiation $\rho_0 = 1.810 \pm 0.033$ g/cm.

$(\rho_0 - \rho)/\rho_0$ is 0.83%, smaller in magnitude than the sample-to-sample variability for the unirradiated density (1.86%) but similar to the variability in the irradiated samples (0.6%). The bubbles size ranges in diameter from 5 to 25 nm, with a mean diameter of 11.9 nm at a number density of 2.0×10^{16} cm^{-3}. The bubble shape is flattened, with an aspect ratio for thickness to diameter of about 0.16. On the basis of the bubble size and distribution the actual volumetric swelling can be estimated at about 0.4 of the spherical value which means about 1%. Therefore, the measured density change of 0.83% appears to be due to the development of internal bubbles. This indicates that beryllium swelling under neutron irradiation is predominantly a gas-driven swelling, so that void formation from radiation damage can be neglected.

The ANFIBE calculated volumetric swelling ranges from 0.61% to 0.98% depending on both helium content and material properties. The agreement between the calculated swelling data and the experimental estimated value of 0.83% is satisfactory. On the other hand, the resultant calculated swelling by means of Billone's correletion is up to about 60% lower than that calculated with ANFIBE.

Literature:

[1] M. Dalle Donne, et al., "Measurement of the Thermal Conductivity and Heat Transfer Coefficient of a Binary Bed of Beryllium Pebbles". Proc. 3rd IEA Int. Workshop on Beryllium Technology for Fusion, Mito, October 22-24, 1997.

[2] F. Scaffidi-Argentina, et al. "Electrical and Metallographic Characterization of Beryllium Pebbles". Proc. 20th Symposium on Fusion Technology, Marseille, September 7-11, 1998.

[3] R.A. Anderl, et al., "Steam-Chemical Reactivity Experiments for Irradiated Be", ITER Task Report ITER/US/96/TE/SA-18, Chemical Reactivity Data Task S 81 TT 14, Idaho National Engineering Laboratory, October 1, 1996.

[4] R.A. Anderl, G.R. Longhurst, M.A. Oates, R.J. Pawelko, "Tritium and Helium Retention and Release from Irradiated Beryllium", Proc. 3rd IEA Int. Workshop on Beryllium Technology for Fusion, Mito, October 22-24, 1997.

[5] M.C. Billone, M. Dalle Donne, R.G. Macaulay-Newcombe, "Status of Beryllium Development for Fusion Applications", Fusion Engineering & Design 27 (1995) 179-190.

[6] F. Scaffidi-Argentina et al., "ANFIBE A Comprehensive Model for Swelling and Tritium Release from Neutron-Irradiated Beryllium-I: Theory and Model Capabilities" Fusion Technology, Volume 32, Number 2 (1997) 179-195.

[7] F. Scaffidi-Argentina et al., "ANFIBE A Comprehensive Model for Swelling and Tritium Release from Neutron-Irradiated Beryllium-II: Comparison of Model Predictions with Experimental Results" Fusion Technology, Volume 33, Number 2 (1998) 146-163.

[8] M. Dalle Donne, et al., "Behavior of Beryllium Pebbles under Irradiation". Proc. 3rd IEA Int. Workshop on Beryllium Technology for Fusion, Mito, October 22-24, 1997.

Staff:

G. Piazza
F. Scaffidi-Argentina
H. Werle

ERB 5004 CT 980021 (NET/98-433)
Definition of an ITER Primary Wall Module Medium Scale Mock-up Test Programme

As an extension of the ITER shield analysis reported in the PKF report 1996/97 this task is an investigation into the possibility of a meaningful medium-scale mock-up test.

The weighted objectives of a mock-up test are (i) achieving material-interface stress ranges comparable to those in the ITER shield; (ii) matching the stress patterns of the ITER module, i.e. producing critical stresses in similar locations and (iii) reaching interface temperatures as close to the ones in ITER as possible.

For the module, it had been shown that cyclic thermal expansion of the massive steel block is a major source of interface stresses. The view in the previous report, that thermal cycling of the mock-up back region is not a reasonable option, still holds. However, finite-element analyses have been carried out for a constant-temperature back region to explore how effective (i) a tailoring of radiation-heater power in the existing back region channels, (ii) a reversal of the flow direction in the first-wall cooling channels and (iii) the surface heating of both FW and part of the poloidal-end surface are.

Results indicate that the described largely FIWATKA-compatible conditions can indeed impose stress patterns similar to those in the ITER shield, even though stress ranges at critical locations trail by factors mostly between one and three.

With the geometry investigated differing from the latest ITER shield design, no effort was made to optimise the mock-up conditions; this step is left to the detail design of a mock-up.

B. Dolensky
S. Hermsmeyer
G. Hofmann
K. Schleisiek

ERB 5004 CT 980023 (NET/98-472) ITER Reference Breeding Blanket Design (Stage 2); Materials Assessment, Pebble Bed and Tritium Analysis

In the frame of the ITER Reference Breeding Blanket Design, several activities like the evaluation of the purge gas pressure drop in the pebble beds (ceramics and Be), the exploration of the DEM (MIMES) code capabilities, and the tritium analysis in the pebble beds (ceramics and Be) have been performed.

To reduce the tritium permeation to beryllium through the walls of the tubes, in the ceramics the velocity of flowing helium has been fixed at 25 cm/s. Consequently the velocity of the purge gas in the Be pebble beds is fixed so that there the calculated pressure drop of 2.5 kPa is the same as in the breeder material.

For the analysis of the thermal-mechanical interactions between the pebble bed and the stainless steel structure of the breeding blanket a continuous (FEM) or a discrete element approach (DEM) can be used.

The DEM approach is very interesting because of its capability to provide information on the interaction between single pebbles and on the distribution of voids in the bed, and, in close interaction with ENEA, CEA and the joint EBP/EU HT, the exploration of the capabilities of the Discrete Element Method 2-dimensional code MIMES [2] has been performed.

Experiences with the DEM have shown that the 2-dimensional approach is quite rough and, as the possibility of rearrangement of the pebbles in 2-dimensions is strongly reduced, higher stresses were calculated in comparison with a 3-dimensional approach. Unfortunately, from the numerical point of view the use of a 3-dimensional DEM code was very time-consuming because of the extremely high number of pebbles which should be considered, and is not practicable. Also a DEM/FEM coupling, as proposed at MIT, would present too high computational time as well as computational costs.

The total tritium inventory in the breeder material has been calculated according to methods described in [3].

The breeder material assumed for the ITER reference breeding blanket design [1] is lithium zirconate (Li_2ZrO_3), which is used in the form of a single size pebble bed (ϕ = 1-1.5 mm) with a packing fraction of 58.4%. The others two candidate breeder materials [1] are lithium titanate (Li_2TiO_3) and lithium silicate (Li_4SiO_4). Both breeder materials are used in the form of single size pebble beds (ϕ = 0.8-1.2 mm for the Li_2TiO_3 and ϕ = 0.25-0.63 mm for the Li_4SiO_4) with a packing fraction of 60.2% and 64% respectively. The resulting total tritium inventory is 6.7 g, 79.7 g and 146 g for Li_2ZrO_3, Li_2TiO_3 and Li_4SiO_4 respectively.

No data are presently available from in-pile tritium release experiments for beryllium. Release kinetics and total amount of released tritium from Be are determined out-of-pile by either stepped-temperature anneal or thermal ramp desorption tests. The "Beryllium" [4] as well as the EXOTIC-7 [5] experiments carried out in the HFR reactor in Petten are detailed and significant tests for investigating the tritium release kinetics in irradiated beryllium pebbles. In agreement with previous studies the release starts at about 500 ºC and achieves a maximum at about 700 °C. The equations correlating the experimental results for the tritium residence time in beryllium shown in Fig.1, are:

τ [months] $=4.226X10^{-11}$ X exp(19240/T)

for 653 K < T < 723 K

τ [months] = 0.021 X exp(4743/T)

for 723 K ≤ T < 923 K

At temperatures below about 400 °C, essentially all produced tritium is retained in beryllium.

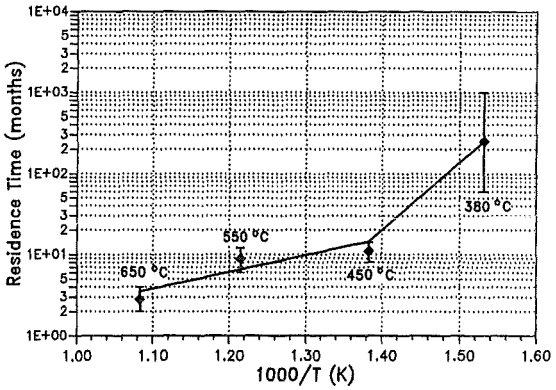

Fig. 1: Residence time vs. annealing temperature for neutron-generated tritium in beryllium [6].

Calculations of the tritium inventory remaining in the beryllium at the ITER blanket-end-of-life have been also performed. Of the total tritium produced in the blanket during its life, a tritium accumulation of a few kg is expected. According to the ANFIBE [7,8] calculations, in the case of an average neutron fluence of 1 MWy/m^2 at blanket end of life (EOL), about 1 kg of tritium will be retained in beryllium, whilst about 2.7 kg will be retained in case of an average EOL neutron fluence of 3 MWy/m^2.

Literature:

[1] K. Ioki, M. Ferrari, "ITER Design Description Document WBS 1.6B – Tritium Breeding Blanket System", Final Design Report, G 16 DDD2 98-06-10 W0.4, June 1998.

[2] J.R.Williams et al., "MIMES: user manual", Intelligent Engineering System Laboratory, MIT Boston (USA), March 1995.

[3] M. Dalle Donne, et al., "DEMO-relevant Test Blankets for NET/ITER", KfK Report 4929, Kernforschungszentrum Karlsruhe, Oct. 1991.

[4] Conrad and R. May, "Project D282.01, Beryllium, Final Irradiation Report", Report HFR/95/4262, Petten, May, 1995.

[5] R. Conrad, R. May, "EXOTIC-7, Irradiation Progress Report No. 11", Technical Memorandum HFR/95/4196, JRC Petten, April 1995.

[6] F. Scaffidi-Argentina and H. Werle, "Tritium Release from Neutron Irradiated Beryllium: Kinetics, Long-Time Annealing and Effect of Crack Formation", Proceedings of the Second IEA International Workshop on Beryllium Technology for Fusion, Jackson Lake Lodge, 1995.

[7] F. Scaffidi-Argentina et al., "ANFIBE A Comprehensive Model for Swelling and Tritium Release from Neutron-Irradiated Beryllium-I: Theory and Model Capabilities" Fusion Technology, Volume 32, Number 2 (1997) 179-195.

[8] F. Scaffidi-Argentina et al., "ANFIBE A Comprehensive Model for Swelling and Tritium Release from Neutron-Irradiated Beryllium-II: Comparison of Model Predictions with Experimental Results" Fusion Technology, Volume 33, Number 2 (1998) 146-163.

Staff:

G. Piazza
F. Scaffidi-Argentina
H. Werle

Material Assessment

For the EU-helium-cooled pebble bed blanket (HCPB) extensive calculations of relevant irradiation parameters have been performed in order to give guidance for future irradiation experiments and to illustrate how far with the existing irradiation facilities such parameters can be adapted.

For the structural material in the DEMO-breeding blanket – a ferritic martensitic steel – the number of atomic displacements per atom and per full power year (dpa/FPY) and the yearly production rates of hydrogen and helium via nuclear reactions have been calculated and are plotted in Fig. 2.

They are based on detailed Monte Carlo Neutronic Transport (MCNP)-calculations [1] and use the standard models to determine the above parameters. For this blanket configuration a maximum neutron wall load of 3,5 MW/m^2 is assumed which leads at the First Wall position to an integrated neutron flux of $1{,}25 \cdot 10^{15} n/cm^2 \cdot s$, 30 dpa/FPY, 1400 atomic ppm H and 330 appm He/FPY. The radial dependence of these parameters is very strong and reflects the reduction of neutron flux and the relative softening of the neutron spectrum.

For comparison, in a typical reactor position in the HFR-Petten where many irradiation experiments are performed an effective accumulation of 2,6 dpa/FPY is reached and the important generation rates of hydrogen and helium are much lower than under fusion neutron irradiation. The relation of these figures is not changed if in a high-flux position up to 9 dpa/FPY are accumulated, with the consequence that the correct He/dpa and H/dpa relations (11-2,75 appm He/dpa and 45-10,3 appm H/dpa) cannot be achieved. Irradiations in the core region of fast reactors may provide higher displacement rates per annum (up to 30 dpa/FPY), but the relative production rates of H and He are even lower than in the material test reactors. This confirms that a fusion-specific irradiation facility is needed in order to clarify the synergistic effect of high displacement and transmutation reactions.

Similar calculations have been performed for the ceramic breeder material Li_4SiO_4 in the HCPB-DEMO blanket. The data for the power density and other important parameters like the displacement rate and the Li-burn-up are plotted in dependence of the radial distance from the First Wall in Fig. 3.

A thermomechanical analysis has shown that for the envisaged neutron wall load of max. 3,5 MW/m^2 the limit is set by the ceramic breeder material rather than by the structural alloy. Again for the planning of future irradiation experiments in fission reactors or other facilities the above parameters like the burn-up/dpa relation should be adapted to the real situation in the fusion environment as near as possible.

Literature:

[1] U. Fischer and P. Norajitra; Neutronics and thermal mechanical analyses for design variants of the EU-helium-cooled pebble bed DEMO blanket. Proceedings 20th Soft Conference, Marseille, F, September 7-11, 1998

Staff:

E. Daum
K. Ehrlich
U. Fischer

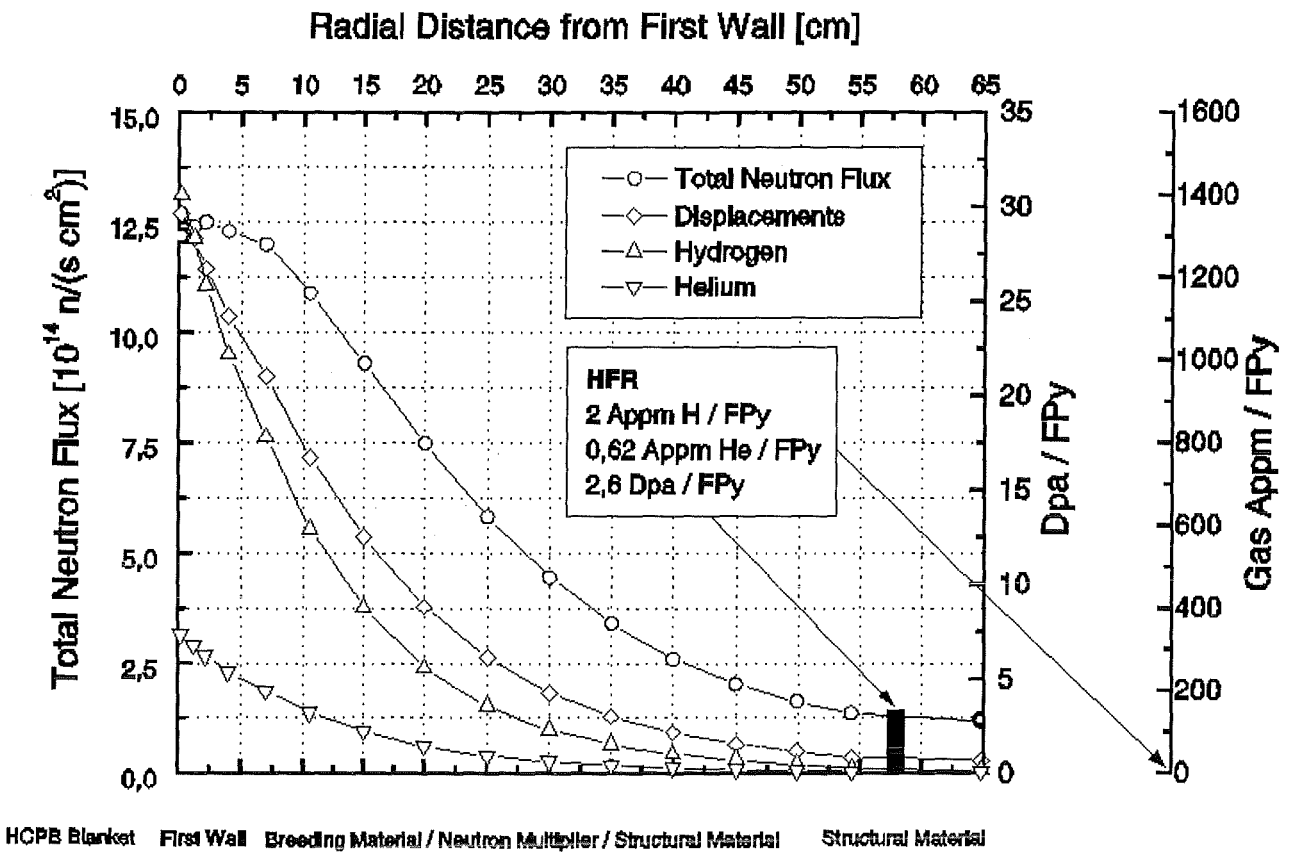

Fig. 2: Radial dependence of neutron flux and damage parameters in the HCPB-outboard breeding blanket for the structural material (Fe-base)

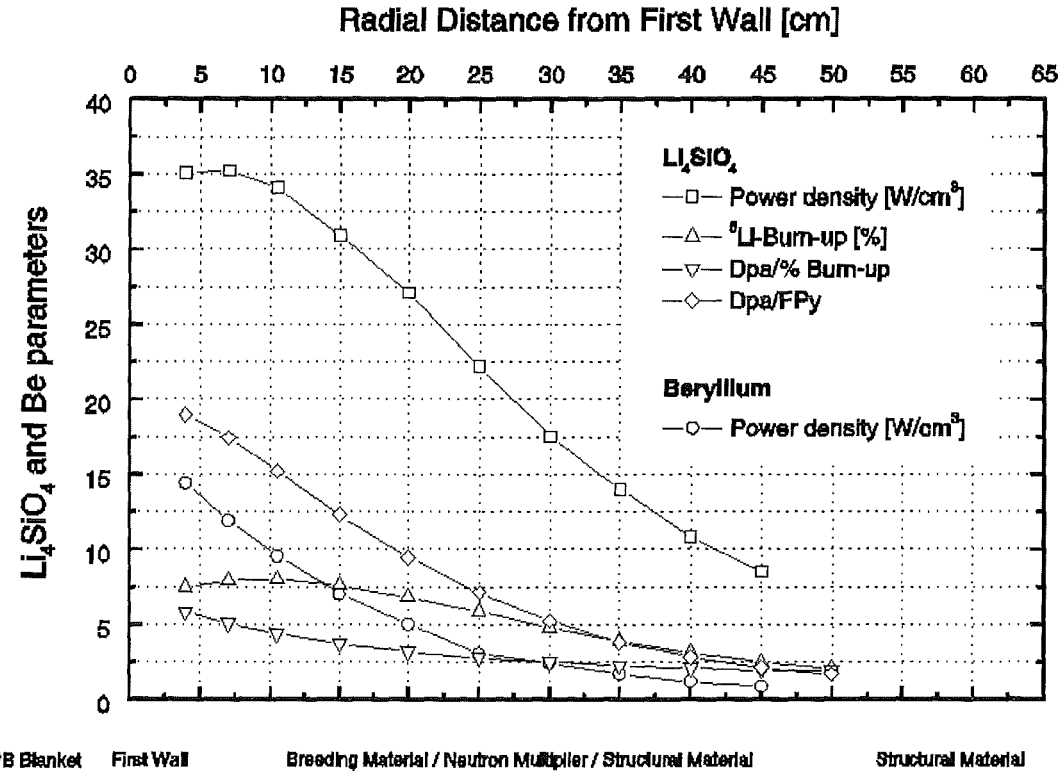

Fig. 3: Radial dependence of characteristic parameters in the HCPB-outboard breeding blanket for the ceramic breeder Li_4SiO_4 and the neutron multiplier beryllium

Long-Term Technology Programme

1. The European Blanket Project (EBP)

The European Blanket Project (EBP) was established in late 1995 and includes three subprojects covering R&D work on:

- a water-cooled lithium lead blanket (WCLL),
- a helium-cooled pebble bed blanket (HCPB), and
- structural materials (SM) for WCLL and HCPB.

At the end of 1996 a reorientation of the long-term blanket and structural materials activities within the EBP was proposed by the Commission and endorsed by the FTSC-P. The revised work programme for 1997/98 covers the period up to the end of the Fourth Framework Programme.

All three subprojects of the EBP utilize a harmonized work breakdown structure, comprising three levels: work packages, tasks, and subtasks. The contributions in this report are on the subtask level.

2 Other Long-Term Technology Activities

Besides the blanket-related tasks FZK contributes to the fields „Materials for DEMO", „Safety and Environment" and „Socio-Economics

WP B 1
DEMO Blanket Feasibility and Design

B 1.1.1
Segment Design Adaptation to New Specification

Nuclear Design Analyses for the EU HCPB Demo Blanket

The investigations have been continued to study design variants of the EU HCPB demo blanket with regard to the breeder material, the pebble bed layer height, the ^{6}Li-enrichment and the structural material. To this end, systematic neutronics analyses have been performed for the ceramics breeder materials Li_4SiO_4, Li_2ZrO_3 and Li_2TiO_3 by varying the breeder pebble bed height between 9 and 14 mm, the ^{6}Li-enrichment between 25 and 90 at%, and considering the low activation (LA) steel EUROFER as structural material [1]. The Beryllium pebble bed height and the cooling plate thickness has been kept at 45 and 8 mm, respectively. Neutronics calculations have been performed with the MCNP Monte Carlo code [2] and nuclear data from the European Fusion File EFF-1 [3] making use of the three-dimensional 11.25° torus sector model developed previously for the DEMONET configuration [4].

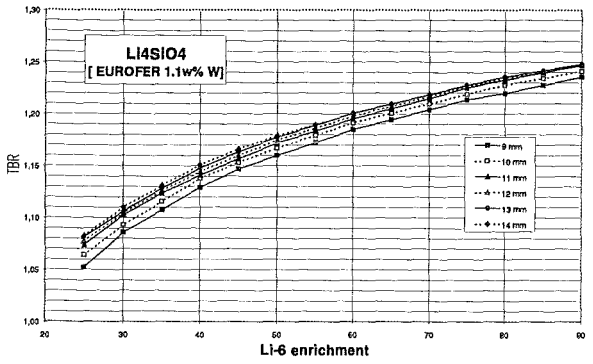

Fig. 1: Dependence of TBR on ^{6}Li-enrichment and pebble bed height for Li_2ZrO_3

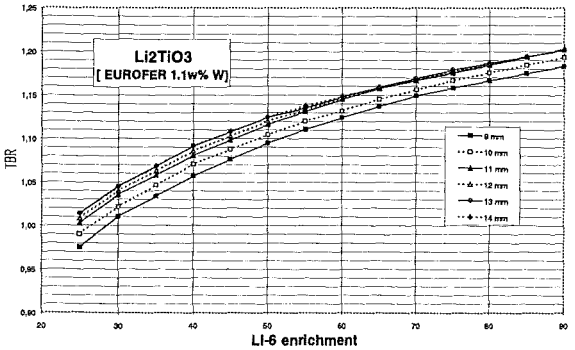

Fig. 2: Dependence of TBR on ^{6}Li-enrichment and pebble bed height for Li_2TiO_3

Results are displayed in the figures for the global tritium breeding ratio of the three breeder material variants. The dependence of the TBR on the breeder pebble bed height is rather modest while the opposite is true for the ^{6}Li-enrichment. When using the LA steel EUROFER as structural material, a ^{6}Li-enrichment is required of 35-40 at% for Li_4SiO_4, 65 -75 at% for Li_2ZrO_3 and 55-65 at% for Li_2TiO_3 to achieve at the target value for the global TBR at 1.13 to 1.14. This is required to arrive at a final TBR=1.05 when taking into account 10 blanket ports (ΔTBR $\cong$ 0.06-0.07) and the burn-up effect (ΔTBR $\cong$ 0.01-0.02 at a full power operation of 20,000 hours).

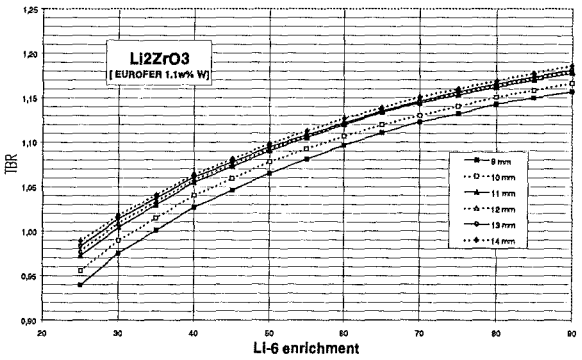

Fig. 3: Dependence of TBR on ^{6}Li-enrichment and pebble bed height for Li_2ZrO_3

The Lithium burn-up is higher for Li_2ZrO_3 and Li_2TiO_3 due to the lower Lithium number density and the required higher ^{6}Li-enrichment as compared to Li_4SiO_4. For the design variant with 9 mm breeder bed height and EUROFER structural material e. g., the maximum Lithium burn-up amounts to 9.3, 18.3 and 14.6 at% for Li_4SiO_4, Li_2ZrO_3 and Li_2TiO_3, respectively, at a full power operation of 20,000 hours .

With regard to the breeding performance it is concluded that any of the lithium ceramics investigated may be used as breeder material in the HCPB demo blanket. However, Li_2TiO_3 and Li_2ZrO_3 necessitate a higher ^{6}Li-enrichment by 20 to 35 at% as compared to Li_4SiO_4 and result in a higher Lithium burn-up by up to a factor two.

Thermal-mechanical Analyses

Thermal-mechanical calculations have been performed with the ABAQUS Finite Element code considering the 9% Cr martensitic steel T91 as blanket structural material because it has similar properties as EUROFER and has been qualified for the RCC-MR code while material data are not yet available for EUROFER [1].

New experimental data, obtained in 1997 at FZK, were used for the thermal conductivity of the Li_4SiO_4 pebble bed. The thermal conductivities and bed-to-wall heat transfer coefficients of Li_2TiO_3 and Li_2ZrO_3 as well as the bed-to-wall heat transfer coefficient of the Li_4SiO_4 pebble bed have been based on the Schluender correlations. With regard to the maximum tolerable ceramic temperature, the objective has been to keep a design limit of about 100 K below the maximum allowable temperature (to account for hot spots uncertainties) which is about 1024°C for Li_4SiO_4 [4], as dictated by the lithium partial pressure. For Li_2TiO_3 and Li_2ZrO_3, preliminary temperature limits were assumed of 1150°C and 1100°C according to ref. [5] and [6], respectively.

Table 1 shows the calculated maximum temperatures in the different materials as a function of the pebble bed height and the required ^{6}Li enrichment. The beryllium pebble bed height (45 mm) and the hydraulic values are kept constant in all cases. In the ceramic pebble bed the maximum power density decreases slightly with a larger pebble bed height while the maximum temperatures rise more strongly due to a square dependence with values lying between 879°C and 1181°C for Li_4SiO_4, 919°C and 1207°C for Li_2TiO_3 and 991 and 1318°C for Li_2ZrO_3, respectively. Considering a preliminary design limit of about 920°C for Li_4SiO_4, about 1050°C for Li_2TiO_3 and about 1000°C for Li_2ZrO_3, respectively, a layer thickness of 9 mm was found to be suitable for all the three breeding materials so that their

Table 1: Power densities and maximum temperatures for different ceramic breeder pebble bed heights at the required ^{6}Li enrichment

	Li_4SiO_4						Li_2TiO_3						Li_2ZrO_3					
Li Enrich. (at%)	40	40	40	40	40	40	65	65	60	60	55	55	75	75	70	70	65	65
h (mm)	9	10	11	12	13	14	9	10	11	12	13	14	9	10	11	12	13	14
Max. pow. density (W/cm^3)																		
Steel (FW)	25	25	25	25	25	25	25	25	25	25	25	25	25	25	25	25	25	25
Be pebble bed	14	14	14	14	14	14	14	14	14	14	14	14	14	14	14	14	14	14
Cer pebble bed	43	40	38	37	36	34	42	40	37	36	34	32	41	39	36	35	33	31
Max. temp. (°C)																		
Steel (FW)	502	502	502	502	501	501	502	502	502	502	502	502	502	502	502	502	502	502
Be pebble bed	628	630	629	629	628	628	629	630	629	629	629	629	629	630	629	630	629	629
Cer pebble bed	879	924	976	1054	1121	1181	919	963	1010	1094	1146	1207	991	1045	1096	1185	1251	1318

maximum temperatures can be kept under reasonable limits with sufficient reserve for uncertainties.

The maximum temperatures mentioned above in the case with EUROFER/T91 structure are about 10-20 K higher than those in the case with MANET structure because of the higher power densities in the ceramics resulted from the higher Li-6 enrichments required [1]. The maximum temperatures in beryllium pebble bed are about 630°C in all cases. The maximum T91 FW temperature amounts to 502°C and is smaller than that of MANET (515°C) due to the better thermal conductivity which results in moderate secondary stresses in the structures. All total stresses have been proven in detailed two and three-dimesional stress analyses to be well below the allowable limits according to the RCC-MR code assuming 8 MPa pressure in the whole blanket and a max. FW surface heat load of 0.5 MW/m².

Literature:

[1] U. Fischer, P. Norajitra: Neutronics and Thermal-mechanical Analyses for Design Variants of the EU Helium-cooled Pebble Bed Demo Blanket, Proc. 20th Symp. on Fusion Technology, Marseille, 7-11 September, 1998, pp.1149-1152

[2] J. F. Briesmeister (ed.), MCNP - A General Monte Carlo N-Particle Transport Code, Version 4A, LA-12625-M, November 1993

[3] P. Vontobel, A NJOY Generated Neutron Data Library Based on EFF-1 for the Continuous Energy Monte Carlo Code MCNP, PSI-Bericht Nr. 107, September 1991

[4] M. Dalle Donne (Comp.), European DEMO BOT Solid Breeder Blanket, Kernforschungszentrum Karlsruhe, KfK 5429, November 1994

[5] N. Roux, Compilation of Properties Data for Li2TiO3, Proceedings of the 6th International Workshop on Ceramic Breeder Blanket Interactions, p. 139, October 22-24 1997, Mito city, Japan.

[6] Prepared by D.J.Suiter, Lithium based oxide ceramics for tritium breeding applications,Report MDC E2677 UC-20, June 1983.

Staff:

U. Fischer
P. Norajitra
K. Schleisiek

WP B 2
ITER Test Blanket Module Feasibility and Design

B 2.1.1
TBM Design, Analysis and Integration in ITER

Nuclear Design Analyses

In addition to the neutronics and activation design analyses performed previously for the HCPB Blanket Test Module in ITER [1], the shielding efficiency was assessed by calculating the radiation loads to the vacuum vessel and the TF-coil adjacent to the test blanket port at the highest loaded locations.

According to the requirements specified by ITER, the test blanket system has to be designed for a total first wall neutron flux of 1 MW/m^2. With regard to shielding, the most crucial requirements refer to the reweldability of the vacuum vessel, resulting in an upper limit for the helium production of about 1 appm, and to a peak radiation dose to the electrical insulator of the toroidal field (TF) coil of $3 \cdot 10^8$ rad.

Table 1 shows the results of three-dimensional Monte Carlo shielding calculations performed for a 9 degree ITER torus sector model with horizontal outboard blanket port, support frame and integrated HCPB test blanket modules. It is concluded that the required design limits can be clearly met with the current test blanket port configuration.

Table 1: Radiation loads to the TF-coil and the vacuum vessel at a TBM first wall fluence of 1 MWa/m^2.

	HCPB TBM	Design limits
Vacuum vessel		
Helium production [appm]	0.09	1.0
TF-coil		
Peak dose to electrical insulator (Epoxy) [rad]	$9.4 \cdot 10^7$	$3 \cdot 10^8$
Peak displacement damage to copper stabiliser [dpa]	$2.2 \cdot 10^{-5}$	$6 \cdot 10^{-3}$
Peak fast neutron fluence (E>0.1 MeV) to the Nb_3Sn superconductor	$6.2 \cdot 10^{16}$	$1 \cdot 10^{19}$
Peak nuclear heating in winding pack [mWcm^{-3}]	0.03	1.0

Thermal and Mechanical Analyses

The three-dimensional thermal-mechanical analyses of the TBM, in particular for the cyclic operation of ITER, were completed [2]. They confirmed the preliminary statement that the primary stresses in the TBM are moderate, and the temperature differences cause secondary stresses, which lead to total stresses close to the allowable limit. Additional analyses are necessary on the superposition of stresses resulting from mechanical, thermal, and electromagnetic loads, on the thermal-mechanical interaction between the Be armor, the pebble beds and the steel structure, and on the stress evaluation according to design rules like ASME and RCC-MR.

Electromagnetic Analysis

The Finite Element Method program AENEAS [3], developed at FZK to study transient eddy current problems as well as magnetic fields and forces in non-linear magnetic materials [4], has been used for the electromagnetic analysis of the TBM.

1. Force Calculation

Electromagnetic force distributions have been calculated for centered disruptions (CD) with different discharge times (10ms, 25ms and 50ms) and for 50ms upward and downward vertical displacement events (VDE). Resultant forces and torques have been derived at the TBM support. Normal components of forces (F_N) and torques (T_N) for the ITER reference CD (50ms) are shown as a function of time in Fig. 1 and Fig. 2. A pulling F_N of 0.2 MN in the direction of the plasma center acts on the TBM even during normal operation. The resultant F_N of the LF distribution originating during the disruption achieves a max. value of 0.12 MN in positive (outward) normal direction, contributing to a reduction of the total F_N acting on the support. However, if we consider the spatial distribution of the forces on the TBM structure, we can observe that whereas the MFs act predominantly in the radial direction, the LFs are differently directed depending on the eddy current patterns in the structure. Therefore, during a disruption the loading of the structure can be locally (for example on the first wall) higher than during normal operation. Considering the T_N we note that the only significant contribution is given from the LF (max. 0.8 MNm). For faster CDs (10ms and 25ms), analogous behaviours with increasing peak values are obtained for F_N and T_N given by LF contribution (respectively 0.26 MN and 1.75 MNm for a 10ms CD).

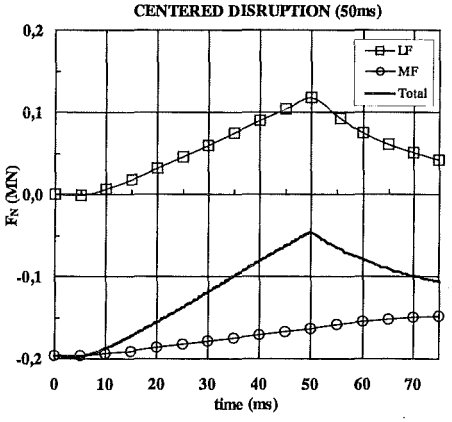

Fig. 1: Normal component of the resultant force acting on the TBM support. Magnetization (MF) and Lorentz (LF) contributions are also shown.

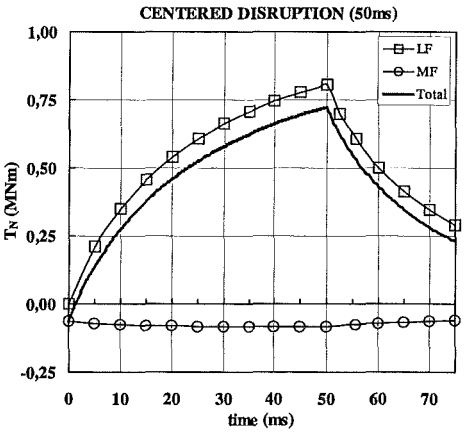

Fig. 2: Normal component of the resultant torque acting on the TBM support. Magnetization (MF) and Lorentz (LF) contributions are also shown.

The effect of the magnetization on the LF (stronger magnetic flux density) has been evaluated carrying out the same electromagnetic analyses for a nonmagnetic structural material. For the reference CD (50ms) peak values of the LF contribution have been calculated as F_N=0.07 MN and T_N=0.65 MNm. Upward and downward VDE have been also analysed, but from Table 2 - showing the maximum values of the total resultant forces and torques acting on the support for the reference CD (50ms) and upward and downward VDEs - it is evident that the most critical event for the TBM is represented by a centered plasma disruption.

Table 2: Maximum Values for reference plasma disruption events.

Max Values	F_N (MN)	$\|F_T\|$ (MN)	T_N (MNm)	$\|T_T\|$ (MNm)
CD (50ms)	**-0.20**	**1.14**	**0.72**	**0.32**
Up. VDE (50ms)	**-0.20**	0.08	0.47	0.25
Down. VDE (50ms)	**-0.20**	0.12	0.49	0.22

For the normal components also the direction is indicated whereas for the tangential components only the magnitudes are presented.

2. Error Field Calculation

The magnetic field produced by the magnetized matter of the TBM (error field) has been calculated to evaluate the effect of the TBMs on the toroidal magnetic field in the plasma region. Fig. 3 shows the magnitude of the error field as a function of the toroidal angle in the plane Z=1.7m and for different radius values. The solid curve corresponds to a circle taken around the outer edge of the plasma (R=10.947m). Toroidal magnetic field ripple values δ_{Fe} for the same have been calculated following [5]. At R=10.947m results $\delta_{Fe} \cong 0.85\%$, but it can be observed that near the module, δ_{Fe} changes very rapidly with R. Changes in δ_{Fe} have also been obtained by varying the Z coordinate.

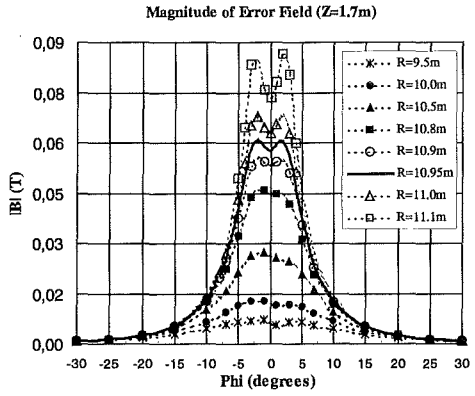

Fig. 3: Magnitude of the error field as a function of the toroidal angle in the plane Z=1.7m and for different R near the TBMs.

Design Studies

The design of the TBM has been revised taking into account the results of the manufacturing tests (see subtask B 3.1.1) and of the thermal-mechanical analyses. The modifications concern mainly the height of the pebble beds (ceramic breeder: 15 mm, beryllium: 53 mm), the caps, and the manifolds (see Fig. 4). The manufacturing route of the TBM has been adjusted to the revised design.

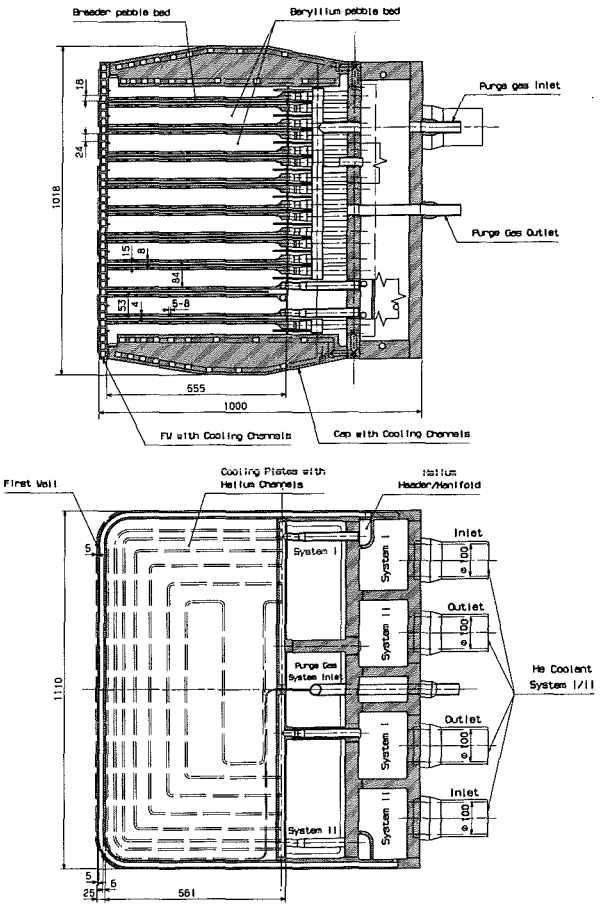

Fig. 4: Vertical and horizontal cross section of the HCPB-TBM

Literature:

[1] U. Fischer, H. Tsige-Tamirat: Neutronic and Activation Analysis of the EU HCPB Test Blanket Module in ITER, Proc. 20th Symp. On Fusion Technology, Marseille, 7-11 September, 1998, pp. 1157-1160.

[2] M. Lenartz, S. Hermsmeyer, K. Schleisiek, I. Schmuck: Thermal-mechanical Analysis of the European HCPB ITER Test Blanket Module. Proc. 20th Symp. On Fusion Technology, Marseille 7-11, September 1998, pp. 1373-1376

[3] P. Ruatto, "Entwicklung einer Methode zur Berechnung der Elektromagnetischen Kräfte durch Magnetfeldänderungen in ferromagnetischen Strukturen", Karlsruhe, FZK, FZKA 5683, 1996.

[4] L.V. Boccaccini. and P. Ruatto, "Effect of the presence of ferromagnetic structural material on the DEMO Helium Cooled Pebble Bed Blanket during plasma disruptions", in Proc. of the 19th SOFT Conference, Lisboa, 1996, pp.1519-1522.

[5] N. Doinikov et al., "Analysis of the main field disturbance sources and tentative analysis of the correction system. (Design Task D-324-3)", ITER Report, 1996,pp.37-42

Staff:

L. Boccaccini
H.J. Fiek, Fa. TWK
U. Fischer
S. Gordeev
S. Hermsmeyer
T. Lechler
M. Lenartz
P. Ruatto
K. Schleisiek
I. Schmuck
H. Tsige-Tamirat

B 2.2.1
TBM Ancillary, Equipment Design

The design work on the Tritium Extraction System and on the Coolant Purification System prepared for the ITER Design Description Document [1] has been completed by

- an estimation of the space requirements which included a proposal for an arrangement of the two systems in the same room,
- a three-dimensional layout of the systems which are shown in the following figures.

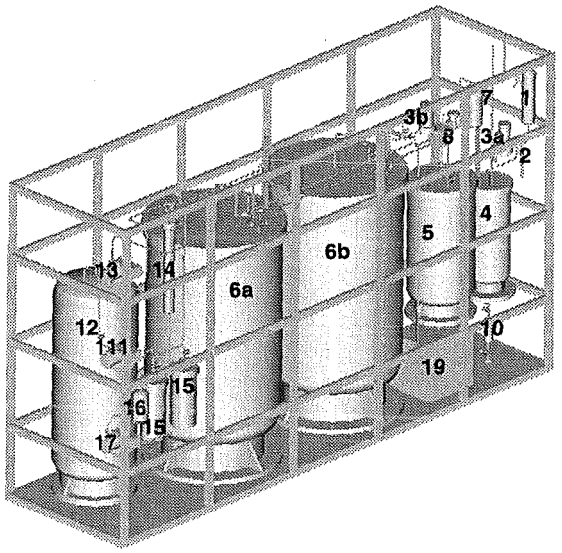

1	Cooler	10	Water Collector
2	Filter	11/13/17	Blower
3a/b	Tritium Monitor	12	Relief Tank
4	Cold Trap	14	Diffusor
5	Recuperator	15	Getter Bed
6a/b	Low Temp. Adsorber	16	Helium Buffer Vessel
7	Heater	19	Gaschromatograph
8	Compressor		

Fig. 1: Layout of the Tritium Extraction System

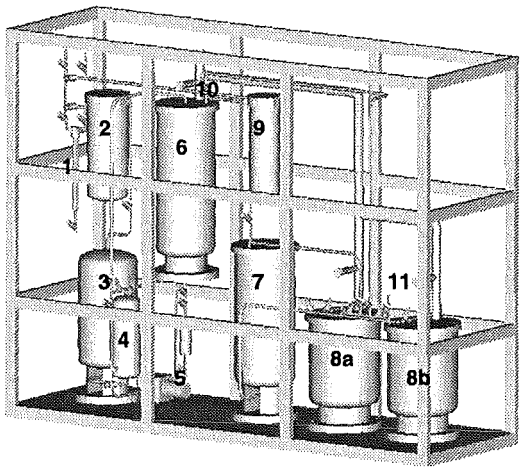

1	Water Separator	6	Cold Trap
2	Electrical Heater	7	Recuperator
3	Catalytic Oxidizer	8a/b	Low Temp. Adsorber
4	Cooler	9	Electric Heater
5	Blower	10/11	Relief Valves

Fig. 2: Layout of the Coolant Purification System

The numbers of the components shown in Fig. 1 correspond with the numbers in the process flowsheet shown in the preceeding report [2]. Additonal details can be found there and in [1].

[1] European Helium Cooled Pebbel Bed (HPCB) Test Blanket, ITER Design Description Document, Status 1.7.1998, FZKA 6127, 1998

[2] Nuclear Fusion Project, Annual Report of the Association Forschungszentrum Karlsruhe / Euratom, October 1996 – September 1997, FZKA 6050, Dec. 1997

Staff:

H. Albrecht
E. Hutter

WP B 3
ITER Test Blanket Module Fabrication

B 3.1.1
Development of Fabrication Methods and Manufacturing of Mock-ups

Introduction

The design of the European Helium-Cooled Pebble Bed (HCPB) blanket (see subtasks B 1.1.1 and B 2.1.1) makes it necessary to investigate, develop and qualify fabrication and inspection techniques which enable the manufacturing and assembly of the DEMO blanket segments and in particular the test blanket module to be tested in ITER. The work of the past year was concentrated on the following four fabrication steps:

- Diffusion welding of first wall (FW) sections and cooling plates, in particular with milled grooves to produce plates with integrated cooling channels.
- Bending of the diffusion welded FW plates to obtain a section of the U-shaped segment box.
- Welding of the cooling plates to the FW at the inside of the segment box.
- Manufacturing of a semi-scale mock up.

The material used in these investigations is the ferritic-martensitic steel MANET 2.

Diffusion Welding of FW and Cooling Plates

Diffusion welding experiments on plates with internal cooling channel structures performed in a vacuum facility under axial mechanical pressure have produced promising results. However, no parts with blanket-related dimensions can as yet be welded. For this reason, tests are now being carried out in hot isostatic presses (HIP), because such plants exist in the appropriate size. Some first HIP experiments on structures of the first wall and of the cooling plates did not produce acceptable results despite the use of the same welding parameters (pressure, temperature, time) as had been employed in the mechanical press.

A second test series were conducted in two different process steps: (1) HIP diffusion welding of the specimens equipped with pressure plates and tightly encapsulated in a sheet metal enclosure. (2) Subsequent HIP welding at very high pressure (1500 bar) of one half of a specimen part each of the same specimens, but this time with open cooling channels.

Comparisons of the strength levels determined in subsequent examinations after each of the two welding steps indicated clearly improved results after the second HIP cycle; however, the desired strength goals were not reached [1].

The same procedure was employed in further tests in which specimens were encapsulated and welded at higher HIP gas pressures. Again, subsequent open HIP greatly improved strength. In a specimen plate of the first wall, the 0.2 % proof stress was determined to be 522 to 661 Mpa, and the tensile strength was seen to be 625 to 735 Mpa. These levels are within the range of the base metal. The strength levels of the cooling plate are clearly lower despite roughly the same degree of initial forming. A slight bulge in the cooling channel ribs in both types of plate is indicative of excessive gas pressure in encapsulated welding. Micrographs show an intermediate layer in the joining zone [2].

Further HIP diffusion welding tests are planned which will be carried out at a reduced pressure with plates with differently prepared joining surfaces (see below), with the addition of getter material, and the use of a different anti-stick agent in encapsulated welding.

An alternative to the two-step HIP procedure described above is the seal-welding of the joints and subsequent high-pressure HIP bonding in a single step. Two FW specimens have been manufactures applying laser and TIG welding for sealing of the ribs between the cooling channels and EB welding for the outer seals. In the latter step the joint is evacuated at the same time. Visual and ultrasonic examinations of the specimens showed satisfactory results. Destructive examinations have still to be carried out.

Besides these component related tests, a basic program is carried out in the FZK facility HIP 3000 to determine the optimum diffusion welding conditions. Before the HIP step the welding specimens are evacuated and sealed by EB welding. The quality of the diffusion weld is determined by metallographical examinations and tensile, bending and impact tests.

The following HIP conditions were applied in the tests:

surface roughness:	2 µm
temperature:	980 – 1050 °C
pressure:	500 – 1500 MPa
welding time:	3 h
post-weld heat treatment:	3h / 750 °C

The tensile and bending properties (strength, ductility) of the diffusion welded joints was in general in the range of the base material. In contrast, the impact tests did not yet yield satisfactory results.

The metallographic inspection showed at high magnification (1000 x) precipitations in the joining zone as in the component related tests described above. For more detailed investigations the AUGER scanning electron microprobe (SEM) with an internal cleavage tool was used which allows inspection of microspecimens cut by spark erosion. The first examinations showed different contaminations of the joint area (Si,K,Cl,H,O,N) with a thickness of up to 400 nm. Probably they developed during the machining and EB welding.

To reduce the possibility of contamination, the surface preparation procedure was modified: grinding was replaced by dry high-speed cutting, and a special cleaning procedure with acetone immediately before leak-tight welding. Preliminary measurements are encouraging, but further examinations are necessary to confirm this result.

Bending of FW Plates

To complement the earlier bending investigations a test series was carried out on diffusion-welded FW plates with material addition for the machining of the ribs needed for the welding of the cooling plates. The material addition to the inner wall was 15 mm which allows manufacturing of ribs of 11 mm height including some bending tolerances. For the material addition to the outer surface an optimum thickness of 6 mm was obtained. Hence, the total thickness of the plates in the final test series was 46 mm, the inner bending radius being 50 and 75 mm, respectively. The main results can be summarized as follows:

- No cracks were detected during the non-destructive and destructive examinations of the bent plates.
- The specified bending angle can be realised with a tolerance <0.5 °.

- The reduction of the cooling channel height amounts to maximum 20 % without and 14 % with filling material
- The machining of the outer surface to the final shape is possible with elementary geometries (planes, cylinders) without exceeding FW thickness variations of 0.5 mm.

Welding of Cooling Plates to the FW Box

The cooling plates separating the ceramic breeder and the beryllium pebble beds have to be joined to the bent FW box by TIG welding. Earlier tests had demonstrated the principal feasibility of this manufacturing process. As the final step of development a cooling plate of 500 x 500 mm in size was joined to a stiff U-shaped frame by fully mechanized TIG welding. The application of this procedure is necessary because the small distance of the cooling plates does not allow hand-welding. The welding was carried out by Siemens/KWU Company using a small-size torch and a CNC machine-tool with four axis of freedom [3,4]. The suitability of the equipment used was confirmed and flawless welds with the metallographical structures and mechanical properties usual for ferritic-martensitic steels were obtained. With this demonstration the development of the welding technique for joining the cooling plates and the FW has been successfully completed with the exception of a smaller torch allowing welding with cooling plate distances of <20 mm.

Manufacturing of a Semi-scale Mock-up

The manufacturing of a semi-scale mock-up is an integral demonstration of the feasibility to manufacture the structural parts of a HCPB blanket according to the reference fabrication procedure. Shape and size of the mock-up (see Fig. 1) have been selected according to the HEFUS test section described under B 3.2.1. The size is 500 x 250 x 280 mm. The FW box includes 8 cooling channels and five cooling plates which may be replaced by dummy plates. The most important manufacturing steps to be demonstrated with this mock-up are:

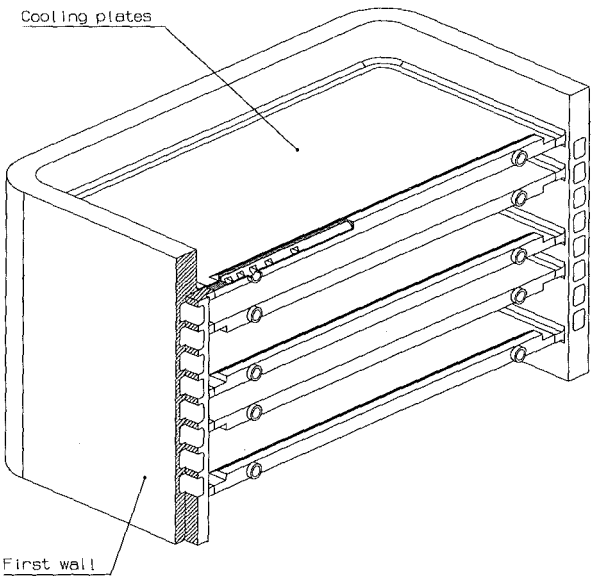

Fig. 1: Isometric view of the semi-scale mock-up

- Fabrication of a plane FW plate with integrated cooling channels according to the "grooved plate method"
- Bending of the FW plate to the U-shape of the box
- Machining of the bent FW plate to final shape including the welding ribs
- Welding of five cooling or dummy plates to the FW box.

The mock-up will be manufactured until spring 1999.

Literature:

[1] G. Reimann: Diffusionsschweißversuche zur Herstellung von Plattenbauteilen aus MANET II mit inneren Kühlkanälen für Blanketmodule, PKF-Bericht Nr.103, Februar 1998

[2] G. Reimann: Diffusionsschweißversuche in Heißisostatischen Pressen zur Herstellung von Plattenbauteilen mit inneren Kühlkanälen für Blanketmodule, PKF-Bericht Nr.115, Juni 1998

[3] Waligora: Vorversuche zum vollautomatischen Einschweißen der Kühlplatten in die U-förmig gebogene Wand des HCPB-Blankets. Siemens Arbeitsbericht Nr. KWU NW-A/97/32 (1997)

[4] Engelhard: Einschweißen einer Kühlplatte in die Erste Wand. Siemens Arbeitsbericht KWU NW-A/97/49 (1997)

Staff:

B. Dafferner
H.J. Fiek, Fa. TWK
S. Gordeev
P. Graf
J. Heger
T. Lechler
E. Nold
G. Reimann
R. Ruprecht
L. Schäfer
K. Schleisiek
L. Schmidt
P. Weimar

B 3.2.1
HEBLO Tests and Construction of Test Sections for HEBLO and HE-FUS3

1. HEBLO Test Section

The HEBLO experiments to be carried out with a small-scale test section at Forschungszentrum Karlsruhe (FZK) are an integral part of the European HCPB blanket program with the main objective to demonstrate the feasibility of the HCPB blanket construction including the testing of diffusion welds and simulating of thermocyclic load on the pebble beds.[1].

1.1 Design of the HEBLO Test section

The detailed construction of the small-scale test section for HEBLO based on the HCPB blanket concept has been completed. The central part of the HEBLO test section (Fig. 1) is of a box-like shape with a poloidal height of 84 mm, radial depth of 155 mm and a toroidal length of 233 mm. It is provided with a first wall (FW) (Pos. 1) with 1 ½ cooling channels and a cooling plate (CP) (Pos. 3) that is connected to the FW by means of TIG welding. Both FW and CP are manufactured by means of diffusion welding according to the "grooved plate method". The ceramic and beryllium pebble beds separated by the cooling plate will be heated up simulating the internal heat sources during the experiment by the electrical heating plates (Pos. 2 and 7, respectively), which are fixed at each symmetry plane of the pebble beds. A further heating plate 3 for simulation of the maximum surface heat load from the plasma (0.5 MW/m²) is fixed outside on the first wall (Pos. 5). The heating plates consist of 10 mm thick MANET plates with cut-in grooves. They contain the resistance wire heaters and the

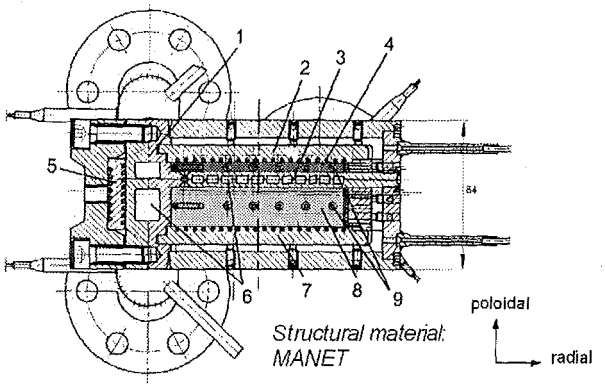

1 diffusion welded FW
2 heating plate (4 kW) for CER
3 diffusion welded cooling plate
4 CER pebble bed (Li_4SiO_4)
5 heating plate (3.6 kW) for FW
6 helium cooling channels
7 heating plate (5.4 kW) for BE
8 BE pebble bed
9 thermocouples

connections to the cold ends, which are secured by caulking.
Fig. 1: Poloidal-radial cross section of the central part of the HEBLO test section.

The pebble beds are covered by gas-permeable holding-down plates. Purge gas is supplied via two small tubes with their outlets near the FW and passed through the beds from below at slight overpressure. The two cooling channels of the first wall are entered separately by He cooling gases of 8 MPa with a temperature of about 250°C and 300°C, respectively. These two cooling gas flows are combined after having passed the FW. Subsequently, the He is passed through an external additional heater which is connected in series to the FW channels. There, the gas is heated up to about 325°C and then passed through the cooling plate. Thermocouples are installed for measurements in the beds, at the heating plates and in the cooling gas.

All components of the test section are made of the ferritic-martensitic steel MANET. Fig. 2 shows the diffusion welded components (first wall and cooling plate) and one of the optimized heating plates with a maximum power of 5.4 kW. The best diffusion welding results were achieved with precision-ground surfaces of about 2.5 µm R_t roughness at a welding temperature of 1050°C and a surface pressure of 20–25 MPa. By means of ultrasonic testing, the welds were proved to be free of defects. Each of the heating plates has been equipped with two high-temperature heaters of 2 mm in diameter and NiCr 8020 leads. They are connected in parallel and located in the grooves. The heaters are connected with the cold ends having a diameter of 4 mm via adapters fixed in the grooves on the heating plate. To improve heat transfer, the grooves are filled with a nickel-base solder by high-temperature soldering following by heat treatment at 750°C/2 h and grinding of the heater and cold end grooves to final dimension. After adjusting of the plate, positioning of the thermocouples and installation of the thermocouple and heater plugs, final electrical testing can

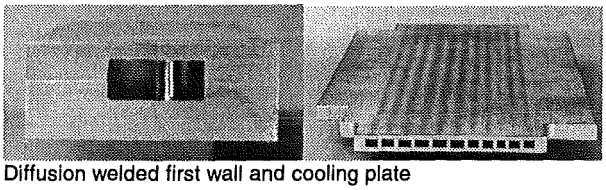

Diffusion welded first wall and cooling plate

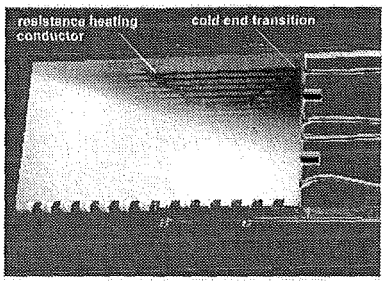

Heating plate

Fig. 2: Fabrication of the components for the HEBLO test section.

be performed.

1.2 Connection between Test Section and HEBLO

Connection with the HEBLO facility and its components made of austenitic material is ensured by flanges with special sealings. The different thermal expansions of the pipelines of HEBLO and of the test section are compensated by bellows that are pressure-tight up to 10 MPa. The test section is thermally insulated and installed into a safety tank (diameter 414 x 20 mm, length 1200 mm) designed for an internal pressure of 8 MPa. Flanges of the type MANET-stainless steel for the connection between the test section and the HEBLO facility were checked for tightness. The flanges survived about 150 thermal cycles between 270°C and 430°C at 8 MPa helium.

1.3 Modification of the HEBLO Facility

Following the modification and extension of the HEBLO facility, the entire loop system and the modified control technology was started up again and tested. The program control units and control loops for gas supply, mass flows, heating sections etc. were optimized and tested under maximum power. The temperatures required in the individual sections could be

reached. For the entire loop (without test insert), the pressure losses were determined at various mass flows in good agreement with the calculation. The current supplies and automatic control systems for the heating plates were also tested successfully.

1.4 Outlook

Preparation works for the test section including thermal-hydraulics design and adaptation, HEBLO reconstruction and recommissioning, preliminary tests and fabrication of the components have progressed well. Final assembly including the filling of the pebble beds and welding to the test insert are being performed at the moment. The safety tank is ready for use and has been accepted by the TÜV (German Technical Control Board) already.

2. HE-FUS3 Test Section

The HE-FUS3 experiments to be carried out with medium-scale test section at ENEA/Brasimone are partly integrated tests on the European HCPB blanket with the main objective to investigate the thermal and mechanical blanket behavior under steady state, cyclic power and accidental conditions.

2.1 Design of the HE-FUS3 Test Section

The preliminary planning envisages two test sections. The first test section will mainly be directed towards the investigation of the thermal-mechanical behavior of the pebble beds, whereas the second test section will preferentially serve to investigate the thermal-mechanical behavior of the blanket structures. Accordingly, main emphasis in the design and layout of the first test section will be put on the thermal design of the pebble beds; the structures will be considered only as far as it is necessary to provide the correct boundary conditions of the beds. The design of the mock-up to be tested in HE-FUS is scheduled for the second half year of 1998. ENEA is mainly responsible for this task, but some technical support by FZK is envisaged.

A general problem of out-of-pile experiments is the lack of volumetric heat sources. In the HE-FUS3 experiments it is intended to simulate these sources by heating plates (HP) located inside the pebble beds. This leads to approximately linear temperature profiles across the pebble bed height whereas in a bed with

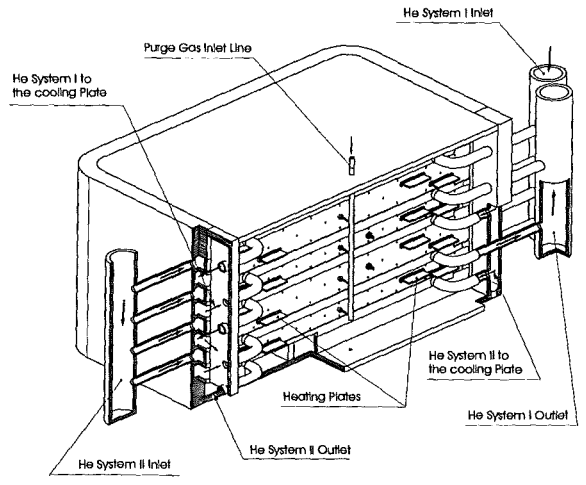

Fig. 3: Isometric view of the HE-FUS3 test section.

constant volumetric heating (and constant thermal conductivity) the temperature distribution is parabolic. To obtain nevertheless a representative temperature distribution it has been suggested to put into each pebble bed two heating plates. This leads to a trapezoidal profile with a constant temperature between the HPs (if the power of the two heaters and the temperatures of the cooling plates (CP) are identical). For the investigation of the thermal-mechanical behaviour of the pebble bed, the HPs should be positioned such that for given minimum and maximum temperatures the same average bed temperature is attained. This condition is fulfilled when the bed is split into three layers of equal thickness.

The conceptual design of the test section as proposed by FZK is shown in Fig. 3. It consists of two ceramic breeder and two beryllium beds with three sub-pebble beds and HPs each. The total poloidal height of the beds including five CPs of 8 mm thickness amounts to 200 mm. The First Wall (FW) plate has the usual thickness of 25 mm with 8 integrated cooling channels of 14 x 18 mm cross section (cooling channel pitch 24 mm).

The manufacturing of the test section box is based on the techniques being presently developed for the HCPB blanket. The main steps are:

- Diffusion welding of the FW plate according to the "grooved plate method".
- Bending of the FW plate to obtain the U-shaped box.
- Machining the U-shape FW to final dimension including the welding ribs for the CPs.
- TIG welding of the five CPs to the FW box.

Thermohydraulic and thermal-mechanical calculations have been carried out with the codes FIDAP and CATIA/ELFINI to determine the temperature and stress distribution in the test section and the deformations due to the temperature field. The analyses confirm the feasibility of the test section but some design improvements seem to be necessary.

The main conclusions derived from the work can be summarized as follows:

1. With two heating plates (HPs) in each pebble bed a reasonable approximation of the poloidal temperature distribution in pebble beds with internal power generation can be attained. However, the temperature difference across the HPs leads to a discontinuity in the upper range of the temperature field which may be of importance for the thermal-mechanical behaviour of the beds. The temperature difference in the heater is mainly determined by the thermal resistance between the insulator and the cover of the HPs. To improve the heat transfer a design is suggested which allows the ingress of helium into the gaps of the HPs. Further analyses and experimental investigations of this issue are necessary.

2. For the proposed test section design, the desirable temperature rise of 150 to 200 K requires a helium mass flow rate of 0.08 to 0.11 kg/s. With two helium systems and a one-pass flow scheme in the FW cooling channels of the FW this leads to low helium velocities and low heat transfer coefficients. If necessary, an improvement can be attained by increasing the mass flow rate (maximum value 0.15 kg/s in HE-FUS), and by a multiple-passflow scheme.

3. The temperature distribution in the test section box causes significant deformations of the structures. In particular, the FW surface heating leads to bowing of the FW. In order to obtain clean and predictable boundary conditions for the pebble beds, it is reasonable to design the test section in such a way that the FW temperatures are as

homogeneous as possible. Hence, it could be reasonable to reduce or even to omit the FW surface heating.

4. The calculated stresses in the structural material are much less than in the DEMO blanket and the ITER TBM. This does not injure the objectives of the first HE-FUS3 test section. On the other hand it shows that it will not be easy to design the second test section in view of the envisaged objective to investigate the thermal-mechanical behaviour of the blanket structure.

5. The poloidal thermal expansion of the test section structure is slightly larger than the corresponding value of the ITER-TBM. However, it must be noted that the HE-FUS value has been derived from a 2D calculation including only the front side of the FW, whereas the TBM value has been obtained in a 3D analysis closer to reality. For the final choice of the HE-FUS conditions, 3D calculations have to be carried out, too.

6. The differential expansion between the beds and the structure ("interference") is sufficiently high to cause mechanical interactions and thermal creep in particular in the high temperature region of the breeder pebble bed which is one of the test objectives.

7. The differential thermal expansion between the HPs in the ceramic breeder pebble beds and the test section structure causes a radial displacement of the HPs of 0.85 mm towards the FW. This means that considerable compressive forces will be exerted on the pebbles in the gap between the HPs and the test section box which can cause pebble deformation and cracking in particular during cyclic operation. An improvement of the design is necessary to eliminate this problem.

2.2 Development of Plate-type Surface Heaters

Due to the given thermohydraulic and heating-technical conditions in HE-FUS3, the maximum temperatures can be achieved only by changing the pebble bed heights in the planned test object in comparison to the HCPB blanket design. The above consideration for heating plate arrangement resulted in following HP number and power assuming the ceramic and beryllium pebble bed heights of 15 and 45 mm, respectively:

location	nominal dimension (rad x tor x pol) (mm x mm x mm)	nom. power (kW)	number of HPs (-)
Cer pebble bed	200 x 450 x approx. 4	10	4
Be pebble bed	200 x 450 x approx. 4	25	4
First wall	approx. 4 x 500 x 200	20	1

For the simulation of the radial power distribution, the power profiles of ceramic and beryllium pebble beds are taken into account following the ITER TBM design [2]. The following criteria were considered during heating plate design:

- The radial power profile of the heating plate is to be chosen such that the temperature distribution in the pebble bed of the test object corresponds to that in the pebble bed of DEMO; the temperature distribution is to be monotonous over the heater surface.

- The heating plates should be as thin as possible (approx. 5 mm) because of the small pebble bed height and nevertheless have a sufficient bending strength and/or inherent stability.

- Sufficient electrical insulation must be ensured even at higher temperatures.

- The cold end connections are to be arranged symmetrically in order to avoid asymmetrical loads for the heater.

- Heat transfer from the interior of the heater to the pebble bed must be as good as possible in order to prevent melting through the heater material.

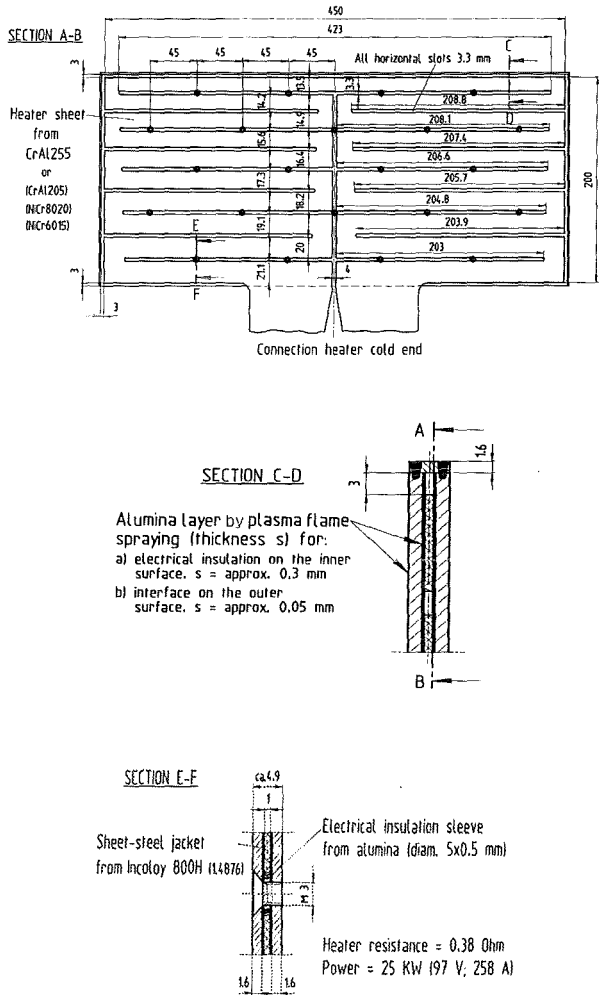

Fig. 4: Heating plate construction for HE-FUS3 test section (e.g. for beryllium pebble bed

Under the above boundary conditions and design criteria, optimization calculations were accomplished. Fig. 4 shows e.g. optimum solution of the heating plate for the beryllium pebble bed. The heaters consist of 1 mm thick MEGAPYR I material. The conductive strips are arranged in two symmetrical halves in a meander-shaped manner. The conductive strip cross section increases from the front first wall-near range towards the rear according to the power profile. The slot width between the conductive strips ranges between 3 mm (horizontal) and 4 mm (vertical). In order to avoid the danger of spark formation, a relatively small voltage of e.g. 97 V was chosen for this case. The cold end connections are arranged symmetrically in the rear range. Sheet metals of Incoloy 800 H and 1 mm in thickness at both sides and at three of the four front surfaces form the heater steel jacket. The front surface in the range of the cold ends remains open. The side steel sheets are interconnected by recessed countersunk head screws of the

size M3 such that a good heat transfer from the heater outwards is ensured (section E-F). Rings of alumina ceramic with a diameter of 5x0.5 mm and a thickness of 0.9 mm prevent an electrical contact of screws and heaters. An about 0.3 mm thick layer of oxide ceramics is provided as the electrical insulation on the inner surface of the side steel sheets. This layer is applied by plasma flame spraying (section C-D). A thinner ceramic layer made of the same oxide ceramics is sprayed onto the outer surface of the steel-jacket sheet with a view to prevent a chemical reaction between the pebble bed and the heating plate. The front lateral metal strips are connected with the side steel sheets by plasma-arc, EB or TIG pulsed welding. There is no need of this welded connection having a high tightness, since the interior of the heaters will be filled automatically with helium purging gas during the experiments. Heat transfer in all gaps of the heating plate is considerably increased by the helium inside. The space between the upper edge of the heater and the front lateral metal strips could be filled with ceramic shaped parts.

Literature:

[1] P. Norajitra, H. Lehning, D. Piel, G. Reimann, R. Ruprecht: State-of-the-art of the third heblo experiment based on the EU Helium-cooled pebble bed blanket concept, Proceedings of the 20th Symp. on Fusion Technology, Sept. 7-11, 1998, Marseille, France, Vol. 2, pp 1187-1190.

[2] Boccaccini, L.V. (Ed.) et al., "European Helium Cooled Pebble Bed (HCPB) Test Blanket. ITER Design Description Document (Status: 1.7.1998)", FZKA 6127, (1998), to be published.

Staff:

S. Gordeev
H. Lehning
P. Norajitra
D. Piel
G. Reimann
R. Ruprecht
K. Schleisiek
I. Schmuck

B 3.3.4
Help in the Detail Design of an In-pile Test Module

Within the European Blanket Program a Blanket Submodule Irradiation experiment is envisaged. Based on a first set of objectives and specifications provided by FZK, SCK/CEN Mol and ECN/JRC Petten prepared conceptual design and cost studies for the reactors BR2/Mol and HFR/Petten, respectively. The BMC discussed these proposals in Sept. 1997 and recommended, in view of the high cost, a critical review of the objectives. This was done by FZK by the end of 1997. Based on the revised specifications, FZK developed proposals for the design of the test elements. Configurations with vertical/rectangular and horizontal/circular breeder beds have been considered [1]. Preliminary analyses have shown that with both options the desired irradiation conditions can be reached. Cooling of the element with reactor water is feasible, hence a helium loop is dispensable. Based on these proposals, SCK/CEN and ECN/JRC revised their proposals. In March 1998 the detail design of the in-pile test was awarded to ECN Petten. In the meantime, the detail design work has been started with the support of FZK [2]. The design variant with the horizontal breeder pebble bed was adopted for the further design studies. A test matrix for the four test elements included in the test rig was elaborated. The detail design work is scheduled to be finished by the end of 1998.

Literature:

[1] S. Hermsmeyer , S. Malang, K. Schleisiek: Design Considerations for a HCPB Test Section for In-Pile Testing. CBBI-7, Sept. 1998, Petten/The Netherlands

[2] J.G. van der Laan, R. Conrad, K. Bakker, J.H. Fokkens, S. Hermsmeyer, S. Malang, B.J. Pijlgroms, C.M. Sciolla, R. van Tongeren, K. Schleisiek: In-Pile Testing of Submoduls for the HCPB DEMO Blanket concept in the HFR Petten. 20th SOFT, Sept. 1998, Marseille/France

Staff:

S. Hermsmeyer
S. Malang
K. Schleisiek

WP B 4
Tritium Control and Requirement for Permeation Barriers

B 4.1.1
Tritium Permeation in the TBM and DEMO

1. Tritium permeation losses from the First Wall

The permeation through the first wall has been evaluated by means of the one-dimensional computer code TMAP4 [1].

1.1 HCPB-DEMO design calculations

Main characteristics [2]:

- bare MANET First Wall (5 mm thick layer separating plasma and helium coolant channel);
- constant incident flux of $1.5x10^{20}$ ions/m^2s^{-1};
- FW permeating surface of 730 m^2 (Inboard + outboard);
- average neutron load of 0.4 MW/m^2;
- average maximal temperature in the first wall of 745 K.

Corresponding to two different grades of oxidation of the FW downstream side in the helium coolant channels, the permeation rate varies between 8.5 and 12 g/d. The two-dimensional geometry does not reduce the permeation more than 6%.

1.2 HCPB TBM-I design calculations

Main characteristics [3]:

- pulsed operation incident flux equal to $1.x10^{20}$ ions/m^2xs with 1000 s pulses and 1200 s plasma dwell time;
- 5 mm thick protective layer of beryllium for a 5 mm thick first wall of MANET;
- neutron load of 0.5 MW/m^2;
- maximal temperature in the first wall of 782 K.

A computational model has been implemented in the computer code TMAP4 to reproduce the available experimental data concerning hydrogen ion implantation in beryllium.

Experimental data [4,5,6,7] have shown that, under ITER-like plasma conditions, the plasma facing surfaces of the beryllium develop high porosity (bubbles) and saturate, leading to a strong uptake of tritium and deuterium ions almost independent of the incident flux. At fluxes typical of ITER, surface erosion of beryllium should be also taken into account.

The 5mm thick coating layer of beryllium was modelled as three segments in series [3]: 50 nm of implantation region, i.e. where most of the bubbles are; a 1 μm thick zone of damaged beryllium influenced by the bubbles and the remaining part of undisturbed beryllium. To accommodate the saturation effects on the plasma side of beryllium, the recombination coefficient has been exponentially modified, thus still allowing a recombination-like boundary condition in the TMAP4 code.

Erosion due to sputtering results in a diffusion in a moving co-ordinate system. It has been taken into account by neglecting the Soret effect for beryllium, i.e. the mass transport due to a temperature gradient. Erosion was included only in the damaged zone. The reduction of the beryllium thickness, leading to a lower inventory and higher permeation, was accounted for by an iterative procedure.

The sputter rate calculated was of $3.25x10^{10}$ m/s, i.e. 2 mm eroded beryllium after a total operational time of about 70 days. For the assumed first wall surface of 1.2 m^2 and the whole operating period, a permeation of about 0.007 g has been obtained. This very low permeation is not appreciably influenced by the use, instead of MANET, of a ferritic steel like T91.

2. Tritium permeation losses from the purge flow system

The major contribution to the permeation is represented by the tritium coming from the lithium orthosilicate beds (Li_4SiO_4), as the permeation from the beryllium bed is negligible.

Identical procedures have been applied to both DEMO and TBM-I designs [2,3]. In the DEMO design the total permeation from the purge flow system through the total permeating surface (inboard + outboard = 9120 m^2) was of 0.78 g/d. The smaller tritium production and the lower wall temperatures in the TBM-I lead, for a total permeating surface of about 10 m^2, to a tritium permeation not greater than 0.3 mg/d.

3. Conclusion

Table 1 summarise the results of tritium permeation calculation for DEMO and TBM-I design.

Table 1: Tritium permeation in DEMO and TBM-I

Design	First Wall	Purge gas
DEMO	8.5-12 g/d	0.8 g/d
TBM-I	< 0.1 mg/d	0.3 mg/d

With a coating layer of beryllium, the permeation through the first wall is strongly reduced. As far as the permeation is concerned, the choice of the steel to be used together with beryllium does not play an important role.

What remains to be modelled is the influence of carbon on the retention and permeation of beryllium-clad surfaces. There are no many data available about how much of the carbon that will be sputtered from high-heat-flux surfaces in the divertor will be transported to the main plasma chamber and end up on the first wall, where carbon film build-up should not be a problem. The hydrogen implantation in the first wall seems in any case to be significant at depths, that result in development of the described open porosity.

Literature:

[1] G.R. Longhurst et al., TMAP4 User's Manual, INEL, EGG-FSP-10315 (1992).

[2] L. Berardinucci, M.Dalle Donne, Proc. of 19th SOFT, Lisbon, Portugal, Sept. 16-20, (1996) 1427-1430.

[3] L. Berardinucci, Modeling of Tritium Permeation through Beryllium as Plasma Facing Material, ICFRM-8, Sendai, Japan, to be published in J.Nucl.Mat.

[4] M.I. Guseva, A. Yu Birukov, V.M. Gureev, L.S. Daneljan et al., J. Nucl. Mat., 233-235, (1996) 681-687.

[5] V.N. Chernikov, V.Kh. Alimov, A.P. Zakharov et al., J. Nucl. Mat., 233-237, (1996) 860-864.

[6] A.A. Haasz and J.W. Davis, Proc. 12th Int. Conf. On Plasma Surface Interactions in Contr. Fusion Devices, St. Raphael (1996).

[7] R.A. Causey, K.L. Wilson, Journal of Nuclear Materials, 212-215, (1994) 1436-1442

Staff:

L. Berardinucci
L.V. Boccaccini

B 4.2.1
Manufactoring of Test Section for Tritium Permeation Experiments

An important operational and safety issue for fusion reactors is the permeation of tritium through structural materials. For the HCPB blanket, tritium gets mainly to the environment by permeation from the helium coolant system through the INCOLOY 800 steam generator walls into the steam cycle. Therefore, the tritium permeation mechanisms through this material are of large interest.

The goal of the present investigations is, therefore, the development of permeation barriers by in-situ oxidation of the INCOLOY 800 surface.

Permeation experiments with INCOLOY 800 disks were performed both in JRC/Ispra and in FZK using different experimental set-ups [1]. Deuterium permeated from a high pressure gas side to a low pressure gas side. The high pressure gas contained a given amount of H_2O.

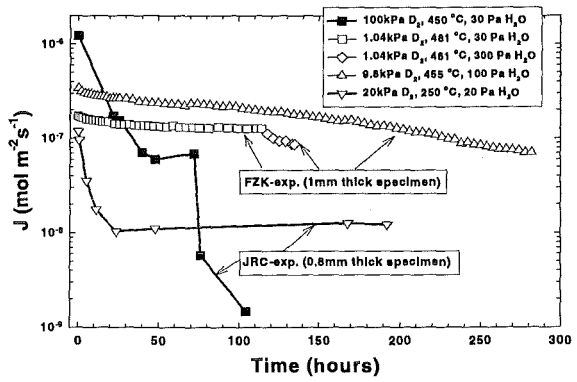

Fig. 1: Permeation rates as a function of exposure time for different H_2O to D_2 ratios at various temperatures

Figure 1 shows the time dependent permeation flux as a function of time. The Ispra data show a strong decrease after the start of the experiment whereas the FZK data exhibit only a slight decrease. The reason for these differences are different cleaning procedures for the test specimens. The important result, however, is that for all specimens after some days of operation the permeation fluxes are much lower than those for the bare material. These values (not shown in the figure) are larger by a factor of ≈ 20, and ≈ 100 for temperatures of ≈ 250 °C, and ≥ 450 °C, respectively.

The permeation reduction due to the formation of these oxide layers is sufficiently large in order to obtain a relatively small Coolant Detritiation System for a Be- or W-coated First Wall.

Literature:

[1] A. Perujo, H. Feuerstein, J. Reimann, "Tritium permeation reduction through the HCPB steam generator by in-situ oxidation", Proc. 20th Symp. on Fusion Techn., Eds.: B. Beaumont, P. Libeyre, B. de Gentile, G. Tonon; Marseille, France, 7-11 Sept. 1998, Vol. 2, 1437-1440

Staff:

Perujo (JRC/Ispra)
J. Reimann (FZK)

WP B 5
Tritium Extraction and Helium Purification

B 5.1.1
Design of Helium Purification and Tritium Extraction Systems

1. Description of the Test Facility PILATUS

In the following, the design of the test facility PILATUS (*Pi*lot-*A*nlage zur *Tri*tium *S*eparation) is decribed which will be operated in the Tritium Laboratory Karlsruhe (TLK) to test and to optimize the tritium extraction process steps for two helium loops of a solid breeder blanket, i.e. the Tritium Extraction System (TRS) and the Coolant Purification System (CPS).

An installation formerly forseen for the technical infrastructure of the lab is presently being adopted to accomodate the new facility. The installation is already furnished with all the peripheral equipment needed for a tritium facility, i.e.

- glove box including systems for pressure control and for continuous atmospheric purification;
- connection to the central supply station for helium, nitrogen, and pressurized air;
- connection to the central tritium retention system for the pumping exhaust gases;
- access to the TLK remote control and safety systems.

In addition, some components of the former installation, e.g. an evacuation system, several sections of the gas manifold, a 100 l gas buffer vessel, and a tritium storage bed (U-bed) can be employed in the new facility. A flowsheet of the PILATUS facility is shown in Figure 1.

The facility consists of several groups of components:

- Evacuation System,
- Gas Supply System for He, H_2, O_2, N_2, H_2O, and HT (the latter will be supplied from an U-bed),
- Central Loop which includes a gas buffer vessel, a gas circulator (metal bellows compressor), and the analytic instrumentation to determine gas concentrations at the inlet and outlet of the process components,
- Main process components, i.e. cold trap, cryogenic adsorber, and oxidizer,

An additional U-bed as storage bed for H_2/HT at the end of an experiment and/or after release from the adsorber bed.

Each process component is so arranged that it can be tested separately or in combination with other components. Thus, it will be possible to determine the efficiency of each component as well as of the complete processes of tritium extraction and coolant purification.

2. Description of the Main Components

2.1 Gas Supply System

The Gas Supply System has the task to simulate the solid breeder blanket as a continuously supplying source of purge gas containing helium as carrier gas plus hydrogen, tritium, and impurities like O_2 and N_2. At the beginning of a test, helium is supplied into the evacuated central loop. The other gas species are added in the concentrations mentioned in 2.5 for location A1 and later on continuously refilled according to their removal in the process components.

2.2 Cryogenic Cold Trap

A cryogenic cold trap is foreseen for the removal of Q_2O. It has been chosen instead of an adsorber bed to avoid additional purge gas for subsequent unloading (it would be again necessary to extract Q_2O from this purge gas). The trap is operated at temperatures < -100°C; at such a low temperature, the residual humidity should be less than 0.02 vpm.

An evaluation of cryogenic cold trap experiments described in the literatue [2-4] has shown, however, that it is difficult to reach

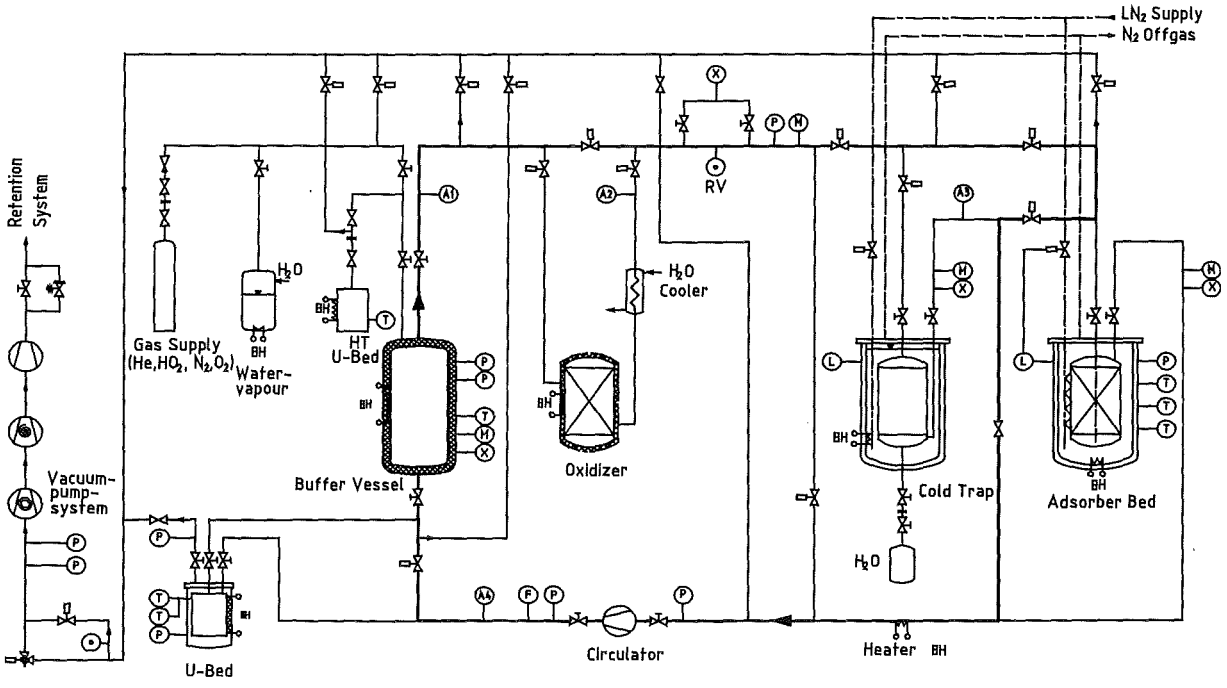

Fig. 1: Flowsheet of the PILATUS Facility

a humidity in this range. Because of spontaneous aerosol formation it can be necessarry to use a filter to trap ice particles; but small particles (≤ 1 µm) can pass through the filter, while larger particles will clogg the filter and may finally lead to an unacceptable drop of pressure.

To obtain a good removal efficiency, the formation of ice aerosol particles must be prevented; this can be done by cautious cool down, i.e. by avoiding fast under-cooling and / or critical supersaturation which is the reason for spontaneous aerosol generation.

It is currently examined, if a cryogenic cold trap designed for the removal of Xenon from the dissolver off-gas of a reprocessing plant [5] can be used to study the process of ice formation. The cold trap available from FZJ Jülich is equipped with two windows for this purpose.

Some Design Parameters of the FZJ Cold Trap	
Throughput:	≤ 10 Nm^3/h
Gas pressure:	1 – 8 bar
Freezing area:	1.3 m^2
Volume of the freezing zone:	35 l
Gas velocity (cooling channel)	≤ 8 cm/s
Temperature (controlled profile):	80 – 120 K
Diameter:	424 mm
Height:	786 mm
Heater power:	300 W

2.3 Cryogenic Adsorber

The cryogenic adsorber is a 5A molecular sieve bed cooled with liquid nitrogen. Its main task is the removal of the hydrogen isotopes from the purge gas; however, gaseous impurities like nitrogen or oxygen, and residual moisture are retained as well. The bed contains filters at the down-stream and upstream side to prevent particulate material from being transferred during loading or unloading operations. In addition, the bed is equipped with an electrical heater. At the end of an adsorption test, the bed is only slightly warmed up to -150°C. At this temperature, the hydrogen isotopes will desorb almost quantitatively, while oxygen and nitrogen will remain adsorbed. The released H_2/HT is stored in the U-bed. Removal of N_2 and O_2 is obtained by warm-up to room temperature, and a complete regeneration of the adsorber bed is performed at 300°C. In both cases, the desorbing gases are sent to the Central Tritium Retention System of the TLK.

2. Catalytic Oxidizer

The catalytic oxidizer is used to convert the hydrogen isotopes Q_2 to Q_2O at a temperature of about 300°C. The unit contains a precious metal catalyst (Pt or Pd on aluminia). An over-stoichiometric amount of oxygen is added to obtain a quantitative conversion. It will be tried to minimize the amount of water that will be retained on the catalyst due to its hygroscopic property. This will be done by employing different types of catalyst materials as well as by optimizing the size and the temperature of the bed.

The hot gas leaving the oxidizer is cooled again to room temperature by a water cooler installed downstream of the oxidizer unit.

2.5 Analytic Instrumentation

The design and operation of the analytic instrumentation is a challenging task for two reasons:

a) For each process component, the inlet and the outlet concentrations of the relevant gas constituents have to be determined accurately to quantify the efficiency of the various process steps;

b) As it is foreseen to have a constant gas mixture in the buffer vessel during each test, it will be necessarry to analyze the residual concentrations in the gas coming from the process components *and* to control the supply of the constituents into the buffer vessel.

The most relevant measurements and the required sensitivity ranges are summarized in the following table; the locations where gas samples are taken for analysis are indicated in Figure 1.

Location	Constituent	Sensitivity Range (vpm)
A 1	H_2	10 – 1000
	O_2	10 – 100
	H_2O	5 – 50
	HT	0.2 – 2
A 2	H_2	1 – 100
	O_2	1 – 100
	H_2O	10 – 100
A 3	H_2O	0.1 – 50
	HTO	0.01 – 2
A 4	H_2	0.1 – 100
	O_2	0.1 – 10
	HT	≤ 2

Conclusions

The described facility for tritium extraction and coolant purification is currently being designed in detail. The work performed so far indicates that it is an ambitious aim to achieve a humidity reduction from 10-50 vpm to a level of ≤ 0.1 vpm. The presence of HTO as a radioactive tracer in the gas is helpful to carry out analyses with the required sensitivity. It will be difficult, however, to handle the problem of ice aerosol formation. Aside from the high demands on the analytic instrumentation, it is not expected, that similar difficulties will arise for the other process components, i. e. for the oxidizer and the cryogenic adsorber.

Literature:

[1] Albrecht, H. et al., European Helium Cooled Pebbel Bed (HPCB) Test Blanket, ITER Design Description Document, Status 1.7.1998, FZKA 6127, 1998

[2] Chabot, J. et al., Cold Trap Development, CEA-Rapports SCECF 282 (Dec. 1992), SCECF 303 (May 1993), SCECF 329 (Dec. 1993)

[3] Housiadas, C., Schrader, K. H.,Testing of a water vapour cold trap for atmospheric detritiation, Fusion Technology, Proc. 19th Soft Conference, Elsevier 1997, p 1217

[4] O'hira S. et al., Test of the Cold Trap in the JAERI Fuel Cleanup System in the Tritium Test Assembly, JAERI-M 93 - 087 (1993)

[5] Hackfort, H. et al., Verfahren zum Ausfrieren von Xenon aus dem Auflöserabgas von Wiederaufarbeitungsanlagen, Jül - Spez - 287, December 1984

Remark:

Progress of future work will be reported under Task No. TR 6

Staff:

H. Albrecht
G. Neffe
E. Hutter

WP B 6
Demonstration of Blanket Safety

B 6.1.1
Safety Approach for the TBM and DEMO

Following the comprehensive non-site specific safety report (NSSR-2) for ITER, a safety analysis was performed for the European helium-cooled pebble bed (HCPB) test blanket module (TBM), emphasising very unlikely accident scenarios envisaged as category IV events (expected frequency of occurrence 10^{-6}/a<f<10^{-4}/a) with limited consideration given also to the behaviour of the TBM under category V (f<10^{-6}/a) accident scenarios. The aim was to demonstrate the compatibility of the HCPB TBM system with ITER safety rules. The findings were documented in the comprehensive design description document (DDD) for ITER [1]. Compact versions were prepared as appendix to the NSSR-2 and in [2]. A brief system description, the methods applied, and the results of the investigation are summarised in the following paragraphs.

HCPB system description

The TBM represents a poloidal section of the corresponding DEMO blanket segment. It employs alternating layers of ceramic breeder material (≈120 kg) and beryllium (≈450 kg) in form of small pebbles. The layers of 1.1 cm and 4.5 cm thickness, respectively (TBM-I design), are separated by cooling plates with integral cooling channels, and the whole stack is encapsulated in a strong actively cooled so-called blanket box. Two separate primary heat transport loops with 2x0.95 MW heat capacity are foreseen. The helium inventory of 15 kg is circulated at a pressure of 8 MPa with inlet/outlet temperatures of 250°C/350°C. The tritium released from the pebble beds is carried by a purge gas flow at 0.1 MPa to the tritium extraction system (TES). The location of the TBM in ITER, along with the ancillary subsystems characterised in [3], is depicted in Fig. 1. The tight arrangement of the heat transport system components with thermal insulation in the wedge-shaped vault compartment is illustrated in Fig. 2.

Accidents investigated and safety concerns

Four groups of accidents were analysed (Tab. 1). LOCA-IN: loss of coolant into the vacuum vessel (VV) caused by disruption-induced first wall (FW) failure of four cooling channels, two per loop, and steam ingress into the VV; LOCA-EX: spontaneous guillotine break of the main cooling pipe

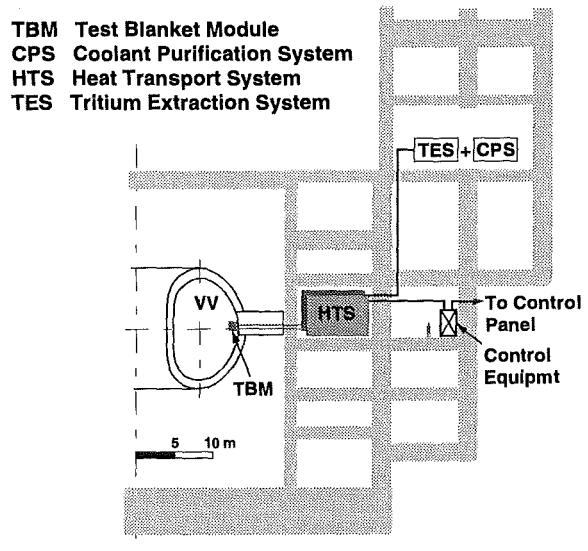

Fig 1: Space allocation for the TBM system in ITER

C = Circulator
E = El. heater
F = Dust filter
H = Heat Exchange (HX)
I = Instrum. & Control
T = Tanks
V = Valves

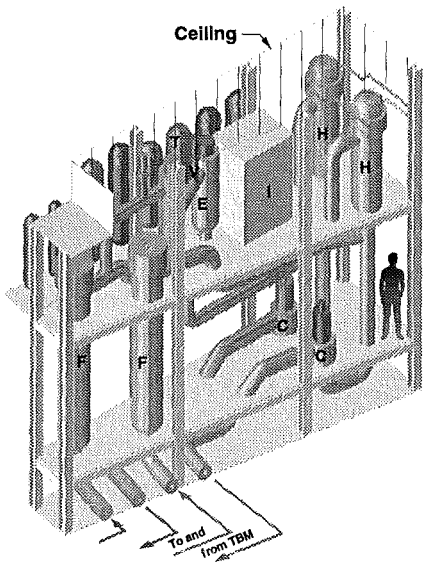

Fig 2: Arrangement of the TBM heat transport system (HTS)

upstream of the circulator with triggered shutdown at 10s and subsequent disruption causing FW failure and blowdown of the second loop into the VV; LEAK: spontaneous TBM-internal leak from both loops with pressurisation of the TBM box and purge gas system and delayed shutdown with disruption; LOFA: inadvertent control valve closure leading to undetected complete loss of flow in both loops and disruption, at TBM FW surface melting. In all cases a disruption-induced loss of off-site power is postulated to occur at 10% overpower, implying pump trips in primary and secondary loops and in ITER shielding blankets. Thus, the concerns are: (a) VV pressurisation, (b) vault pressure build-up, c) purge gas system pressurisation, (d) temperature evolution in the TBM, (e) decay heat removal capability, (f) tritium and activation products release from the TBM system, (g) hydrogen and heat production from Be/steam reaction, and (h) Be/air chemical heat production. Details are described in [1].

Method of analysis

(i) The RELAP5/MOD3.2 code was used to calculate the flow rates, pressures, and temperatures in the TBM cooling circuits during the transients, where a single circuit was modelled to represent the two identical loops. The model includes (details can be found in [4]) the TBM proper, circulator, dust filter, helium-to-water heat exchanger (HX), a buffer tank for pressure control, and the bypass to the HX for inlet temperature control. (ii) Temperatures in the TBM front part have been analysed with FIDAP. The 3D finite element model represents the blanket box with 7 cooling channels, the smallest unit cell with repetitive flow pattern, and part of the breeding zone. (iii) A 1D heat transport model with 22 elements has been set up to analyse the decay heat transport after shutdown. It represents a radial column cut out of the TBM from the FW to the shield and accounts for thermal conduction, radiation across elements with high helium fractions, and radiation from the bounding surfaces. (iv) The beryllium chemical reaction (hydrogen production rate and exothermic heat) has been estimated based on the temperature history from the 1D heat transport analysis, applying

Table 1: Accident characterisation

Accident	Category	Failure Location	Break size	Shutdown delay
LOCA-IN	IV (V)	FW	4 channels	0 s
LOCA-EX	IV	Cold leg	78.5 cm^2	10 s
LEAK	IV	Headers	78.5 cm^2	1000 s
LOFA	V	Valves	none	118 s

correlations defined by ITER.

Transient analysis results

The results of the four accident groups investigated are summarised below with an overview of the numerical findings given in Table 2.

LOCA-IN: The discharge of the helium coolant from both cooling loops through the broken FW channels lasts for about 20 s. The loop pressure drops from 8 MPa to the level of the VV pressure, which builds up accordingly from zero to the small value of about 3500 Pa. The temperature in the first wall experiences a short rise by 215 K from disruption loads (assumed are 4.2 MW/m^2 for 1 s) which relaxes fast as do the temperatures in the beryllium and breeder pebble layers. Typical long-term temperature in the TBM stays below 480°C since the heat is dissipated from the front and back surface by radiation, given a pessimistic reference ITER FW temperature evolution. Curves are similar to those depicted in Fig. 3 for the LOCA-EX case. As a category V parameter variation it was postulated that the disruption causes a breach of the TBM box allowing steam ingress into the beryllium pebble beds. The total accumulated hydrogen produced is 100 g. The chemical heat is negligible. The tritium release from the TBM system is inherently small. The most mobile fraction of the order 1 mg only is carried with the helium coolant. The amount of tritium which could be liberated from the beryllium pebbles is estimated to be at most 114 mg. The tritium which might be released from the tritium extraction subsystem is judged to be negligible if the isolation valves are closed. Other mobile activation products in the helium cooling system are expected to be small.

LOCA-EX: The discharge of the helium coolant from one loop into the vault lasts for about 5s. Accordingly, the vault pressure builds up from 0.1 to 0.1045 MPa. The temperature evolution shows a sharp burst in the FW caused by the disruption and a moderate increase in the long run, peaking at 480°C about 2 hours after shutdown (Fig. 3). A parameter variation assumed disruption-induced failure of the FW. The pressure in the VV then increases spontaneously from zero to 1700 Pa by discharging the helium from cooling loop 2, creating a vault/VV bypass. This leads to venting of the VV at a rate of 15 Pa/s, levelling off to the equilibrium pressure of ~50000 Pa. Since the peak Be temperature at the FW stays below 500°C, the chemical reaction is not critical. The tritium release with the coolant is of the order of 1 mg.

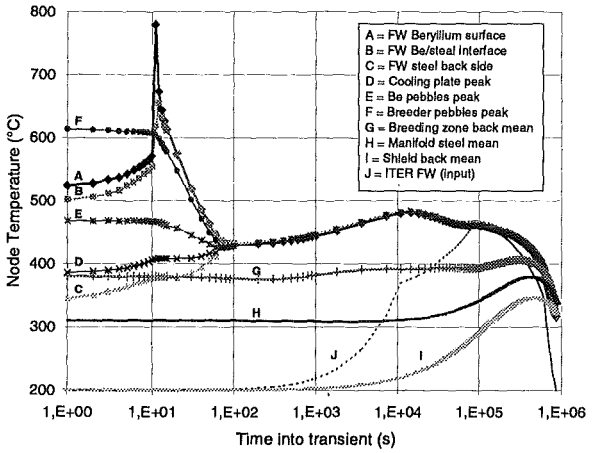

Fig. 3: Temperature evolution in selected nodes of TBM (composite of results from FIDAP and 1D calculations)

LEAK: After rupture of the main headers in the TBM the coolant pressure in the loops decreases temporarily by 20%, recovering to 90 % of the nominal pressure level within one second.

Table 2: Results of safety analysis

Concerns	LOCA-IN	LOCA-EX	LEAK	LOFA
VV pressurisation	3.5 kPa	50 kPa		3.5 kPa
TBM pressurisation			8 MPa	
Vault pressurisation		4% in 5s		
TES pressurisation	0.1 MPa		0.2 MPa	
Temperature rise in FW	215K	265K	215K	785K
Temperature rise in BZ	≈0	≈0	≈0	≈220K
Long-term temp. TBM	480°C	480°C		<500°C
Decay heat removal	passive	passive	gravity	passive
Be/air reaction at FW		negl.		
H_2 from Be/steam FW	negl.			120 g
H_2 from Be/steam	100g			
Chem. heat production	<<DH			large
Tritium release into VV	114 mg	0.5 mg		110 mg
Tritium release to vault		0.5 mg		

Hence, heat removal from the TBM remains unaffected until the disruption occurs at 1000s. After shutdown the system pressure is stable for the next hour. The pressure in the TES rises to the set point of 0.2 MPa within less than 0.5s, requiring fast pressure controlled shutters. The remaining gravity driven mass flow rate in the main loops of 1.7 % of nominal after pump trip is sufficient to transfer the decay heat from the TBM. The large thermal inertia of the system, in combination with the maintained high pressure, avoids significant temperature changes. Since the TBM box cannot sustain the full system pressure, pressure relief must be provided which has to be worked out.

LOFA: Pressure and flow transients upon FW failure at surface melting occurring at 118s is similar to the LOCA-IN case and is thus uncritical. The temperature evolution calculated with FIDAP shows typical ramps of up to 8 K/s in the FW and 3 K/s in the pebble beds before shutdown. Thereafter, the 1D model yields peak temperatures in the beryllium pebble beds of 780°C lasting for several minutes and falling below the 500°C level after about 15 hours. The estimated chemical heat at the TBM FW is substantial, if steam ingress from other ITER components is postulated during the high temperature phase. For instance, at the beryllium melting temperature the chemical heat would exceeds the radiated heat by a factor of 4.7. The cumulative hydrogen produced amounts to 120 g after 1 hour.

The following conclusions are drawn: The HCPB TBM system complies with ITER safety rules. The VV pressurisation upon LOCA is inherently small. The TBM box and TES pressure build-up require counter measures. The vault pressure is not suited as shutdown signal for ex-vessel LOCA. The FW temperature rise is dominated by the disruption load specified. The Breeding zone temperature rise is small in all category IV cases. Passive decay heat removal at low temperature is assured at all times. The chemical heat and hydrogen production from the beryllium pebble beds are generally small. The tritium and activation products release are inherently small.

Literature:

[1] Boccaccini, L. V. et al.: European Helium Cooled Pebble Bed (HCPB) Test Blanket, FZKA 6127, to be published.

[2] Kleefeldt, K.; Gabel, K; Schmuck, I: Safety assessment of the helium-cooled pebble bed test blanket module for ITER, in Proceedings of the 20th SOFT, Marseille, 1998.

[3] Albrecht, H. et al.: Helium loops of an ITER HCPB test blanket module, in Proceedings of the 17th IEEE/NPSS SOFE, San Diego, 1997.

[4] Gabel, K. and Kleefeldt, K.: Thermal-hydraulics analysis of the HCPB test blanket module for ITER during normal

operation and accidents, FZKA 6059, 1998.

Staff:

K. Kleefeldt
I. Schmuck

WB B 7
Demonstration of Blanket Reliability

B 7.1.3
Contribution to Common Blanket System Data Base

Common Data Base

This Subtask is connected with the Tasks B 7.2.2 and A 7.1.3. All data used there will be inserted in a common data base. The use of the same data for different design options allows to limit error sources in comparative evaluations. The activity was continued as a permanent part of the reliability analyses

Probabilistic fracture mechanics assessment

Currently used failure rates for availability studies are usually obtained from in-service experience of various classes of components and welds. No information about material parameters and loading uncertainties is usually part of the analysis.

An activity was therefore started with the aim of establishing failure rates that are based on in-service loading condition as well as on the fracture mechanics description of present or assumed flaws. A probabilistic analysis is performed which allows to assess the uncertainty in material and loading parameters using a fracture mechanics assessment procedure [1].

A reference case was chosen from the currently developed ITER test blanket module with data taken from the literature and from current design analyses.

The analysis is mainly based on the R6 design code from which basic ideas also are adopted in the development of ITER/DEMO design rules. Main difficulty is that due to the different design philosophy the necessary input data are not readily available and that the stress analysis performed in current design practice is purely elastic. Results from probabilistic analyses of expected failure rates are therefore of limited absolute value, however, sensitivity analyses will give important hints on dominant physical variables.

First results will be available in a forthcoming report [2] and may be used to set up a scheme for the analysis of selected important welds.

Literature:

[1] L. Cizelj, H. Riesch-Oppermann, ZERBERUS - the code for reliability analysis of crack containing structures, KfK-Report 5019, 1992.

[2] H. Riesch-Oppermann, Probabilistic fracture mechanics assessment for the HCPB test blanket module, Report FZKA 6193 (to appear).

Staff:

H. Riesch-Oppermann
H. Schnauder

B 7.2.2
TBM System Availability

The availability/unavailability of the HCPB Test Blanket System is an important accompanying factor in design and development. The interaction between R&D and improvements mainly in the welding procedures lead to changes and simplifications. But also more detailed thermal and structural mechanic calculations had an influence of modifications. Considered in the reliability analysis is only the test blanket module. A new analysis of the auxiliary cooling system is not necessary at present time, because there are no changes since the last evaluation.

The failure rates for the analysis are taken from the common data base (A and B 7.1.3). The most critical point is the question of the mean repair or exchange time. A repair of the test blanket module inside the VV is not envisaged and will therefore be excluded. For exchange of a defect component a mean time of 8 weeks is considered as reasonable. But, this time must be seen in interaction with the entire remote handling concept, which is not finally worked out and defined yet.

For the test blanket module an overall failure rate of $\lambda = 5.35 \times 10^{-7}/h$ is calculated. This results in an unavailability of 7.19×10^{-4} which is equal an availability of 99.93 %. Compared with the unavailability of the first version of the test blanket module this is a reduction of the unavailability of about 15 %, supposing the design pressure will be reduced.

The impact of a statistic variation of the components unavailability on the overall result of the test blanket module has been analysed by a Monte Carlo simulation. Assuming an error factor of 10 uniform for all components the result will vary between $U_{0.95} = 1.7 \times 10^{-3}$ and $U_{0.05} = 1.4 \times 10^{-4}$ corresponding to an error factor of 3.5 within the confidence limits of 5 and 95 %. That means 90% of all possibilities in a lognormal distribution are within that limits.

As the calculation is performed with probabilities one can also relate the variation to the mean repair time. In this case the unavailability range of 1.4×10^{-4} to 1.7×10^{-3} would correspond with a variation of the MTTR between 2.3 and 28 weeks. This is based on the assumption that the MTTR of 8 weeks is the 50 %-value in the distribution.

Literature:

C. Nardi, B. Bielak, M. Eid, T. Pinna, H. Schnauder, Availability of the European Test Blanket Systems and their Influence on ITER, 20th SOFT, 7-11 September 1998, Marseille, France

Staff:

H. Schnauder

WP B 8
Development of Ceramic Pebbles

B 8.1.1
Development of Li_4SiO_4 Pebbles

For the European Helium Cooled Pebble Bed (HCPB) blanket slightly overstoichiometric lithium orthosilicate pebbles (Li_4SiO_4+ SiO_2) have been chosen as a reference material. Other ceramic materials, also in the form of pebbles, are being developed as alternatives to lithium orthosilicate, i.e. overstoichiometric lithium metatitanate (Li_2TiO_3 + TiO_2) and lithium metazirconate (Li_2ZrO_3 + ZrO_2) developed by CEA.
The DEMO blanket is expected to have an operation time of 20000 hours, with a maximum nominal temperature of - 900 °C in the front of the blanket. In order to compare the long term behaviour of the three breeder materials at such high temperature and in a blanket-typical atmosphere (He + 0.1% H_2), long term annealing experiments have been carried out at Forschungszentrum Karlsruhe [1]. To achieve representative final DEMO conditions for the pebbles in less than 20000 hours, it has been decided to use in the test a temperature higher than that foreseen in the blanket. The relationship between the annealing and blanket temperature has been determined on the basis of the creep activation energy, because creep is the most important phenomenon at the maximum nominal temperature. For the chosen temperature of 970 °C an experimental annealing time of 96 days is required.
The test specimens were:

- Overstoichiometric Li_4SiO_4 + SiO_2 pebbles supplied by Forschungszentrum Karlsruhe and fabricated by SCHOTT Glaswerke by melting-spraying process.
  Pebble diameter: 0.25 mm-0.63 mm;
  density : 98 % TD (Theoretical Density: 2.4 g/cm^3).
- Overstoichiometric Li_2TiO_3 + TiO_2 pebbles supplied by CEA and fabricated by the agglomeration-sintering process.
  Pebble diameter: 0.8 mm-1.2 mm;
  density: 90 % T.D. (Theoretical density: 3.45 g/cm^3).
- Overstoichiometric Li_2ZrO_3 + ZrO_2 pebbles supplied by CEA and fabricated by the extrusion-spheronization-sintering process.
  Pebble diameter: 1.0 mm-1.5 mm;
  density: 87 % T.D. (Theoretical density: 4.19 g/cm^3).

The experiment has been performed in an oven consisting of three tubes of Al_2O_3, one tube for each material, with separate purge gas flow (Fig. 1). At the tube inlets the pressure of the purge flow and its H_2O content were measured. The water content in the purge flow was also measured at the outlets together with the mass flow. In order to have information on the lithium vaporization during the experiment, sintered steel filters have been used at the tubes outlets. The purge flow was 0.6 l/h of 99.9 % He + 0.1 vol % H_2 .

Before starting the annealing experiment a thermal conditioning of all three ceramics has been performed in air:

- two weeks at 1000°C for lithium orthosilicate. The purpose of the thermal conditioning was to make the material as stable as possible before the annealing tests. Due to the rapid quenching during the production process of Li_4SiO_4 a metastable phase $Li_6Si_2O_7$ exists. This phase decomposes completely into Li_4SiO_4 and Li_2SiO_3 during the conditioning.
- 10 hours at 500°C for lithium metatitanate and lithium metazirconate. For lithium metazirconate the thermal conditioning was intended to eliminate the water adsorbed in the material. Lithium metatitanate was also annealed only to have the same starting condition of Li_2ZrO_3.

Sampling of the specimens was made for the material at the beginning of the annealing, after the thermal conditioning and after 3, 6, 12, 24, 48, 96 days. To characterise the ceramics the following analyses have been performed:

- chemical analyses. The measurements of Li-content have been done using the atomic emission spectroscopy (AES), the X-ray fluorescence analysis (XFA) has been used to measure the amount of Si, Zr and Ti;
- X-ray diffraction analysis (XRD) for the phase composition analysis;
- scanning electron microscopy (SEM) and light-microscopy for the structure analysis;
- He-pycnometry and Hg-porosimetry for density and porosity measurements;
- Brunauer, Emmet and Teller (BET) method for the specific surface area measurement;
- crush load determination;
- uniaxial compression tests of pebble beds (after 96 days) [2].

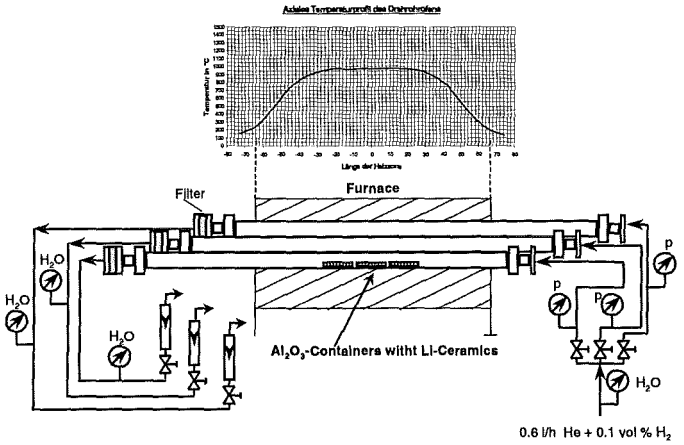

Fig. 1: Schematic of the equipment used in the annealing experiments

Results

Considering the results of the examinations the following conclusions can be drawn:

- In Li_4SiO_4 the thermal conditioning produces the largest changes in the structure. During the annealing the only significant change in orthosilicate pebbles is the diffusion of metasilicate through the material. In some pebbles the lithium metasilicate reaches the surface covering it with a layer with thickness up to 10 µm (Fig. 2). If these pebbles are in contact the surface layer of Li_2SiO_3 can form sintering necks. These sintering necks are weak and very modest mechanical action could break them. After the thermal conditioning there is a reduction of the measured mean crush load from 7.8 ± 2.4 N to 6 ± 2.3 N. The measured mean crush loads are characterised by large scattering, and it is rather difficult to make a quantitative assessment of its change during the annealing experiment. After 96 days a mean value of 4.5 ± 2 N has been measured. Chemical analyses do not show any change in the lithium content of the lithium orthosilicate pebbles.
- In Li_2TiO_3 (Fig. 3) the pre-annealing at 500 °C has no significant effect on the structure of the material. During

the annealing there is an increase in the grain size (it is about 1.5 µm at the beginning and, after 96 days, it grows up to about 25 µm). After 48 days the pebbles became black, but this colour change does not correspond to any change in the microstructure of the pebbles, and no additional phase could be detected. The colour change may be caused by a slight oxygen sub-stoichiometry of the material. After the annealing in Li_2TiO_3 there is a slight reduction of the porosity. The not spherical shape of the pebbles and the material heterogeneity cause a scattering in the measured crush loads, therefore, also for metatitanate , it is difficult to see a significant increase or decrease of the crush loads after the 96 day annealing. Also in this case no reduction in the lithium content of the pebbles could be measured by chemical analysis.

- Also in Li_2ZrO_3 the pre-annealing had no significant effect on the pebble microstructure, the grain growth is modest (the dimensions are between 2 and 4 µm after 96 days), and, after the annealing, the pebbles were slightly denser. A porous, not uniformly distributed layer of ZrO_2 is formed at the surface of the pebbles during the annealing (Fig. 3) and chemical analyses showed a reduction in the average Li/Zr atomic ratio. Both these results suggest the vaporisation of lithium from the metazirconate pebbles. A slight decrease of the average crush load has been observed.

The filters at the outlets of the three tubes were analysed by atomic absorption spectrometry (AAS). No vaporised lithium has been observed after the thermal conditioning in case of Li_2TiO_3 and Li_2ZrO_3 . After the 96 day annealing about 0.0005 wt % of Li was found in each of the three tubes (the measured percentage refers to 1 g of filter material). It is possible that the lithium from the ceramic pebbles was deposited on the colder outlet of the tubes before reaching the filter. This would explain why no increased lithium amount was found in the filter of the tube containing Li_2ZrO_3. The uniaxial pressure tests did not show significant differences for any of the three ceramic materials.

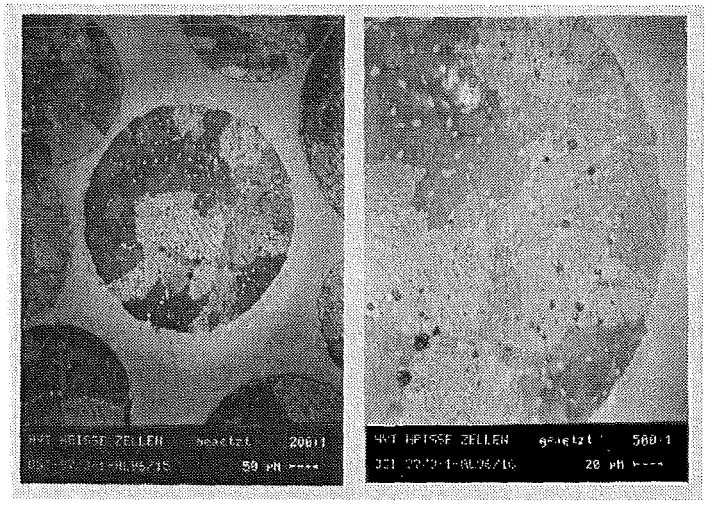

Fig. 2: Cross section of a lithium orthosilicate pebble after 96 day annealing

Uniaxial compression tests

The uniaxial compression tests with Li_4SiO_4 were continued and first corresponding experiments were performed with metatitanate Li_2TiO_3 and metazirconate Li_2ZrO_3 in a temperature range between ambient and 700 °C. The aim of these experiments is the determination of the moduli of deformation for the first pressure increase and pressure decrease and the thermal creep behaviour. Fig. 4 shows characteristic results for thermal creep .

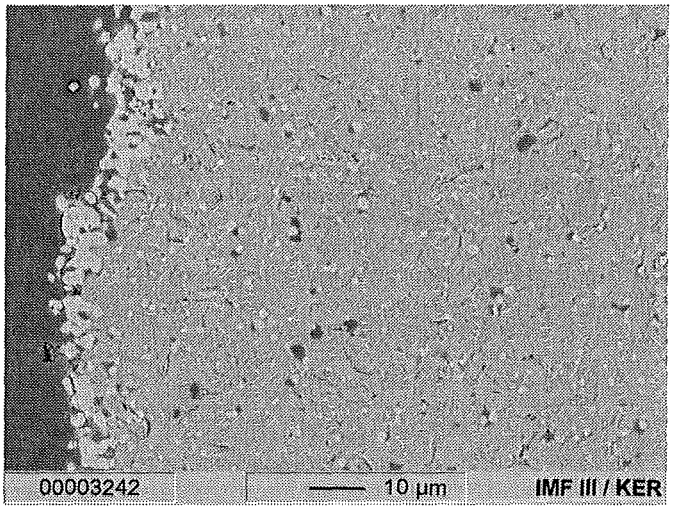

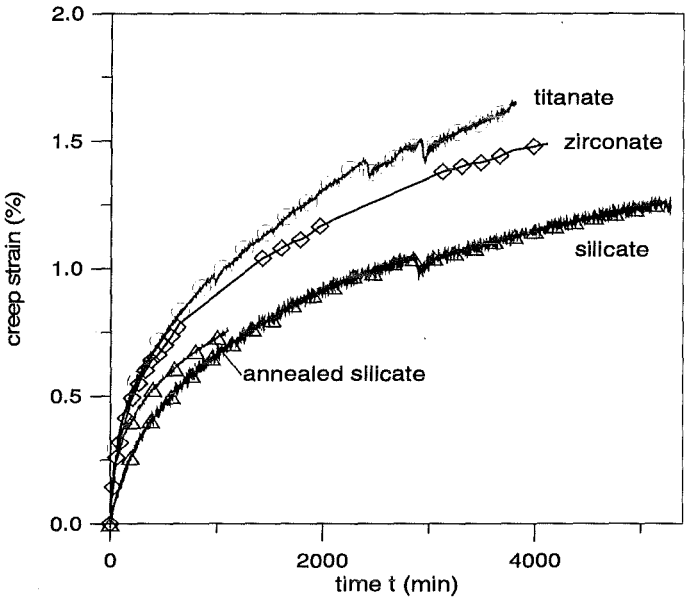

Fig. 3: Cross section of a Li_2ZrO_3 pebble after 96 days

Fig. 4: Thermal creep of titanate, zirconate, and silicate at 700 °C and 6.3 MPa

Literature:

[1] G. Piazza, M. Dalle Donne, H. Werle, E. Gühnter, R. Knitter, N. Roux, J.D. Lulewicz, "Long term Annealing of Ceramic Breeder Pebble for the HCPB DEMO Blanket". Proceedings of the CBBI-7, 14-16 Sept. 1998, Petten, the Netherlands.

[2] J. Reimann, S. Müller and K. Tomauske, "Thermomechanical Behaviour of Ceramic Breeder Pebble Beds". Proceedings of the CBBI-7, 14-16 Sept. 1998, Petten, the Netherlands.

Staff:

M. Dalle Donne
A. Goraieb
E. Günther
E. Kaiser
K. Kleykamp
D. Knebel
R. Knitter
S. Müller
G. Piazza
J. Reimann
H. Ziegler

B 8.3.1
Contribution to the PIE of Li_4SiO_4 Pebbles Irradiated in the HFR Petten

EXOTIC-7

EXOTIC-7 was the first in-pile test with ^{6}Li-enriched (50 %) lithium orthosilicate (Li_4SiO_4) pebbles and with DEMO representative Li-burnup. Post irradiation examinations of the Li_4SiO_4 have been performed at the Forschungszentrum Karlsruhe (FZK) to investigate the tritium release kinetics, the effects of Li-burnup and of contact with beryllium during irradiation as well as the mechanical stability changes due to irradiation. The mechanical strength of both irradiated and unirradiated pebbles has been examined by means of crush tests, in which a continuously increasing load is imposed to a single pebble until it breaks [1].

Three irradiation capsules were examined:

- Capsule 28.1 containing Li_4SiO_4 pebbles of 0.1-0.2 mm diameter (Li-burnup 10 %);
- Capsule 28.2 containing Li_4SiO_4 pebbles of 0.1-0.2 mm diameter and Be pebbles of 2 mm and 0.1-0.2 mm diameter (Li-burnup 18.1 %);
- Capsule 26.2 containing Li_4SiO_4 pebbles of 0.1-0.2 mm diameter and beryllium pebbles of 2 and 0.1-0.2 mm diameter (Li-burnup 13.3 %).

Pebbles fabrication and mechanical behaviour

The small pebbles (^{6}Li-enrichment 50 %) used in the EXOTIC 7 irradiation have been produced by spraying liquid material. They are overstoichiometric with about 1 wt % SiO_2 addition. The chemical analysis of the pebbles has shown very low content of impurities (Table 1). The presence of carbon is due to the fabrication process which uses high ^{6}Li-enriched lithium carbonate.

Table 1: Impurity content in the Li_4SiO_4 pebbles

Element	Quantity (wt %)
Al	0.067
C	0.3
others	<0.009

Crush tests at room temperature have been performed to characterise the mechanical behaviour of single pebbles before and after irradiation. In these tests a continuously increasing load is imposed by a piston to a single pebble until it breaks. The load application rate was 0.2 mm/min and, due to the small quantity of available irradiated material, 10 measurements have been done for the irradiated pebbles and 16 for the unirradiated. Pebbles with 0.15 mm diameter have been used in the crush load tests. Using the Hertz's theory for the pressure between two bodies in contact, the breaking stress corresponding to each crush load, i.e. the tensile stress at the border of the contact surface between pebble and support plate, has been calculated.

In Table 2 the average stresses and the standard deviation of the measurements are shown.

Table 2: Calculated average breaking stresses for irradiated and unirradiated Li_4SiO_4 pebbles

Capsule Nr.	Breaking stress (MPa)
26.2	860.8 ± 65.8
28.1	880.4 ± 59.2
28.2	873.3 ± 44.1
unirradiated	827.1 ± 83.6

There is no significant change in the mechanical stability of single pebbles due to irradiation. The breaking tests were correlated by means of the Weibull statistics. Figs. 1 and 2 show the failure probability as function of the breaking stress for not irradiated pebbles and irradiated lithium orthosaillicate from capsule 26.2.

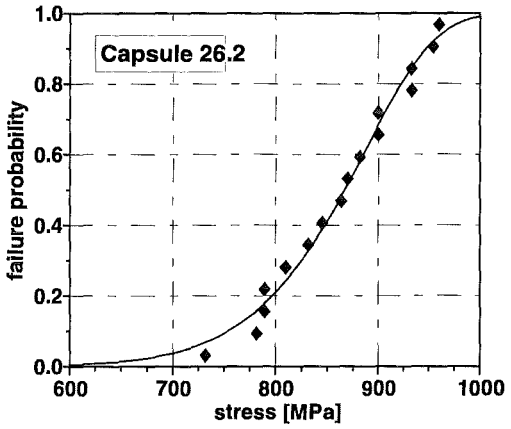

Fig. 1 Weibull failure probability versus breaking stress

Also micro-hardness measurements indicated no significant radiation induced changes. Measurements according to Vickers indicated hardness levels of 283 for unirradiated orthosilicate, and 319 for orthosilicate with 10% burn-up.

Tritium release

The tritium release rate from pure Li_4SiO_4 bed of capsule 28.1-1 is characterised by a broad main peak at about 400 C and by a smaller peak at about 800° C. The broad main peak was observed in all previous studies with low Li-burn-up (< 3 %). The release rate of the Li_4SiO_4 from the mixed beds of capsule 28.2 and 26.2-1 shows again these two peaks, but most of the tritium is now released from the 800° C peak. This shift of release from low to high temperature may be due to the higher Li-burnup (capsule 28.1-1 Li-burnup 10 %, capsule 28.2 Li-burnup 18.1 %, capsule 26.2-1 Li-burnup 13.3 %) and/or due to contact with Be during irradiation. Due to the very difficult interpretation of the in-situ tritium release data, residence times have been estimated

on the basis of the out-of-pile tests. The residence time for Li_4SiO_4 from caps. 28.1-1 irradiated to 10 % Li-burnup agrees quite well with that of the same material irradiated at Li-burnup lower than 3 % in the EXOTIC-6 experiment. In spite of the observed shift in the release peaks from low to high temperature, also the residence time for Li_4SiO_4 from caps. 26.2-1 irradiated to 13.3 % Li-burnup agrees quite well with the data from EXOTIC-6 experiment. On the other hand, the residence time for Li_4SiO_4 from caps. 28.2 (Li burn-up 18.1 %) is about a factor 1.7-3.8 higher than that for caps. 26.2-1. Based on these data one can conclude that neither the contact with beryllium nor a burn-up up to 13 % have a detrimental effect on the tritium release of Li_4SiO_4 pebbles, but at 18.1 % Li burn-up the residence time is increased by about a factor three.

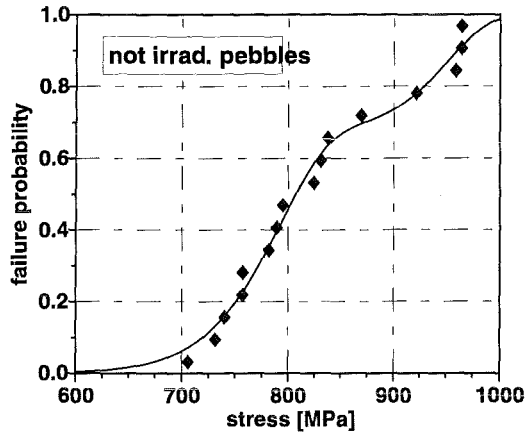

Fig. 2: Weibull failure probability versus breaking stress for not irradiated material

EXOTIC-8

Although a small addition of TeO_2 to Li_4SiO_4 improves the tritium release of the pebbles, this material is not suited as breeder material because the Te is released at higher temperatures. Therefore in EXOTIC-8, the two capsules containing (Li_4SiO_4 + TeO_2)-pebbles have been unloaded and have been replaced by a capsule with the reference materail (Li_4SiO_4 + 2.2 wt% SiO_2) enriched to 50 % ^6Li.

Literature:

[1] G. Piazza, F. Scaffidi-Argentina et al., "Characterisation and Post-Irradiation Examinations of Lithium-Orthosilicate and Beryllium Pebbles Irradiated in the EXOTIC-7 Experiment", FZKA Report, to be published.

Staff:

M. Dalle Donne
E. Damm
H.D. Gottschalg
H. Häfner
E. Kaiser
K. Kleykamp
D. Knebel
B. Neufang
R. Pejsa
G. Piazza
O. Romer
F. Scaffidi-Argentina
H. Steiner
A. Wacker
G. Weih
P. Weimar
F. Weiser
H. Werle
H. Ziegler

WP B 9
Behaviour of Beryllium under Irradiation

B 9.1.1
Characterization and optimization of beryllium pebbles.

The heat transfer parameters (i.e. thermal conductivity and heat transfer coefficient) of the binary beryllium pebble bed have been obtained by experimental investigations and correlated as a function of temperature and of the interference between bed and constraining walls, due to the differential thermal expansion. In this test the beryllium pebble bed was contained in the annulus between an outer steel tube and a heater rod. The correlations allow an easy application for the calculations in the blanket.

However, these correlations have been obtained for a very stiff containment, so that they can be directly applied only in cases where very small deformations of the containing walls due to the pressure exerted by the bed are expected. This is the case, for instance, where containing plates have similar pebble beds on both sides.

Two kind of experiments were performed:

- a series of experiments with a thermal insulation on the outside surface of the outer tube. The heater rod was heated to temperatures ensuring that the differential thermal expansion between outer tube and beryllium pebbles is zero, so that no constraint is exerted on the pebble bed;
- a series of experiments with a water cooling on the outside surface of the outer tube to ensure that various levels of constraint are exerted on the pebble bed.

The differential thermal expansion between bed and bed containment walls ("interference") produces a compression of the bed which increases the contact surface area of the pebbles.

Figure 1 shows the thermal conductivity of the binary pebble bed without constraint ($\Delta\ell/\ell = 0$) versus the average pebble bed temperature [1]. The bed thermal conductivity varies very little with bed temperature. This is because the beryllium thermal conductivity decreases with temperature, whereas the thermal conductivity of helium increases with temperature and the two effects somewhat compensate each other.

Figure 2 shows the results of the experiments with water cooling, i.e. with pebble bed constraint ($\Delta\ell/\ell > 0$), in the plots of Be pebble bed thermal conductivity $K/K_{(\Delta\ell/\ell = 0)}$ versus the percentage ratio of the interference $\Delta\ell$ to the width of the pebble bed ℓ. As expected, the effect of $\Delta\ell/\ell$ [%] is linear, as the increase of the ratio of the contact surface to the cross section of the pebbles is also linear. Because this increase is quite small in comparison to the pebble diameter, and neglecting a second order contribution, it is proportional to $\Delta\ell/\ell$ [%].

The equation correlating the experimental results for the thermal conductivity is:

$$k[W/mK] = \left(7.3145 + 1.00652 \cdot 10^{-4} \cdot T_m\right) \cdot \left(1 + 7.259 \cdot \frac{\Delta\ell}{\ell}[\%]\right)$$

In case of $\Delta\ell/\ell = 0$ the experimental results for the temperature dependence of k are valid for T_m in the temperature range 130°C - 600°C. The values for the case of $\Delta\ell/\ell > 0$ are measured in the temperature range between 10° C and 160° C and are valid for $\Delta\ell/\ell$ [%] in the range 0-0.1 %.

Figure 3 shows the heat transfer coefficient at the inner tube wall of the pebble bed without constraint ($\Delta\ell/\ell$ =0) versus the temperature of the inner tube wall [1].

Figure 4 shows the results of the experiments with water cooling, i.e. with pebble bed constraint ($\Delta\ell/\ell > 0$), in the plot of Be pebble bed/wall contact heat coefficient $\alpha/\alpha(\Delta\ell/\ell = 0)$ versus the percentage ratio of the interference $\Delta\ell$ to the width of the pebble bed ℓ. As expected, also for the heat transfer coefficient the effect of $\Delta\ell/\ell$ [%] is linear, however only for $\Delta\ell/\ell$ [%] > 0.015 (see Figure 4), the increase for $\Delta\ell/\ell$ [%] < 0.015 being much stronger. More R&D work is necessary to determine the reasons for such a behavior at low values of $\Delta\ell/\ell$.

In case of $\Delta\ell/\ell = 0$ the experimental results for the temperature dependence of α are valid for T_w in the temperature range 130°C-600 °C. The values for the case of $\Delta\ell/\ell > 0$ are measured in the temperature range between 10° C and 160° C and are valid for $\Delta\ell/\ell$ [%] in the range 0-0.1 %.

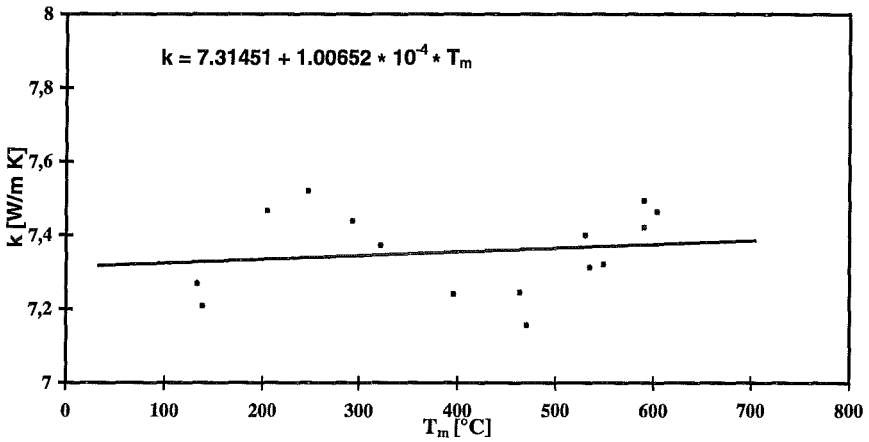

Fig. 1: Thermal conductivity as a function of the mean bed temperature (case without constraint: $\Delta\ell/\ell = 0$).

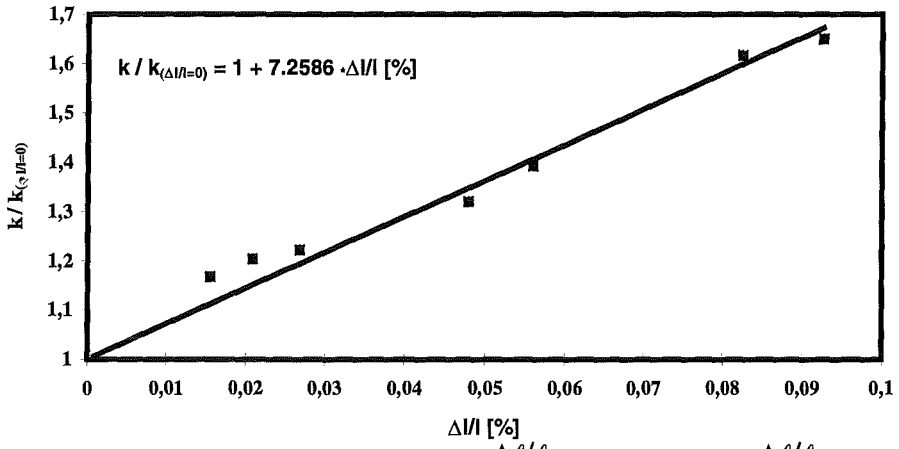

Fig. 2: Thermal conductivity as a function of $\Delta\ell/\ell$ (case with constraint: $\Delta\ell/\ell > 0$)

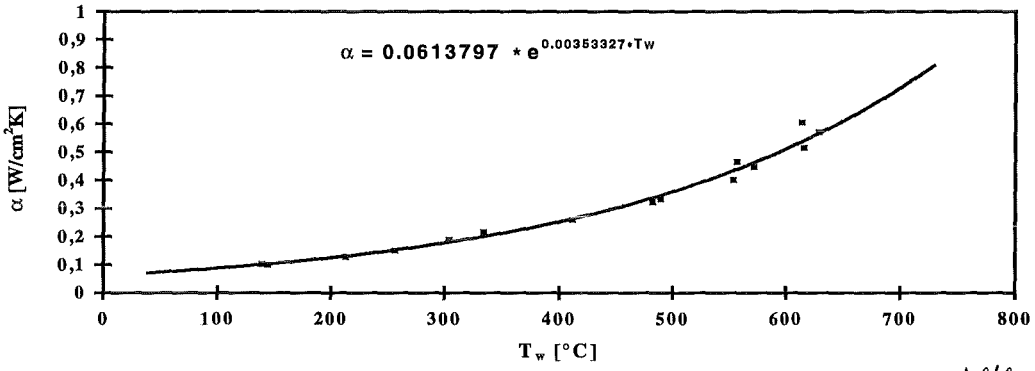

Fig. 3: Heat transfer coefficient at the wall as a function of the wall temperature (case without constraint: $\Delta\ell/\ell = 0$).

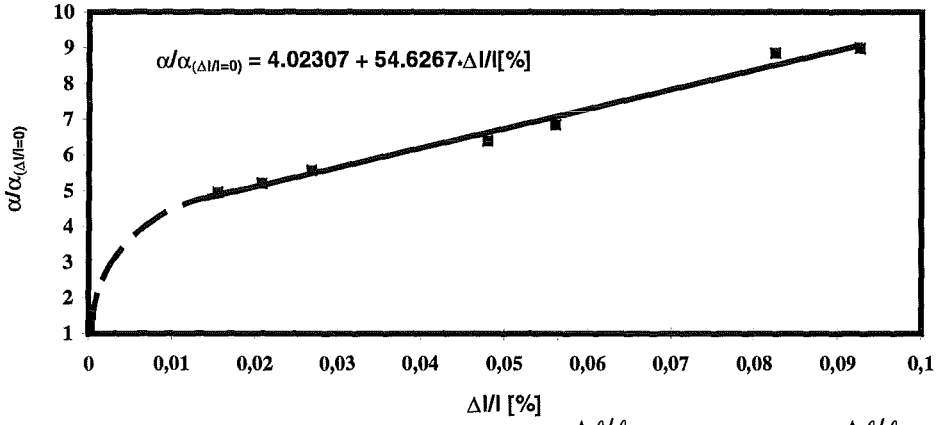

Fig. 4: Heat transfer coefficient at the wall as a function of $\Delta\ell/\ell$ (case with constraint: $\Delta\ell/\ell > 0$).

The equation correlating the experimental results for the heat transfer coefficient is:

$$\alpha\left[W/cm^2K\right] = 6.138\cdot10^{-2}\cdot f\cdot\exp\left(0.0035332\cdot T_w\right)$$

with:

$$f = 4.023 + 54.63\cdot\frac{\Delta\ell}{\ell}[\%] \qquad for \quad \frac{\Delta\ell}{\ell}\geq 0.015$$

and

$$f = 1 \qquad for \quad \frac{\Delta\ell}{\ell}[\%] < 0.015\%$$

Literature:

[1] M. Dalle Donne, et al., "Measurement of the Thermal Conductivity and Heat Transfer Coefficient of a Binary Bed of Beryllium Pebbles". Proceedings of the 3rd IEA International Workshop on Beryllium Technology for Fusion, Mito, October 22-24, 1997.

Staff:

M. Dalle Donne
G. Piazza
F. Scaffidi-Argentina
H. Werle

Chemical Analysis of Unirradiated Beryllium Pebbles

Beryllium intermediate product for the fabrication of spheres with diameters of 0.1 and 2 mm was produced by a modified Kroll process. In is final processing step, the digested beryl mineral was reduced by Mg to Be metal (melting point 1289°C) according to the reaction BeF_2 + Mg = Be + MgF_2. Different precipitates were observed in metallographic sections of the material which was analysed by wavelength dispersive X-ray microanalysis including that of Be. The main impurity phases were $Be_{13}Mg$, Be_{13}(Mg, Zr, U), Mg_2Si, Mg-Al phases and Al_2O_3. The two-phase Mg-Al precipitates have the lowest melting point at 437°C. Annealing between 790 and 690°C had no influence on the composition of the phases. The material was used for the irradiation experiments CORELLI-2, Be/Pe and EXOTIC-7 [1,2].

As the concentration of the impurity phases was high the Be intermediate product was submitted to a successive refining operation through vacuum melting by means of which the volatile components (e.g. Mg) were removed from the Be melt. Thereupon the melt was sprayed by an inert gas jet forming 0.1 to 0.2 mm diameter spheres. Especially the Mg concentration was reduced to less than 0.01 %. The main impurity phases observed in metallographic sections were Al_5Fe_2 (melting point 1169°C; possibly also in the composition Al_3Fe, peritectic point about 1160°C) and SiC (peritectic point 2830°C). Annealing of the material between 870 and 690°C did not result on principle in different impurity phase compositions. SiC reacted to silicides of Cr, Fe and Mg. The solubility limit of the major impurity elements in Be at 800°C is: 0.010 mol % Fe, 0.010 mol % Al, 0.006 mol % Si, < 0.004 mol % Mg, 0.002 mol % Cr [3].

The formation of the suggested phase $AlFeBe_4$ could not be confirmed that would have been expected according to the phase diagram of the ternary Al-Be-Fe system [4], see fig. 1. The observed maximum solubility of Al and Fe in Be at 800°C is marked by a solid circle in the figure. Probably, the Fe/Al ratio in Be is too low for an $AlFeBe_4$ formation. The high annealing temperature of the Be pebbles could also be a reason for the disappearance of $AlFeBe_4$ because this phase decomposes above 850°C [5].

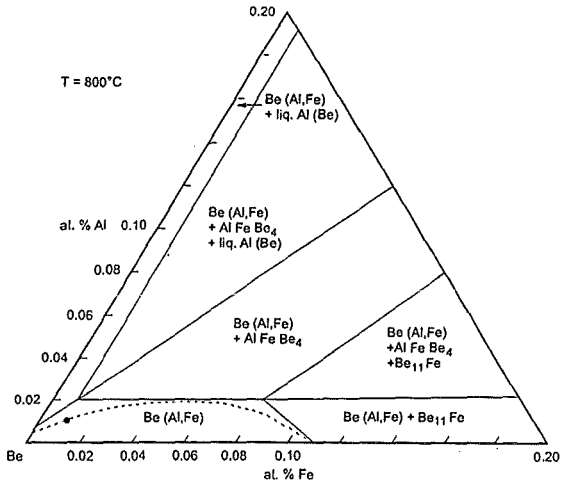

Fig. 1: Isothermal section of the Be apex of the ternary Al-Be-Fe system at 800°C (from Myers and Smugeresky [4]) and solubility limit of Al and Fe in Be measured by X-ray microanalysis [3].

Literature:

[1] H. Kleykamp, H. D. Gottschalg, in PKF annual report 1995/96 (1997) 11

[2] H. Kleykamp, H. D. Gottschalg, IMF-Ber. 026, PKF-Ber. 070 (1996)

[3] H. Kleykamp, H. D. Gottschalg, IMF-Ber. 045, PKF-Ber. 117 (1998)

[4] S. M. Myers, J. E. Smugeresky, Met. Trans. A 7 (1976) 795 and A9 (1978) 1798

[5] H. D. Rookbsy, J. Nucl. Mater. 7 (1962) 205

Staff:

H. Kleykamp
H. D. Gottschalg
E. Kaiser

B 9.2.1
Behaviour of Beryllium Pebbles under Irradiation

Beryllium pebbles are being considered in fusion reactor blanket designs as neutron multiplier. Examples are the European Helium Cooled Pebble Bed (HCPB) DEMO Blanket and the ITER Reference Breeding Blanket [1,2]. Solid breeder blankets with lithium ceramics as breeder and steel as structural material require beryllium to increase the tritium breeding ratio (TBR) performance. In the present HCPB DEMO as well as in the ITER breeding blanket design the beryllium is used in form of small pebbles. Because it is important to achieve a high beryllium density in the blanket a binary bed of larger and smaller beryllium pebbles is used, which allows to achieve a bed packing factor of about 80%.

Based on safety considerations, tritium produced in beryllium during neutron irradiation represents one important issue. In fact, due to the relatively slow tritium release at normal blanket temperatures, tritium is accumulated in beryllium but may be released during an uncontrolled temperature increase. Therefore, for safety considerations a good knowledge of tritium inventory and release kinetics is important. In this paper the results of a first series of long-time out-of-pile annealing experiments with two types of beryllium pebbles are presented.

1. Experiments

1.1 Samples and Irradiation Conditions

The material used for the analyses consists of two types of beryllium pebbles with a diameter Φ of 0.1-0.2 mm and 2 mm, produced by the Brush Wellman company. The 2 mm pebbles were produced by the Fluoride Reduction Process (FRP), which is an intermediate step in the process of winning beryllium from ore [3]. Since they are an intermediate product their shape is generally not perfectly spherical and these pebbles contain significant amounts of impurities, notably fluorine and magnesium. The 0.1-0.2 mm pebbles were made by the Rotating Electrode Process (REP). This process consists of arc melting the end of a long beryllium cast cylinder which is rotating about its axis. Molten droplets of metal are thrown off the end of the rotating cylinder and solidify in flight. As angular velocity of the beryllium target increases, the pebble diameter and the variation in the pebble diameter are reduced. Sharp particle size distribution and controllable pebble size are the characteristics of this method. Possible pebble diameter from the REP is from 0.2 mm to 2.5 mm [4]. Before irradiation, mixtures of large and small pebbles were dried by purging them with helium at 650 °C for 3 hours and filled into steel capsules. The capsules were evacuated, then filled with 1.1 bar helium and closed by welding. The capsules were irradiated over four reactor cycles in the HFR-Petten reactor (irradiation "Beryllium") at a temperature of about 420 °C to a fast neutron fluence (E_n >1 MeV) of about $1.0 \cdot 10^{21}$ cm^{-2} [5]. After irradiation the samples were handled under inert atmosphere before annealing.

1.2 Facilities and Procedures

After removal from the reactor the tritium inventory of several samples was determined by heating up to 1100 °C and purging them with 50 SCCM He+0.1vol% H_2. For tritium annealing investigations, the samples were inserted at definite positions in a tube furnace to achieve the desired annealing temperatures of 380, 450, 550 and 650 °C and were purged with 50 SCCM He+0.1vol% H_2 for two months. After removal from the annealing furnace, the residual tritium inventory was determined by purging and heating the samples up to 1100 °C in the tritium release facilities. For the 0.1-0.2 mm REP pebbles all tritium is already released after several hours at 1000 °C. On the other hand, this temperature is not high enough to release all the tritium from the 2 mm FRP pebbles which require a temperature of 1050 °C. In fact, by heating some 2 mm FRP samples to even higher temperatures, it has been checked that essentially all tritium is released at 1050 °C within several hours. The tritium activity of the purge gas is measured with an ionisation chamber. The heating procedure used for the annealing tests consists in a temperature linear ramp with 5 °C/min heating rate.

2. Results and Discussion

The measured specific tritium inventory after the in-pile irradiation is 1633±259 MBq/g and 1971±101 MBq/g for 2 mm FRP and 0.1-0.2 mm REP pebbles, respectively. The residual specific inventory after annealing is shown in the Figures 1 and 2 as a function of annealing time with the annealing temperature as parameter for FRP and REP pebbles respectively.

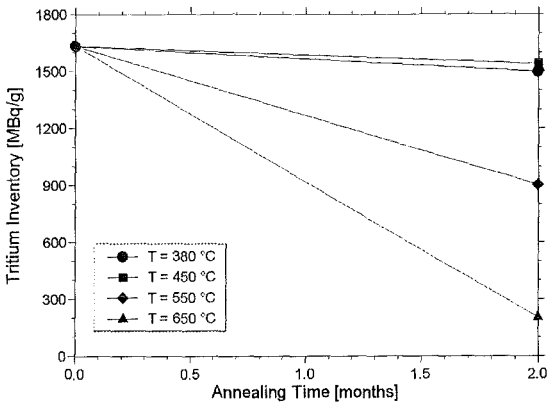

Fig. 1: Residual tritium inventory as a function of time for 2 mm FRP pebbles.

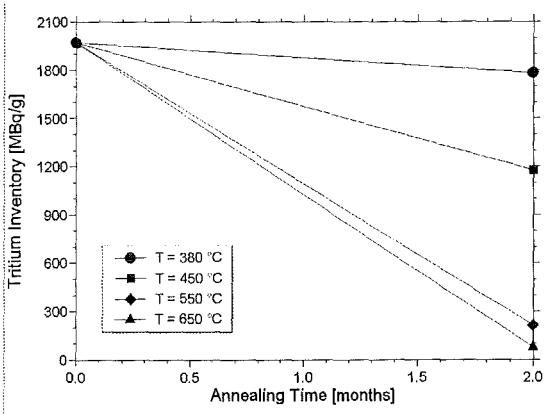

Fig. 2: Residual tritium inventory as a function of time for 0.1-0.2 mm REP pebbles.

In general the tritium release is very slow below 400 °C for both kind of pebbles, and less than 10% of the initial inventory was released after 2 months at 380 °C. The major difference between the two kind of pebbles becomes visible at 450 °C where the small REP pebbles release about 40% of the tritium inventory, while the larger FRP pebbles release less than 10%. At 550 °C the different tritium release of the small and large pebbles becomes even more significant (90% and 45% are released, respectively). At 650 °C the cumulative release was 88-96% for both kind of pebbles. The long-time inventory data are summarised in Table 1.

The pretty slow long-time release for both kind of pebbles is consistent with the tritium release kinetics observed in the tritium release tests with 5 °C/min heating up to 1100 °C (Figures 3 and 4). In these tests the release rate is generally very small below 600 °C and the maximum release rate is observed for the small pebbles at 810-820 °C and for the large pebbles between 1040 °C and 1080 °C.

3. Conclusions

Commercially available beryllium pebbles with 0.1-0.2 mm and 2 mm in diameter manufactured by Brush Wellman, USA, from two manufacturing methods and irradiated in the HFR were annealed up to 2 months at temperatures up to 650 °C in a flowing He+0.1vol% H_2 purge gas atmosphere. The inventory before and after annealing was determined by heating the samples up to 1100 °C with a He+0.1vol% H_2 purge gas.

In general, the tritium release is very slow below 400 °C for both kind of pebbles and less than 10% of inventory was released after 2 months at 380 °C. At 450 °C the small REP pebbles release about 40% of their tritium inventory, while the larger FRP pebbles release only less than 10%. At 550 °C the different tritium release among small and large pebbles becomes more significant and the release is about 45% and 90% for the large and small pebbles respectively. After 650 °C the cumulative release was 88-96% for both kind of pebbles.

These results are consistent with the tritium release kinetics observed in the short time tritium release experiments. In these tests the release rate is very small below 600 °C and the temperature at which the maximum release rate is observed ranges between 810 °C and 820 °C in case of the small REP pebbles, while for the large FRP pebbles it ranges between 1040 °C and 1080 °C. This fact may be of a great importance for in-reactor operation especially in case of off-normal conditions.

Literature:

[1] M. Dalle Donne et al., "Development of the EU Helium-cooled Pebble Bed Blanket", in Proceedings of the 4th International Symposium on Fusion Nuclear Technology, Tokyo, Japan, April 6-11, 1997. To be published.

[2] K. Ioki, M. Ferrari, "ITER Final Design Report, Design Description Document WBS 1.6B, Tritium Breeding Blanket System". To be published.

[3] D.E. Dombrowski, Personal Communication, Brush Wellman, 1997.

[4] T. Iwadachi et al., "Production of Various Sizes and Some Properties of Beryllium Pebbles by Rotating Electrode Method", in Proceedings of the 3rd IEA International Workshop on Beryllium Technology for Fusion, October 22-24, 1997, Mito City, Japan, pp 33-38.

[5] R. Conrad and R. May, "Project D282.01, Beryllium, Final Irradiation Report", Report HFR/95/4262, Petten, May, 1995.

	2 mm FRP Pebbles		0.1-0.2 mm REP Pebbles	
Inventory [MBq/g] / T_{ann}[°C]	Before annealing	After 2 months (Residual Inventory)	Before annealing	After 2 months (Residual Inventory)
380	1633 ± 259	1499 (91.8%)	1971 ± 101	1782 (90.4%)
450	1633 ± 259	1540 (94.3%)	1971 ± 101	1176 (59.7%)
550	1633 ± 259	903 (55.3%)	1971 ± 101	213 (10.8%)
650	1633 ± 259	203 (12.4%)	1971 ± 101	77 (3.9%)

Table 1: Tritium specific inventory for small and large beryllium pebble

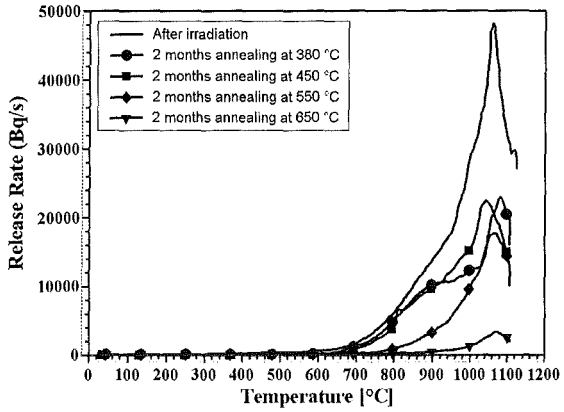

Fig. 3: Tritium release rate as a function of annealing temperature for 2 mm FRP pebbles.

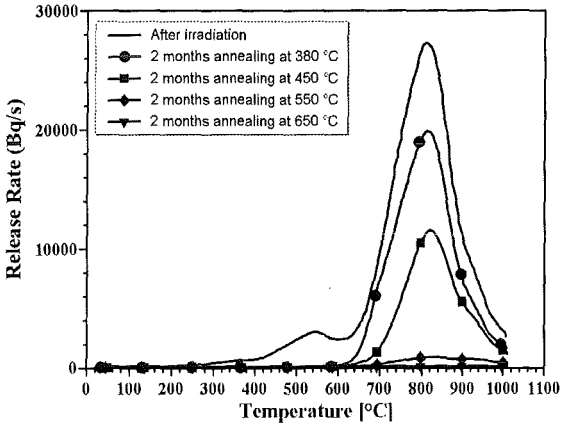

Fig. 4: Tritium release rate as a function of annealing temperature for 0.1-0.2 mm REP pebbles.

Staff:

E. Damm
M. Dalle Donne
D. Knebel
F. Scaffidi-Argentina
H. Werle
H. Ziegler

WP A 2
ITER Test Blanket Module Feasibility & Design

A 2.1.3
MHD Evaluation and Diffusion Bonding Technique Application

Although the MHD pressure drop is not a feasibility issue in the WCLL design, MHD effects nevertheless lead to new questions to be technically solved.

Therefore the **MHD-issues** of the WCLL-blanket [1] have been identified and evaluated [2]. It has been found that from the issues - 1) Fringing magnetic fields at the inlet and outlet of the blanket ($V_0 \perp B$), 2) manifolds/distributors at the blanket header (bends, in which the flow direction changes from parallel to *B* to perpendicular to *B*), 3) subdistributors in the blanket header (flow perpendicular to *B*), *4)* flow in parallel feeding/ draining ducts, 5) flow in parallel ducts of the breeding area and 6) the U-turn at the bottom of the blanket (see Fig. 1) - the flow in the subdistributors of the header (3) turns out to contribute most to the MHD pressure drop.

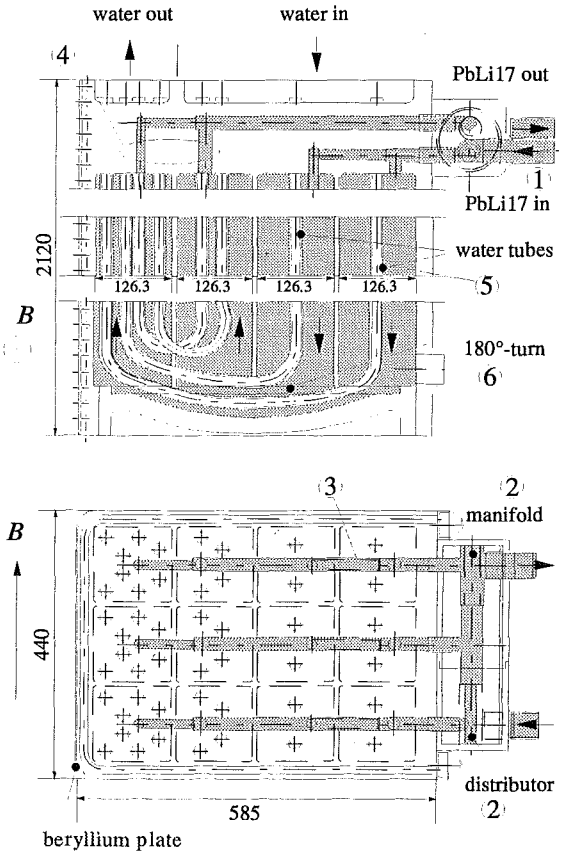

Fig. 1: Sketch of the water-cooled liquid lead blanket concept (WCLL) foreseen for the ITER test module. Top: Side cut of the module. Bottom: cross-section cut through the top of the blanket. The numbers denote MHD flow regions: 1. Flow in fringing field. 2. Manifold/ distributor. 3. Subdistributor perpendicular to B. 4. Feeding/draining pipe flow. 5. Flow in breeding zone. 6. Flow in the U-turn

Therefore any attempt to reduce the overall MHD pressure drop of the circulated liquid metal has to start with the improvement of these channels. The other problem related with the MHD pressure drop is the flow distribution between the individual ducts. Especially the rather complex header requires a MHD adapted design to guarantee the required flow rate in each channel. An electrical decoupling of the ducts would partially overcome the possible malfunctions. The study has also shown that at least a minimal convection flow is necessary to prevent tritium hot spots in regions where due to MHD effects the convective motion produced by the external circulation system (pumps) is suppressed.

In the frame of the design studies a concept modification has been proposed which improves the MHD behaviour with respect to the flow distribution in the large breeding zone channels and the pressure drop in the ducts of the Pb-17Li distributor (see Fig. 2).

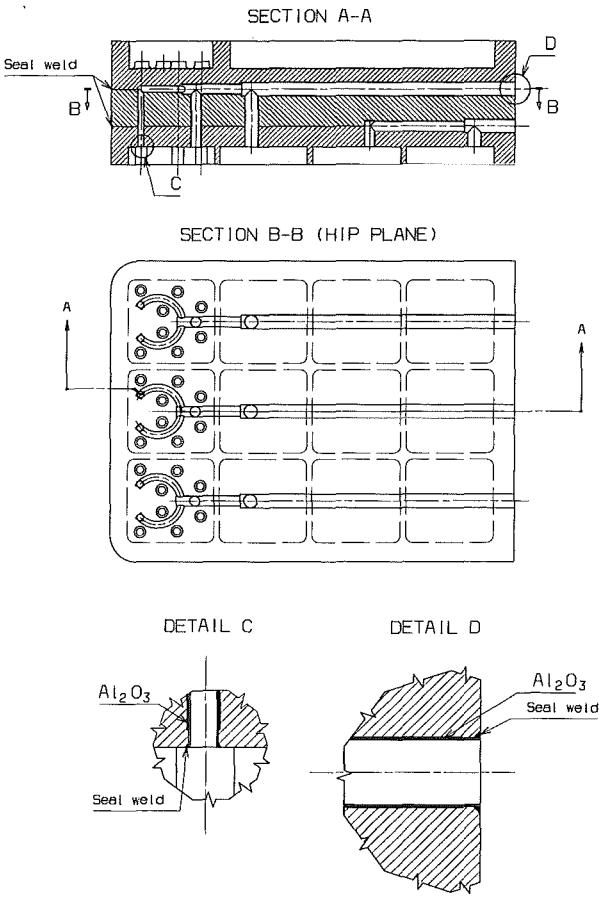

Fig. 2: Improved design of Pb-17Li ducts with flow channel inserts

The proposed design necessitates the manufacturing from three single plates which must be joined – after the machining of Pb-17Li ducts – by diffusion bonding in a hot isostatic press (HIP). Before bonding the faces to be joined must be sealed. At the outer surface this can easily be done by seal welding, whereas the inner ducts must be sealed by a thin-walled tube. Covering this tube at the outer surface with an electrically insulating ceramic layer provides a kind of a Flow Channel Insert (FCI) which had already been proposed earlier to reduce the MHD pressure drop in channels with coolant flow perpendicular to the magnetic field direction [3]. Calculations of the MHD pressure drop for the subdistributor holes with FCI's show a reduction by about a factor of 7 compared with the previous design without FCI's. Preliminary tests on the manufacturing of these FCI's are under way (see subtask A 3.4.2).

Additionally the magnethydrodynamic flow in ducts with infinitely thick walls corresponding to the conditions existing in the sub-

distributor channels is investigated. The flow is evaluated by an asymptotic analysis valid for strong magnetic fields. The solution for current and potential in the wall is obtained by the solution of an integral equation. For the special case of a circular pipe the results are confirmed by the use of conformal mapping. It is found that in circular pipes the velocity profile is of slug flow type. In square ducts high velocity jets are possible. These jets may be located along the diagonal or along the side walls if the diagonal or the side walls are aligned with the magnetic field, respectively. The pressure drop depends essentially on the ratio of the wall to the liquid metal electrical conductivity and may be considerably lower than in perfectly conducting ducts. For the WCLL conditions (SS-walls, LiPb as liquid metal and the corresponding dimensions) the MHD pressure drop is about 50% less than calculated with the standard correlations used up to now.

Literature:

[1] Fütterer, M. et al. 1996 DMT 96/349 SERMA/LCA/1911.

[2] Stieglitz, R.; Barleon, L. (1997), MHD aspects and experimental activities in fusion blanket designs, Proc. IEA Intern. Workshop on Liquid Metal Blanket Experimental Activities, Paris, France, Sept. 16-18, 1997

[3] John, H., Malang, S., Sebening, H. (editors) 1991, DEMO-relevant test blankets for NET/ITER, FZK Report 4908

Staff:

L. Barleon
S. Gordeev
K. Schleisiek

WP A 3
ITER Test Module Fabrication

A 3.4.2
Adaptation of Diffusion Bonding to TBM Box Fabrication

Within subtask A 2.1.3 a design modification was elaborated which uses flow channel inserts (FCI) to reduce the MHD pressure drop in the ducts distributing/collecting the Pb-17 Li in the tube plate of the ITER test module. The FCI is a thin-walled steel tube covered with a ceramic electrical insulater. To allow the insertion of the FCI's the tube plate is split into three layers which are joined subsequently by diffusion bonding (HIP). As a first step to develop this fabrication technique a small-scale test specimen was manufactured (see Fig. 1).

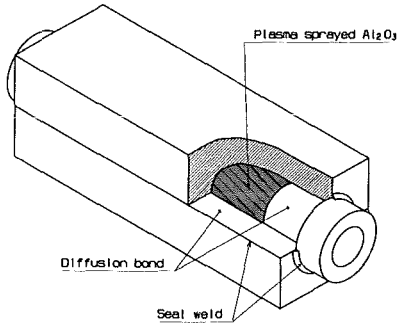

Fig. 1: Diffusion bonded test specimen with a "flow channel insert"

If the non-destructive examinations show a good quality of the specimen, it will be used in MHD tests to verify the effectiveness with regard to MHD pressure drop reduction. Subsequent destructive testing is envisaged.

Another manufacturing technology developed for the HCPB blanket with potential applicability to the WCLL blanket is the bending of plates with cooling channels, in case of the WCLL circular channels or inserted tubes.

For the manufacturing of the blanket structure the "DEMO fabrication scheme" is one alternative method. It includes bending of the FW plate to obtain the U-shape of the box. As the FW geometry is completely different from that of the HCPB FW, special tests were carried out to study the feasibility of the bending process, the accuracy of the bending angle, and the variations of the channel geometry during bending. The test plates (material MANET II) with a size of 300 x 114 mm had 3 cooling channels of 8 mm diameter produced by deep hole drilling. The plate thickness varied between 22 and 28 mm; one of the plates had an undulated surface according to the actual WCLL DEMO blanket design. The bending radius was 50 and 75 mm, respectively. Some channels were filled with an eutectic BiSn alloy as filler material.

The results of the non-destructive and destructive examinations of the bent plates can be summarized as follows: The bending procedure can be carried out at room temperature. To prevent instabilities the FW plate must be supported by a sandwich plate. Neither ruptures nor surface cracks of the bent plates could be found. The accuracy of the bending angle is better than one degree. The height of the cooling channels is reduced during bending by up to 14.5 %; the cross section reduction amounts to maximum 11 %. The use of a filling material reduces the deformation of the cooling channels significantly.

Further bending tests are envisaged on diffusion bonded FW plates with inserted steel tubes and Cu as compliant layer between the tubes and the plates.

Staff:

H.J. Fiek, Fa. TWK
S. Gordeev
T. Lechler
K. Schleisiek

WP A 4
Tritium Control and Permeation Barriers (PB)

A 4.1.2
Fabrication and Characterisation of Permeation Barriers made by Hot-Dipping

In the end of 1998 the coating qualification procedure for tritium permeation barriers on martensitic low activation steel has to be finished. FKZ/IMFIII developed a coating method which combines the hot dipping technology with an appropriate heat treatment in order to form an Al-based coating system which consists of a ductile Fe-Cr-aluminide layer and an alumina layer on top. This scale structure guarantees firstly a sufficiently high permeation reduction factor due to the alumina layer and secondly an Al activity below the alumina layer which from thermodynamical point of view should be high enough to enable rehealing in case of failure of the alumina layer.

The basic characterisation of the FZK standard coating on tubes and sheets has been carried out last year already [1,2]. Newer results describe the behaviour of the scale under stresses and additional heat treatment cycles. These results are important in regard to the compatibility of the permeation barrier production with the Double Wall Tube (DWT) and ITER test module fabrication sequence. Bending tests and HIP experiments were carried out. It was shown that the permeation barrier production on DWT is in perfect agreement with the proposed ITER test module fabrication sequence. However, bending of heat treated or HIPed DWT has to be avoided as demonstrated in Figure 1. HIPing can be used instead of an atmospheric heat treatment without any negative consequences for the scale structure.

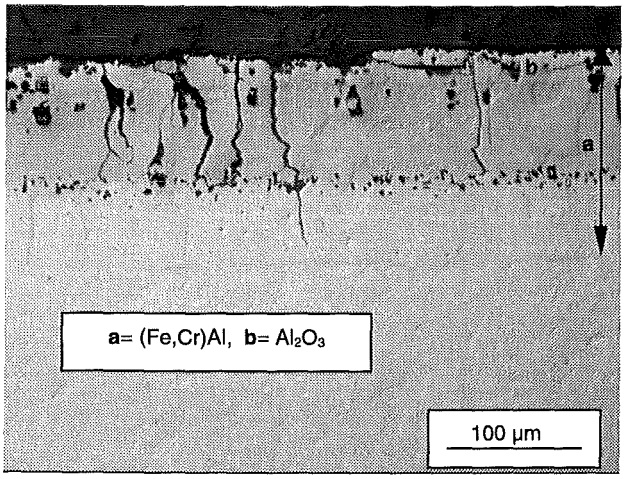

Fig. 1: Cross section of coated F82H-mod. sheet after about 10% bending. Cracks penetrate deep into the Fe-Cr-aluminide zone.

In the frame of the coating qualification procedure the H_2 permeation through the coating was measured in comparison to uncoated steel by a reference laboratory (JRC Ispra). Three coated sheet specimens have been tested in a temperature range between 250 and 450°C and at 1 bar H_2. For the first one, the alumina top layer was removed by polishing prior to testing in order to investigate the efficiency of the Fe-Cr-aluminide layer. The measured Permeation Reduction Factor (PRF) was about 500. The two other specimen were tested with the alumina layer on top. They showed PRFs of about 3000 and a high reproducibility. A PRF of 1000 was requested by the designer group. Therefore it can be concluded that the coating developed at FZK/IMFIII fulfils all requirements of an efficient tritium permeation barrier. Further permeation tests will be carried out at the reference laboratory on coated tube specimens. The permeation behaviour of the various coatings under cycling load and in Pb-17Li will be investigated.

Regarding the compatibility of the coating with Pb-17Li at 480°C and for a flow rate of about 0.3 m/s it must be said that up to an exposure time of 2000 h no attack could be observed. It is foreseen to continue the corrosion test up to 8000 h. Since FZK is reference laboratory for compatibility testing with Pb-17Li also the corrosion behaviour of coatings produced by other techniques (CVD+MOCVD, VPS) is investigated.

Literature:

[1] K. Stein-Fechner, H. Glasbrenner, J. Konys, O. Wedemeyer, FZK report FZKA 5926, June 1997

[2] H. Glasbrenner, K. Stein-Fechner, J. Konys, Z. Voß, O. Wedemeyer, FZK report FZKA 6079, March 1998

Staff:

H. Glasbrenner
J. Konys
K. Stein-Fechner
Z. Voß
O. Wedemeyer

A 4.2.2
Permeation Reduction Factors (PRF) in Gas and Corrosion in Pb17Li

A method to measure permeation rates of D_2 through metals under different conditions was developed and tested. The measurement of H_2 permeation is also possible to study isotopic effects. The limits of the method and possible errors were evaluated. The method can be used to investigate oxide coatings on metals, as requested for fusion reactors to reduce the loss of tritium.

In a first series of 10 experiments, permeation rates were measured for MANET (bare and oxidised at 500°C in air), molybdenum, nickel and Incoloy 800. For an upstream partial pressure of 1 bar D_2 the functions are in good agreement with the literature. The effects of oxidation by air, for Incoloy with a mixture of 0.3 mbar H_2O in a feed gas with 10.4 mbar D_2, and the possibility for insitu reduction of surface oxides by D_2 were investigated. The highest permeation rates for a metal were found after this reduction step, no surface effects were seen any more ($P \approx p^{0.5}$).

An internal FKZ report was published [1] describing the method of measurement and first results which also contains recommendations for future experiments to improve the accuracy of results and to avoid errors.

Literature:

[1] H. Feuerstein, S. Horn, Permeation of Deuterium through Metals, March 1998, internal report HIT 1/98

Staff:

H. Feuerstein
H. Glasbrenner
S. Horn
O. Wedemeyer

WP A 6
Safety related Activities for DEMO and ITER Test Module

A 6.2.3
Analysis of LOFA

The LOFA analysis for the WCLL TBM, intended as supplement to the studies performed for DEMO in 1996 and as comparison to the work performed by the WCLL team, has been dismissed because of unforeseen manpower shortage in 1997. Consequently, the sub-task objective has been revised as follows: Review of the WCLL TBM safety assessment and contribution to establishing near-term R&D needs in WCLL safety. Work is scheduled for the period Oct. to Dec. 1998.

Staff:

H. Kleefeldt

WP A 7
Demonstration of Blanket Reliability

A 7.1.3
Contribution to Common Blanket System Data Base

This Subtask is connected with the Tasks A 7.2.3 and B 7.1.3. All data used there will be inserted in a common data base. The use of the same data for different design options allows to limit error sources in comparative evaluations. The activity was continued as a permanent part of the reliability analyses

A 7.2.3
TBM System Availability

The availability/unavailability of the WCLL Test Blanket Module (TBM) including the Test Blanket Auxiliary Systems (TBAS) is an important factor concerning the availability of ITER. The availability is determined by failure rates and the mean repair/ exchange times (the down times for repair or exchange) of the components. There exist large uncertainties leading to different interpretations of the importance of systems and the definition of acceptable down times.

The large influence of the TBAS in particular the Pb17Li-System on the availability leads to explore the possibilities of operation at least temporarily without that system. As far as it will be possible is an open question yet, but in case of DEMO it seams to be impossible.

An operation of the TBM without a pressure suppression precaution inside the VV is not possible. The main reason for that is, the thermal expansion of the liquid metal which is four times higher than of the box structure material. Therefore, minor temperature changes would lead to a damage of the structure if the liquid metal circuit inside the VV is completely isolated by the valves (pressure tight). The pressure increase due to the production of T and He is an additional critical factor. While the increasing T concentration probably can be tolerated in view of the radioactivity concentration and probably also the solubility in the liquid metal, the production of He is critical. A rough estimation concerning the pressure increase by He production starting with a pressure of 2.5 MPa induced by the MHD pressure drop and assuming incompressibility of the liquid metal and in the structure show an increase of the pressure by 2.5 MPa/d, supposing continuos ITER operation.

A pressure control system between the TBM and the insulating valves outside the VV seams to be the simplest solution. But this possibility needs some more analysis work, probably also R&D. If finally the operation of the TBAS without a shut down of ITER in case of leakage and/or water-liquid-metal-reactions is still possible is at present intensively discussed but still an open question.

Literature:

C. Nardi, B. Bielak, M. Eid, T. Pinna, H. Schnauder, Availability of the European Test Blanket Systems and their Influence on ITER, 20th SOFT, 7-11 September 1998, Marseille, France

Staff:

H. Schnauder

WP A 10
MHD Effects

A 10.1.1 and 10.2.1
Evaluation of Natural Convection and Turbulence, Natural Convection Experiments

1. Introduction

In currently investigated liquid-metal (LM) blankets for fusion reactors the LM - a lithium-lead alloy - serves mainly as breeding material [1]. The externally forced flow required for a continuous circulation of the breeding material is very weak and has within the breeding zone typically mean velocities on a scale of a few mm/s. Therefore, buoyant flow may become dominant in the whole blanket influencing heat transfer and the distribution of the concentration of the tritium generated within the liquid metal breeder [2].

Buoyant flow in breeding blankets can be caused by temperature differences within the LM due to volumetric heating and the heat removal through the cooled walls and/or tubes. The knowledge of the velocity distribution is important for the evaluation of the heat transfer and is of special interest with respect to the concentration distribution of the tritium generated within the LM [3].

In order to avoid tritium hot spots in the corner near the first wall a transport velocity of at least 10^{-6} m/s is necessary.

Out of pile experiments on natural convection of volumetric heated LM under MHD-conditions cannot be realized because any electrical heating would interact with the MHD phenomena to be investigated. Therefore we decided to restrict our experiments to the investigations of the natural convection flow between a heated and a cooled plate. With the experimental verification of numerical results reliable predictions of the flow patterns appearing in the blanket can be made.

2. The experiment

In order to investigate the influence of the magnitude and the orientation of the magnetic field on the behaviour of natural convection three types of experimental arrangements are used (see Fig. 1), where the types b) and c) are the most relevant cases with respect to WCLL application.

a) Heat transfer by natural convection in a horizontal flat box with an aspect ratio 2 cm x 20 cm x 40 cm heated from below and cooled on the top wall with a vertical magnetic field.

b) The same box horizontally arranged in a horizontal magnetic field and

c) The vertical arranged box in a horizontal magnetic field. By this arrangement the conditions of the WCLL blanket are adapted and modelled.

The experiments are conducted in the normal conducting magnet (type a) experiment) or in the superconducting solenoid magnet (type b) and c)) of the MEKKA laboratory [3] which allow to measure in magnetic fields of up to 2.1 and 3.5 Tesla respectively.

The Test Section

A cross section through the test apparatus used for the type c) experiments is shown in Fig. 2. The heated side wall - a 20 mm thick copper plate - is heated by 40 electrical heater rods embedded and brazed in grooves in order to improve the heat transfer. This heater allows to operate with an electrical power up to 12 kW corresponding to a heat flux of up to 15 W/cm^2 and enables Rayleigh-numbers up to 10^5. The cooled wall - again a copper plate - is cooled and kept at constant temperature of about 100 °C by a boiling pool of water. All other walls are made of 1.5 mm stainless steel. To homogenize the boiling heat transfer a particle bed of glass spheres with a diameter of 5 mm is used. The vapor from the boiling pool is recondensed on a water cooled heat exchanger located outside the magnet.

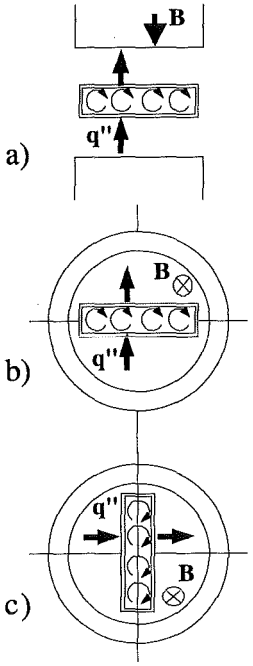

Fig. 1: The three types of experimental arrangement

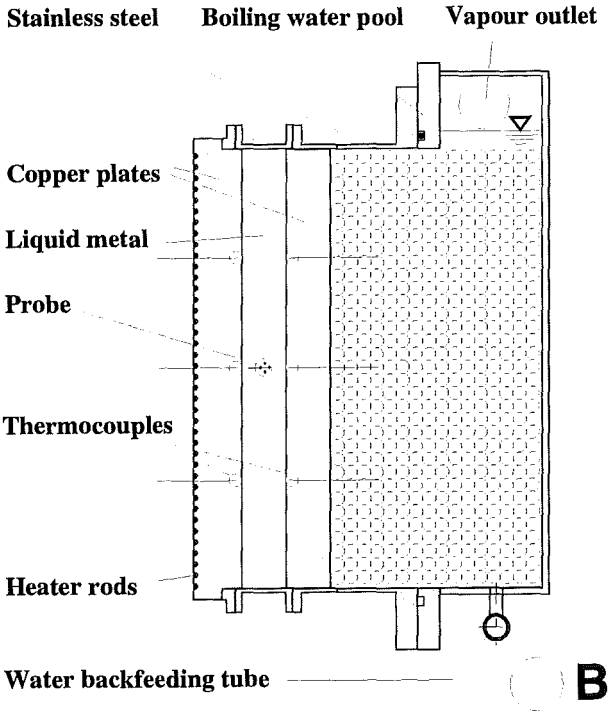

Fig. 2: The test section WUEMAG 2

The test section is modified from WUEMAG 1 by changing only the evaporation cooling system of the cold side wall (formerly the top wall) by displacing the insitu recondensation cooler to the outside. Therefore a more detailed description may be found elsewhere e.g. [3].

3. Theory: (2D) formulation of the problem

In three-dimensional (3D) magnetohydrodynamic flows the kinetic energy of vortices whose axes are inclined to the direction of the magnetic field is immediately removed by Joule's dissipation and the vortices will be strongly damped (see e. g. [5-8]). Vortices whose axes are aligned with the direction of the magnetic field are not affected by the field as long as the fluid is of infinite extend in the direction of the magnetic field. So if the magnetic field is strong enough a 2D flow pattern of convective rolls aligned with the direction of the magnetic field will evolve.

In the presence of Hartmann walls electric currents induced by the fluid motion are closing in the viscous Hartmann layers and in the electrically conducting Hartmann walls. Thus, the fluid motion is damped by an additional Lorentz force. Integrating along magnetic field lines, taking into account symmetry conditions and the thin wall condition, these 3D currents can be taken into account and the problem can be described by 2D equations (B is parallel to the x-axis):

$$\Delta_{yz}\Phi = \frac{b}{b+c}\omega, \qquad (1)$$

$$\frac{1}{Pr}\left[\partial_t\omega+\partial_y\psi\partial_z\omega-\partial_z\psi\partial_y\omega\right] = \Delta_{yz}\omega+Ra\,\partial_y T-\frac{\omega}{\tau}, \qquad (2)$$

$$\frac{1}{\tau} = \frac{M}{b}+\frac{M^2\cdot c}{b+c}, \qquad (3)$$

$$\partial_t T+(v\cdot\nabla)T=\Delta_{yz}T \qquad (4)$$

where

(x, y, z) is the Cartesian coordinate system,

Φ is the electric potential,

b is the half dimensionless extension of the layer in the direction of the magnetic field,

c is the wall conductance ratio $c=s\sigma_w/h\sigma$,

$\omega=(\nabla\times v)\cdot e_x$ is the vorticity,

ψ is a 2D stream function defined by $v=-\partial_z\psi$ and $\omega=\partial_y\psi$,

τ is a characteristic time scale for the decay of vorticity,

$1/\tau$ is the magnetic damping,

$Pr=\nu/\kappa$ is the Prandtl-number,

$\kappa=\lambda/\rho c_p$ the thermal diffusivity, λ the thermal conductivity, ρ the density and c_p the specific heat of the LM,

$Ra=\alpha\, g\Delta T h^3\kappa^{-1}\nu^{-1}$ is the Rayleigh number,

$M = h\cdot B\sqrt{\sigma/\rho\nu}$ the Hartmann number

with h the distance between the heated and cooled plate, B the magnetic field strength; σ, ρ and ν are the electrical conductivity, the density and the kinematic viscosity of the LM, T is the temperature.

The heat transfer is characterized by the Nusselt-number $Nu = q''\cdot h\cdot\lambda^{-1}\cdot\Delta T^{-1}$ with q" the heat flux and ΔT the temperature difference between two plates.

4. Results

Experimental:

The essential results of the type a) experiments are already published in [3]. Typical results from the type c) experiment - most relevant for WCLL application - are shown in Fig. 3a-c. When the Hartmann number is increased from hydrodynamic flow (M=0) first the Nusselt number increases to a maximum at M=75. If the magnetic field is increased further, the Nusselt number decreases down to Nu=1 at M=800 what indicates the state of pure heat conduction. Looking at the intensity of temperature fluctuations, in figure 3b, the values are increasing simular to the Nusselt number. Beyond the maximum the values are decreasing fast to zero and thus above M=200 laminar flow is indicated. Unless the flow is laminar above M=200 significant convective heat transport is indicated by the large Nusselt numbers. The occurance of a maximum in the Nusselt number can be explained by a significant change in the structure of the time dependent convective flow pattern. This is demonstrated in figure 3c on the two isotropy coefficients calculated from the fluctuating part of the temperature gradient recorded by a probe arranged in the midplane of the gap, (see Fig. 2):

$$A_y = \frac{\overline{(\partial_x T')^2}}{\overline{(\partial_y T')^2}} \qquad A_z = \frac{\overline{(\partial_x T')^2}}{\overline{(\partial_z T')^2}}$$

Starting from high values at M=0 both isotropy coefficients are decreasing with increasing magnetic field. Thus an evolution of the flow from its initially three-dimensional state at M=0 into an increasingly two-dimensional (2D) state is indicated. As 2D-flow is less dissipative the convective heat transfer is enhanced and leads to higher Nusselt numbers. Above M=75 the damping effect of the magnetic field becomes dominant and the Nusselt numbers decrease. In the region of laminar flow an evaluation of isotropy coefficients is not possible. But from the increasing tendency towards 2D-flow at higher Hartmann numbers we can assume even higher two-dimensionality. With the indication of 2D-flow above M=50 we can apply the above developed 2D-equations to predict heat transfer in fusion blankets.

The dimensionless numbers Nu, Ra and Pr are calculated using the thermophysical data of NaK taken from [4] at the mean temperature

$$\overline{T}=\frac{1}{2}\left(T_{Bot}+T_{Top}\right).$$

Theoretical:

In Fig. 4a and b the results of the 2D-calculations for the arrangement c), most relevant for WCLL application, are shown. In Fig. 4a the Nu-number as a function of the damping parameter $1/\tau$ is given for a Rayleigh-number Ra=10^5, where the damping parameter is given by

$$1/\tau = M/b'+M^2\cdot c/\left(b'+c\right)$$

with the Hartmann-number M as defined in Chapter 3, the wall conduction ratio $c = \sigma_W \cdot t_W / (\sigma_l \cdot h)$ and the dimensionless extension in the direction of the magnetic field $b' = b/h$.

In Fig. 4b the corresponding flow patterns are shown for an increasing damping parameter (from left to right).

From Fig. 4a we can see if the damping parameter $1/\tau$ will exceed 10^4 the Nusselt-number will decrease to 1.0 and a single big vortex will be expected. This may be the case for the WCLL application (M > 2000) where in the case of non electrically insulated structural walls $1/\tau$ may exceed this value. If the dividing walls as well as the cooling tubes are fully electrically insulated the damping parameter in some substructures may decrease to $1/\tau \leq 2.0 \times 10^3$. This means that in this case multirolls may appear improving the heat and mass transfer.

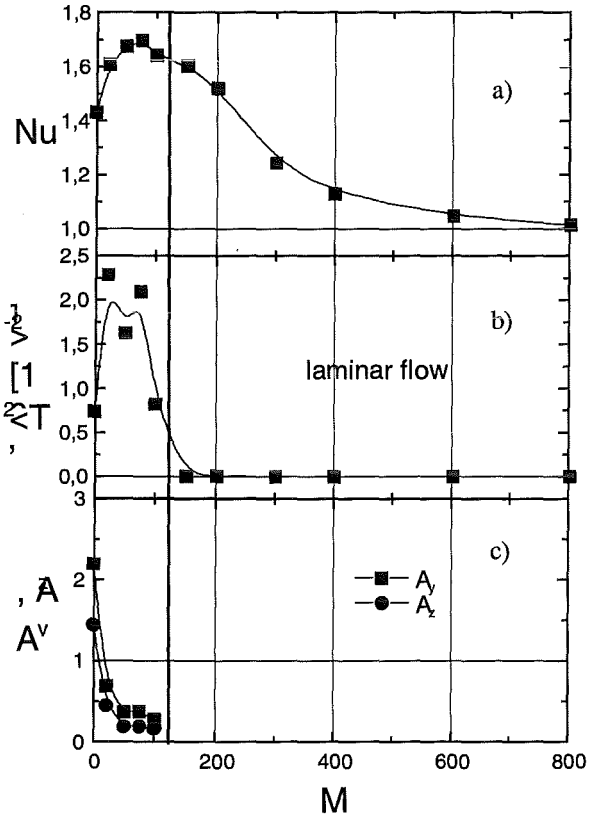

Fig. 3: The measured Nusselt-numbers Nu, the turbulence intensity $\langle T'^2 \rangle$ and the isotropy cefficients A for different Hartmann-numbers M at a constant power P=2400 W

5. Summary and Conclusions

Experiments on natural convection in a flat vertically oriented box with a horizontal magnetic field (type c) arrangement) are conducted. The measured dependence of the Nusselt number from the Hartmann numbers M at constant applied power show a complete suppression of any convection for $M \geq 800$.

The calculations made for the same arrangement relevant for WCLL application indicate that under fusion relevant conditions ($M \geq 5000$) even in the case of fully electrically insulated walls the convection pattern is reduced to one big vortex and the corresponding Nusselt number Nu decreases to 1.

Therefore we conclude that natural convection under fusion blanket conditions does not play an important role in improving the heat transfer but may help to avoid tritium hot spots.

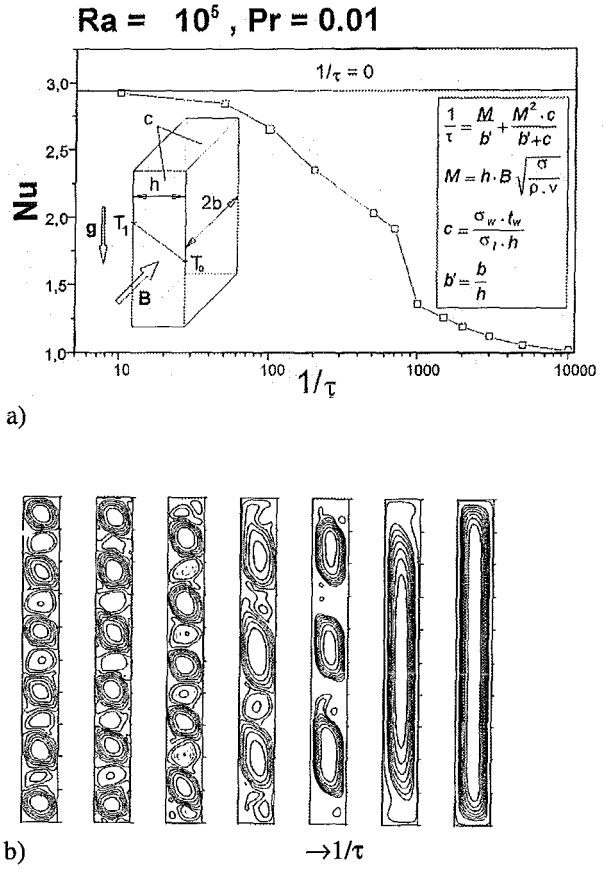

Fig. 4: Nusselt number as a function of the damping parameter $1/\tau$ and the corresponding flow patterns

Literature:

[1] Giancarli, L. et al. (1992), Water-cooled lithium-lead blanket design studies for DEMO reactor, Fusion Technology 21, 2081

[2] Stieglitz, R.; Barleon, L. (1997), MHD aspects and experimental activities in fusion blanket designs, Proc. IEA Intern. Workshop on Liquid Metal Blanket Experimental Activities, Paris, France, Sept. 16-18, 1997

[3] Barleon, L.; Burr, U.; Mack, K. J.; Müller, U. (1997) Natural Convection Phenomena in Magnetic Fields of Liquid Metal Fusion Blankets, Ref. [2]

[4] Barleon, L.; Mack, K. J.; Stieglitz, R. (1996) The MEKKA-facility, a flexible tool to investigate MHD-flow phenomena, FZKA-5821

[5] Lehnert, B. (1956), An instability of laminar flow of mercury caused by an external magnetic field, Proc. R. Soc. London, A 233, 299-310

[6] Kolesnikov, Y., Tsinober, A. (1972), An experimental study of two-dimensional turbulence behind a grid, Fluid Dynamics 9, 621-624

[7] Sommeria, J. Moreau, R. (1982) Why, how and when MHD turbulence becomes twodimensional, Journ. of Fluid Mechanics 118, 597-618

[8] Chandrasekhar, S. (1961) Hydrodynamic and Hydromagnetic Stability, Oxford University Press, Dover Publications, Inc. New York

Staff:

L. Barleon
U. Burr
M. Frank
Vollmer
K.J. Mack

SM 1.2.1, SM 1.3.1
MANITU Irradiation Program

1. Introduction

The MANITU irradiation and impact-toughness testing programme on promising low-activation ferritic/martensitic steels with an array of irradiation parameters covering doses of 0.2/0.8/2.4 dpa and temperatures of 250/300/350/400/450°C has been completed. Particular emphasis was to be laid on the further evolution of the impact properties with increasing dose at the different irradiation temperatures, and on the behaviour of the different alloys in comparison to each other, especially at the critical lower irradiation temperatures. The investigations had shown for irradiation parameters of 0.8 dpa that the US-heat, referenced as 'ORNL', had yielded the lowest ductile-to-brittle transition temperatures (DBTT).

During the irradiation experiment one specimen holder was removed after a dose level of 0.8 dpa and a new specimen holder containing 3 other materials has been inserted for an irradiation of up to 0.8 dpa again. The impact test data for these materials are now available.

2. Materials

The materials included in the second 0.8 dpa rig are: OPTIFER-IV, OPTIMAR and GA3X. OPTIFER-IV is part of the OPTIFER development series and therefore comparable to OPTIFER-Ia. OPTIMAR has been developed for conventional usage and is comparable to MANET-I. GA3X (manufactured by MITSUBISHI, delivered by BATTELLE, D.S. Gelles) is similar to F82H std. except for a higher Chromium content.

The tables below shows the main differences in the chemical composition of all materials within the MANITU program.

Alloy	Cr [%]	W [%]	V [%]	Ta [%]	B [ppm]
GA3X	9.2	2.1	0.31	0.01	-
F82H std.	7.7	2.1	0.19	0.02	-
ORNL	8.9	2	0.23	0.06	-
OPTIFER-IV	8.5	1.2	0.23	0.15	40
OPTIFER-Ia	9.3	1	0.26	0.07	61
OPTIFER-II	9.5	(1.2 Ge)	0.28	0.02	59

Alloy	Cr [%]	Ni [%]	Mo [%]	V [%]	B [ppm]
OPTIMAR	10.5	0.6	0.6	0.2	72
MANET-I	10.8	0.9	0.8	0.2	85
MANET-II	9.9	0.7	0.6	0.2	70

3. Experimental

The Charpy specimens have been produced parallel to the rolling direction (l-t) of the material plates and according to the European standard for sub-size specimens. The same type has already been used in our previous investigations to enable a direct comparison of the results. For the same reason, all tests have been carried out with the same instrumented facility which is installed in the Hot Cells. For each experiment the force-vs.-deflection curve was recorded and the impact energy was determined by integration. As usual this quantity was drawn against the test temperature and from this the characteristic values upper shelf energy (USE) and ductile-to-brittle transition temperature (DBTT, i.e. temperature at USE/2) were derived.

The irradiations of the MANITU programme were all carried out in the HFR, Petten.

4. Results

The results for an irradiation temperature of 300°C have been drawn up in Fig.1.

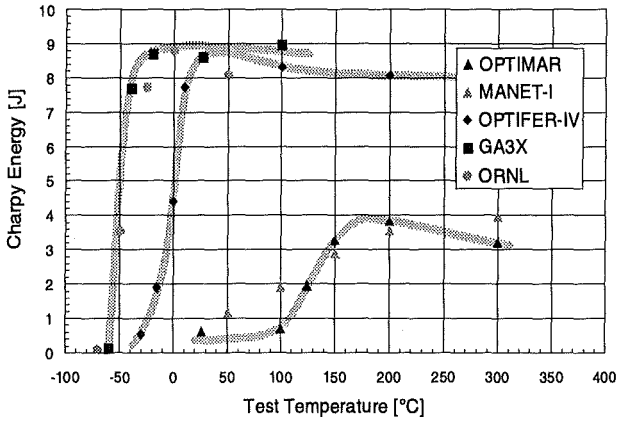

Fig.1: Impact Energy vs. Test temperature Curves

It can be seen, that both, DBTT and USE of the GA3X steel are in the range of the ORNL alloy and the results for OPTIMAR are slightly worse than for MANET-I.

5. Discussion

The negative influence of the B-content has been discussed in detail in [1]. The DBTT values of OPTIFER-IV and GA3X fit nicely into this discussion while the relatively high value for OPTIMAR (compared to MANET-I) can be explained by the low tempering temperature of 700°C. An overview of the DBTT is given in Fig. 2.

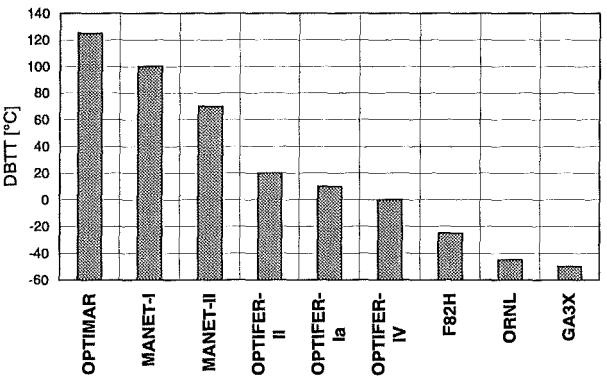

Fig. 2: DBTT after irradiation to 0.8 dpa at 300°C

Literature:

[1] M. Rieth, B. Dafferner, H.D. Röhrig, Proceedings of the ICFRM-8, October 26-31, 1997, Sendai, Japan.

Staff:

J. Aktaa
B. Dafferner
W. Kunisch
H. Ries
M. Rieth
O. Romer

SM 1.4.1/SM 6.2.2
Effects of Radiation Hardening and He in LAM / Fatigue properties under irradiation

The Dual Beam Facility of FZK, where α-particles (≤104 MeV) and protons (≤40 MeV) are focused onto a target, was developed as a research tool for materials within the European Fusion Technology Program. This high energy dual beam technique allows the simulation of fusion neutrons by systematic variation of hydrogen, helium, and damage production in thick metal and ceramic specimens as well as the simulation of Tokamak relevant thermal and mechanical loads in proposed plasma-facing materials. In the 4th frame program (1995-98) the investigations included:

- Comparison of the conventional steels with reduced activation steels for tensile and charpy properties, especially helium and dpa effects as well as microstructural stability (WP SM 1.4.1), and
- Effects of irradiation on fatigue properties for reduced activation steels including crack morphology investigations (WP SM 6.2.2).

In the following the activities done within the reporting period are summarized.

1. Characterization of irradiation effects on impact properties of martensitic 7-12% Cr-steels

Whether or not helium generated by inelastically scattered fusion neutrons will influence the impact properties at lower irradiation temperatures, is a matter of concern and subject of ongoing discussions. Therefore, changes in the charpy properties of the reduced activation type 8Cr-2WVTa steel F82H-mod after implantation of 300 appm Helium and 0.2 dpa at 250 °C have been investigated and compared with HFR irradiated specimens. The results are compared with investigations on neutron irradiated specimens having the same damage dose of 0.2 dpa but a much smaller helium content. Instrumented charpy impact tests are a very sensitive and thus useful tool for the alloy development, because irradiation causes an increase in the ductile-brittle transition temperature (DBTT) and, at higher damage levels, a decrease in the upper-shelf energy (USE). Both effects generally reflect a degradation in fracture toughness. To explain the experimental results, a model was developed that is able to distinguish between helium and displacement damage effects.

A stress induced cleavage fracture model has been applied to describe the observed irradiation hardening and helium embrittlement effects on the shift in ductile to brittle transition temperature DBT of martensitic 7-12% Cr steels. Due to the dynamic loading, multiple micro-cracking occurs in these steels within the plastic zone ahead of the crack tip. Micro-crack nucleation develops primarily at larger carbides (e.g. $M_{23}C_6$) and lath or primary austenite grain boundaries. Cleavage fracture by unstable micro-crack propagation is assumed to occur if the maximum principle stress at a characteristic distance ahead of the crack tip exceeds a critical value. Taking into account the sample geometry dependent stress intensity, this description corresponds to a condition where locally the material strength σ_{ε^*} is larger than the dynamic fracture stress σ_f^*; that is, as soon as the stress maximum inside that local zone reaches the dynamic fracture stress σ_f^*, unstable micro-crack coalescence occurs and the crack propagates catastrophically. Therefore the relationship

$$\sigma_{\varepsilon^*} \geq \sigma_f^* \qquad (1)$$

is valid below the transition temperature *DBTT* and characterizes the regime of dynamic quasi cleavage fracture. The arrival at the fracture stress σ_f^* is correlated with a critical local strain ε^* that initiates the unstable micro-crack propagation at a given critical micro-crack length l^*. Using the Griffith's criterion, the fracture stress can be written as

$$\sigma_f^* = \sqrt{\frac{4E\gamma_{eff}}{l^*\pi}} \qquad (2)$$

where γ_{eff} is the effective interface energy of helium bubbles dependent on plastic deformation and crack path. With this correlation the fracture stress depends on the microstructure by γ_{eff} and l^*, and is a function of temperature via the Youngs modulus E. On the other hand the strength $\sigma_{\varepsilon^*} = \sigma_0(\varepsilon^*) + \sigma_e(T,\dot{\varepsilon})$ can be characterised by the athermal stress $\sigma_0(\varepsilon^*)$ and the temperature depending flow stress component $\sigma_e(T,\dot{\varepsilon}) = P\exp(-\beta_d T)$. The parameter $\beta_d(\dot{\varepsilon})$ describes the temperature behaviour at the strain rate and P the Peierls stress, that is, the thermal flow stress at T=0 K. With this expression and eqs. (1)-(2) the temperature shift $\partial(DBTT)$ can be described by irradiation induced changes of $\sigma_0(\varepsilon^*)$ and σ_f^*:

$$\frac{\partial(DBTT)}{DBTT_0} = \frac{k_d}{P}\partial(\sigma_0(\varepsilon^*) - \sigma_f^*) \qquad (3)$$

In general $k_d(\beta_d) \geq e$, where *e* is the Euler number.. However, tempered martensitic 7-12% Cr steels are near the broad minimum $\beta_d = 1/T_0$, where the boundary value $k_d = e$ can be used as good approximation. Allowing an irradiation induced change $\Delta\sigma_f^*$ of the fracture stress and using for the irradiation induced hardening

$$\Delta\sigma_{irr} = \Delta\sigma_{a,i} + \Delta\sigma_{a,He} + \Delta\sigma_{e,i} \qquad (4)$$

the additive contributions $\Delta\sigma_{a,i}$ for athermal defects (e.g. loops, precipitates), $\Delta\sigma_{a,He}$ for helium bubbles, and $\Delta\sigma_{e,i}$ for small defects which could be thermally activated (e.g. Frenkel pairs, small defect clusters), eq. (3) can be written as

$$\frac{\Delta DBTT}{DBTT_0} \cong \frac{k_d}{P}\left[1 + \frac{\Delta\sigma_{a,He} - \Delta\sigma_f^*}{\Delta\sigma_{a,i}}\right]\Delta\sigma_{a,i} \qquad (5)$$

Because in our application $\Delta\sigma_{e,i}$ is much smaller than $\Delta\sigma_{a,i}$, the influence of $\Delta\sigma_{e,i}$ on k_d/P is also small. According to eq. (2), the temperature dependent reduction of the fracture stress can be written as $\Delta\sigma_{f,\Delta T}^* = 0.5\sigma_f^*\,\Delta E/E$. From eqs. (4) and (5) follows, that the irradiation induced total shift *ΔDBTT* of the ductile-brittle transition temperature depends primarily on the transition temperature $DBTT_0$ of the unirradiated material, on the Peierls stress P as well as on the athermal stress contribution $\Delta\sigma_{a,i}$. The influence of σ_f^*, $\sigma_0(\varepsilon^*)$ and $\Delta\sigma_{e,i}$ on *ΔDBTT*, however, is much smaller. *ΔDBTT* is also independent of β_d, as long β_d remains constant. Altogether, the shift in the transition temperature can be characterised for individual alloys by

plots showing $\Delta DBTT/DBTT_0$ versus $\Delta\sigma_{a,i}$. For such plots, the model predicts a linear to parabolic dependency.

At lower doses the irradiation hardening can be described fairly well by $\Delta\sigma_{a,i} \cong k_i\sqrt{dpa}$, while the hardening of helium bubbles might be given by $\Delta\sigma_{a,He} \cong k_{He}\sqrt{C_{He}}/d_{He}$ according to Orowan by-pass mechanism. k_i and k_{He} are temperature depending constants, C_{He} is the helium concentration inside the bubbles and d_{He} the bubble diameter. Helium bubble decoration of fracture relevant inner surfaces ($M_{23}C_6$ precipitates, lath boundaries) reduces the fracture stress σ_f^* by lowering the interface energy γ_{eff}. This behaviour might be expressed $\Delta\sigma_f^* \propto \sqrt{C_{He}}$ in a phenomenological way. With these assumptions, the irradiation induced relative shift $\Delta DBTT/DBTT_0$ should increase at lower doses in a linear way with $\sqrt{dpa}$ and $\sqrt{C_{He}}$ until asymptotic saturation is reached.

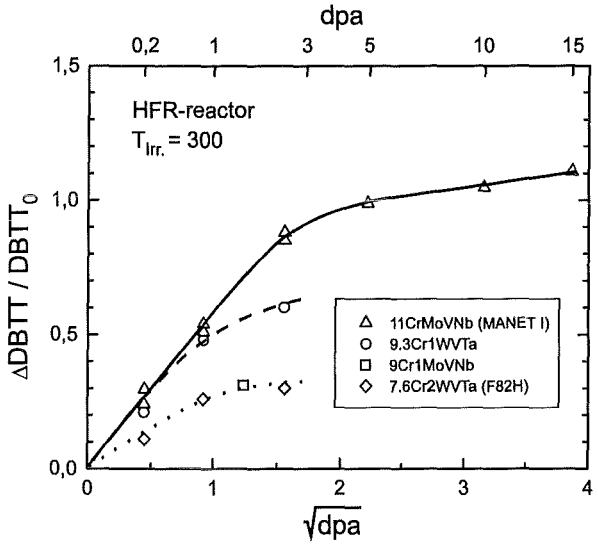

Fig. 1: Normalised shift of DBTT vs. displacement damage of various martensitic 7-12 % Cr steels following neutron irradiation at 300 °C.

Fig. 1 shows the irradiation induced increase of $\Delta DBTT/DBTT_0$ as a function of $\sqrt{dpa}$ for the conventional 11CrMoVNb steel MANET-1 and for reduced activation 7.6-9.3CrWVTa steels following neutron irradiation at 300 °C. The MANET-1 steel shows the strongest temperature shift and reaches at 5 dpa with a value of $\Delta DBTT/DBTT_0 \cong 1$ nearly saturation. The correlated proportional constants are $k_i \cong 201\text{MPa/(dpa)}^{-0.5}$ and P = 900 MPa. On the other hand the 7-10CrWTa steels, but also the 9Cr1MoVNb alloy, show a much smaller irradiation induced shift. With $\Delta DBTT/DBTT_0 \leq 0.3$ the F82H steel has the most favourable properties, and with P ≅ 1000 MPa, $K_d = e$ the related coefficient k_i amounts to only 76.5 MPa/(dpa)$^{-0.5}$. These k_i-coefficients determined from Fig. 1 are compatible with the irradiation induced hardening $\Delta\sigma_{irr}$ measured after cyclotron irradiation to 500 appm He and 0.3 dpa (Fig. 2). The irradiation conditions of the helium implantation of the tensile and charpy-V specimens are given in table 1.

Fig. 2 shows for the MANET-1 steel the observed influence of the irradiation temperature T_{irr} on $\Delta DBTT/DBTT_0$ after neutron irradiation to different damage doses. Obviously, $\Delta DBTT/DBTT_0$ depends in accordance with the irradiation hardening $\Delta\sigma_{irr}$ sensitively on irradiation temperature. It is important to note, that (i) in spite of the relatively high helium content of 85 appm, $\Delta DBTT/DBTT_0$ decreases above about 400 °C to small values ≤ 0.1 where the transition from irradiation hardening to softening occurs, and (ii) although this helium production is almost completed at 1 dpa, $\Delta DBTT/DBTT_0$ still increases significantly with damage dose below about 400 °C until a quasi saturation level is reached. These observations emphasise that in the long run of neutron irradiations the displacement damage induced hardening rather than the helium content dominates the embrittlement. The small $\Delta DBTT$ shift around 400 °C, where irradiation induced hardening and softening are almost balanced, might indicate directly that fraction of embrittlement that can be correlated with the helium induced reduction of fracture stress σ_f^*. That is, at 400 °C and 85 appm helium the helium related $\Delta DBTT$ shift would be about 35 °C.

Table 1: Parameters of the alpha-particle cyclotron irradiations

	Charpy specimens	Tensile specimens
T_{irr} (°C)	250	60-550
He^{++}-ion energy (MeV)	0-104	0-60
Damage rate (dpa/s)	(4.4-7.3) x 10^{-7}	(1.4-1.8) x 10^{-6}
He impl. rate (appm/s)	(6-10) x 10^{-4}	(2.5-3.0) x 10^{-3}
Damage dose (dpa)	0.22	0.30
He concentr. (appm)	300	500

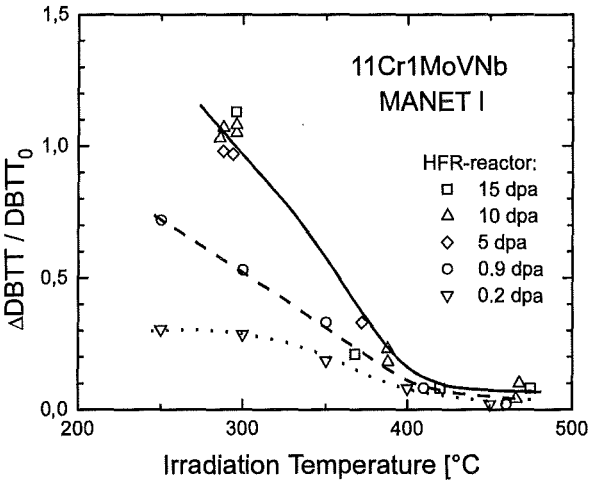

Fig. 2: Normalised shift of *DBTT* vs. irradiation temperature of the MANET-1 steel.

The effect of helium at the lower irradiation temperature of 250 °C was directly determined by the comparison of neutron irradiated (<8 appm He, 0.2 dpa) specimens with helium implanted (300 appm He, 0.2 dpa) ones. Fig. 3 shows, that after neutron irradiation the same low damage dose amounts to a $\Delta DBTT$ shift of 18 °C while a much higher shift of 42 °C has been observed after helium implantation.

In summary, the experimental data of this work mainly based on MANET-1 and F82H irradiations have demonstrated that under dynamic loading conditions helium can contribute clearly to the embrittlement of tempered martensitic steels. However, at temperatures below about 400 °C the tensile measurements after helium implantation show a significant contribution of displacement damage (loops, precipitates) to hardening. Whether this translates quantitatively into *DBTT* shift for neutron irradiated materials is experimentally not yet fully established. A phenomenological model is proposed that correlates the dynamic quasi cleavage fracture of tempered martensitic steels with irradiation induced changes of the strength and of the fracture stress. Although micro-mechanical and microstructural features are not yet included in detail, the model is able to distinguish quantitatively between helium and displacement damage induced embrittlement. It predicts that the relative shift in the ductile-brittle-transition temperature $\Delta DBTT/DBTT_0$ should be basically proportional to the square root of the dpa dose and, in an additive manner, also to the square root of the helium content which in turn is also not a fixed quantity, but depends on the evolution and characteristics of irradiation.

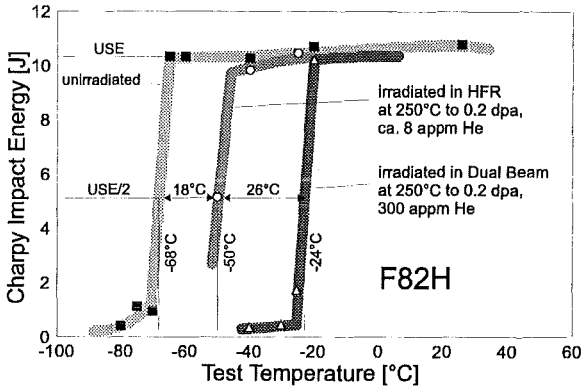

Fig. 3: Impact energy vs. test temperature curves showing the effect of helium and displacement damage in F82H-mod.

2. Fatigue Behaviour and Development of Micro-cracks in F82H after Helium implantation at 200-250 °C

In this work, strain controlled fatigue experiments have been performed on F82H followed by a detailed crack analysis. Fot this purposes, a cyclotron based irradiation programme with relevant helium accumulation was performed on suitable fatigue specimens having carefully polished surfaces. The application of a high resolution long-range optical microscope with subsequent REM and TEM analyses allows a direct correlation between crack morphology, microstructural details and fatigue data. Based on these methods, relevant results from the fracture analyses of the fatigue loaded reduced activation reference alloy F82H-mod are presented and discussed.

The tested hollow specimens had a square cross section optimized by elastic-plastic finite element calculations, a wall thickness of 0.40 mm and a gauge length of 10 mm. The heat treatment following the fabrication consisted of 1040°C/0.5h + 750°C/1h resulting in a fully tempered martensite with carbides mainly of type $M_{23}C_6$ which lie along former austenite grain boundaries and lath boundaries. Prior to fatigue testing some of the specimens were irradiated at a blanket relevant temperature of 250 °C with a degraded 104 MeV α-particle beam to get a homogeneous concentration of 400 appm helium within the gauge volume. Continuous strain controlled cycling has been applied at 200 °C with a cycle ratio of R=-1 and a strain range between $\Delta\varepsilon_{total}$=0.4% and 0.9%.

During every fatigue test several hundred scans with a surface area of 7.0x10.0 mm^2 were recorded by triggering the camera automatically at maximum strain at a predefined cycle N. The analysis of the surface cracks was performed by characterizing a crack or crack network as function of $N/N_{failure}$ in terms of total crack length, segment length L_n, segment density and orientation α_n with respect to the specimen axis. To assure proper statistics, more than 20.000 crack segments have been analyzed. After fatigue testing the fatigue specimens were further investigated by metallographic methods and by scanning and transmission electron microscopy.

All specimens fatigue tested at $\Delta\varepsilon_{total}$ = 0.9% show a high density of homogeneously distributed small micro-cracks, while at smaller total strain ranges of 0.4-0.5% the density of micro-

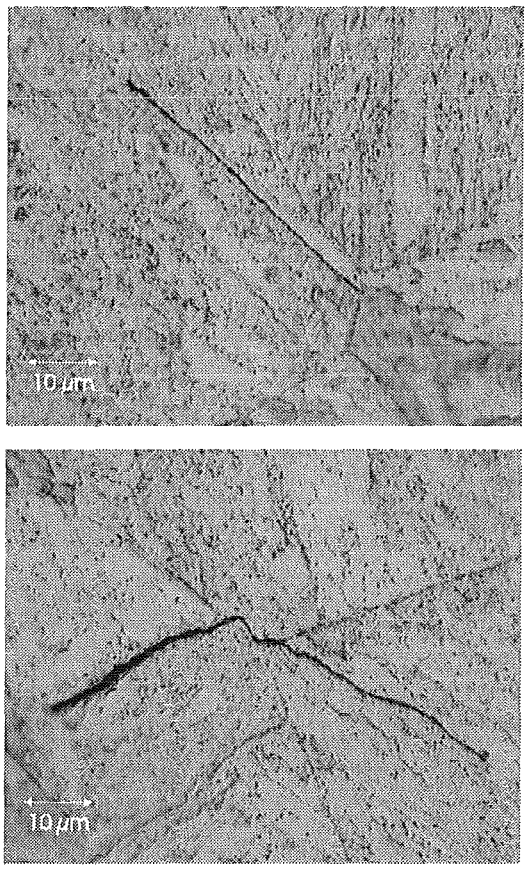

Fig. 1: Micrographs showing micro-cracks oriented along rows of $M_{23}C_6$ precipitates. Crack arrest (top) and change of direction (bottom) at a boundary.

cracks is also smaller. Apart from very few exceptions micro-crack initiation and propagation is observed inside the grains, that is, the fracture behavior is completely dominated by transcrystalline cracking.

Figure 1 shows clearly that the underlying microstructure has a considerable influence on the overall crack behavior. Practically all micro-cracks are oriented along Cr-rich precipitates mainly of type $M_{23}C_6$. These very fine secondary precipitates were formed at inner surfaces during the final heat treatment, that is, at grain and in the vast majority at lath boundaries. Microstructural barriers and the orientation of the martensite lath pack-

ages play an important role for the crack growth behavior. Often micro-cracks stop e.g at a grain boundary as figure 1 (top) shows. The propagation of a micro-crack into an adjacent grain or lath package is usually accompanied by a change of the crack orientation. A typical example for such a behavior is illustrated in fig. 1 (bottom). It became obvious during the crack pattern analyses that the orientation of the cracks is not uniformly distributed although the orientations of the martensite laths and consequently the rows of the segregated $M_{23}C_6$ precipitates are completely isotropic as careful statistical investigations have shown. With respect to the orientation distribution, the micro-cracks of both, irradiated and unirradiated specimens, can be classified into two categories (i) low $\Delta\varepsilon_t$ and (ii) high $\Delta\varepsilon_t$. This classification is based on a determination of the angle α_n between crack segment and load axis in steps of 10 degrees and is weighted according to the related accumulated segment length.

(i) Low total strain ranges (0.4-0.5%): After intrusions and extrusions have been developed, crack initiation starts slowly between N/N_f = 0.1and 0.2 with a pronounced maximum between 40 and 50 degree. Obviously an angle consistent with 45° which describes the orientation of maximum shear stress in the continuum is clearly preferred in this case. It is important to note, that at low strain ranges and perfectly polished specimen surfaces, micro-crack initiation starts practically without exception on intrusions and extrusions that develop in a first step in the direction of maximum shear stress along suitably oriented lath boundaries.

(ii) High total strain ranges (0.8-0.9%): After a few cycles micro-crack initiation and propagation start with an orientation maximum of crack segments between 50 and 60 degree. This maximum can be interpreted in a natural way by a superposition of two different crack initiation processes. The first one is the already mentioned shear stress driven plastic deformation along lath boundaries oriented close to 45 degree, while the second component can be attributed to interface separation induced by normal stress that has its maximum at 90 degree. At higher strain ranges the local stress and the related plastic deformation are obviously sufficient for interface separation e.g. between primary precipitates and the matrix.

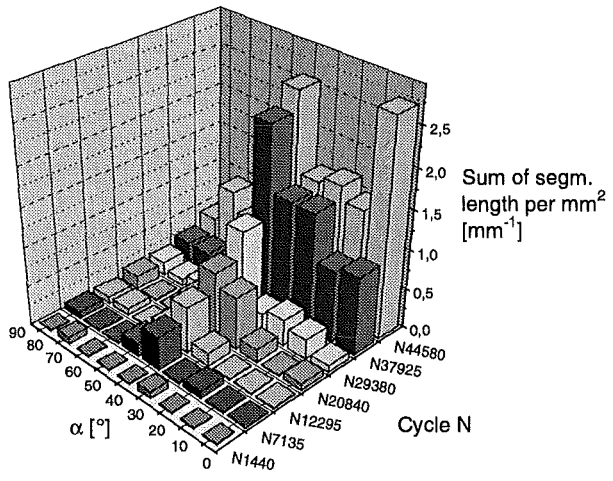

Fig. 2: Distribution of segments vs. N and angle to load axis for an unirradiated specimen tested at $\Delta\varepsilon_t$ = 0.44%.

The formation of branched cracks starts always with the development of individual cracks, that is, at the beginning of fatigue testing one crack corresponds to a single segment. In a second step either crack initiation increases the number of single cracks or the cracks propagate by keeping a low segment production rate. Depending on the total stain range and microstructural modifications prior to fatigue testing e.g. by irradiation, either mechanism can dominate. If single cracks start to coalesce or if the segment density is very high, crack interaction can no longer be neglected. This is why in this study the analysis is concentrated on crack segments and individual cracks rather than on the investigation of crack networks. The present investigations of the ferritic/martensitic steel F82H-mod confirm the general consensus of data published on many other materials, that during the initial phase of fatigue testing small micro-cracks are formed with high crack growth rates in unirradiated specimens independent of the strain range as shown in fig. 3. Once the segment length has reached 75(±10) µm, which corresponds closely to the mean grain diameter of this material, the crack stops or changes the direction. That is, within the whole strain range the micro-crack morphology in the unirradiated condition is largely controlled by microstructural barriers.

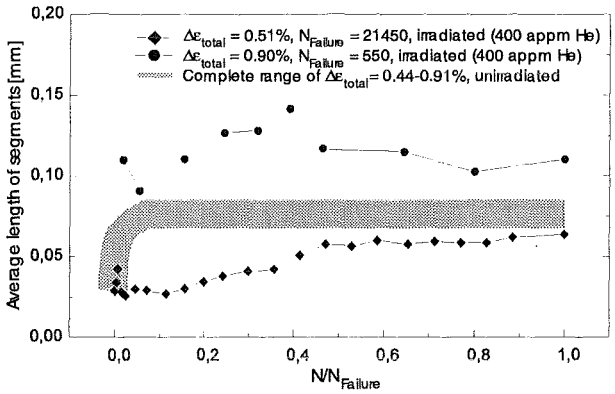

Fig. 3: Effect of strain range and pre-implantation of 400 appm helium at 250 °C on the fatigue crack growth behavior of the ferritic/martensitic steel F82H-mod.

The behavior of irradiated specimens, is quite different as fig. 3 shows. At high strain ranges microstructural barriers are surmounted already during the first few cycles and early network formation of cracks follows resulting in fatigue life reduction by a factor 5-7. In this case the early formation of cracks can be attributed to an increase of the total stress amplitude of almost 200 MPa due to irradiation hardening. However, at small $\Delta\varepsilon_{total}$ the total stress amplitude of irradiated and unirradiated specimens is not very different. In this case, the growth of micro-cracks is impeded by very small irradiation induced defects (e.g. dislocation loops, helium bubbles, defect clusters) before they are able to reach barriers like grain and lath boundaries, resulting in a lifetime which is two times that one of unirradiated specimens.

Literature:

[1] R. Lindau, E. Materna-Morris, A. Möslang, D. Preininger, M. Rieth and H.D. Röhrig; „Influence of Helium on Impact Properties of Reduced-Activation Ferritic/Martensitic Cr-Steels"; ICFRM-8 Conference, Oct. 25-30 1997, Sendai; Journ. Nucl. Mater. in press.

[2] D. Preininger, Werkstoffwoche'98, Okt 12 1998, Munich, Proceedings

[3] J. Bertsch, Mikroskopische Untersuchungen der Bildung von Ermüdungsrissen an zwei ferritisch-martensitischen Stählen im unbestrahlten und vorbestrahlten Zustand, FZKA Report 5984, September 1997.

[4] J. Bertsch, A. Möslang, H. Riesch-Oppermann, ECF-12 Conference, Sheffield, September 14-17 1998, Proceedings.

Staff:

S. Baumgärtner
J. Bertsch
G. Bürkle
R. Lindau
A. Möslang
D. Preininger

SM 2.1.4
Mechanical Properties & Microstructure of Reduced Activation Ferritic/Martensitic Steels (RAF)

Material Development

In the frame of the European Technology Program the Japanese steel F82H.mod. is being investigated parallel to the European steel OPTIFER. The characterization work on F82H-mod., in the as received condition 1075°38'+750°1h, and OPTIFER, in the reference condition 1075°30'+750°2h, are practically finished. An additional activity is to study the influence of preceeding ageing treatments, heat treatments with lower hardening temperatures (950-1000°C) and a temperature transient up to 875° on the creep rupture behaviour at 500°.

Work on F82H-mod. [1]

In the annual report 96/97 it had been shown, that ageing treatments (550°-600°-5000h) have no influence on the tensile properties, but that there is a clear shift to higher temperatures for the A_v/T-curves and DBTT. Results of creep tests in the temperature range 450-650° with rupture times to 7000h also showed no influence on 1% yield-limit and rupture time. The values are in the scatter band for the as received condition (Fig. 1).

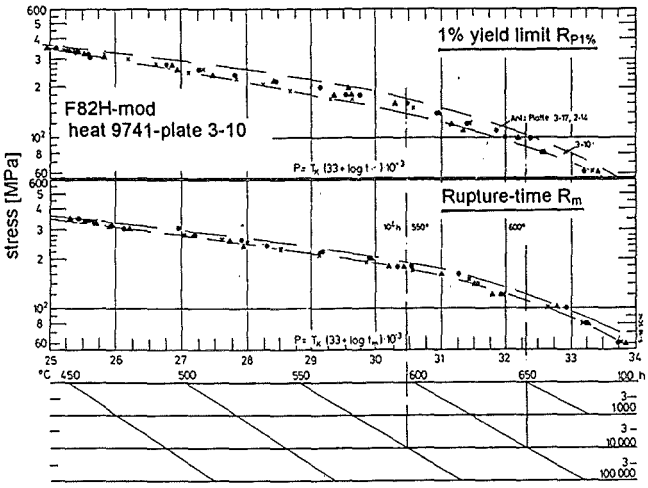

Fig. 1: Influence of ageing-treatments on 1% yield-limit and rupture time in a Larson-Miller-master curve

Included in this scatter band are also the results of specimens with a lower hardening temperature (950°+750°, 1000°+750° resp.). Creep tests for this heat treatments were made in the T-range 500-650° with rupture times up to 5000h.

Specimens in the as received condition were heated in the creep machine for a short time up to 875° (7-9'>Ac_{1b}) about 7-9°C higher than the Ac_{1b} temperature and cooled-down to the test temperature of 500°. Such a temperature treatment produces a mixed structure of annealed martensite, undercooled austenite and ferrite. The results of such creep tests with a T-transient show a significant reduction of the creep properties. These tests were made parallel to the dual-phase condition 875°+750°, which also show pronounced reduced properties in tensile and creep tests.

Work on OPTIFER [2]

Table 1 gives the composition of OPTIFER-variants which are investigated at FZK and which are precursors to the EUROFER 97 alloy.

The influence of variation of the hardening temperature on the tensile properties in the test range RT-700° has been determined for OPTIFER-alloys both with and without W. Both variants have the best properties for ultimate tensile strength R_m and yield-limit $R_{p0,2}$ in the reference condition 1075°+750°. With lower hardening temperatures (950°, 1000° resp.) we get a reduction of 15-20%. In creep- and creep-rupture tests (450-650°) this effect is even more significant (Fig. 2).

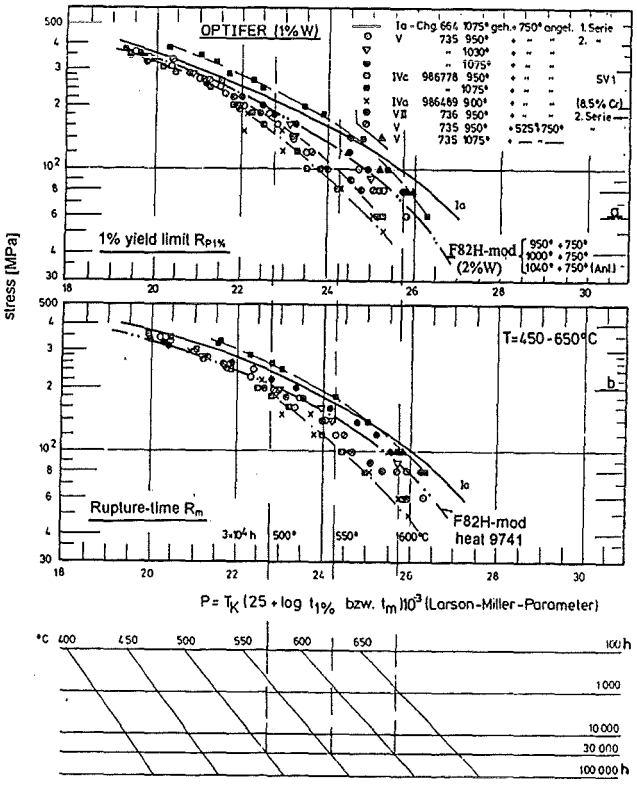

Fig. 2: Influence of the heat-treatment to the creep- and creep-rupture behaviour of OPTIFER-alloy in comparison with F82H-mod.

Therefore, in the reference condition (1075°+750°) the OPTIFER with W has a better creep behaviour than F82-mod., but worse behaviour with hardening temperatures in the range 950-1030°. On the other hand, the impact behaviour clearly improves with a lower hardening temperature.

Tests with different batches show also the strong influence of O_2-content. Contents of >100 ppm on impact properties have a strong negative influence on the A_v/T curve and DBTT shows a strong shift to higher temperatures. Investigations on the behaviour of a OPTIFER-W alloy after ageing treatments at 550°, 600°, 625°/5000h are presently performed for hardness, structure, tensile-, impact- and creep tests.

variant	heat	Cr %	C →	Mn	V	Ta	W	Ge	P ppm	S →	B	N_2	O_2	Ce	Remarks
Ia	664	9,3	0,10	0,50	0,26	0,066	0,96	-	46	50	61	155	47	<10	
Ib')	667	9,5	0,12	0,49	0,234	0,163	0,98	-	40	10	63	62	87	410	First series (with B) 25 kg heats
II	668	9,5	0,125	0,49	0,28	0,018	0,006	1,2	43	20	59	159	90	<10	SV4=melting vacuum induction furnace + remelting vacuum arc furnace
III	666	9,32	0,12	0,49	0,248	1,60	0,024	-	40	20	64	173			
IVa	986489	8,5	0,11	0,57	0,23	0,15	1,16	-	40	40	40	600	35		
IVb	986635	8,1	0,12	0,29	0,21	0,08	1,57	-		60	30	200		<20	SV1=open melting + remelting vacuum arc furnace 150 kg heats
IVc	986778	9,05	0,13	0,52	0,25	0,09	1,00	-	40	30	-	540	190	<20	
(≙Ia)	986779	9,35	0,12	0,54	0,26	0,07	1,03	-	40	30	-				
	986780	9,15	0,12	0,55	0,24	0,12	1,05	-	40	40	-				
	986781	9,35	0,12	0,57	0,26	0,08	1,00	-	30	50	-				
V (≙Ia)	735	9,48	0,115	0,39	0,245	0,061	0,985	-	35	25	2	225	60		Second series (without B) 25 kg heats SV4
VI (≙II)	734	9,35	0,125	0,61	0,275	0,083	0,005	0,38	43	30	2	250	160	<100	
VII (≙IVa+b)	736	8,38	0,09	0,37	0,205	0,069	1,03	-	36	25	2	263	170		

9-98-SCHI

Table 1: Chemical composition of the OPTIFER-alloys (without undesirable tramp-elements)

Literature:

[1] M. Schirra, A. Falkenstein, P. Graf, S. Heger, H. Kempe, M. Klotz, H. Zimmermann, „Der Einfluß der Vergütungsbehandlung, der Stabilisierungsglühung und einer Temperaturtransiente auf Gefüge und mechanische Eigenschaften des Stahles F82H-mod." Interner Bericht IMF/PKF, Juli 1998

[2] M. Schirra, S. Heger, H. Kempe, M. Klotz, H. Zimmermann, J. Lapeña, „Untersuchungen zu physikalischen und mechanischen Eigenschaften der OPTIFER-Legierungen". FZKA-6167, in press

[3] L. Schäfer, M. Schirra, ICFRM-8, 26.-31.10.97, Sendai, Japan, Beitrag S081-062, „Influence of thermal ageing on tensile and impact bending properties of the steel grades OPTIFER and F82H-mod.". To be published in J. Nucl. Mater.

[4] M. Schirra, Ch. Adelhelm, P. Graf, S. Heger, H. Kempe, H. Zimmermann, M.P. Fernandez, J. Lapeña, FZKA 6008, Dez. 1997, „Arbeiten zur Grundcharakterisierung am niedrigaktivierenden Stahl F82H-mod. Im Vergleich zu OPTIFER"

[5] E. Materna-Morris, M. Schirra, 20. Vortragsveranstaltung VDEh-„Langzeitverhalten warmfester Stähle und Hochtemperaturwerkstoffe", Düsseldorf, 28.11.97, Tagungsband, „Der Einfluß des Gefüges auf das mechanische Verhalten der niedrigaktivierenden martensitischen Stähle mit 8% Cr oder 9,5% Cr (F82H-mod. bzw. OPTIFER)"

[6] M. Schirra, K. Ehrlich, M.P. Fernandez, J. Lapeña, Jahrestagung Kerntechnik '98, München, 26.-28. Mai, Beitrag 810, Seite 597-800, „Auslegungsrelevante Festigkeitskennwerte des niedrigaktivierenden martensitischen Stahles F82H-mod."

[7] A. Hishinuma, A. Kohyama, R.L. Klueh, D.S. Gelles, W. Dietz and K. Ehrlich, „Current status and future R&D for reduced-activation ferritic-martensitic steels". ICFRM-8, Invited paper to be published in the Proceedings of ICFRM-8, in press

[8] K. Ehrlich, „structural materials for fusion reactors". Invited paper on CIMTEC'98 – Forum on New Materials, Florence, I, June 14-19, 1998. Proceedings in press

Staff:

E. Daum
K. Ehrlich
A. Falkenstein
P. Graf
S. Heger
E. Materna-Morris
L. Schäfer
M. Schirra
H. Zimmermann

SM 2.2.1
Fatigue and Creep Properties of Base Material F82H mod. and OPTIFER IV

1. Introduction

Structural components of a DEMO-blanket are subjected during service to alternating thermal and mechanical stresses as a consequence of the pulsed reactor operation. Of particular concern is the fatigue endurance of Reduced Activity Ferrite-Martensite (RAFM) steels like the Japanese steel F82H mod. and the German steel OPTIFER IV under cyclic strains and stresses produced by these temperature changes. In order to design such structures, operating under combined mechanical and thermal cycling, fatigue life has to be examined in isothermal fatigue tests for materials data generation and in thermal fatigue for verification of design codes.

In this report measured isothermal mechanical (LCF) and thermal low-cycle fatigue (TCF) data of the RAFM steels F82H mod. and OPTIFER IV are compared, partly to those of MANET II ferrite-martensite steel.

2. Experiments

Cylindrical samples of F82H mod. and OPTIFER IV, respectively - solid in case of LCF and hollow in case of TCF - have been used for the experiments. Both materials have been tested in air under LCF- and under TCF-conditions, respectively.

The LCF tests have been performed with computer-controlled MTS servohydraulic testing machines operating in strain controlled push-pull mode. Triangle wave forms are applied with constant strain rates of $3x10^{-3}$ 1/s in case of LCF tests. More detailed informations about the test procedure are received from [1].

For the LCF experiments, solid specimens of 77 mm length and of 8.8 mm diameter in the cylindrical gauge length of the specimen have been used. Where 21 mm is the initial gauge length of the axial extensometer.

The TCF test rig consists of a stiff load frame for mechanical clamping of the sample, which is directly heated by the digitally controlled ohmic heating device. Cylindrical specimens are used with similar outer dimensions as the above mentionned solid specimens, but with a wall thickness of 0.4 mm. Variable strain rates are applied at TCF test mode, due to the constant heating rate of 5.8 K/s and variable temperarure changes.

Since both, temperature and mechanical strain cycling are taking place, mechanical strain is available only after subtraction of the thermal strain from the net strain [2].

In case of LCF the influence of two different normalizing temperatures - 1075°C and 950°C - upon cylic lifetime on OPTIFER IV solid cylindrical specimens has been studied. In both cases the tempering temperature was constant with T=750°C. The results are compared to F82H mod. samples, which were tested in the tempered as received condition (Normalizing: 1040°C and tempering: 750°C).

3. Results

A comparison of isothermal fatigue behavior at a temperature of 450°C between the two RAF steels OPTIFER IVa and F82H mod. shows Fig. 1. For total strain ranges ≥ 1 %, the number of cycles to failure is nearly indentical. A different result can be seen at total strain range levels of less or equal 0.6 % for both RAFM steels. The isothermal fatigue lifetime of the OPTIFER IVa steel with the lower normalizing temperature of 950°C shows significantly better isothermal fatigue lifetimes as compared to the RAFM steels, normalized at higher temperatures (F82H mod. at 1040°C and OPTIFER IVa at 1075°C).

The comparison of thermal fatigue behavior between F82H mod., OPTIFER IV and MANET II with the higher normalizing temperatures in respect to total strain range vs. number of cycles to failure is depicted in Fig. 2. Both, the tempered F82H mod. and OPTIFER IV show at a temperature change of 200 - 600°C e.g. at increasing total mechanical strain ranges a drastic reduction in number of cycles to failure of about one order of magnitude compared to MANET II.

In respect to plastic mechanical strain range the comparison results for the thermomechanical fatigue behavior of the tempered F82H mod. and OPTIFER IV samples in much higher strain values than for MANET II. But the behavior still follows qualitatively a MANSON-COFFIN relationship.

The total stress range during thermomechanical fatigue of the tempered F82H mod. and OPTIFER IV samples result in much lower stress values than for MANET II.

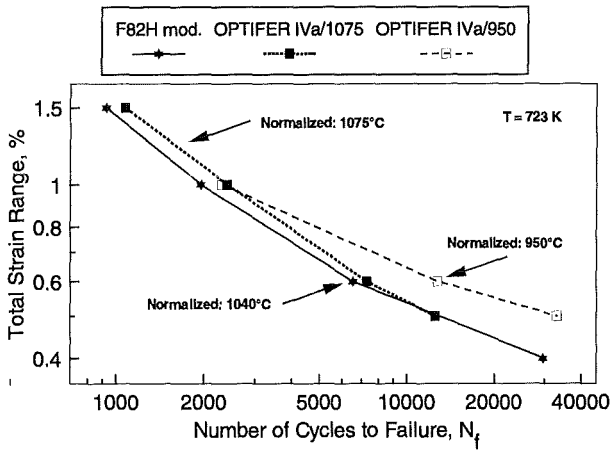

Fig. 1: Comparison of isothermal fatigue behavior between the RAFM-steels OPTIFER IV and F82H mod.

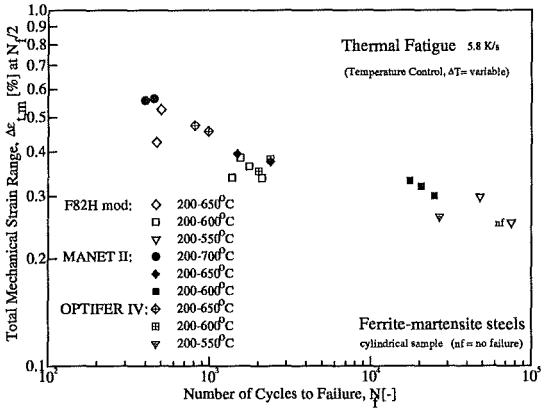

Fig. 2: Comparison of total mechanical strain range of thermal fatigue behavior between F82H mod., OPTIFER IV and MANET II.

4. Thermal fatigue round robin (TFRR)

The four participants of TFRR, which are ENEA, Italy, ENSTIM, France, JRC, Netherlands and FZK, Germany, performed thermal fatigue and thermomechanical fatigue tests in air atmospere with heating and cooling rates of about 5 K/s. The temperature range is defined to 200°C - 600°C. Mechanical clamping of the sample in case of thermal fatigue was performed at the low temperature (200°C) of the cycle. A total mechanical strain value in out of phase thermomechanical fatigue experiments had been choosen to 0.4%.

All partners performed a set of experiments and delivered the data to FZK, where they are analysed now and prepared to be reported on an ASTM symposium about thermomechanical fatigue in Nov. 1998 [3].

5. Postirradiation thermal fatigue experiments

In a German – Russian cooperation between FZK, IMF II, Karlsruhe and CRISM "Prometey", St. Petersburg, a programme for postirradiation thermal fatigue was defined. As irradiation facility the WWR-M-type reactor in Petersburg Nuclear Physics Institute (PNPI) with vacuum temperature control is used.

Neutron irradiation of Russian type cylindrical specimens with notches made from a Russian ferritic-martensitic steel 05K12N2M (Fe-05C-12Cr-2Ni-Mo) and the European ferritic-martensitic reference steel MANET II (10.3Cr-0.65Ni) to be thermal cyclically tested in the Russian postirradiation thermal fatigue test facility has been performed in the WWR-M-type reactor of PNPI with fluences of $1x10^{25}$ n/m^2 at a temperature of about 300 °C. Ampule devices with German type specimens made of F82H mod., MANET II and 05K12N2M had been qualified during an experimental irradiation in respect to temperature distribution, maintainance of constant irradiation-temperature of about 300 °C and neutron monitoring.[4]

Two types of postirradiation test facilities are available. In a Russian thermal fatigue facility first postirradiation tests already started and a modified German thermal fatigue facility is ready to be shipped to Russia.

6. Multiplicative model for thermal fatigue degradation

Available LCF data can hardly be used straightforward for a conservative prediction of lifetime of test blanket structural materials of International Thermonuclear Experimental Reactor (ITER) designed for essentially non-stationary thermal conditions. At the same time, TMF - data on candidate materials of test blankets are rather poor and very hard to accumulate. As a matter of fact, the working area for steels in ITER application (temperature range 150 °C to about 400°C and plastic strain range up to 0.3 %) is situated in the gap between the LCF- and TMF-data available.

A "straightforward" way of interpolation by due averaging the material response at LCF conditions over the temperature range in cycle appears to be non-conservative. LCF- and TMF-data of MANET-II steel, when represented in logarithmic axes in plastic strain range versus lifetime, allows, to employ a simple multiplicative model for TMF degradation (Fig. 3). According to this model, the strain-related LCF degradation at the mean temperature in cycle is multiplied by a factor reflecting the effect of temperature oscillation. On this basis an interpolation has been carried out between available LCF- and TMF-data, thus predicting TMF lifetime of this steel within ranges of plastic strain and temperature actually expected under ITER conditions. The latter ranges still are not covered by the thermal fatigue experiments performed on rigidly constrained specimens [5].

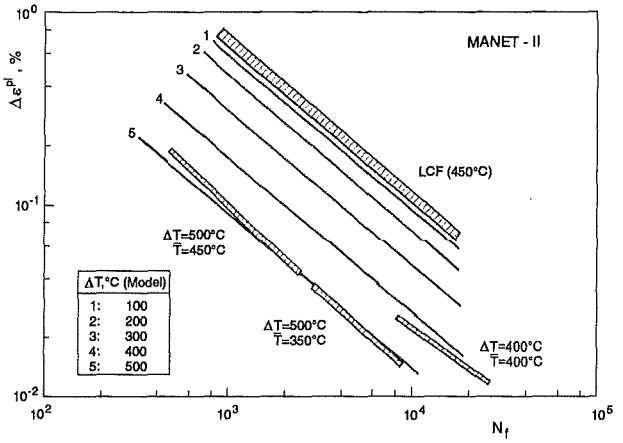

Fig. 3: Comparison of TMF and LCF data for MANET-II in plastic strain range, $\Delta\varepsilon^{pl}$ at $N_f/2$ versus number of cycles to failure, N_f

Literature:

[1] A. F. Armas, M. Avalos, I. Alvarez-Armas, C. Petersen and R. Schmitt: „Dynamic Strain Aging Evidences during Low Cycle Fatigue Deformation in Ferritic-Martensitic Stainless Steels", accepted for publication in a special issue of Journal of Nuclear Materials.

[2] C. Petersen: „Thermal Fatigue Behavior of Low Activation Ferritic-Martensitic Steels", accepted for publication in a special issue of Journal of Nuclear Materials.

[3] J. Bressers, G. Filacchioni, C. Petersen and F. Rézaï-Aria: „A European Round Robin in Thermo-mechanical Fatigue Behavior of a 9%Cr Low Activation Ferrite-Martensite Steel", to be presented on 3rd ASTM-Symposium on Thermomechanical Fatigue Behavior of Materials, 4.-5. Nov. 1998, Norfolk, Virginia, USA.

[4] L. Belyaeva, A. Orychtchenko, C. Petersen and V. Rybin: „Postirradiation Thermocyclic Loading of Ferritic-Martensitic Stuctural Materials", accepted for publication in a special issue of Journal of Nuclear Materials.

[5] A. Zisman, V. Rybin, C. Petersen and R. Schmitt: „Multiplicative model for out-of-phase thermal fatigue degradation of ferritic-martensitic steel MANET II", accepted for publication in Journal of Nuclear Materials.

[6] H. Kiewel, J. Aktaa and D. Munz: „Use of Viscoplastic Material Models in Thermocyclic Failure Analysis", in Proc. Of 19th Intern. Symp. on Modelling of Structure and Mechanics of Materials from Microscale to Product, Sept. 1998, Roskilde, Denmark.

[7] R. Kühner and J. Aktaa: „Numerical and Experimental Investigations of Temperature-rate Terms in Modelling the Inelastic Material Behaviour", in Proc. Of 4th Intern. Conf. On Low Cycle fatigue and Elasto-Plastic Behaviour of Materials, Sept. 1998, Garmisch-Partenkirchen, Germany.

[8] J. Aktaa, H. Kiewel and J. Turki: „Modelling of the influence of damage on the deformation behaviour by a self-consistant embedded cell model", accepted for publication in Computational Materials Science.

Staff:

J. Aktaa
M. Klotz
C. Petersen
M. Pfeifenroth
D. Rodrian
R. Schmitt

SM 3.8.1
Corrosion of RAF/M Steel in Liquid Pb-Li

The martensitic low activation steels MANET, Optifer IVa and F82H-mod. have been exposed to flowing Pb-17Li at 480°C for maximal 8000 h. The flow rate of the corrosive medium Pb-17Li was 0.3 m/s. In order to investigate the corrosion kinetic of the steels it was necessary to interrupt the test after 1000, 2000, 3000, 4000, 6000 and 8000h, to remove some specimens from the loop and to characterise their corrosion damage.

The corrosion rate, i.e. the metal loss rate, was determined by several methods. At first, the adherent Pb-17Li was removed from the specimen surface by washing in a mixture of CH_3COOH, H_2O_2 and C_2H_6O (1:1:1). After cleaning the specimens were weighed. The difference of the sample weight before and after testing is taken as a first indication of the amount of metal loss. Secondly, the remaining specimen diameter was measured. The difference between the diameter of the cylindrical corrosion specimens before and after testing is another value which describes the metal loss due to corrosion in Pb-17Li. However, the applicability of both described methods requires uniform corrosive attack, i.e. metal loss must occur uniformly over the whole sample surface. Cross sectional investigations have shown that this is not the case for the present investigations. In Figure 1 a typical example of the corrosion pattern of the studied steels is shown. Locally corrosive attack has occurred but even after longer exposure times there are still areas without any attack. Taking non attacked areas as a reference line the metal loss could be determined on the cross section using optical or electron microscopy.

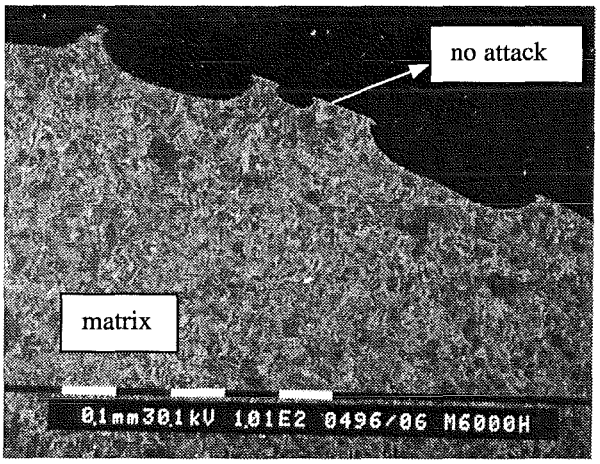

Fig. 1: Cross section of MANET (etched), exposed for 6000 h in Pb-17Li at 480°C.

Results of the metal loss measurements by means of SEM are indicated in Figure 2. The graphs reveal that the investigated steels show only small variations in the corrosion behaviour. For areas where attack has occurred the corrosion kinetic is not constant. It seems that the metal loss rate is more enhanced during the first 6000 h whereas it slows down with longer durations. Duplications of the test will have to validate this observation.

Investigations of the corrosion mechanism has revealed that for areas where no attack occurred a few nm thin Fe-Cr-oxide layer protects the material. This oxide has been formed probably by annealing after sample machining and gets desolved during sample exposure to liquid metal (Fe-Cr-oxides are not stable in Pb-17Li). Surface investigations of attacked areas revealed the existence of porous corrosion products which are composed of Fe, Cr, W, Mo, V and O. A first idea is that Fe and Cr get desolved in the liquid metal, leaving a matrix which is relatively enriched by the steel elements W, Mo and V which are known to have a very low solubility in Pb-17Li. Up to now it is not yet possible to give any information on the existing phases in the corrosion layer. More detailed analyses are foreseen. The corrosion pattern in Fig. 1 is an indication for the fact that the porous corrosion products are not adherent and spall off during exposure or during cleaning. In order to get information on the real state of the specimen in the loop it is foreseen for a next test series not to clean the specimens from the adherent Pb-17Li before cross section preparation.

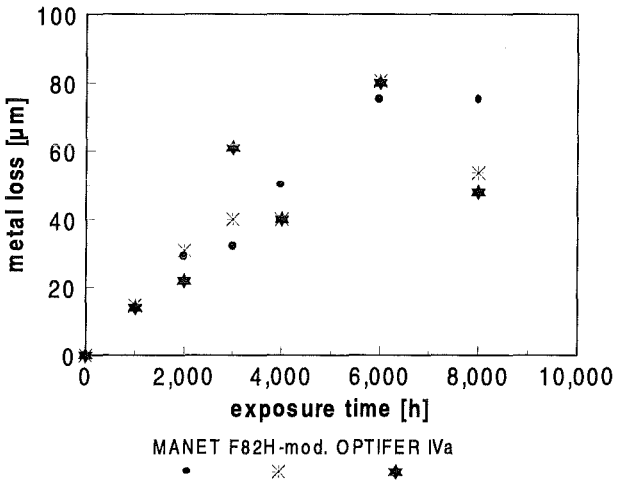

Fig. 2: Metal loss data versus exposure time for MANET, F82H-mod. and Optifer IVa

Additionally to the bare alloys coated specimen are under investigation now. The coatings on Al-base were produced by various techniques: VPS, CVD+MOCVD and Hot Dip. After 2000 h exposure no attack could be observed on all coated specimens.

Staff:

H. Glasbrenner
K. Stein-Fechner
Z. Voß

SM 4.2.1
Weldability Tests (Diffusion Welding)

A new diffusion welding experiment had been carried out at 980 °C under uniaxial pressure. The following parameters are varied:

1. Steel grade: MANET-II; F82H mod; OPTIFER-IV.
2. Uniaxial pressure: σ_p = 16; 22; 29; 35 MPa.
3. Roughness of the welding surfaces: 0,5 µm ≤ R_z ≤ 8,5 µm.
4. Thermal treatment after welding: T_{AU}; T_{AN}.
5. Test method: tensile-, bending-, impact bending tests.

First test results show identical mechanical properties of welded specimens compared to the unwelded base metal tested in tensile and bending tests, whereas impact bending tests show considerable differences in welded and unwelded specimens.

Staff:

L. Schäfer

SM 5.1.1
Lifetime Prediction and Requirements for Material Data

Under this task two different kinds of activity are performed.

(1) The ISDC (ITER INTERIM STRUCTURAL DESIGN CODE) is assessed for its appication to materials of less ductility as to be used in the blanket test modules (TBM). The results of this activity within a working group will be given in a report by end of 1999.

(2) For lifetime predictions of components under combined thermal and mechanical loadings of complex history continuum mechanical (viscoplastic) material models including damage have been developed. These models are implemented into the finite element code ABAQUS using as interface the UMAT-subroutine. A tool for identification of material parameters from uniaxial (however non-standard) experiments based on neural networks has been developed.

Staff:

E. Diegele
G. Rizzi

SM 5.2.1
Fracture Mechanics Studies

Objective

The objective of this subtask is the development and application of methods that allow to generate design-relevant fracture mechanics material parameters on the basis of micromechanical failure models.

A characteristic feature of these models is the utilization of a 'hybrid' approach, which means extraction of material parameters for brittle or ductile fracture from (fracture) mechanics experiments by accompanying Finite Element stress analyses.

The main advantage of this so-called 'Local Approach' with respect to global failure criteria is the fact that a mechanism-based fracture description is combined with a numerical stress analysis. Geometrical size effects are thus already accounted for within this approach. Limitations of the local approach originate from different fracture mechanisms. Knowledge of fracture mechanisms is therefore essential, so that fractography invariably is an essential part of the evaluation of experiments.

Local fracture criteria have achieved a high performance level during the last two decades. They establish a link between metallurgy and mechanical engineering and they are currently incorporated in design codes such as e.g. the R6 code of British Electric, which in turn also serves as input for ITER/DEMO design considerations.

Experimental results

Experiments on notched round bars (RNB) at three temperature levels (-150°C, -75°C, and RT) were performed using three selected notch geometries [2]. The experiments were performed on F82Hmod in the reference condition. For the determination of cleavage fracture parameters, the load and corresponding diametral contraction were continuously recorded. An optical system was used for the recording of the specimen shape and the diameter at fracture. Results of the experiments showed that fracture appearence was different for different notch geometries. The differences were most pronounced at –75°C and RT. Strain induced anisotropy was observed to develop caused by the deformation of martensite laths in the necking region and axial cracks initiated preceding the onset of fracture. This behaviour is clearly related to the martensitic microstructure and is presently not included in the general cleavage fracture model, which therefore has to be applied with some care.

Evaluation of cleavage fracture parameters

In a first step, transferability of fracture parameters was assessed via the statistical evaluation of samples of fractured specimens at one temperature level. A postprocessor WEISTRABA for the finite element code ABAQUS was generated for this purpose [1]. For –150°C, results of a numerical analysis showed a good agreement of fracture parameters for the 1mm and 2mm notched specimens [3], whereas for the 5mm specimen, numerical evaluation was not performed because of an apparently different fracture mode with considerably larger strains at fracture. Results of the fractographic investigations are required for a suitable adaptation of the cleavage fracture evaluation procedure.

In Fig. 1, results for the 1 and 2mm notched specimens at –150°C are shown as example for the numerical evaluation. The results show no statistically significant deviation.

It is, however, obvious from the preliminary (i.e. not including fractography) results of the experiments, that it is necessary to adapt the procedure to the specific fracture mode and that the martensitic microstructure of the F82Hmod steel does not allow an unmodified application of the usual Weibull stress calculation procedure.

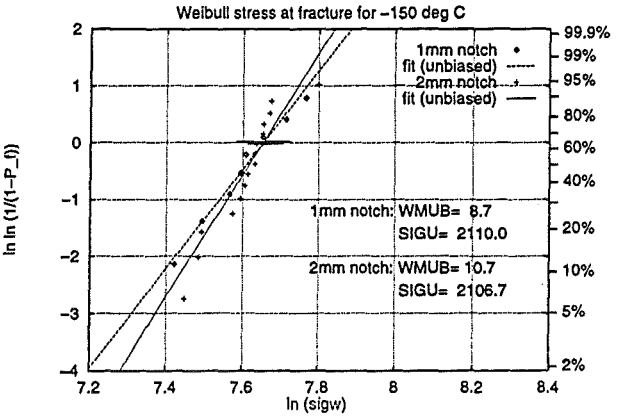

Fig. 1: Maximum likelihood results for the Weibull stress sigw for two notch geometries at -150° C. Horizontal bars indicate confidence intervals for the location parameter SIGU.

Also, presence of ductile damage preceding cleavage fracture has still to be included into the model.

Conclusion

The application of a local cleavage fracture model to the fracture behaviour of RNB specimens showed that the martensitic microstructure of F82Hmod has a distinct influence on the fracture mode leading to the formation of axial cracks especially for shallow notches and at the higher temperature levels. This mechanism has to be incorporated into the cleavage fracture model to allow transferability statements.

Testing of precracked round bar specimens is currently under preparation. This serves two purposes: to demonstrate transferability from notched to precracked specimens and to establish a fracture toughness data base.

Literature:

[1] H. Riesch-Oppermann, A. Brückner-Foit, WEISTRABA - A code for the numerical analysis of Weibull stress parameters from ABAQUS finite element stress analyses, - Procedural background and code description - FZKA Report 6155, Forschungszentrum Karlsruhe, August 1998.

[2] Nuclear Fusion Project Annual Report of the Association Forschungszentrum Karlsruhe / EURATOM October 1996 - September 1997, FZKA 6050, December 1997, 118f.

[3] H. Riesch-Oppermann, E. Diegele, A. Brückner-Foit, Application of Local Approach to cleavage fracture behaviour of the F82Hmod ferritic martensitic structural steel, in: M.W. Brown, E.R. de los Rios, K.J. Miller (eds.), Fracture from Defects: Proc. of the 12th Biennial European Conf. on Fracture (ECF 12), Sheffield, September 14-18, 1998, Vol. II, 751-756, EMAS, Cradley Heath, 1998.

Staff:

J. Aktaa
E. Diegele
M. Klotz
C. Petersen
H. Riesch-Oppermann
G. Rizzi
M. Walter

SM 5.3.2
Procurement Specification for a RAF/M Steel EUROFER 97

After elaboration of a technical specification for the supply of a weldable reduced activation ferritic martensitic steel of the 9CrWTaV type (EUROFER 97), a call for tender for the supply of 3.5 tons semi-finished products (plates, forging, filler wire and tubes) – following the rules of EU orders – had been launched Europe-wide. After the technical evaluation of all tenders BÖHLER EDELSTAHL GmbH in Austria had been selected and proposed to the European Commission as supplier which finally accepted this proposal.

The first two ingots of 1.5 tons have been melted and remelted in vacuum arc furnaces and were partially used for the determination of production parameters and other preliminary examinations. Further ingots are being produced so that the acceptance of the semi-finished products can be expected for April/May 1999.

Literature:

[1] R. Lindau, E. Materna-Morris, L. Schäfer, M. Schirra, „Characterization of the Ferritic-Martensitic 8% Chromium Steel F82H-mod., 20th Symp. On Fusion Techn., Marseille, France, 7.-11. Sept. 1998

Staff:

R. Lindau

Neutron Source

ERB 5004 CT 970072 (NET/97-453) Evaluation and Refinement of the Conceptual Design of the Experimental Test Assembly of the D-Li Neutron Source

Following the recommendations of the FPCC in January, 1997, the IEA/IFMIF Subcommittee at their meeting in Brussels on January 30-31 proposed a new plan for the activities in 1997-98. The objective of the plan was to maintain the viability of the project in 1997-98 and to be in a position to begin engineering design and development work in the near future. This phase of work was called Conceptual Design Evaluation (CDE). The design leaders met in Paris on February 3 to redefine the tasks to focus on evaluation of technical issues resulting from the conceptual design activity. The IFMIF work continues to be coordinated by the international leadership team as for the CDA phase (1994-96).

The need to develop a structural material that can withstand the high-energy neutron flux environment expected for the first wall and blanket regions of deuterium-tritium (D-T) fusion reactors is recognized as one of the key challenges remaining in the program aimed at producing commercial fusion power. IFMIFs mission is (i) to provide a neutron source with an energy spectrum simulating that of fusion neutrons at sufficient intensity and irradiation volume to test samples of candidate materials up to about full lifetime of anticipated use in a fusion DEMO reactor in a reasonably short operation time, and (ii) to calibrate data generated from fission reactors and particle accelerators. Initial studies have indicated that a volume of about 0.5 L is required in a region producing a flux equivalent to 2 MW/m^2 (0.9 x 10^{18} n/m^2-s) or greater. A fraction of this volume, about 0.1L would be available at a flux equivalent to 5 MW/m^2 for accelerated testing. The design concept consists of a deuteron accelerator producing particle energies in the range of 30 to 40 MeV. The deuterons interact with a flowing liquid lithium target (D-Li) producing high energy neutrons with a peaked flux around 14 MeV. The resulting high energy neutrons will interact with a set of test assemblies located immediately behind the Li-Target. Designs for the four major technical subsystems

- Accelerator System
- Lithium Target System
- Test Facility System, and
- Conventional Facilities

has been developed in parallel during the CDA phase and extended during the CDE phase (1997-98). In 1997-98, progress was reviewed and checked with international conference calls and by meetings of each of the three main facility groups (Accelerator, Target and Test Facilities). Meetings of the Subcommittee and design leaders were held in October and November 1997 to review the results of the work and to plan for the work in 1998. Two general group meetings were held in 1998.

Within the present CDE phase, the FZK activities concentrate on key engineering development items of the Test Facility System as well as on an optimization of the suitability of IFMIF for the fusion materials community in terms of irradiation parameters, specimen geometries and test matrixes. For the CDE phase, the international coordination of the „User's requirements" and the „Test Facilities Systems" is organized by two FZK members. In the following, the FZK activities of the reporting period are summarized.

1. Test Facilities Engineering

During the IFMIF CDE phase the main activities have been concentrated on (i) critical evaluation of CDA design concept, (ii) improvement and completion of reference design, and (iii) fabrication of test apparatus to confirm design concept of key devices that cannot rely on existing experience.

An important outcome of the reviewing process at the beginning of the CDE phase was, that the overall Test Facilities design concept, carried out through IFMIF CDA phase, has been confirmed. However, in spite of the fact that the bulk of devices specified for the Test Facilities can be designed and fabricated with today's technology, various development efforts are necessary to establish a facility which combines overall structural integrity, high reliability, feasible and tested remote maintenance operations, and advanced safety standards. Significant progress could be achieved at FZK also during the second year of the CDE with respect to hardware design and with respect to fabrication of a subsized high flux test module.

1.1 High Flux Test Module HFTM

Providing a test module for specimen temperatures up to about 1000 °C is one of the most challenging design requirements for the IFMIF Test Facilities. The successful development of a He-cooled test module would provide for any material a broad temperature window as well as flexible and very safe operating conditions.

The initial design of the helium gas cooled high flux test module was improved significantly. The gas coolant ducts are now integrated part of the test apparatus to increase the coolant efficiency and the overall mechanical stability. Another activity during the reporting period was to carry out detailed thermo-hydraulic calculations in order to reduce the pressure drop of the HFTM in the CDA design. Also the shape of the rigs in helium flow direction was changed resulting in a lower hydraulic resistance. These updates of the reference design are shown in fig.1. The helium is now streaming from the bottom of the rigs upwards, it flows along both sides of the test modules (better cooling efficiency) and the rigs are opened on top and bottom to guarantee similar helium pressure inside and outside the rig walls. Another important feature is that all rigs can be disassembled and re-assembled individually after the module cover is opened and the electrical signals are disconnected from the rig plug unit. In the revised reference design the HFTM has 27 vertical rigs arranged in three rows, each consisting of 9 rigs. A parameter study has been performed to specify the gas gaps and to calculate the available temperature window inside each of the 27 rigs of the reference test module. The idea to increase the structural integrity by using a structural material (e.g. specimen capsules, rigs, test module) of the same type as for the specimens themselves, is confirmed by recent data sets on irradiated RAFM steels.

In order to test fabricability, remote handling, heat removal etc, a detailed design for a sub-sized test apparatus has been done. The developed design is a test module that is in the geometry and the material very similar to the reference design but has only 9 instead of 27 rigs. That is, helium flow channels, hydraulic diameter, wall thickness etc. reflects basically the reference design. The FE-analyses of the sub-sized test module have shown that for reference helium gas coolant conditions and a wall thickness of 2mm (reduced activation steel F82H-mod, unirradiated) the maximum stress does not exceed 170 MPa and therefore is considered to be not critical. The maximum displacement was calculated to 0.16 mm in the turning point of the helium coolant and is also very moderate. Although it might not be necessary for a conceptual design, both values could be reduced significantly by dedicated design improvements when moving towards an engineering design phase.

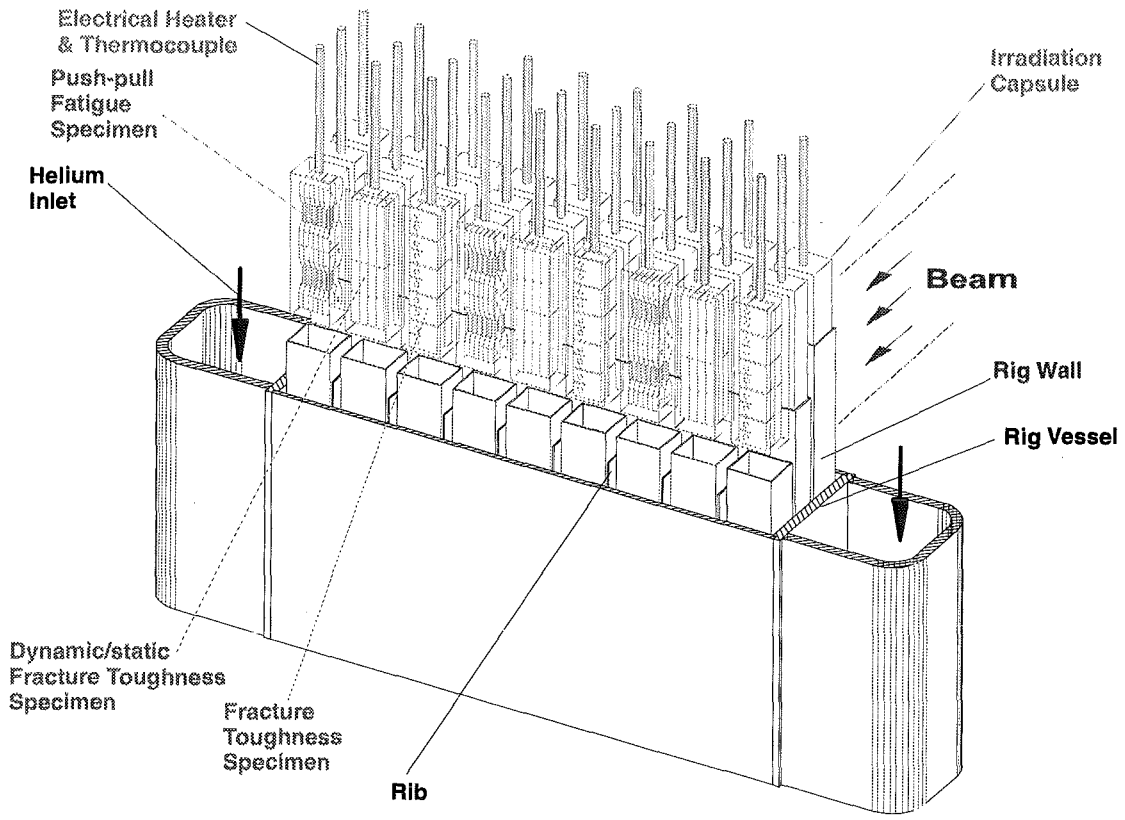

Fig. 1: Design configuration of the helium gas cooled high flux test module (HFTM) showing 27 rigs assembled with instrumented capsules and various types of test specimens.

Due to the nature of the CDE phase, this sub-sized test module could not be fabricated. This is why a smaller test module with only one rig has been selected as test object to verify key parameters of the helium gas coolant concept. As fig. 2 shows, this single-rig test module consists of a hollow canister with a square cross section (gray hatched) housing the specimen capsule which has an integrated ohmic heating. Inside this rig the specimens are replaced by one specimen dummy that is also heated by ohmic heaters. In case of accelerator shut down during the irradiation experiments it is necessary to control and adjust the temperature of the specimens. The heated zone of the specimen dummy has a length of about 50 mm and therefore adequately reflects the height of the IFMIF beam foot print. The outer diameter of this conductor is 1mm and the maximum specific power is 400 W/m. With a heated active length (capsule) of 92 cm a total of 368 W can be generated. The nuclear power of the real specimens will reach 250 W. In this way both, the nuclear heating in the specimens and in the specimen capsule can be simulated in a manner representative for expected IFMIF heat loadings. The gas gaps, the wall thickness of all structural RAFM steel (F82H-mod), the overall rig, capsule and specimen dummy dimensions are practically identical with the IFMIF reference design.

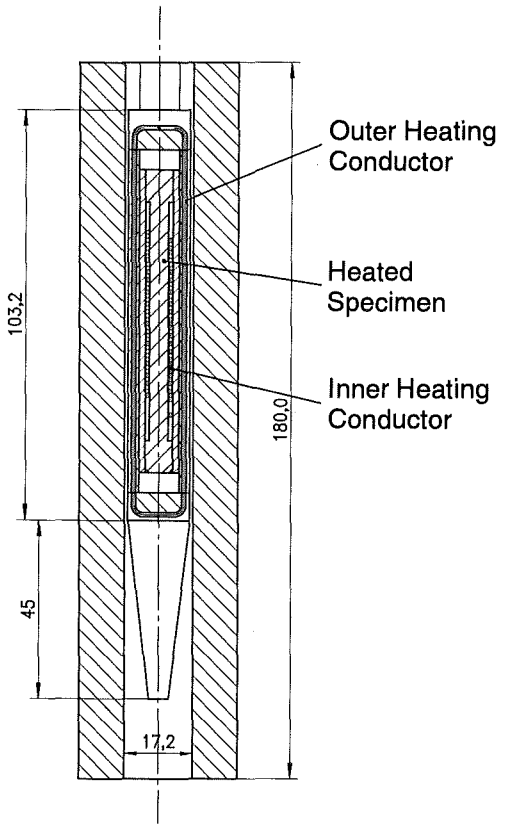

Fig. 2: Fabricated single-rig test module housing one rig with a fully instrumented specimen capsule.

Fig. 2 shows also the helium gas inlet (bottom) and outlet (top). Presently this single-rig test module is fabricated and assembled at FZK. After the integration of this test module in a suitable helium gas loop a variety of parameter studies are foreseen to verify experimentally (i) fabricability of devices with RAFM steels, thermo-hydraulic calculations, and (iii) structural integrity during and after thermal cycling test to high specimen and capsule temperatures. For these kind of experiments, different rig geometries for high specimen temperatures (0.1 mm gas gap between inner rig wall and specimen capsule) and for low specimen temperatures (0.5 mm gas gaps) are foreseen.

1.2 Medium Flux Test Modules MFTM

In order to increase the efficiency of the available irradiation volume and the flexibility in the test matrixes, a design concept has been developed by FZK that allows the simultaneous irradiation of two independent test modules in this flux region. Therefore, in the current reference design concept the vertical test assembly VTA2 of the medium flux region is equipped with two individual test modules: (i) a module for in-situ creep-fatigue experiments housing a miniaturized universal testing machine for simultaneous testing of three independent push-pull fatigue specimens, and (ii) a module for in-situ tritium release experiments on various ceramic breeder materials. Instead of ceramic breeders, these sub-test modules can also be equipped with any PIE specimens. The design of the tritium release test module has been significantly improved by FZK during the beginning of the reporting period. The design improvement has been mainly by the requirements to effectively use the available volume of 6 L and to allow the simultaneous irradiation of both in-situ test modules. Fig. 3 shows that tritium release test module with helium gas coolant ducts, piping for sweep gas, instrumentation, and specimen arrangement.

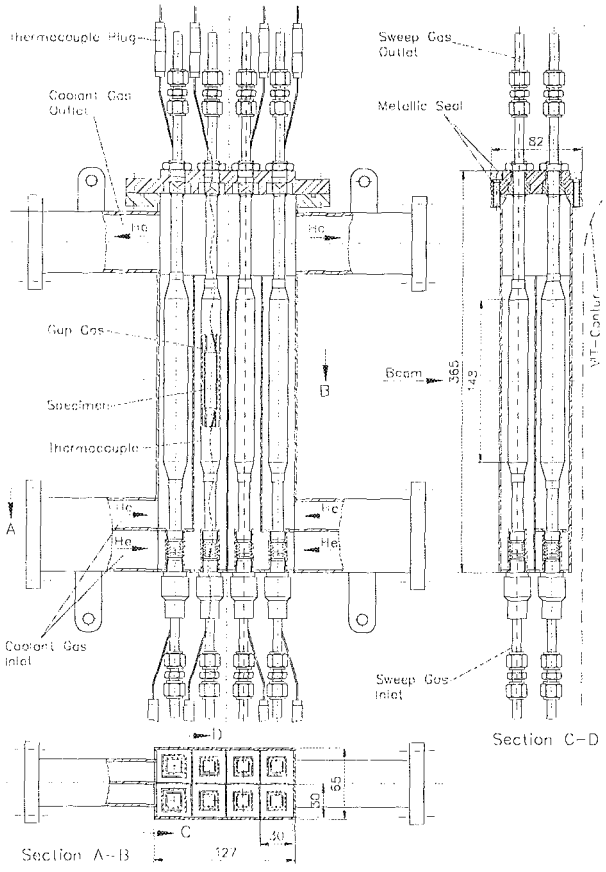

Fig. 3: Front view (left), elevation view (right) and cross section (bottom) of the tritium release test module for ceramic breeders.

Literature:

[1] K. Ehrlich and A. Möslang, "IFMIF – An international fusion materials irradiation facility", Nucl. Instrum. and Methods in Phys. Research B 139 (1998) 72-81.

[2] M. Class; "Layout and design of a helium gas cooled test module for IFMIF", Internal report (German) IMF 050 (FZK), 1998.

[3] A. Möslang and R. Lindau, Proceedings of the IEA-Technical Workshop on the IFMIF Test Facilities, Karlsruhe, Germany, July 7 - 9, 1997, Forschungszentrum Karlsruhe, FZKA 5993, December 1997

[4] C. Antonnucci, E. Daum, J.R. Haines, S. Jitsukawa, A. Möslang, K. Noda and S. Zinkle, "Overview of the IFMIF Test Facility", ICFRM-8, Sendai, Japan, October 1997, Journal of Nuclear Materials, in press.

[5] E. Daum, A. Möslang, M. Sokcic-Kostic, "Collection of IFMIF Neutronic Calculations for Test Modules with NaK and He-Cooled High Flux Test Cells", Internal Report (German), IMF 036, FZK, July 1997

[6] K. Noda, K. Ehrlich, S. Jitsukawa, A. Möslang and S. Zinkle, User's requirements for IFMIF, ICFRM-8, Sendai, Japan, October 1997, eingeladener Vortrag, Journal of Nuclear Materials, in press.

[7] T. E. Shannon, H. Katsuta, H. Maekawa, R. A. Jameson, M. Martone, A. Möslang, M. J. Rennich, V. Teplyakow; „IFMIF (International Fusion Materials Irradiation Facility): A High Intensity Deuteron Beam Application", EPAC'98, June 22-26, Stockholm; Proceedings in press

[8] A. Möslang, "IFMIF Test Facilities", ANS Accelerator Applications Conference (AccApp'98), September 20 - 23, 1998, Gatlinburg, TN, USA.

2. Neutronics and Users Aspects

Neutronics work has focused on the evaluation of activation cross-section data, improvements of the d-Li neutron source model and a full characterization of the irradiation parameters of the high flux irradiation test module using the newly developed computational tools and nuclear cross-section data. In addition, an IFMIF simulation experiment was performed at the Karlsruhe Isochronous Cyclotron for measuring the neutron yield, neutron spectrum as well as Be-7 and tritium yields.

2.1 Intermediate Energy Cross Section Data

Over the past period, the evaluation work being performed in co-operation with the Institute of Nuclear Power and Engineering (INPE) Obninsk, Russian Federation, has been devoted to the generation of an Intermediate Energy Activation File (IEAF) comprising activation and transmutation cross-section for all kinematically allowed reactions up to 150 MeV neutron energy. So far, the IEAF the library contains activation cross sections for the elements Z = 9 - 42, 49, 69, 72 - 75, 79 and 83 [1,2]. For each of these elements, all the isotopes present in the European Activation Library EAF-97 are included. EAF-97 also is the source of the data below the neutron energy of 20 MeV. The new activation and transmutation cross-section files were prepared according to standard ENDF-6 format rules that allows to specify the reaction products by Z,A identifiers. As a result, there are no restrictions to the number of activation and transmutation reactions that can be handled. This is vital in view of the multitude of reaction channels existing at energies above 20 MeV.

Activation calculations at these higher energies require an activation/inventory code which is able to accommodate the numerous open reaction channels (up to 170 per isotope). Therefore, the recently developed and benchmarked ALARA activation code was chosen for IFMIF activation calculations. Neutron flux spectra were calculated in a 205-group structure (175 vitamin-j groups plus 30 groups of uniform lethargy width) using the McDeLi neutron source model and used together with the new IEAF cross-section data as input for ALARA calculations for the IFMIF high flux test module [3]. In addition to the activation and decay heat results themselves, shown in

figure 4 for the IFMIF high flux test region and for the DEMO-reactor, the importance and completeness of the libraries was shown by comparison to various other libraries. In particular, this comparison showed that various approximations, such as assuming that the activation cross-section is either zero or constant at energies above 20 MeV, are not able to accurately calculate the activation or decay heat for iron in the high flux test region. In addition, by comparing one library consisting of the IEAF data alone to another library consisting of the IEAF data supplemented by data from EAF97 for those isotopes which are not yet available, it was shown that the currently available set of isotopes is complete enough for the activation analysis of iron.

2.2 Neutron Source Model

A complete reassessment of the stripping and evaporation components of the d-Li nuclear model was carried out, resulting in a more physically sound model for the neutron source term.

Previous implementations of the stripping model were drawn directly from the original research by Serber and based heavily on assumptions that are not valid given the physical parameters of IFMIF. In particular, IFMIF has a relatively low initial deuteron energy (40 MeV compared to Serber's 190 MeV), and the thick target means that stripping reactions occur at energies down to about 6 MeV. The assumption of high energy deuterons was implemented primarily to reduce the semi-classical momentum distribution to either a closed-form angular cross-section or closed-form energy cross-section. These results from Serber were then simply multiplied to create a double-differential cross-section, making a further (and incorrect) assumption that the two distributions are independent. By removing the original assumption of high energy and implementing the model by directly sampling the semi-classical momentum distribution, the physical basis for the model is improved greatly.

The theoretical development of the evaporation model was reconsidered with assumptions and approximations made to suit the specific conditions of the d-Li reaction at energies between the coulomb barrier energy (~1.5 MeV), used as a lower energy threshold for this reaction, and an upper energy threshold of 15 MeV. More importantly, a simplistic linear model was added to roughly include the contributions from all neutrons which may be emitted after the primary evaporation, so-called "subsequent evaporations", as first suggested during the FMIT analysis.

While some of the models continue to be crude approximations to the real physics of the reaction, they have been fit to experimental data sets with more rigorous requirements on the fitting process than in previous models. For example, the total cross-sections were required to have realistic shapes and conversions between inertial reference frames were directly applied rather than approximated.

2.3 IFMIF Simulation Experiment

An IFMIF simulation experiment was performed at the Karlsruhe Isochronous Cyclotron for measuring the neutron yield, neutron spectrum and the yields of the radionuclides Be-7 (53.3 days half-life) and tritium (12.3 years half-life). The first two of these quantities are of fundamental importance for validating the calculational neutron source term model. The analysis of these raw data (in FZK/JAERI collaboration) is in progress. The Be-7 and tritium production yields are important for the operation of the IFMIF target in view of radiation protection, and for designing the vacuum system which will have to handle part of all of this tritium load. The Be-7 and tritium measurements and their results are reported in the following.

Two identical stainless steel containers having 1.1 mm wall thickness and 9.7 cm^3 volume were filled in an argon atmosphere with pure lithium metal and then closed by laser beam welding. The austenitic steel type 1.4571 was selected because it exhibits very low tritium permeation. The Li thickness in the beam direction was 21.8 mm, slightly more than the range of 40 MeV deuterons. The containers were irradiated as internal targets within the cyclotron by the full-energy beam of 52 MeV. Since 52 MeV deuterons lose about 12 MeV in traversing 1.1 mm of steel, the deuterons entering the lithium had the correct energy. One container (target A) was used for preliminary tests with varying beam current. The other one (target B) was irradiated for 16.5 hours at 3μA. The beam current was always recorded by a current digitizer and scaler to determine the total charge, i.e., the number of deuterons. More

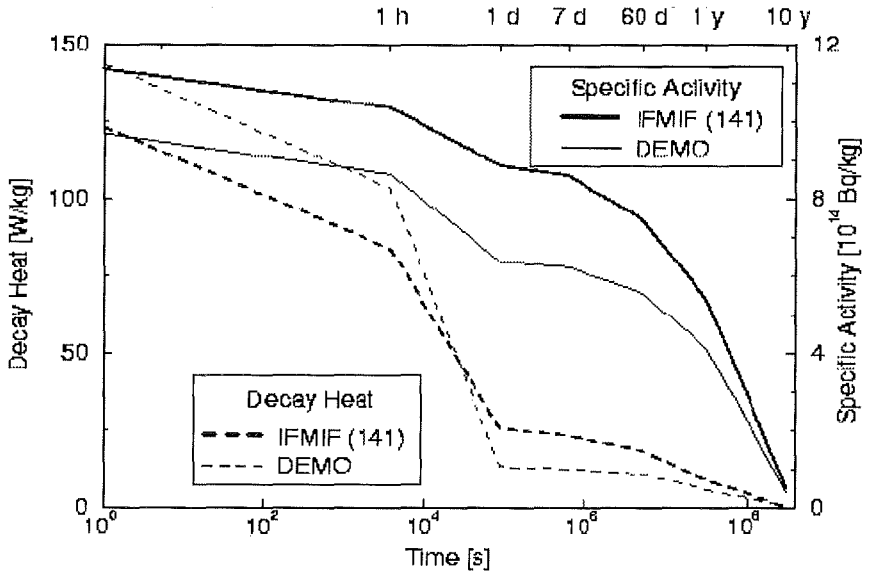

Fig. 4: Activity and decay heat for one position of the IFMIF high flux test module and for the first wall of the DEMO-reactor.

details about the experiment are found in Ref.[4].

(i) Beryllium-7 measurement: After a cooling time of about 100 days to decrease the considerable activity induced in the steel, the 478 keV γ-ray line from target B was measured with a 25% efficiency, high purity germanium spectrometer. The spectrometer had to be reduced in counting efficiency for this measurement by using a lead collimator in front of the detector. The collimator introduces a small systematic uncertainty due to the unknown spatial distribution of the Be-7 within the finite-size Li target. Therefore, two separate sets of measurements were taken with collimators of different dimensions. Systematic differences between Be-7 activities measured with the two collimators were not found. Corrections were applied for γ ray absorption in the steel case (8%) and within the lithium (4%, assuming all radiation to be emitted at a depth of half the lithium thickness in the direction of measurement, i.e., 7 mm). One major difference between IFMIF and the present simulation experiment is the steel target wall on the beam entrance side. A very rough estimation, assuming a similar mean cross section per nucleus for deuteron loss in steel at 40 to 52 MeV as in lithium at 0 to 40 MeV, gives a deuteron beam loss of about 1%.

The result is given in Table 1.The 'production cross section' given is the average over deuteron energy, assuming that all Be-7 originates from the $^{6}Li(d,n)^{7}Be$ reaction. From the scatter of several Be-7 and calibration measurements and the uncertainties of the corrections, an overall uncertainty of 10% is estimated for the yield.

(ii) Tritium measurement: For the tritium measurement, both of the targets were subjected to a well established standard procedure. The tritium was released by heating the target to several hundred °C in a quartz tube through which a gas stream of 95% Ar + 5% H_2 was flowing at 50 ml/min. The gas was subsequently oxidized in passing through a CuO bed. The resulting H_2O+HTO was absorbed in a molecular sieve. The molecular sieve was periodically changed and eluted with water. This water was then analyzed for tritium in an automated liquid scintillation system (Beckman Instruments LS 6000TA). The result (tritons per 100 incident deuterons), after correcting for the 1% deuteron loss in the steel case (see above), is 2.36 in target A and 2.23 in target B, with an estimated uncertainty of about 5% in either measurement. The final result is given in Table 1. The production cross section given there is analogous to the one for Be-7, but referring to the $^{7}Li(d,t)^{6}Li$ reaction.

The result is given in Table 1. A fictitious production cross section averaged over deuteron energy can be derived from the yield, assuming that all Be-7 originates from the $^{6}Li(d,n)^{7}Be$ reaction. Its value (which is very plausible for a charged-particle induced nuclear reaction) is also given in the table. From the scatter of several Be-7 and calibration measurements and the uncertainties of the corrections, an overall 1s uncertainty of ±10% is estimated.

2.4 Irradiation Parameters of the High Flux Test Module

On the basis of the newly developed computational tools and data, a comprehensive characterization of the neutronics of the high flux test region (HFTR) has been carried out with focus on Fe as the major constituent of ferritic-martensitic iron based alloys [5-10]. To this end, detailed three-dimensional geometrical models have been developed for use with the MCNP Monte Carlo code including - in addition to the HFTR - the medium flux test module (MFTM) with displacement damage levels between 1 and 20 DPA/FPY, the low flux test module (LFTM) with 0.1-1 DPA/FPY, and the very low flux test module (VLFTM) with less than 0.1 DPA/FPY.

Numerical results for the HFTR and comparisons to relevant fusion reactor data are displayed in Table 2. It is found that IFMIF covers a broad range of fusion reactor irradiation conditions without deteriorating the material irradiation parameters in spite of its high energy spectrum tail. In addition, the normalized energy transfer function W(T), indicating the cumulative probability that displacement damage will be caused by a primary knock-on atom (PKA) with energy less than T, compares very favorably with fusion reactor spectra [5], thus qualifying IFMIF as a suitable facility for irradiation experiments under fusion typical conditions.

The main results obtained thus far with regard to irradiation performance and conditions are as follows:

- The total neutron flux gradient in the HFTR is 20 - 30 %/cm. As a result, the use of miniaturised specimens is required and, furthermore, the HFTM design needs to allow the orientation of the samples along directions with minimized gradients.
- The high energy fraction of the neutron flux (E_n > 14.6 MeV) is 15 - 20 % of the total neutron flux throughout the HFTR. This fraction increases the displacement and gas production rates significantly and allows accelerated irradiation tests in IFMIF.

Table 1: Experimental results of radionuclide production in the target.

	Atoms per 100 deuterons	Mass per full-power year	Production cross section[1)]
Be-7 ($T_{1/2}$ = 53.29 d)	0.274 ±10%	1.57 g	362 mb per Li-6 atom
H-3 ($T_{1/2}$ = 12.32 a)	2.39 ±4%	5.89 g	255 mb per Li-7 atom

[1)] see text

Table 2: Comparison of irradiation parameters in the High Flux Test Region of IFMIF and the first wall data in ITER and DEMO

Irradiation parameter	IFMIF	ITER	DEMO
Total neutron flux [n/(s cm^2)]	4 x 10^{14} - 10^{15}	4 x 10^{14}	7.1 x 10^{14}
Neutron flux, E_n >14.6 MeV [n/(s cm^2)]	4 x 10^{13} - 2 x 10^{14}	-	-
Hydrogen production [appm/FPY]	1000 - 2500	445	780
Helium production [appm/FPY]	250 - 600	114	198
Displacement production [DPA/FPY]	20 - 55	10	19
H/DPA ratio [appm/DPA]	35 - 50	44.5	41
He/DPA ratio [appm/DPA]	9.5 - 12.5	11.4	10.4
Nuclear heating [W/cm^3]	30 - 55	10	22
Wall load [MW/m^2]	3 - 8	1.0	2.2

- The DPA-to-gas ratios are in the same range as in ITER or DEMO first wall flux spectra. Thus IFMIF can simulate fusion reactor conditions with regard to material irradiation characteristics.

- The evaluated uncertainty of the neutron source yield causes a relatively large uncertainty of the available high flux (≥20 dpa per full-power year) volume.

- There is available high flux volume above and below the proposed high flux test module design.

- The displacement damage qualification shows that IFMIF fits the fusion reactor damage characteristics better than other neutron sources do.

Following the achievements obtained thus far in the field of the IFMIF neutronics, further work is required to reduce the uncertainty of the neutron source function, as this uncertainty is directly transmitted into all neutronic responses and the estimated irradiation volumes. Furthermore, the investigations have to be extended to cover more materials both in the HFTR and the medium and low flux test modules. Investigations are underway to study the possibility of applying a neutron reflector around the test modules to arrive at a softer neutron spectrum as well as an increased neutron flux density.

Literature:

[1] Yu. Korovin et al.: Evaluation and Test of Nuclear Data for Investigations of Neutron Transport, Activation and Transmutation in Materials by Intermediate and High Energy Particles, in: Int. Conf. on Nuclear Data for Science and Technology (NDST'97), Trieste, Italy, 1997 (G. Reffo et al, eds.), Conference Proceedings vol. 59 part I, Editrice Compositori, Bologna 1997, pp. 851-855

[2] Yu. Korovin et al.: Radiation Damage and Processes of Activation and Transmutation in Materials Irradiated by Intermediate and High Energy Particles, in: Int. Conf. on Emerging Nuclear Energy Systems, June 28 -July 2, 1998, Tel Aviv, Israel (proceedings to appear)

[3] P.P.H. Wilson: Activation Characterisation of the High Flux Region of the International Fusion Materials Irradiation Facility [IFMIF], Proc. 20th Symp. on Fusion Technology, Marseille, France, September 7-11, 1998, pp. 1203-1206

[4] U. von Möllendorff, H. Feuerstein and H. Giese, Measurements of radioactivity production in the IFMIF target, Proc. 20th Symp. on Fusion Technology, Marseille, France, September 7-11, 1998, pp. 1445- 1448

[5] E. Daum, U. Fischer, A. Yu. Konobeyev, Yu. A. Korovin, V.P. Lunev, U. von Möllendorff, P.E. Pereslavtsev, M. Sokcic-Kostic, A. Yu. Stankovsky, P.P.H. Wilson, D. Woll, Neutronics of the High Flux Test Region of the International Fusion Materials Irradiation Facility (IFMIF), report FZKA 5868, Forschungszentrum Karlsruhe, 1997

[6] P. Wilson, E. Daum. U. Fischer, U. von Möllendorf, D. Woll, Neutronics Analysis of the International Fusion Materials Irradiation Facility [IFMIF] High Flux Test Volume, contribution at ANS Accelerator Applications Topical Meeting, Albuquerque, New Mexico, November 1997, Fusion Technology 33 (1998) 136-145

[7] E. Daum, P.P.H. Wilson, U. Fischer and K. Ehrlich, Characterization of the Irradiation Parameters in the IFMIF High Flux Test Region, Contribution to ICFRM-8, Sendai, Japan, October 1997 (to appear in J. Nucl. Materials)

[8] E. Daum, P.P.H. Wilson and A. Möslang, Characterization of the Volume for High Dose Irradiations with IFMIF, Contribution to ICFRM-8, Sendai, Japan, October 1997 (to appear in J. Nucl. Materials)

[9] E. Daum, Damage characterization in IFMIF and comparison with ITER and DEMO devices, Contribution to the IFMIF User Group Meeting held in Sendai, Japan, November 1st, 1997 (Proceedings in print as a JAERI report)

[10] E. Daum, A. Möslang and M. Sokcic-Kostic, Neutronic Calculations for IFMIF Test Modules, ANS Accelerator Applications Conference (AccApp 98), September 20 - 23, 1998, Gatlinburg, TN, USA (proceedings to appear)

Staff:

G. Bürkle
E. Daum
K. Ehrlich
H. Feuerstein
U. Fischer
H. Giese
U. von Möllendorff
M. Sokcic-Kostic
A. Möslang
G. Schmitz
E. Wiegner
P. Wilson
D. Woll

Nuclear Data Base

The development of a nuclear data base is an integral part of the Long-term Fusion Technology Programme. In the framework of this programme, FZK contributes to the development and qualification of the European Fusion File (EFF), the European Activation File (EAF) and the International Fusion Evaluated Nuclear Data Library (FENDL).

Benchmark Analyses for EFF-3 and FENDL-2 Evaluations

In the framework of the EFF project, benchmark analyses are being performed as part of the quality assurance procedure for the newly developed EFF-3 data evaluations. To this end, the processed data are benchmarked in Monte Carlo transport calculations against competing data evaluations as well as integral experiments.

First analyses have been performed with the new ^{9}Be EFF-3 evaluation of IRK Vienna [1]. The following integral Beryllium benchmark experiments have been considered: the KANT (Karlsruhe) and the OKTAVIAN (University of Osaka) spherical shell transmission experiments and the FNS (JAERI Tokai-mura) slab time-of-flight (TOF) experiment. In either case three-dimensional MCNP-calculations have been applied to obtain the neutron leakage spectra. The new ^{9}Be EFF-3 evaluation in general gives similar results as the FENDL-1 (ENDF/B-VI) and FENDL-2 (JENDL-FF) evaluations with a slightly less neutron population in the 5-10 MeV range. A significant underestimation is observed in the FNS slab experiment at larger angles and in the leakage spectra of the spherical shell experiments as well. In these cases, the old LANL ^{9}Be evaluation used in EFF-1 still agrees best with the measured spectra. In particular, this is true for the spherical shells leakage spectra in the 1-5 MeV energy range, where there remains a strong underestimation with EFF-3 as with FENDL-1 and -2 (Fig. 1).

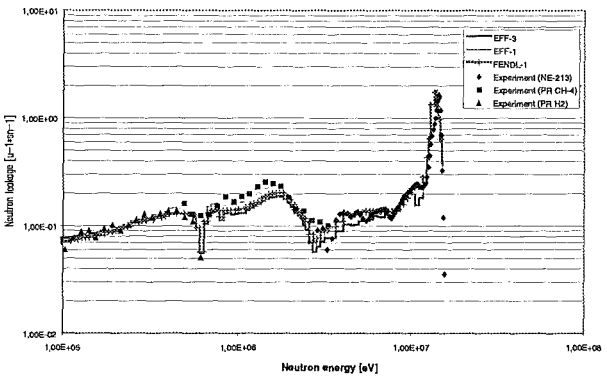

Fig. 1: Neutron leakage spectra in the KANT Beryllium spherical shell experiment(r_i=5 cm, r_o=22 cm) [2]

With regard to the ^{56}Fe cross section data being currently under development, both the TUD iron benchmark experiment and the ITER bulk shield experiment have been re-analysed. The new ^{56}Fe EFF-3.1 data evaluation provided recently by ENEA Bologna and the FENDL-2 data library which contains the current ^{56}Fe EFF-3.0 evaluation have been considered. The erroneous photon production cross-section of the latter file has been corrected in the FENDL-2 library. There is now better agreement with the measured photon flux spectra, see e. g. Fig. 2 for the photon lekage spectrum in the TUD iron slab experiment. In addition, the ^{56}Fe EFF-3.1 evaluation has provided a better agreement in the 5-10 MeV energy range of the neutron flux spectra as compared to ^{56}Fe EFF-3.0.

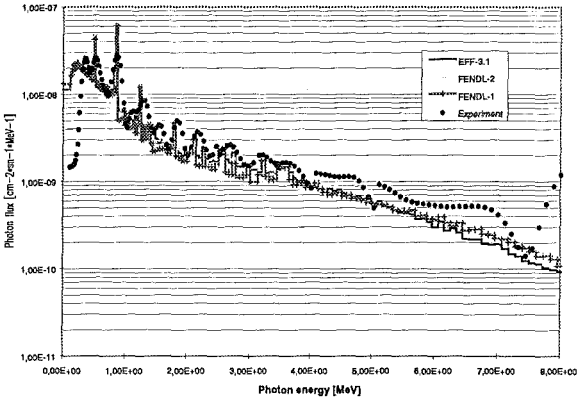

Fig. 2: Photon leakage spectra in the TUD iron slab experiment (t=30 cm) [3]

Monte Carlo Sensitivity and Uncertainty Analyses

With the forthcoming EFF-programme, the assessment of uncertainties in the nuclear responses will become a major neutronic issue. To allow the application of sensitivity/uncertainty computational tools to both complex fusion reactor configurations and integral experiments, the use of the Monte Carlo approach is mandatory. At the Hebrew University of Jerusalem, a novel computational technique has been recently developed and implemented into a local update to the MCNP4A code [4]. This technique allows to calculate point detector sensitivities based on the use of the differential operator method. Along with the covariance matrices, uncertainties of point detector responses, e. g. leakage flux spectra in integral experiments, can be calculated. Once validated, the same basic approach can be applied to fusion reactor design calculations to assess the uncertainty of nuclear responses.

In a first step, the Monte Carlo sensitivity approach for point detectors has been applied to the TUD iron benchmark experiment using EFF-2.4 and EFF-3.0 ^{56}Fe data [5]. As an example, Table 1 shows the relative sensitivities of the neutron leakage fluxes to the specified EFF-3 ^{56}Fe reaction cross sections in a coarse 5 group representation.

The resulting uncertainties obtained with the EFF-2.4 and EFF-3.0 covariance data are displayed in Tables 2 together with results from two-dimensional deterministic sensitivity/uncertainty calculation using the TWODANT/SUSD code package. As compared to the experiment, the calculated uncertainties are lower than the experimental ones below 5 MeV but higher above that neutron energy. At the same time, the measured high energy flux is underestimated suggesting to decrease, in the first place, the inelastic scattering cross sections in the high energy range in agreement with the sensitivity results.

Table 1: Relative sensitivity [%/%]of the neutron leakage flux integrals in the TUD iron benchmark experiment to ^{56}Fe EFF-3 reaction cross sections integrated over all energies

Energy range [MeV]	<0.1	0.1-1	1-5	5-10	>10	total
Elastic scattering (MT=2)	-2.39	-1.22	-1.32	-0.89	-0.61	-1.33
(n,2n) –reaction (MT=16)	0.19	0.11	-0.19	-0.54	-0.98	0.03

1st level inelastic scatt. (MT=51)	0.16	-0.01	-0.98	-0.18	-0.11	-0.11
Continuum inelastic scatt. (MT=91)	-0.22	-0.19	-0.25	-1.35	-1.75	-0.28

Table 2: Uncertainties [%] of calculated neutron leakage fluxes in the TUD iron slab experiment due to uncertainties in the ^{56}Fe cross section data and experimental uncertainty

Energy range [MeV]	MC-calculation		2d S_N-calculation	Experiment. uncertainty
	EFF-2.4	EFF-3.0	EFF-3.0	
<0.1	9	9	-	-
0.1-1	4	3	3	11
1-5	20	1.6	2	2.2
5-10	27	8	10	2.9
>10	19	4	14	1.9
Total	4	3	-	-

Literature:

[1] V. Pronyaev, S. Tagesen, H. Vonach, Evaluation of all important neutron cross sections for ^{9}Be and evaluation of the secondary neutrons from the interactions of neutrons with Be in the neutron energy range from 10^{-5} eV - 20 MeV, Institut für Radiumforschung und Kernphysik, Universität Wien, EFF-Doc 552 (1997).

[2] U. von Möllendorff, A.V. Alevra, H. Giese, F. Kappler, H. Klein and R. Tayama, Measurements of 14 MeV neutron multiplication in spherical beryllium shells, Fusion Engineering and Design 28(1995), 737-744

[3] H. Freiesleben et al., Experimental Results of an Iron Slab Benchmark, Technische Universität Drseden, TUD-PHY-94/2, Februar 1995.

[4] R.L. Perel, J.J. Wagschal, and Y. Yeivin, Nucl. Sci. Eng., 124 (1996), 197-209.

[5] U. Fischer, R. Perel, H. Tsige-Tamirat, Y. Wu, Monte Carlo Uncertainty Analysis for an Iron Shielding Benchmark Experiment, Proc. 20th Symp. on Fusion Technology, Marseille, 7-11 September, 1998, pp.1153-1156

Staff:

U. Fischer
R. Perel
H. Tsige-Tamirat
E. Wiegner
Y. Wu

Activation Library

Safety analyses of reactor designs such as ITER and DEMO require among others a reliable data base for neutron-induced radioactivity. The European Activation System EASY[1] consists of the inventory code FISPACT and the European Activation File EAF. The ongoing coordinated effort of integral experiments to validate EASY was continued in this period with work on vanadium alloys. Samples of different vanadium alloys were activated and subsequently measured for γ activity. Activations in a pure 14-MeV neutron field were performed by TU Dresden[2]. Activations in an intense white fast-neutron field ranging up to 20 MeV were performed at Karlsruhe[3].

1. 14-MeV activations by TU Dresden

Samples of the alloys V3Ti1Si, V4Ti4Cr and V5Ti2Cr with masses of 0.3 ... 0.6 g and with an area of 10 mm x 10 mm were activated at the high-intense neutron generator SNEG-13 [4] at Sergiev Posad. Each material was irradiated at two positions, at an angle of 4^0 with respect to the deuteron beam direction where the mean neutron energy is 14.93 MeV with a spread of 0.54 MeV f.w.h.m. (position 1) and at 73^0 with (14.37±0.07)-MeV neutrons (position 2). The background component of thermal and intermediate neutrons was measured by ^{115}In(n,gamma) activation and found to be 10^{-5} of the total flux at the sample positions. The 14-MeV neutron flux was monitored by ^{93}Nb(n,2n)-activation with thin Nb foils attached in front and at the back of the vanadium sample.

Each material was irradiated in two separate runs, a short one (30 min) with fluence of the order of 10^{12} neutrons/cm^2 and a longer one (45.6 h) with fluence of about $2 \cdot 10^{14}$ neutrons/cm^2. In this way radioactivities with half-life between 2 min and more than 300 d could be investigated.

Gamma spectra were taken from the irradiated samples with Ge(Li)-spectrometers several times during decay from 3 min up to about 100 d. The activities of the following nuclides were identified by gamma energies and half-life: ^{24}Na, ^{27}Mg, ^{28}Al, ^{29}Al, ^{46}Sc, ^{47}Sc, ^{48}Sc, ^{45}Ti, ^{51}Ti, ^{52}V, ^{51}Cr, ^{54}Mn, ^{57}Co, ^{58}Co, ^{95}Zr, ^{92m}Nb and ^{99}Mo. These nuclides produce, after 3 min of decay, more than 99% of the total heat and of the gamma dose rate, and after 1 year of decay, when the activity of the sample is further decreased by almost 6 orders of magnitude, they are the origin of about 92% of the heat and of more than 99% of the gamma dose rate.

Calculations with the most recent version EASY-97 were carried out for each of the investigated samples taking into account the time profile of irradiation and using the chemical composition of the material as determined by X-ray fluorescence analysis. A 175-group cross section library (VITAMIN-J structure) produced with a flat micro-flux weighting spectrum was used, to avoid falsifying influences of a weighting spectrum with fusion peak at 14.1 MeV for reactions with threshold in the 14-MeV region [5], and it was collapsed with the neutron flux spectrum at the sample positions.

The total activities calculated for the three alloys in sample position 1 are compared in Fig. 1 with the sum of the experimentally determined activities, after normalization to a sample mass of 1.0 g and a neutron fluence of 1.0×10^{12} cm^{-2}, for those decay times at which gamma spectra were measured.

The activation behaviour of the materials is quite similar for decay times shorter than about 80 h , whereas significant differences appear for longer times. These are mainly connected with the Cr content of the samples. For comparison, the activation profile of the ITER structural material AISI 316 LN (IG) is inserted in Fig. 1 [5]. The differences to the vanadium alloys amount to 1 - 2 orders of magnitude.

The uncertainties of the calculated activities, which include both cross section and half-life uncertainties, are shown in Fig. 1 by error bars. A typical value is 30%. All of the experimental points are within or very close to these bars, and a general validation of EASY-97 for activation of vanadium alloys by 14-MeV neutrons can be claimed.

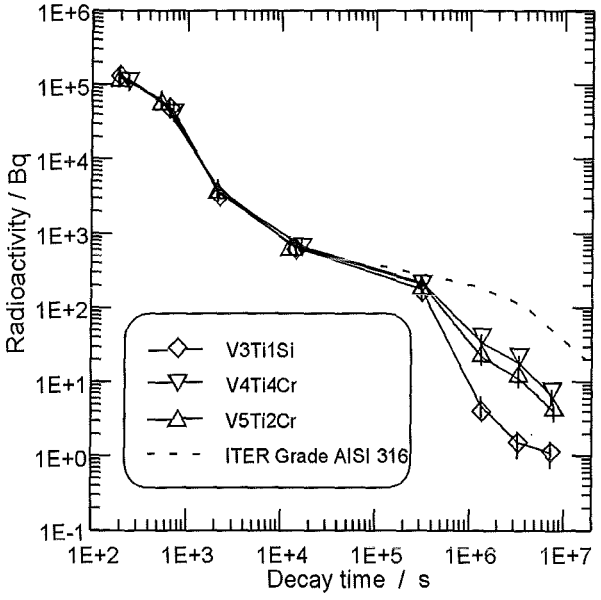

Fig. 1: Measured total activities, normalized to a sample mass of 1.0 g and to a neutron fluence of 1.0×10^{12} neutrons/cm^2 in comparison with the corresponding calculated activities (solid lines) and their uncertainty bars.

However, there are over- and underestimated activities in the total one. The ratios of calculated-to-experimental values (*C/E*) for the dominant activities are shown in Table 1. Again, the results for sample position 1 are presented. The position 2 results are included only for those activities where the difference of the neutron energies between position 1 and 2 has significant influence on the reactions producing the radionuclide and on the *C/E*. If the reactions contributing to a particular activity are very different between the three alloys, e. g. as for ^{52}V, the *C/E* are separately presented. In most cases the shares of the reactions are equal for the three alloys and the *C/E* obtained are consistent. Then the average value is given. The *C/E*-ranges in column 5 represent the total experimental uncertainties only, but not the calculated ones. They are estimated with the statistical and systematic errors of the gamma spectroscopy and of the neutron flux monitoring, and with adding the uncertainties of the gamma yield data used and of the elemental content. Usually they are smaller than the uncertainties of the calculated activities, and may be used for improving the calculational tools.

The largest overestimation is obtained for ^{47}Sc, with a clear dependence on the neutron incidence energy. The largest underestimation is observed for ^{52}V in V3Ti1Si, where, because of a Cr content of less than 0.001%, only the ^{51}V(n,gamma) reaction produces the radionuclide. With increasing shares of (n,p) and (n,d) reactions on Cr in V5Ti2Cr and in V4Ti4Cr the *C/E* are enhanced. As a first step the ^{51}V(n,gamma)-data should be checked and possibly re-evaluated.

Table 1: Dominant radionuclides in vanadium alloys, their half-life, the gamma rays used to determine the activity, the ratio of calculated-to-experimental activity obtained, the uncertainties of the experimental values as C/E-range and the portions of contributing nuclear reactions (Italic print for sample position 2, otherwise position 1 results).

Radio-nuclide	Half-life	Gamma-Energy (keV)	C / E calculation/ experiment ratio	C/E-range with the experimental uncertainties	Reaction Contribution
^{28}Al	2.25 min	1779	0.77	0.72 ... 0.83	^{28}Si(n,p) 99.5% ^{29}Si(n,d) 0.50%
^{48}Sc	83.82 d	889 1121	0.94	0.89 ... 0.99	^{46}Ti(n,p) 55.8% ^{47}Ti(n,d) 20.8% ^{46}Ti(n,p)m 14.5% ^{47}Ti(n,d)m 8.9%
^{48}Sc	*83.82 d*	*889* *1121*	*0.88*	*0.83 ... 0.92*	*^{48}Ti(n,p) 62.2%* *^{47}Ti(n,d) 15.2%* *^{46}Ti(n,p)m 16.2%* *^{47}Ti(n,d)m 6.4%*
^{47}Sc	3.35 d	159	2.18	2.04 ... 2.33	^{47}Ti(n,p) 24.1% ^{48}Ti(n,d) 43.3% ^{50}V(n,a) 5.6% ^{51}V(n,na) 26.8%
^{47}Sc	*3.35 d*	*159*	*1.65*	*1.54 ... 1.76*	*^{47}Ti(n,p) 39.1%* *^{48}Ti(n,d) 43.9%* *^{50}V(n,a) 7.6%* *^{51}V(n,na) 9.1%*
^{48}Sc	43.67 h	175 984 1038 1312	1.04	0.99 ... 1.10	^{48}Ti(n,p) 10.6% ^{51}V(n,a) 89.3%
^{45}Ti	3.08 h	511	1.15	1.00 ... 1.30	^{46}Ti(n,2n) 100%
^{51}Ti	5.8 min	320 609 928	1.07	1.00 ... 1.15	^{51}V(n,p) 100%
^{52}V *in V3Ti1Si*	3.75 min	1434	0.37	0.34 ... 0.40	^{51}V(n,g) 100%
^{52}V *in V4Ti4Cr*	3.75 min	1434	0.91	0.87 ... 0.95	^{51}V(n,g) 18.9% ^{52}Cr(n,p) 78.2% ^{53}Cr(n,d) 2.9%
^{52}V *in V5Ti2Cr*	3.75 min	1434	0.60	0.56 ... 0.65	^{51}V(n,g) 30.4% ^{52}Cr(n,p) 67.2% ^{53}Cr(n,d) 2.4%
^{51}Cr *in V3Ti1Si*	27.7 d	320	1.47	1.20 ... 1.73	^{51}V(p,n) 93.9% ^{52}Cr(n,2n) 4.2% ^{54}Fe(n,a) 1.8%

The ^{51}Cr activity in V3Ti1Si originates from protons produced in (n,p) and (n,pn) reactions. It can be calculated by a formalism for the treatment of sequential charged particle reactions developed at Karlsruhe [6].

In the same way as for the vanadium alloys, the previously obtained experimental results on the steels AISI 316 LN(IG), MANET and F82H were analysed with EASY-97. Also for these materials the *C/E* values revealed in detail several discrepancies which demand improvements of the nuclear data base.

Literature:

[1] R. A. Forrest, J-Ch Sublet and J. Kopecky, J., "The European Activation System", in Proc. of the Conf. on Nuclear Data for Science and Technology, Trieste, Italy, May 19-24, 1997, pp. 1140-1144.

[2] K. Seidel et al., "Measurement and analysis of radioactivity induced in vanadium alloys by 14-MeV neutrons", presented at 20th SOFT, Marseille, France, Sept. 7-11, 1998.

[3] U. von Möllendorff et al., „Activation test of vanadium alloys with a deuteron-beryllium neutron source", presented at 20th SOFT, Marseille, France, Sept. 7-11, 1998.

[4] V. D. Kovalchuk et al., "Neutron generator SNEG-13; neutron and photon field characteristics", Report IAE-5589/8, Russian Research Centre "Kurchatov Institute", Moscow, 1992.

[5] H. Freiesleben et al., "Experimental investigation of activities induced in fusion reactor materials by 14MeV neutrons", 4th Intern. Symp. on Fusion Nuclear Technology, Tokyo, Japan, April 6-11, 1997; Fusion Engineering and Design, in print.

[6] S. Cierjacks, P. Oblozinsky and B. Rzehorz, "Nuclear data libraries for the treatment of sequential (x,n) reactions in fusion materials activation calculations" Report KfK 4867, Karlsruhe, 1991

Staff:

H. Freiesleben
D. Richter
K. Seidel
S. Unholzer

2. White-spectrum activations by FZK

The 'white' deuteron-beryllium neutron source employing a 19-MeV deuteron beam of the Karlsruhe isochronous cyclotron produced a neutron flux density of 1.71×10^{11} neutrons/cm^2/s averaged over the 1 cm^2 samples. The source yield and neutron spectrum were obtained in collaboration with JAERI, Tokai-mura, Japan by activation foil dosimetry with subsequent unfolding calculations[6]. The a-priori guess spectrum required as input to the unfolding procedure was obtained by Monte-Carlo calculations using the MCNP-4A code [1] together with the M^{C}DELI neutron source routine [2]. These calculations also served for scaling the result from the 5x5mm^2 dosimetry foils to the 10x10mm^2 steel samples, in view of the pronounced anisotropy of the neutron source. The unfolded and scaled spectrum is shown in Fig. 2, together with a typical spectrum of the DEMO reactor for comparison.

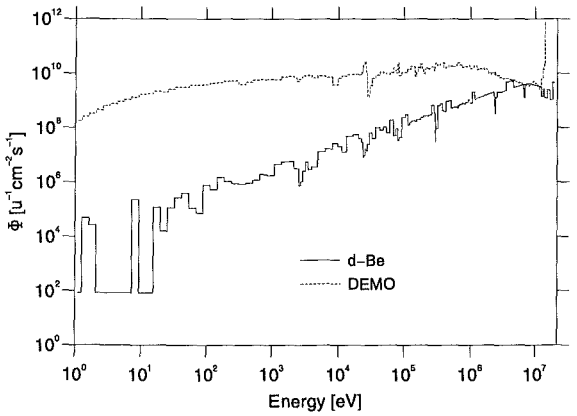

Fig. 2: Neutron spectra of the d-Be source and of DEMO (neutrons per unit lethargy, cm^2 and s)

The same alloys V3Ti1Si ('A') and V5Ti2Cr ('B') as in the TU Dresden work were investigated. Interest was centered on the longer-lived nuclides (halflives beyond about 1 day). The two samples were irradiated simultaneously for 65 h. Three 25-µm Ni foils interspersed with the samples served to monitor the neutron flux decrease over the stack thickness. The gamma activities of the samples were measured repeatedly after different cooling times using a 150 cm^3 high-purity germanium detector with a personal-computer based 4096-channel analyzer. The energy range covered was 0.1 to 2 MeV. The system was calibrated for both energy and efficiency using calibrated gamma ray sources. The sources or samples were placed at least 10 cm from the detector face. From the observed gamma spectral lines, activities in Bq were deduced, using decay data from Ref. [3].

Activation calculations were performed using the fusion inventory code FISPACT-97 with cross section data from EAF-97. The measured neutron spectrum described above in the 175-group VITAMIN-J structure was used to collapse the cross sections. Specific activities and gamma dose rates at the different cooling times were calculated for the total flux and irradiation time given above.

Table 2 presents the results as ratios *C/E* of calculated over measured activity. The uncertainty of the measured activities is generally about ±10% or better. Larger (estimated) uncertainties, due to limited counting statistics, are indicated in the table. A dash indicates that the nuclide could not be identified in the gamma spectrum. The *C/E* results for Nb-95 have '<' marks because the Mo content of the samples is only known as an upper limit. They are included to indicate that this radionuclide was positively identified in the γ spectra. The gamma dose rate fractions f_D in the table are taken from the inventory calculation.

At the investigated cooling times, Sc-46 is by far the dominant nuclide. It is produced from the Ti content of the alloys by (n,p) and (n,d) reactions, partly via the isomeric Sc-46m, and is predicted with excellent accuracy.

Sc-47 is, with our neutron spectrum, mostly produced by the ^{51}V(n,nα)^{47}Sc reaction. The marked overestimation of this activity may be due to imperfections of that cross section at higher energies. With 14-MeV neutrons (see Part 1 above) the share of this reaction is much smaller and the *C/E* is closer to unity.

The Cr-51 in alloy B originates almost completely (98%, according to the FISPACT pathway analysis) from the ^{52}Cr(n,2n) reaction. Alloy A, however, has no detectable Cr content. The Cr-51 found in this case is produced essentially (95%) by a sequential charged-particle reaction, ^{51}V(p,n)^{51}Cr, induced by protons originating from (n,p) reactions. This complex activation pathway may explain the overestimation of Cr-51 in alloy A.

The longest lived radionuclide found experimentally is Co-60. All the detected Co isotopes originate essentially from the Ni impurity. The reasons for the general underestimation of their inventories are not clear.

A trace activity of Ta-182 (114 d halflife) was identified in alloy B. It may originate from a W impurity, which was not searched for in the chemical analysis.

Literature:

[1] J. Briesmeister (ed.), report LA-12625-M (1993)

[2] E. Daum et al., „Neutronics of the high flux test region of the International Fusion Materials Irradiation Facility (IFMIF)", report FZKA-5868 (1997)

[3] R.B. Firestone, V.S. Shirley, C.M. Baglin, S.Y.F. Chu, and J. Zipkin, *Table of Isotopes, 8th ed..*, New York, Wiley 1996

Staff:

H. Giese
U. von Möllendorff
H. Tsige-Tamirat
P. Wilson

Table 2: Ratios *C/E* of calculated over experimental activity

$T_{½}$ Halflife
f_D Fraction of calculated γ dose rate at given cooling time
A dash means that the nuclide could not be identified in the γ spectrum

Cooling time:		41d		115d		112d	
Alloy:		A		A		B	
	$T_{½}$	f_D	***C/E***	f_D	***C/E***	f_D	***C/E***
Sc-46	84d	97.7	**0.97**	98.1	**0.97**	98.2	**1.00**
Sc-47	3.3d	0.15	**6.2**	--	--	--	--
Cr-51	28d	0.07	**2.7**±20%	0.02	**2.5**±20%	0.7	**1.17**
Mn-54	312d	0.2	**0.85**	0.4	**0.84**	0.4	**1.77**
Co-56	77d	0.01	--	0.01	**0.07**±20%	0.005	**0.08**±50%
Co-57	272d	0.005	**0.21**	0.008	**0.23**	0.004	**0.13**
Co-58	71d	1.3	**0.35**	1.2	**0.34**	0.55	**0.19**
Co-60	5.3a	0.01	**0.2**±50%	0.02	**0.2**±30%	0.01	**0.13**±30%
Zr-95	64d	0.1	**0.6**±30%	0.1	**0.38**	0.005	--
Nb-92m	10d	0.08	**0.5**±40%	0.001	--	0.005	--
Nb-95	35d	0.1	**(<0.6)**	0.16	**(<0.6)**	0.06	**(<2.4)**

SEAFP 2
Long Term Safety Program

Task 2: Improved Coverage of Events

Subtask 2: Event sequence analysis

For subtask 2 two reports have been prepared. The first report covered analyses to accidents as defined in the last annual report on this topic, especially the unmitigated quench in a TF coil. However, it turned out that the board of SEAFP2 requested a different focus for the accident analysis.

This initiated a new effort to identify accidents in the magnet system that specifically impair the integrity of the cryostat. Mechanical interaction between magnet system and cryostat has been investigated already under SEAFP1. Here the thermal interaction is considered. The most intense interaction occurs with shorts and arcs in the coil circuits in the vicinity of the cryostat wall. Amongst of 10 different multiple fault scenario a shorting arc at the bus bar of one coil, during a fast dump of the TF coil system, turned out to be the most severe case.

First analyses of this case revealed that the energy that can be converted in the arc is the stored energy in the shorted coil. Due to the bus bar short induced energy adds on the steady state value such that up to 20 GJ may be stored in the coil, assuming the coil is super conducting. This required a very detailed analysis investigating the quench behavior of the shorted coil. The analysis shows, that the current changes in the TF system change the magnet field such that quench in the shorted coil is achieved, even at low temperatures. Due to that most of the energy of the shorted coil is dumped into the quenching coil and the arc converts only a small fraction of it.

The next interesting question is how the energy converted in the arc can be translated into a hole size of the cryostat. Using the thickness of the cryostat wall a energy density can be determined necessary to melt a hole into the cryostat. Assuming the arc being a point source radiating its energy symmetrically from a point above the cryostat wall, a radius can be found which separates areas of the cryostat wall getting energy densities lower than the boundary value for melt through. This is shown in the figure below. There the hole radius is shown as a function of the wall distance and the energy converted in the arc. In this case it is assumed, that the location of the arc is the same throughout the transient.

Fig. 1: Hole radius in the cryostat wall as a function of arc energy and arc distance from the cryostat wall, energy in J.

Staff:

R. Meyder

SEAL 1.3
Beryllium Behaviour under Irradiation

The beryllium in blanket modules is inevitably oxidized to some extent during construction, and oxide can be located both at the grain boundaries and on the external surface of the specimen.

The external oxide layer could thicken slowly as the result of gettering of air leaks or water desorption over the operating lifetime. Furthermore, in an accident scenario, sudden ingress of air could cause rapid oxidation of the beryllium, accompanied by a temperature rise: clearly in this case the oxide layer would play an important role in determining the amount of tritium released during the accident.

Broken tensile specimens of irradiated western beryllium were used at JRC Ispra to assess the effect of air or water leaks on the release rate of tritium from bulk beryllium in the range of the first wall, and of the breeder, in operational and accidental conditions.

The experiments [1] show that leaks in the first wall temperature range have the effect of slowing tritium release below the level in inert gas, presumably because of thickening of the oxide barrier. During breeder accidents causing a large increase in temperature the presence of water vapor from leaks would cause an increase in tritium release rate above the rate in inert gas at the same temperature. This increase becomes important at 900 °C.

Above 600 °C tritium release rate in humid helium increases with time and finally overtakes the release rate in inert gas as shown in Fig. 1.

Dry air gives a stronger protective effect than water vapor and a factor 3 reduction in tritium release rate at 600 °C diminished to no reduction at 900 °C. On the contrary, humid air increase tritium release compared to inert gas at 600 °C [1].

The ANFIBE code developed at the Forschungszentrum Karlsruhe [2,3] is a sophisticated computer code for calculating both swelling and tritium release under simultaneous irradiation and heating. The tritium release from beryllium in inert gas has been successfully predicted in the whole range of experimental conditions for the experiments performed at the JRC Ispra. However, the code predictions fail for the accident scenarios in which an air/water leak occurs. In this case, the presence of a varying surface oxide layer and its effect on tritium egress cannot be successfully simulated with the present version of the code.

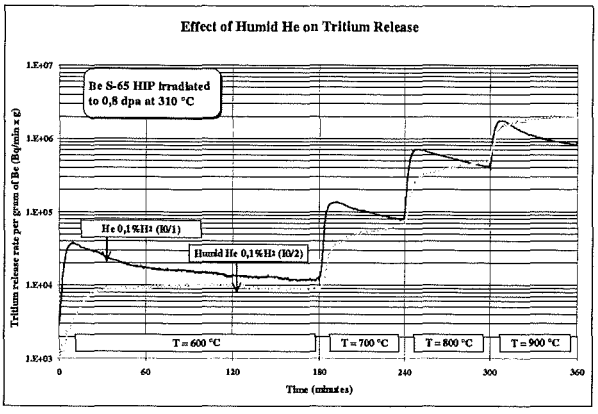

Fig. 1: Effect of water vapor at T>600 °C on tritium release from Be [1].

Literature:

[1] R.A.H. Edwards et al., "Tritium Release from Irradiated Beryllium During and After Surface Oxidation". Proc. 20th Symposium on Fusion Technology, Marseille, September 7-11, 1998.

[2] F. Scaffidi-Argentina et al., "ANFIBE A Comprehensive Model for Swelling and Tritium Release from Neutron-Irradiated Beryllium-I: Theory and Model Capabilities" Fusion Technology, Volume 32, Number 2 (1997) 179-195.

[3] F. Scaffidi-Argentina et al., "ANFIBE A Comprehensive Model for Swelling and Tritium Release from Neutron-Irradiated Beryllium-II: Comparison of Model Predictions with Experimental Results" Fusion Technology, Volume 33, Number 2 (1998) 146-163.

Staff:

Scaffidi-Argentina

Socio-economic Research on Fusion (SERF)

Fusion as a Large Complex System

Contribution 1998

Within the scope of the SERF macrotask S1: "Fusion as a large complex system,
subtitle : Governance", the activities of our group at the FZK-Institute for Technology Assessment and System Analysis (ITAS) consist of

- The description and analysis of the psychological and social impacts of fusion;
- The structure and course of societal conflicts during the introduction of fusion;
- Identification of the actors involved and their strategies and examination of the potentials for consensus and disagreement;
- Development of proposals for the social and cultural integration of fusion technology into the existing energy supply system

We cooperate with Prof. L. Ingelstam, Linköping University, Department of Technology and Social Change, Sweden und Mr. I. Cook, UKEA Fusion, Culham Science Centre, UK

In a first step the societal debate on nuclear fusion in the Federal Republic of Germany has been examined with the help of a literature review. Later on interviews with experts and key actors are planned.

Fusion research has the aim of providing fusion power plants as a source of energy supply to supplement fission reactors in the future. In Germany, future energy policy has been and will continue to be the topic in the debate on energy consensus. Our contribution will provide an introduction to this debate with special emphasis on nuclear fusion. The public discussion on fusion is examined in a media analysis of c. 1100 articles from daily and weekly newspapers and periodicals. Such press articles were sparked off by the immanent decision on further procedure in the construction of Iter, the successes of JET by producing a record value of fusion power in 1997 and the laying of the foundation stone of the fusion research plant Wendelstein 7-X at Greifswald on 19 June 1997 and the Energy Research Conference of the Minister for the Economy of the Land Mecklenburg-Vorpommern of 25 and 26 August 1997.

Our research approach continues with a comparison of the structures of nuclear power and fusion and the analysis of relevant groups of societal actors (political parties, religious denominations, trade unions, industrial associations, grass roots groups and environmentalists, NGOs).

The results were presented at the SERF-IIASA-Workshop: 12.7. - 14.7.1998 on "Fusion Perspectives in Economics, Politics and the Public"

Staff:

G. Bechmann
E. Lessmann
M. Rader

Appendix I: Table of ITER / NET Contracts

Theme	Contract No.	
ITER Magnets and TFMC Stress Analysis	ERB 5000 CT 950064	NET/95-384
High Voltage Components and Sensor Calibration for the ITER TFMC	ERB 5004 CT 970009	NET/96-438
ITER Tritium Plant Engineering Design	ERB 5004 CT 970037	NET/97-450
Evaluation and Refinement of the Conceptual Design of the Experimenal Test Assembly of the D-Li Neutron Source	ERB 5004 CT 970072	NET/97-453
Acceptance Tests of Strands and Sub-Stage CICC's with Respect to Heat Treatment of TFMC Pancakes	ERB 5004 CT 970082	NET/97-458
Design and Related Analyses of the ITER Breeding Blanket	ERB 5004 CT 970099	NET/97-459
Definition of an ITER Primary Wall Module Medium Scale Mock up Test Programme	ERB 5004 CT 980021	NET/98-433
ITER Reference Breeding Blanket Design (Stege 2); Materials Assessment, Pebble Bed and Tritium Analysis	ERB 5004 CT 980023	NET/98-472

Appendix II: FZK Departments Contributing to the Fusion Project

FZK Department	FZK Institut/Abteilung	Director	Ext.
Institute for Materials Research	Institut für Material- und Festkörperforschung (IMF)	I. Prof. Dr. K.-H. Zum Gahr	3897
		II. Prof. Dr. D. Munz	4815
		III. Prof. Dr. H. Haußelt	2518
Institute for Neutron Physics and Reactor Engineering	Institut für Neutronenphysik und Reaktortechnik (INR)	Prof. Dr. G. Keßler	2440
Institute for Applied Thermo- and Fluiddynamik	Institut für Angewandte Thermo- und Fluiddynamik (IATF)	Prof. Dr. U. Müller	3450
Institute for Reactor Safety	Institut für Reaktorsicherheit (IRS)	Prof. Dr. D. Cacuci	2550
Central Engineering Department	Hauptabteilung Ingenieurtechnik (HIT)	Dr. H. Rininsland	3000
Institute for Technical Physics	Institut für Technische Physik (ITP)	Prof. Dr. P. Komarek	3500
Central Experimental Engineering Department	Hauptabteilung Versuchstechnik (HVT)	Dr. K. Schubert	3114
- Hot Cells	- Heiße Zellen (HVT-HZ)	Dr. W. Nägele	3650
- Tritium Laboratory Karlsruhe	- Tritiumlabor Karlsruhe (TLK)	Dr. R.D. Penzhorn	3239
Central Department for Real-time Data Processing and Electronics	Hauptabteilung Prozeßdatenverarbeitung und Elektronik	Prof. Dr. H. Gemmeke	5635

Contributing:

Institute for Nuclear and Particle Physics, Technical University Dresden	Institut für Kern- und Teilchenphysik der Technischen Universität Dresden	Prof. Dr. H. Freiesleben	0351/4635461
Underwater Technology Centre Hannover of the Institute of Materials Science University of Hannover	Unterwassertechnikum Hannover des Instituts für Werkstoffkunde der Universität Hannover	Prof. Dr.-Ing. Dr.-Ing. E.h.mult. H. Haferkamp	0511/7624311

Appendix III: Fusion Project Management Staff

Head of the Research Unit	Dr. J.E. Vetter	ext. 5460 e-mail: joerg.vetter@pkf.fzk.de
Secretariate:	Mrs. I. Sickinger	ext. 5461 e-mail: ingeborg.sickinger@pkf.fzk.de
	Mrs. I. Pleli	ext. 5466 e-mail: ingrid.pleli@pkf.fzk.de
	Mrs. V. Lallemand	ext. 5466 e-mail: vera.lallemand@pkf.fzk.de
Project Budgets, Administration, Documentation	BW. G. Kast	ext. 5462 e-mail: guenter.kast@pkf.fzk.de
Studies, ITER / NET Contracts, Superconducting Magnets, Gyrotron Development	Dr. J.E. Vetter	ext. 5460 e-mail: joerg.vetter@pkf.fzk.de
Tritium Technology, Structural Materials	Dr. H.D. Röhrig	ext. 5463 e-mail: roehrig@pkf.fzk.de
Blanket Technology	Dl. A. Fiege	ext. 5465 e-mail: albert.fiege@pkf.fzk.de

Address: **Forschungszentrum Karlsruhe GmbH**
Nuclear Fusion Project Management

Post Office Box 3640, D - 76021 Karlsruhe / Germany

Telephone No: **07247-82- Extensions .....**

Telefax No: **07247-82-5467**

Telex No: **17 724 716**

world wide web: **http://www.fzk.de/pkf**